Surface Reaction Kinetics for Oxidation and Reforming of H_2, CO, and CH_4 over Nickel-based Catalysts

Zur Erlangung des akademischen Grades eines

DOKTORS DER NATURWISSENSCHAFTEN

(Dr. rer. nat.)

Fakultät für Chemie und Biowissenschaften

Karlsruher Institut für Technologie (KIT)- Universitätsbereich

genehmigte

DISSERTATION

von

Lic. – Chem. Karla Herrera Delgado

aus

San José, Costa Rica

Dekan: Prof. Dr. Peter Roesky

Referent: Prof. Dr. Olaf Deutschmann

Korrefetent: Prof. Dr. Jan-Dierk Grunwaldt

Tag der mündlichen Prüfung: 18 Juli, 2014

Finis coronat opus

Life is not easy for any of us. But what of that? We must have perseverance and above all confidence in ourselves. We must believe that we are gifted for something and that this thing must be attained.

Marie Curie

Abstract

The catalytic conversion of hydrocarbons for the production of hydrogen and syngas (H_2/CO) is of great interest in research and technology. Detailed heterogeneous kinetics can also provide a better understanding of the reactions involved during the catalytic processes commonly used in the synthesis gas production. The developed models can predict conversion and selectivity at varying operation conditions and hence supply guidance to reactor and catalyst design.

In this work, a hierarchical multistep surface reaction mechanism was developed for H_2 and CO oxidation, water-gas shift (WGS), reverse water-gas shift (R-WGS), and the oxidation and reforming of methane over nickel-based catalysts as well as, with slight modifications, for CO methanation. The reaction mechanism consists of 52 reactions with 6 gas phase species and 13 surface species. Important intermediates such as adsorbed HCO and COOH species are included in the kinetic model. The surface reaction mechanism can be applied to the $CH_4/CO_2/H_2O/CO/O_2/H_2$ systems operating in a wide range of external conditions. Models for gas-phase kinetics and flow fields are coupled with the surface mechanism to consider possible gas phase reactions at high pressures and temperatures. The overall thermodynamic consistency of the mechanism is ensured by a numerical approach in which surface reaction rate parameters are slightly modified to be thermodynamically consistent.

Within this study, the kinetics of methane reforming and oxidation as well as systems H_2/O_2, CO/O_2, CO/H_2, $CO/O_2/H_2$, WGS, and R-WGS were investigated in different reactor configurations (plug-flow, fixed-bed, and stagnation-flow reactors) following a hierarchical approach for the development of a reliable mechanism. The product stream was analyzed by FT-IR and MS, which allow time-resolved monitoring.

The mechanism was evaluated against experimental data at varying operating conditions performed in this study and also taken from literature. The model can be applied for industrial applications, quantitatively predicting the effect of inlet compositions, operating conditions. It can be extended to undesirable transient modifications of the active catalytic phase, e.g., by deactivation and coking, which are the main challenge in industrial catalytic reformers.

Kurzfasssung

Die katalytische Umsetzung von Kohlenwasserstoffen zur Herstellung von Wasserstoff und Synthesegas (H_2/CO) ist von akademischem und industriellem Interesse. Detaillierte, auf Elementarschritten aufbauende Reaktionsmechanismen führen zu einem besseren Verständnis der bei der Synthesegasproduktion ablaufenden katalytischen Prozesse. Die hier entwickelten Modelle sind in der Lage, Umsätze und Selektivitäten unter variierenden Bedingungen abzubilden. Dadurch können sie zum Reaktor- und Katalysatordesign herangezogen werden.

In der vorliegenden Arbeit wurde ein mehrstufiger Oberflächenreaktionsmechanismus für die Oxidation von H_2 und CO, die Wasser-Gas-Shift-Reaktion (WGS) und deren Umkehrung (R-WGS) und zur Oxidation und Reformierung von Methan über Nickelkatalysatoren entwickelt. Wird das Modell leicht modifiziert, läßt sich auch die Methanisierung von CO beschreiben. Der Reaktionsmechanismus besteht aus 52 Reaktionen mit 6 Gasphasen-Spezies und 13 Oberflächen-Spezies. Wichtige Zwischenprodukte wie adsorbierte HCO und COOH Intermediate wurden in das kinetische Modell einbezogen. Der Mechanismus ist auf CH_4/CO_2/H_2O/CO/H_2/O_2 Systeme anwendbar, die unter unterschiedlichsten Randbedingungen betrieben werden. Die chemischen Modelle werden mit der Strömung und Gasphasenreaktionsmechanismen gekoppelt, letzteren ist insbesondere bei hohem Druck und Temperatur von Relevanz. Die thermodynamische Konsistenz des Mechanismus wird durch einen numerischen Ansatz gewährleistet, in dem die Geswindigkeitskoefficient der Oberflächenreaktionen physikalisch begründet leicht modifiziert wurden.

Die Kinetik der Methanreformierung und –oxidation sowie deren Teilprozesse H_2/O_2, CO/O_2, CO/O_2/H_2 und WGS über Ni-Katalizator wurden in unterschiedlichen Reaktorkonfigurationen (Strömungsrohr-, Festbett- und Staupunkt-Reaktoren) untersucht. Hierbei wurde ein hierarchischer Ansatz für die Entwicklung des Oberflächenreacktions-mechanismus gewählt. Durch Analyse des Produktstroms mittels FT-IR und MS wurde eine zeitaufgelöste Messung ermöglicht. Der Mechanismus wurde anhand experimenteller Daten unter verschiedenen Betriebsbedingungen überprüft, welche entweder im Rahmen dieser Arbeit gewonnen oder der Literatur entnommen worden. Das verwendete Modell kann für industrielle Anwendungen eingeseht werden, indem er die Auswirkungen von Eduktzusammensetzung, der Betriebsbedingungen. Es kann erweitert werden, Alterungsprozesse wie Deaktivierung und Verkokung von Katalysatoren quantitativ zu prognostizieren, die bei industriell genutzten katalytischen Reformern eine große Herausforderung darstellen.

CONTENTS

1.Introduction

In recent years, much attention has been devoted towards the reforming of light hydrocarbons to produce synthesis gas (H_2/CO), which is an important intermediate in the chemical industry for manufacturing valuable basic chemicals and synthetic fuels, via methanol syntesis, oxo synthesis, and Fischer-Tropsch synthesis [1-6]. Hydrogen as a separate component of the synthesis gas is largely used in the manufacturing of ammonia, in a variety of petroleum hydrogenation processes, and as a clean feed gas for fuel cells [7-9].

Manufacturing syngas constitutes a significant portion of the investments in large scale gas conversion plants based on natural gas [4]. Natural gas mainly constitutes methane, which is one of the cleanest fuels, and an abundant energy source of the world, but often in remote areas. Processes such as steam reforming (SR), partial oxidation (POx) and dry reforming (DR) are the most common catalytic technologies for converting natural gas to synthesis gas in various compositions or to H_2 and CO separately as feedstock [2].

Since 1930, the most important industrial method to produce syngas has been the steam reforming of methane (Eq.1.1) over nickel-based catalysts. Conventional steam reformers deliver relatively high concentrations of hydrogen at high fuel conversion [10]. In this process, two stable molecules are converted into more reactive products [11]. Hence, the reaction is highly endothermic, and requires large efficient external energy supply for the conversion to be economically feasible.

Steam reforming of nickel catalyst always involves the risk of coke formation; which affects the performance of the process severely by the catalyst deactivation.

$$CH_4 + H_2O \rightarrow CO + 3H_2, \quad \Delta H^0_{298} = 205.9 \frac{kJ}{mol} \tag{1.1}$$

Due to increasing environmental concerns about global warming and oil depletion, methane reforming with CO_2 (Eq. 1.2) has gained considerable attention in the field of catalysis, as it offers the opportunity to convert these greenhouse gases (CH_4 and CO_2) into syngas. The dry reforming of methane has been also proposed as an alternative to SR, because it produces syngas with more suitable H_2/CO ratios for processes such as the oxo synthesis of aldehydes or the synthesis of methanol, acetic acid, etc.

$$CH_4 + CO_2 \rightarrow CO + H_2, \quad \Delta H^0_{298} = 247.3 \frac{kJ}{mol} \tag{1.2}$$

However, CO_2-reforming is rarely feasible. At the working pressure of a syngas plant (20–40 bar), the reaction will result in non-complete conversion of methane due to thermodynamics [4]. Furthermore, severe catalyst deactivation becomes the main obstacle with respect to its commercialization [12].

Catalytic partial oxidation of methane (Eq. 1.3) have been intensely studied as a promising option as compared to the endothermic reforming processes due the following advantages*: (i) the reaction is slightly exothermic, hence, no additional steam or heat supply is required; (ii) yields syngas with a H_2/CO mole ratio around 2, which is suitable for methanol and Fisher-Tropsch synthesis processes [3, 13]; (iii) smaller reactors can be used to achieve high CH_4 conversions and at short contact times *[14, 15]. Despite these advantages, the process is complicated. Different pre-treatment conditions or surface states on the catalyst may change the reaction mechanism. Consequently, many studies have been carried out in order to elucidate the kinetics behind this reaction [15-21].

$$CH_4 + \frac{1}{2}O_2 \rightarrow CO + 2H_2, \quad \Delta H^0_{298} = -36.0 \frac{kJ}{mol} \tag{1.3}$$

The reaction mechanism of the partial oxidation of methane to produce syngas is still controversial; two main paths have been suggested: one is the direct oxidation mechanism; here H_2 originates directly from CH_4 decomposition. Further interaction of adsorbed hydrocarbon species CH_x (x = 0, 1, 2, 3) with adsorbed atomic oxygen, produces carbon monoxide [5, 22, 23]. In the indirect route, methane is totally oxidized to CO_2 and H_2O, as long as oxygen is present close to the catalyst surface. Then, the remaining CH_4 is reformed with steam or CO_2 to H_2 and CO [16, 24-27]. The reaction paths for partial oxidation of methane and its kinetics over novel metals have been widely studied by Deutschmann´s research group [28-36].

The different routes mentioned above for syngas production are effective, but more efficient production facilities are required. The properties of the syngas vary with the synthesis in question [37]. Therefore, the choice of technology for syngas manufacture depends on the scale of operation [4].

* The paragraph with the CPOX advantages over reforming processes has been taken from reference [14, 15].

1.1 Motivation

One of the main problems in the catalytic conversion of methane, especially at elevated pressure and temperature, is coke formation. Coke deposition on catalysts and reactor pipe walls are serious problems in many industrial reactors that involve methane as fuel [38-42].

Noble metals have been found to be less prone to coke formation under oxidation and reforming conditions [43]. However, the high prices make them economically unsustainable. Ni based catalysts are preferred in industrial applications due to fast turnover rates, good availability and low costs compared to noble metals, but the use is limited by higher tendency towards coke formation than noble metals [44-47]. At the industrial level, the catalyst properties and operating conditions must be carefully selected to minimize undesirable transient modifications of the active catalytic phase, e.g., by deactivation and coking [11]. Several methods and different nickel-based catalysts have been proposed for reducing coke formation, however, a solution has still not been found [48-50].

In order to optimize both the catalytic oxidation and reforming of methane processes, it is necessary to achieve better understanding of the elementary steps involved in the reaction mechanism at a molecular level, and along with the deactivation kinetics behind coke formation.

Micro-kinetic modeling provides perfect boundaries for models covering different scales [11]. A reliable kinetic model can be coupled with mass and heat transport models in order to provide insight into the behavior of reforming reactors. Therefore, the sequence and interaction of the reaction paths have to be analyzed combining different reaction systems, as the conditions in any flow reactor vary along the flow directions, covering a wide range of mixture compositions that lead to different local reaction rates.

The reforming and oxidation of methane have been studied by several techniques. Different reaction mechanism and corresponding kinetic models, have been proposed. However, despite all the reported experimental and theoretical studies, the detailed path for conversion of CH_4 to syngas and carbon, remain controversial and often contradictory [3]. In a pioneering work, Xu and Froment [51] proposed a reaction mechanism for the steam reforming of methane accompanied by water-gas shift reactions on a $Ni/MgAl_2O_4$. Bradford and Vannice [52] studied the mechanism and kinetics of dry reforming over Ni catalyst with different supports. The authors proposed $*CH_x$ as the reaction intermediary and also suggested that differences in activity for CO_2/CH_4 reforming maybe due to metal-support interactions. Aparicio [53] proposed an overall model that described steam reforming of methane over $Ni/MgO\text{-}MgAl_2O_4$

catalyst. The rate constants of surface elementary reactions were extracted from transient isotopic experimental data by fitting the measured response curves to micro kinetic models. Chen et.al [11, 47] modified Aparicio´s micro-kinetic model for methane reforming with CO_2 and deactivation by carbon formation. Wei and Iglesia [54] proposed a common sequence of elementary steps for CH_4 decomposition, water-gas shift reactions on Ni/MgO catalysts. Isotopic studies and forward rate measurements showed a mechanistic equivalence among all CH_4 reactions. Blaylock et.al [55] developed a micro-kinetic model for methane steam reforming using thermodynamic data from plane wave density functional theory (DFT) over nickel crystals. However, their model did not fit the experimental results for steam reforming at industrial conditions, although the prediction in the forward rate of dissociative methane adsorption is reasonable [55].

Despite all the kinetic studies performed over nickel-based catalysts, the development of a detailed mechanism for simultaneous modeling of partial oxidation, steam and dry reforming of methane, as well as the sub systems behind these reactions (e.g., H_2 and CO oxidation, water-gas shift and its reverse reaction) have not been described yet.

1.2 Methodology and objectives

This study focuses on the development of a multi-step, thermodynamically consistent reaction mechanism for catalytic conversion of methane under oxidative and reforming conditions over nickel catalysts. The modeling approach is based on the mean-field approximation.

The development of the heterogeneous reaction kinetics is based on theoretical studies such DFT, MC, semi-empirical calculations [55-57], as well as experimental kinetic studies. A previous developed model by Maier et al. [58], which serves as the basis for the novel kinetics, has already been successfully applied for steam reforming of methane at a wide range of temperatures and feed compositions [58, 59]. The overall thermodynamic consistency of the mechanism is ensured between 373-1273 K (100-1000 °C) by a numerical approach (Section 2.5).

In a unified surface reaction mechanism, all possible reaction paths and interactions between the chemical species under investigation have to be taken into account. Numerous experiments are carried out at laboratory scale under varying fuel composition and over a wide range of temperature (Section 4 and Section 5).

By following a hierarchical approach, the reactions described below have been studied consecutively:

- Hydrogen oxidation (H_2/O_2)
- Carbon monoxide oxidation (CO/O_2)
- Preferential oxidation of carbon monoxide ($CO/O_2/H_2$)
- Water-gas shift (WGS, CO/H_2O)
- Reverse water-gas shift (R-WGS, CO_2/H_2)
- Methanation of carbon monoxide (CO/H_2)
- Partial oxidation of methane (CPOx, CH_4/O_2)
- Steam Reforming (SR, CH_4/H_2O)
- Dry Reforming of methane (DR, CH_4/CO_2)

The applicability of the mechanism is evaluated against new experimental data obtained from plug-flow, fixed bed, and stagnation-flow reactors, using different nickel-based catalyst at varying operating conditions, along with additional data from literature.

The numerical simulation is performed using DETCHEM^{TM}, which is a software package specifically designed for numerical simulation of flow fields coupled with detailed gas-phase and surface kinetics in chemical reactors at laboratory and technical scale.

Furthermore, the surface mechanism is coupled with a gas-phase model to numerically reproduce the methane reforming experiments at high temperatures and elevated pressure.

The kinetics of the methanation reaction are also studied in order to understand the formation of methane, as a sub product, during the WGS and R-WGS reactions (Section 5). The thermodynamically consistent reaction mechanism developed for $CH_4/CO_2/H_2O/CO/O_2/H_2$ systems, is slightly modified to fit the experimental data obtained for methane formation during WGS and R-WGS reactions.

The developed reaction kinetics can be used as baseline for more complex kinetic models. The mechanism can be also extended to industrial applications, to numerically predict the effect of inlet compositions and operating conditions in technical reactors.

2.Principles of Modeling and Simulation

The key to optimize chemical catalytic processes lies in a better understanding of the elementary chemical reactions and their energetic at a molecular level. *Micro-kinetic modeling has received much attention as a method because it provides a link between models and phenomena across a wide range of multiple conditions and scales. Micro-kinetic models enable the analysis of the interactions between the gas-phase and surface kinetics and transport that take place in a catalytic cycle. Therefore, the simulation of the experiments needs to include appropriate models for mass and heat transfer as well as possible gas phase reactions* [60].

The kinetic parameters are proposed based on information from experimental surface science and theoretical surface science studies. The estimation of these kinetic parameters is discussed in the Section 2. 3. The equations to determine the rate constants in gas phase and on surfaces are presented in the Sections 2.1 and 2.2 respectively.

A detailed multi-step surface reaction mechanism is presented in this work. The model describes the surface kinetics that takes place during the catalytic oxidation and reforming of CH_4 over nickel-based catalyst. The methodology for the mechanism development is described in Section 2.4.

The overall thermodynamic consistency of the mechanism is ensured by a numerical approach, in which surface reaction rate parameters are slightly modified to be thermodynamically consistent. The numerical approach is presented in Section 2.5 [58]. The applicability of the mechanism is tested against experiments carried out in plug-flow, fixed-bed, and stagnation-flow reactors, performed for this study and also taken from literature.

* This paragraph has been taken from reference [60].

2.1 Reaction kinetics in the gas-phase

In many catalytic processes, the reactions do not occur exclusively on the catalyst surface but also in the fluid flow. At high temperatures and elevated pressure, non-catalytic reactions in the gas phase play an essential role in the formation of higher hydrocarbons. Therefore, any reaction simulation needs to include an appropriate model for homogeneous kinetics along the flow models. The species governing equations in fluid flow simulations usually contain a source term such as R_i^{hom} denoting the specific net rate production of species i due to homogeneous chemical reactions [60].

The basis of the equations to describe the reacting kinetics in the gas-phase is derived from the literature [61-65]. Considering a set of K_{g} elementary chemical reactions in the gas-phase, among the total number N_{g} of gas-phase species A_i,

$$\sum_{i=1}^{N_{\mathrm{g}}} v_{ik}^{'} A_i \rightarrow \sum_{i=i}^{N_{\mathrm{g}}} v_{ik}^{''} A_i \tag{2.1}$$

where $v_{ik}^{'}$ and $v_{ik}^{''}$ are the stoichiometric coefficients of the species i in the k^{th} reaction. The total molar production rate in gas-phase $\dot{\omega}_i$ of the species i in homogeneous reactions is given by

$$\dot{\omega}_i = \sum_{k=1}^{K_{\mathrm{g}}} v_{ik} k_{\mathrm{f}k} \prod_{j=1}^{N_{\mathrm{g}}} c_j^{v_{jk}^{'}} \tag{2.2}$$

where $v_{ik} = v_{ik}^{'} - v_{ik}^{''}$ and c_i are the species concentrations.

Being a modified Arrhenius expression; the chemical source term of homogeneous reactions can be expressed by

$$R_i^{\mathrm{hom}} = M_i . \dot{\omega}_i \tag{2.3}$$

$$k_{fk} = A_k . T^{\beta_k} . \exp\left(-\frac{E_{\mathrm{a}k}}{\mathrm{RT}}\right) \tag{2.4}$$

Here, A_k is the pre-exponential factor, β_k is the temperature exponent, $E_{\mathrm{a}k}$ is the activation energy, and a_{jk} is the order of reaction k related to the concentration of species j.

2.2 Heterogeneous reactions

The mechanism of heterogeneously catalyzed gas-phase reactions can be described by the sequence of elementary reaction steps, including adsorption and desorption of the species, surface diffusion and chemical reaction of the adsorbed species [66].

There are different models to describe the reaction mechanism; one of the main approaches is the Langmuir-Hinshelwood mechanism, where the rate of the heterogeneous reaction is controlled by the reaction of the adsorbed molecules, and that all adsorption and desorption pressures are in equilibrium. The rate expression can be derived to be a function of surface coverages of adsorbed species on the surface [67].

Another model is the Eley-Rideal mechanism, which assumes that only one of the molecules adsorbs and the other reacts with it directly from the gas phase, without adsorbing. Figure 2.1 shows a comparison between these two models.

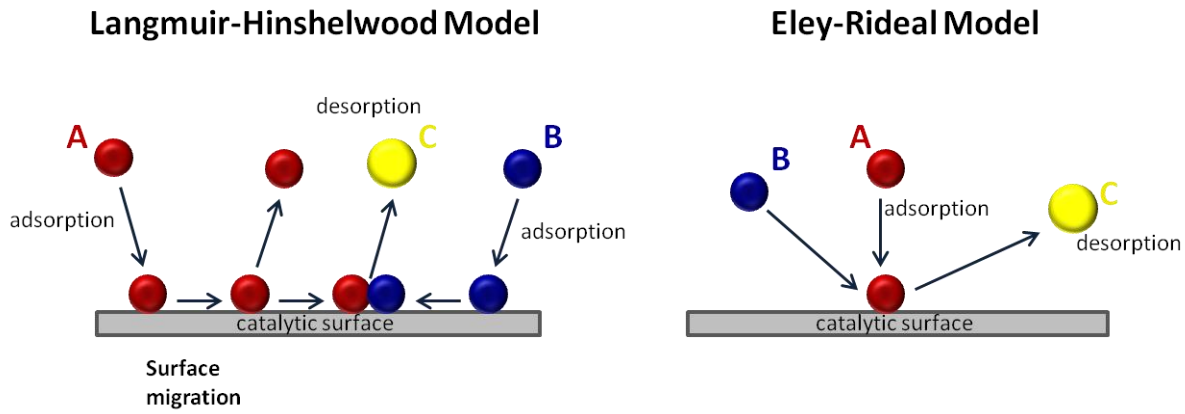

Figure 2.1 *Comparison of Langmuir-Hinshelwood and Eley-Rideal models.*

The reaction mechanism presented in this study is developed based on the Langmuir-Hinshelwood model.

Surface reactions are modeled by a mechanism consisting of elementary-step-like reactions using the mean-field approximation. The approximation is related to the sizes of the computational cells in the flow field simulation, assuming that the local state of the active surface can be represented by means of values for this cell. Therefore, the model assumes randomly distributed adsorbates on the surface which is viewed as being uniform [24, 68]. Under the mean field assumptions, a surface reaction can be expressed as:

$$\sum_{i=1}^{N_g+N_s} \nu'_{ik} A_i \rightarrow \sum_{i=1}^{N_g+N_s} \nu''_{ik} A_i \tag{2.5}$$

where N_g is the number of gas-phase species, N_s is the number of surface species, ν_{ik} the stoichiometric coefficient and A_i denotes the species i. The concentration of the absorbed species can be express in terms of a surface coverage (Θ_i), according to the relation

$$\Theta_i = \frac{c_i \sigma_i}{\Gamma} \tag{2.6}$$

were c_i are the species concentrations, which are given, e.g in mol/m^2, σ_i is the number of surface sites that are occupied by species i, and Γ ($2.6 \cdot 10^{-5}$ mol/ m^2 for nickel) is the surface site density, i.e., the number of adsorption sites per catalytic surface area. Thus, locally resolved reaction rates depend on the local gas-phase concentrations, surface coverage, and temperature.

The total molar production rate $\dot{s}_i$ of surface species on the catalyst is calculated in analogy to gas phase reactions as a product of rate coefficients and concentrations determined by

$$\dot{s}_i = \sum_{k=1}^{K_s} \nu_{ik} k_{fk} \prod_{i=1}^{N_g+N_s+N_b} c_i^{\nu'_{jk}} \tag{2.7}$$

$$(i = 1, \ldots., N_g + N_s + N_b)$$

Here, K_s is the number of surface reactions (including adsorption and desorption), ν_{ik} is the stoichiometric coefficient, c_i are the species concentrations for N_s adsorbed species and, for the N_g and N_b gaseous and bulk species, respectively.

The temperature dependence of the rate coefficients is described by a modified Arrhenius expression where additional coverage dependencies ε_{ik} of the activation energy are taken into account:

$$k_{fk} = A_k T^{\beta_k} \, exp\left[\frac{-E_{ak}}{RT}\right] \prod_{i=1}^{N_s} \exp\left[\frac{\varepsilon_{ik}\,\Theta_i}{RT}\right] \tag{2.8}$$

Here, A_k is the pre-exponential factor, β_k is the temperature exponent, E_{a_k} is the activation energy, and ε_{ik} is used to define coverage dependent activation energies.
The rate for adsorption reactions are calculated using sticking coefficients S_0.

$$\dot{s}_i^{\text{ads}} = S_0 \sqrt{\frac{RT}{2\pi M_i}}\, c_i \cdot \prod_{j=1}^{N_s} \Theta_j^{\nu'_j} \tag{2.9}$$

Here, c_i is the gas-phase concentration of the adsorbate and Θ_j is the coverage of the adsorbing site.

The surface reaction rate is multiplied by two factors to yield the flux of gas-phase species at the gas-catalyst interface.

$$j_{i,surf} = \mathrm{F}_{\text{cat/geo}} \,.\, \eta \,.\, M_i \,.\, \dot{s}_i \tag{2.10}$$

The specific catalytic surface area $\left(\mathrm{F}_{\text{cat/geo}} = A_{\text{cat}}/A_{\text{geo}}\right)$ is the ratio between the active catalytic surface area (A_{cat}) which is calculated from chemisorption measurements and the geometric surface area $\left(A_{\text{geo}}\right)$. Internal mass transfer limitations are taking into account by means of an effectiveness factor η. The effectiveness factor is the ratio of the observed reaction rate to that which would occur in case of diffusion limitations was eliminated.

2.3 Estimation of the rate constants

The kinetic data of each reaction step in the surface reaction mechanism are originated from surface science experiments using numerous techniques to study adsorption, surface reactions and desorption as well as from theoretical studies as Density Functional Theory (DFT), Unity Bond Index-Quadratic Exponential Potential (UBI-QEP), Molecular Dynamics (MD) and Monte Carlo (MC) simulations [56, 69, 70].

Estimation of the Pre-exponential Factor (A_k)

Dumesic et al.[71] proposed that Transition-state theory can be used to make general order-of magnitude estimates for surface reactions under various conditions of surface mobility. Experimental calculations of vibrational frequencies, rotational relaxation times, surface diffusion coefficients, surface entropies of adsorbed species etc., provide important information of the species on the catalyst surface, such information is vital to estimate the pre-exponential factors using transition-state theory and statistical mechanics.

The nominal value of the pre-exponential factor of an elementary reaction is assumed to be $10^{13}\ \mathrm{N_A}/\Gamma(\mathrm{cm^2}/\,\mathrm{mol,s})$, where $\mathrm{N_A}$ is the Avogadro´s number; $10^{13}\mathrm{s^{-1}}$ is the order of magnitude of $\frac{k_B T}{h}$ (k_B the Boltzmann´s constant, h Planck´s constant) and would be the value expected from transition stated theory; $\Gamma = 2.66\mathrm{x}10^{-9}\ \mathrm{mol/cm^2}$ is the site density, that is calculated by assuming a site area of $6.5\mathrm{x}10^{-2}\ \mathrm{nm^2}$ as observed for nickel [58, 72].

Sticking coefficients are used as kinetic data for the adsorption of reactants and products (H_2, CO, CO_2, CH_4, O_2, and H_2O) represented in the reaction mechanism.

Estimation of the activation Energy (E_{a_k})

The activation energy (E_{a_k}) can be determined from theoretical and experimental surface science studies. However, the activation energies estimated from experimental data are more accurate than estimations from theoretical studies. Activation energies obtained by density functional theory methods (DFT) depend on the cluster size [55, 73]. Nevertheless, the data can be also well estimated by the semi-empirical calculations such as unit bond index-quadratic exponential potential (UBI-QEP) approach [74, 75]. Collision and transition-state theories

facilitated the extraction of activation energies from experimental measurements of rate constants over a narrow range of temperatures [71].

2.4 Development of a multi-step surface reaction mechanism

The development of a reliable surface reaction mechanism is a complex process. The methodology for the development of the surface reaction mechanism is explained by Deutschmann [68]. A tentative reaction mechanism is proposed on information from experimental surface science and theoretical surface science studies. Such a mechanism should include all possible paths for formation and consumption of the chemical species under consideration in order to be "elementary like" to be applicable over a wide range of conditions. Numerous experimental data such as conversion, selectivity, coverage, and temperature profiles need to be compared with simulation results based on the proposed mechanism. Therefore, many experiments are carried out at laboratory scale using different reactor configurations and operating conditions. In addition, experimental data from literature are used as well for the evaluation of the mechanism. Simulation of laboratory reactors require appropriate models for mass and heat transfer as well as possible gas-phase reactions in order to evaluate the intrinsic kinetics. Sensitivity and flow analysis leads to the crucial steps in the mechanism for which refined kinetic experiments and data may be needed. The development of a reliable surface reaction mechanism follows the scheme in Figure 2.2.

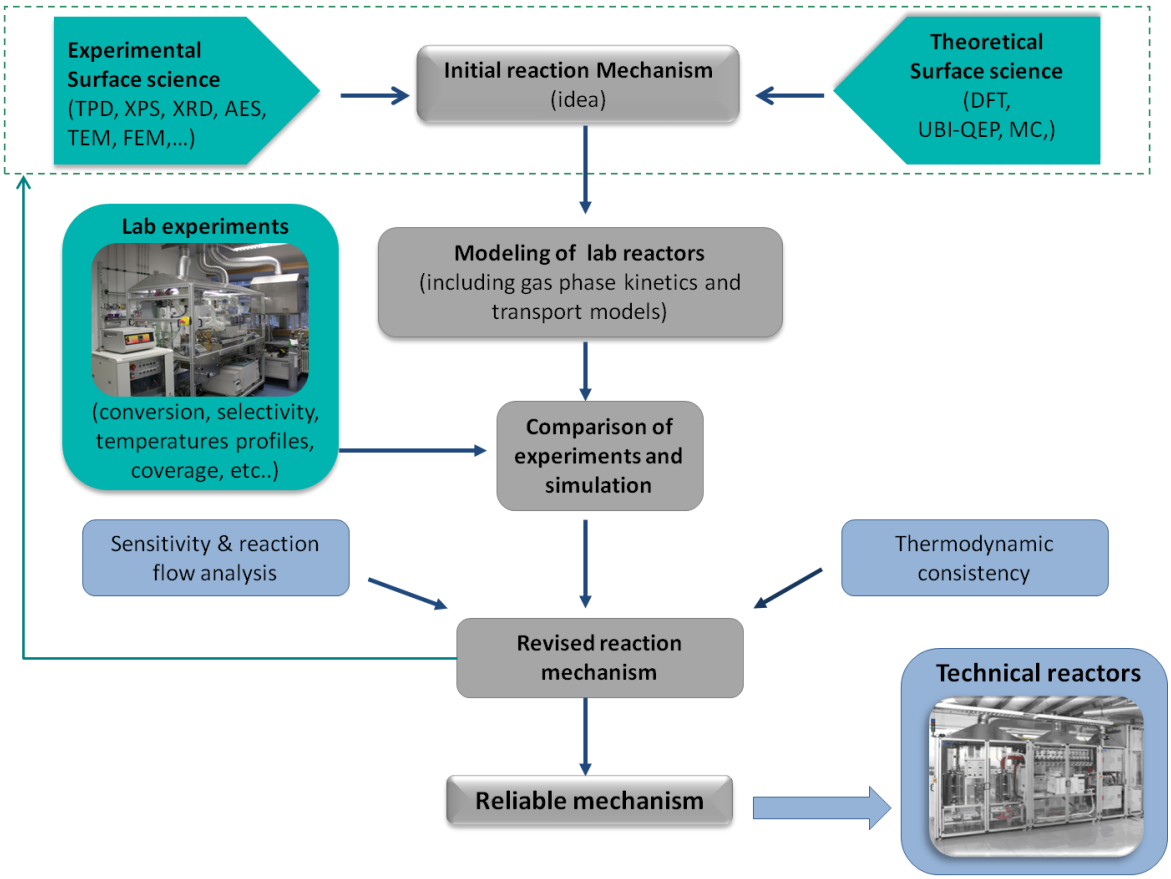

Figure 2.2 *Methodology for the development of detailed reaction mechanism for heterogeneously catalyzed gas-phase reactions. Picture of the technical reactors taken from reference [76] .*

Sensitivity analysis and flow analysis

Sensitivity analysis is used to analyze reaction mechanisms and support their development. The sensitivity analyses identify which kinetic parameter are the most influential on the simulations results. Here, the analysis it carried on surface reactions at constant temperature. The change of amount n_i of species i is given by

$$\frac{\mathrm{d}n_i}{\mathrm{d}t} = A_{\mathrm{cat}}\dot{s}_i \tag{2.11}$$

where A_{cat} is the catalytic surface area. Time dependent sensitivity coefficient $E_{i,k}(t)$ is defined as the logarithmic derivative of the amount of species i with respect to the rate coefficient $k_{\mathrm{f}k}$,

$$E_{i,k}(t) = \frac{\partial n_i(t)}{\partial \ln k_{fk}} \ . \tag{2.12}$$

Using Eq. 2.7 for the total molar production rate is possible to solve for the time development of the sensitivity coefficient

$$\frac{\mathrm{d}E_{i,k}(t)}{\mathrm{d}t} = A_{\mathrm{cat}} \nu_{ik} k_{fk} \prod_{j=1}^{N_g+N_s} c_j^{\nu'_{jk}} \tag{2.13}$$

The sensitivity coefficient describes the contribution of the k^{th} reaction on the production of species i. Eq. 2.13 can be integrated in time along with the solution of the conservation equations of each species. The relative sensitivities of all reactions on the products are more useful than absolute sensitivities during the mechanism development. For that reason, the sensitivity coefficients for a given i are rescaled such that the largest absolute value $|E_{i,k}|$ becomes unity.

Flow analysis determines the main path of production and consumption of the species within the catalytic cycle. It analysis obeys the same equations as previously described for sensitivity analysis. However, in the flow analysis case, just the coefficients $E_{i,k}$ for which species i is an immediate product of reaction k are considered.

Since all of them are non-negative, they can be seen as weights in a directed graph that connects reactants and products along edges of elementary-step reactions. The $E_{i,k}$ are again scaled such that the sum of the weights originating in a root node becomes unity.

2.5 Thermodynamic consistency

One problem in setting up a reaction mechanism is the difficulty to ensure the thermodynamic consistency of the predicted simulation results. Therefore, an adjustment algorithm was developed by S. Tischer, in order to set up thermodynamically consistent surface reaction mechanisms [58]. The procedure is explained as follows.

The equilibrium of a chemical reaction, is defined by the thermodynamic properties of the participating species

$$v_1' A_1 + v_2' A_2 + \cdots \underset{k_\mathrm{r}}{\overset{k_\mathrm{f}}{\rightleftarrows}} v_1'' A_1 + v_2'' A_2 + \cdots \tag{2.14}$$

For given temperature dependent rate coefficients $k_\mathrm{f}(T)$ and $k_\mathrm{r}(T)$, the equilibrium condition yields

$$K_c(T) = \frac{k_{\mathrm{f}k}(T)}{k_{\mathrm{r}k}(T)} \tag{2.15}$$

where $K_c(T)$ is the equilibrium constant with respect to concentration. Expressed with respect to pressures, $K_p(T)$, the equilibrium activities, obey the equation

$$K_p(T) = \exp\left(-\frac{\Delta_{\mathrm{R}k} G(T)}{RT}\right) \tag{2.16}$$

where $\Delta_{Rk} G$ is the temperature dependent change of Gibbs free energy, and R the universal gas constant. The equilibrium condition between a forward (f) and its reverse reaction (r) can be converted by the factor

$$F_{c/p} = \frac{k_{\mathrm{f}k}(T)}{k_{\mathrm{r}k}(T)} = \prod_{i=1}^{N_\mathrm{g}+N_\mathrm{s}} {c_{i,0}}^{\nu_{ik}} \tag{2.17}$$

where $F_{c/p}$ is a conversion factor from partial pressures and coverages to concentrations. Thereby, the reaction rates can be link with the thermodynamic properties by

$$\frac{k_{\mathrm{f}k}(T)}{k_{\mathrm{r}k}(T)} = F_{c/p} \exp\left(-\frac{\Delta_{\mathrm{R}k} G(T)}{RT}\right) \tag{2.18}$$

In logarithmic form, the change of Gibb´s free energy of a reaction can be written in terms of the Gibbs free energies of the gas-phase and surface species.

$$\ln k_{\mathrm{f}}(T) - \ln k_{\mathrm{r}}\,(T) = \ln F_{c/p} - \sum_{i\ (\mathrm{gasphase})} v_i \frac{G_i(T)}{RT} - \sum_{i(\mathrm{surface})} v_i \frac{G_i(T)}{RT} \tag{2.19}$$

However, in the development of surface reaction mechanism, the thermodynamic properties of the gas-phase species are known functions, whereas the potentials of the surface species are often unknown.

A complete surface reaction mechanism typically contains more pairs of reversible surface reactions than surface species. Therefore, the rate coefficients cannot be chosen independently for all reactions. To indentify these dependencies an adjustment procedure is applied in the process of development of a surface reaction mechanism. The adjustment ensures that for a proposed set of rate coefficients thermodynamic functions $G_i(T)$ exist for all surface species.

The basis of the adjustment method is described in a previous work [58]. However, the method was extended to also ensure that functions $G_i(T)$ behave in a thermodynamic way in order to obtain always positive heat capacities.

In the Eq. 2.20 the terms $\ln k_{\mathrm{f}}$, $\ln k_{\mathrm{r}}$ and $\frac{G_i(T)}{RT}$ of the species with thermodynamic properties can be written as functions of the form

$$y_i(T) = a + b \ln T + \frac{c}{T} \tag{2.20}$$

The idea of the adjustment algorithm is to find minimal correction terms $x_{\mathrm{f}k}(T)$ and $x_{\mathrm{r}k}(T)$ such that functions $y_i(T)$ exist for all surface species.

The objective to make a reaction mechanism thermodynamically consistent is now to find minimum changes for the functions $x_k\,(T) = \ln k_{\mathrm{f}/rk}$ and $y_i(T) = G_i(T)/RT$ such that the equation

$$\begin{aligned}(\ln k_{\mathrm{f}k} + x_{\mathrm{f}k}(T)) - (\ln k_{\mathrm{r}k} + x_{\mathrm{r}k}\,(T)) \\ = \ln F_{c/p} - \sum_{i\ (\mathrm{gasphase})} v_i \frac{G_i(T)}{RT} - \sum_{i(\mathrm{surface})} v_i y_i\,(T)\end{aligned} \tag{2.21}$$

Thereby, the adjustment algorithm not only yields a set of thermodynamic consistent rate coefficients, but also suitable thermodynamic potentials for the surface species. The program also ensures a realistic temperature dependency of the functions $G_i(T)$ [77].

2.6 Numerical implementation

Chemical reaction engineering and combustion processes are generally characterized by complex interactions between transport and chemical kinetics. The optimization of catalytic processes not only lies in the development of new catalysts to synthesize a desired product, but also in the understanding of the interaction of the catalyst with the surrounding reactive flow field.

In some reactors, the desired products are mainly produced in the gas phase, especially at high temperatures and elevated pressure, noncatalytic reactions in the gas phase play an essential role in the products formation [68]. Therefore, fluid flow simulations need to include an appropriate model for homogeneous kinetics as well as surface reaction models.

The flow field of multi-component mixtures can be described by the transient three-dimensional (3D) Navier-Stokes equation, coupled with the energy and species equations. The simulation of fluid flows, including detailed schemes for surface and gas phase chemistry has recently received considerable attention due to the development of numerical algorithms and the establishment of detailed elementary reaction mechanisms.

DETCHEM^{TM} software package applies detailed models for the description of the chemical reactions and transport processes [77]. It has been designed for a better understanding of the interactions between transport and chemistry and can assist in reactor and process development and optimization. In this study, the applicability of the kinetic models is evaluated against experiments performed in a continuous-flow, fixed bed, and stagnation-flow reactors.

2.6.1 DETCHEM^{PLUG} and DETCHEM^{PACKEDBED}

The behavior of the plug-flow and fixed bed chemical reactors is modeled using a one-dimensional (1D) description of the reactive flow. For the simulations, tools of the DETCHEM software package DETCHEM^{PLUG} and DETCHEM^{PACKEDBED} are used [77].

The elementary-step reaction mechanism is coupled with a flow-field model. The model assumes that (a) quantities (e.g. velocity, concentrations, temperature) do not vary in the transverse direction, and (b) axial diffusion of any quantity is negligible relative to the corresponding convective term.

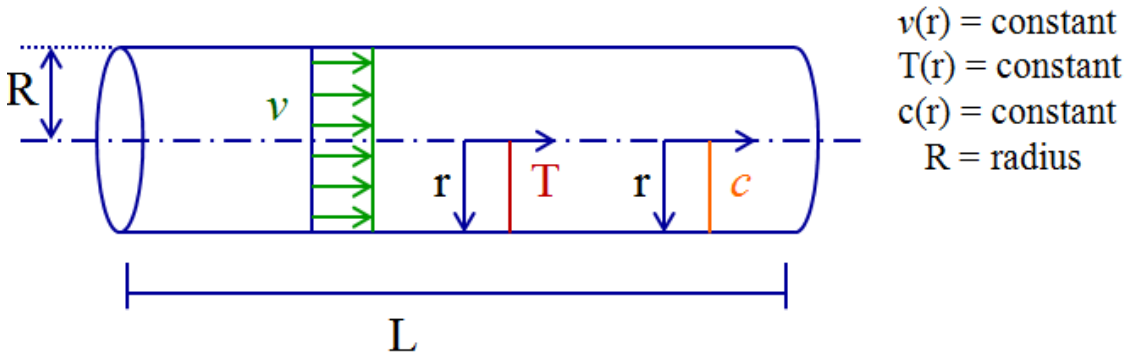

Figure 2.3 *Schematic diagram of a plug-flow reactor*

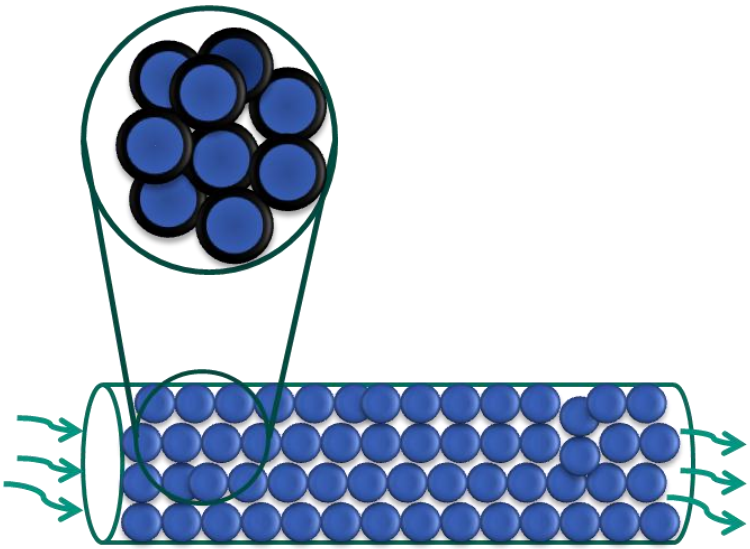

Figure 2.4 *Schematic diagram of a fixed bed reactor.*

Both plug flow and fixed bed are defined by the following set of equations:

Continuity equation

$$\frac{d(\rho u)}{dz} = a_v \sum_{i=1}^{N_g} \dot{s}_i M_i \tag{2.22}$$

Species conservation

$$\rho u \frac{d(Y_i)}{dz} + Y_i a_v \sum_{i=1}^{N_g} \dot{s}_i M_i = M_i (a_v \dot{s}_i + \dot{\omega}_i \varepsilon) \tag{2.23}$$

Conservation of energy

$$\rho u A_c \frac{d(c_p T)}{dz} + \sum_{i=1}^{N_g} \dot{\omega}_i h_i M_i \varepsilon + \sum_{i=1}^{N_g+N_s} \dot{s}_i h_i M_i a_v = \frac{4}{d_h} U (T_w - T) \tag{2.24}$$

and equation of state

$$pM = \rho RT \tag{2.25}$$

Here, the following variables are used: ρ is the density, u is the velocity, a_v is the catalytic area to volume ratio, ε is the porosity, A_c is the area of cross section of the channel, N_g is the number of gas-phase species, N_s is the number of surface species, $\dot{s}_i$ is the molar rate of production of species i by surface reaction, $\dot{\omega}_i$ is the molar rate of production of species i by the gas-phase reaction, M_i is the molecular mass of species i, Y_i is the mass fraction of species i, c_p is the specific heat capacity of species i, h_i is the specific enthalpy of species i, U is the overall heat transfer coefficient, T_w is the wall temperature, T is the gas temperature, p is the pressure, and M is the average molecular weight.

In case of the plug-flow model, the porosity is $\varepsilon = 1$. The area to volume ratio (a_v) defines the circumference to cross section of a plug-flow reactor. For circular channels this parameter is 2/r, where r is the radius of the channel [42].

The area to volume ratio used in the fixed bed model, (a_v) is calculated with Eq. 2.26.

$$a_v = D_{Ni} \cdot \frac{m_{Ni}}{M_{Ni}} \cdot \frac{1}{\Gamma} \cdot \frac{1}{V_{bed}} \tag{2.26}$$

For the calculation a_v, of dispersion D_{Ni} was experimentally determined by chemisorption measurements. The surface-site density value $\Gamma = 2.66 \cdot 10^{-5} \text{mol m}^{-2}$ is taken from the literature [58]. In Eq.2.26, M_{Ni} represents the molar mass of nickel (58.7 g/mol), V_{bed} is the total volume of the catalytic bed (m^3), and m_{Ni} is the net weight. % Ni (g).

2.6.2 DETCHEM^{CHANNEL}

One or two dimensional flow field description of a flow reactor can be used to describe the chemical reactions in monolithic honeycombs or similar reactor configurations based on the solution of Navier-Stokes equations in cylindrical coordinates for asymmetric flow field in radial and axial coordinates. Here, the reactive flow field in the channel is described by steady-state, two-dimensional boundary-layer equations with transport coefficients that depend on composition and temperature [78]. Along the channel, the variations of gas-phase composition in axial and radial directions as well as the axial variation of the surface coverage with adsorbed species are taken into account.

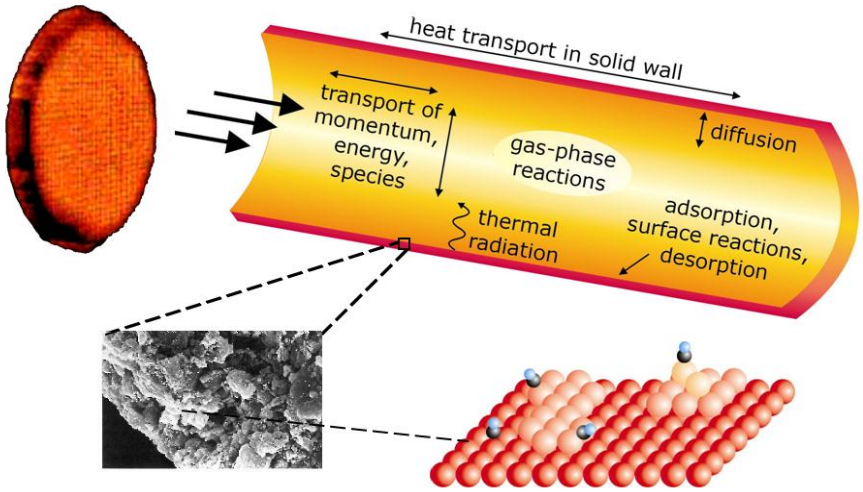

Figure 2.5 *Interaction of chemical and physical processed inside a channel of a catalytic honeycomb. Figure taken from* [68].

The rectangular shaped channel of the catalytic monolith is approximated by a cylindrical channel model. Using given inlet conditions (velocity, species mass fractions), the two-dimensional laminar, isothermal flow field of the fluid at steady state is computed using the boundary-layer approximation, which leads to the following set of equations [78]:

Continuity equation

$$\frac{\partial(r\rho u)}{\partial z} + \frac{\partial(r\rho u)}{\partial r} = 0 \tag{2.27}$$

Axial momentum conservation

$$\frac{\partial(r\rho u^2)}{\partial z}+\frac{\partial(r\rho uv)}{\partial r}=-r\frac{\partial p}{\partial z}+\frac{\partial}{\partial r}\left(\mu r\frac{\partial u}{\partial r}\right) \tag{2.28}$$

Radial momentum conservation

$$\frac{\partial p}{\partial r}=0 \tag{2.29}$$

Species continuity

$$\frac{\partial(r\rho u\mathrm{Y}_i)}{\partial z}+\frac{\partial(r\rho v\mathrm{Y}_i)}{\partial r}=\frac{\partial}{\partial r}(rj_i)+r\dot{\omega}_\iota \tag{2.30}$$

Energy conservation

$$\frac{\partial(r\rho u\mathrm{h})}{\partial z}+\frac{\partial(r\rho v\mathrm{h})}{\partial r}=r\,\mathrm{u}\frac{\partial p}{\partial z}+\frac{\partial}{\partial r}\left(\lambda r\frac{\partial T}{\partial r}\right)-\frac{\partial}{\partial r}\left(\sum_i rj_i\mathrm{h}_i\right) \tag{2.31}$$

where r is the radial coordinate and p the pressure.

Boundary Conditions

$$j_{i,\mathrm{surf}}=\mathrm{F}_{\mathrm{cat/geo}}\,.\;\eta\,.\,M_i\,.\;\dot{s}_i \tag{2.32}$$

The ratio of catalytic to geometric area, $\mathrm{F}_{\mathrm{cat/geo}}$, was calculated with Eq. 2.33 [32]

$$\mathrm{F}_{\mathrm{cat/geo}}=\frac{\frac{D_{\mathrm{Ni}}}{\Gamma}\cdot\mathrm{cat.\,loading}\cdot\mathrm{V}_{\mathrm{Monolith}}}{(\pi\cdot d_{\mathrm{h}}\cdot L_{\mathrm{Monolith}})\cdot\mathrm{N}_{\mathrm{channels}}} \tag{2.33}$$

In Eq. 2.33, the dispersion D_{Ni} is experimentally measured. The surface-site density value $\Gamma = 2.66\cdot10^{-5}\mathrm{mol\,m^{-2}}$ is taken from the literature [58], the total number of channels, $\mathrm{N}_{\mathrm{channels}}$, is calculated from the cell density and the front face of the catalyst.

2.6.3 DETCHEM^{STAG}

A stagnation-flow reactor with analysis of spatially resolved concentrations profiles is a useful tool to investigate heterogeneous kinetics, because it represents a well-defined flow field with a zero-dimensional catalytic surface, which enables coupled modeling of heterogeneous chemistry and reactive flow at steady-state and transient conditions [79-81]. The flow is directed on to a catalytic solid plate, whereby the reactants interact in the boundary-layer. The temperature, velocity, and the species contribution depend linearly on the distance of the catalytic plate. The one- dimensional DETCHEM^{STAG} code, simulates the behavior of a catalytically active stagnation point flow reactor [77, 82]. The model equations couple with flow, energy, species continuity and surface equations, describes the interaction between the active surface and the gas flow in axial direction as well as the one-dimensional boundary layer.

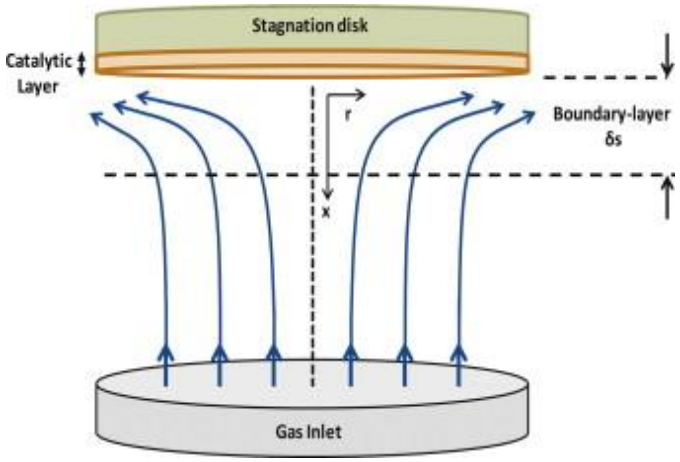

Figure 2.6 *Schematic illustration of the stagnation-flow configuration. Figure taken from reference* [82].

In the stagnation point flow reactor, the catalytically active surface interacts with the surrounding flow. Therefore, model equations consist of three parts, i.e., gas-phase equations, surface equations and boundary conditions. The numerical solution of the stagnation flow reactor is performed by solving the following conservation equations [83].

Mixture continuity

$$0 = \frac{p}{R}\frac{\bar{M}^2}{T^2}\left[T\sum_i \frac{\partial Y_i}{\partial t}\frac{1}{M_i} + \frac{\partial T}{\partial t}\frac{1}{\bar{M}}\right] - 2\rho V - \frac{\partial(\rho v_x)}{\partial x} \tag{2.34}$$

Radial momentum

$$\frac{\partial V}{\partial t} = -\frac{\rho v_{\mathrm{x}}}{\rho}\frac{\partial V}{\partial x} - V^2 - \frac{\Lambda}{\rho} + \frac{1}{\rho}\frac{\partial}{\partial x}\left(\mu\frac{\partial V}{\partial x}\right) \tag{2.35}$$

Eigenvalue of the radial momentum

$$0 = \frac{\partial \Lambda}{\partial x} \tag{2.36}$$

Thermal energy

$$\frac{\partial T}{\partial t} = -\left[\frac{\rho v_{\mathrm{x}}}{\rho} + \frac{1}{\rho c_p}\sum_{i=1}^{N_{\mathrm{g}}} c_{\mathrm{p},i} j_i\right]\frac{\partial T}{\partial x} - \frac{1}{\rho c_{\mathrm{p}}}\sum_{i=1}^{N_{\mathrm{g}}} \dot{\omega}_i M_i h_i + \frac{1}{\rho c_{\mathrm{p}}}\frac{\partial}{\partial x}\left(\lambda\frac{\partial T}{\partial x}\right) \tag{2.37}$$

Species continuity

$$\frac{\partial Y_i}{\partial t} = -\frac{\rho v_x}{\rho}\frac{\partial Y_i}{\partial x} + \frac{1}{\rho}\dot{\omega}_i M_i - \frac{1}{\rho}\frac{\partial j_i}{\partial x} \tag{2.38}$$

Ideal gas law

$$\rho = \frac{p\bar{M}}{RT} \tag{2.39}$$

In these equations, ρ is the density, u the axial velocity, V normalized velocity, Y_i the mass fractions of species i, j_i the diffusion velocity of species i, μ the viscosity, Λ the eigenvalue of the momentum, λ the thermal conductivity, and h_i the enthalpy of species i. In this approach, Eq. 2.32 is again used for the boundary conditions to couple the fluid flow with the catalytic processes at the surface. The ratio of catalytic to geometric surface area, $\mathrm{F}_{\mathrm{cat/geo}}$, is calculated with Eq. 2.40. In this equation, represents the dispersion D_{Ni}, Γ is the active-site density of Ni ($\Gamma = 2.66 \cdot 10^{-5}\mathrm{mol\ m^{-2}}$), m_{Ni} is the net weight. % Ni (g) and $\mathrm{A}_{\mathrm{geo}}$ is the geometrical surface area of the disk $2.38 \cdot 10^{-3}\ \mathrm{m}^2$

$$\mathrm{F}_{\mathrm{cat/geo}} = D_{Ni} \cdot \frac{m_{Ni}}{M_{Ni}} \cdot \frac{1}{\Gamma} \cdot \frac{1}{A_{geo}} \tag{2.40}$$

Since the catalyst has a considerably thick (~100 μm) wash-coat layer, the calculated $F_{cat/geo}$ value cannot be directly applied. The diffusion limitation is taken into account by introducing an effectiveness factor η (E.q 2.32).

2.6.4 DETCHEM^{EQUIL}

DETCHEM^{EQUIL} code calculates the equilibrium mole composition of a given gas-phase mixture, which is defined by its thermodynamic potentials [77].The state of a closed system can be described by pressure p , temperature T, and the number of moles of each species n_i.This state can be expressed in terms of the Gibbs free energy as potential function $G(T, p, n_i)$. If the Gibbs Free Energy reaches a minimum with respect to all possible combinations of n_i, the state system is considered in equilibrium.

For a mixture of ideal gases, the Gibbs free energy is given by the expression

$$G(T, p, n_i) = \sum_i n_i \left(G_i^0(T) + \mathrm{RT} \ln \frac{\mathrm{p_i}}{\mathrm{p^0}} \right) \tag{2.41}$$

where G_i^0 denotes the specific molar free enthalpy at pressure p^0. p_i is the partial pressure according to the ideal gas law

$$p_i = \frac{n_i RT}{V} \tag{2.42}$$

For a reaction k with stoichiometric coefficients v_{ik}, the change of the Gibbs free energy is given by

$$\Delta_k G^0(T) = \sum_i v_{ik}\, G_i^0(T) \tag{2.43}$$

If the reaction *k* is in equilibrium, the solution of Eq. 2.41 yields

$$\Delta_k G^0(T) = -RT \ln \mathrm{K_p}\,(\mathrm{T}) \tag{2.44}$$

This is equivalent to the formulation involving the equilibrium constant. Reaction k is in equilibrium when:

$$K_p = \exp\left(\frac{-\Delta_{Rk} G^0}{RT}\right) = \prod_i \left(\frac{\mathrm{p_i}}{\mathrm{p^0}}\right)^{\nu_{ik}} \tag{2.45}$$

In the Eq. 2.45 the K_p term is defined as temperature dependent equilibrium constant with respect to partial pressures ($\mathrm{p_i}$ and $\mathrm{p^0}$).

DETCHEM$^{\mathrm{EQUIL}}$ program also calculates the enthalpy and entropy of each species as polynomial functions using the thermdata database (Appendix, Table 3).

The equilibrium molar compositions are calculated for constant temperature and pressures in this study.

3.Experimental Studies

In order to experimentally determine the kinetics of the oxidation and reforming of H_2, CO and CH_4 over nickel-based catalysts, several sets of experiments were carried at different experimental conditions and reactor configurations.

The catalytic experiments to determine the kinetics of hydrogen oxidation, CO oxidation, water-gas shift, reverse water-gas shift, reforming and oxidation of methane are carried in the laboratories of the Institute for Chemical Technology and Polymer Chemistry (ITCP) at KIT.

Experimental studies for dry reforming and steam reforming are also performed at different reactor configurations and operating conditions, as part of the investigation for the BMWi DRYREF Project (FZK 0327856A) in cooperation with BASF, Linde group, hte AG, Leipzig University, and TU München. The experimental results were used to develop a heterogeneous kinetic model for methane oxidation and reforming processes on nickel-based catalysts.

The main features of the experimental setups, the catalysts used and the experimental conditions are described briefly in the next sections.

3.1 Fixed bed reactor

Most of the industrial catalytic process are carried out in fixed bed reactors due to simplicity of the technology, ease operation and high conversion per unit mass of catalyst compared with reactor configurations [84]. Fixed bed reactors consist of a compact, immobile stack of solid catalyst within a container [85].

The appropriate fixed bed reactor design needs to be selected depending on the catalytic process in order to improve the performance of the reactor. Strong exothermic reactions increase the temperature in some locations of the catalytic bed, the so-called hot spots. Temperature control thus plays a predominant role in selective reaction control in general and in particular in the case of exothermic multistep reactions.

*The processes taking place in the fixed bed can be described by the following steps [86]:

- Diffusion of the reactants from the gas space through the outer gas-particle boundary layer, macropores, and micropores,
- Chemisorption on active centers,
- Surface reactions,
- Desorption of the products,
- Back-diffusion of the products into the gas space.

Since most of the reactions take place with a considerable heat of reaction, a corresponding heat transport is superimposed on the mass transport. The control of the micro-kinetics consists in micro-pore diffusion, chemisorption, surface reaction, and desorption of the products. In order to optimize the yields, reaction conditions (feedstock concentrations, pressure, temperature, and residence time) should be selected accordance with the process and the micro-kinetic properties of the catalyst. The design of the particles should be also carefully chosen to limit the pressure drop, maximize the specific area of the catalyst, and facilitate the mass and heat transfer through the catalytic bed. Temperature control thus plays a predominant role in selective reaction control in general and in particular in the case of exothermic multistep reactions* [84, 86].

3.1.1 Experimental setup of the fixed bed reactor

A set of kinetic experiments is carried out in a fixed bed reactor. In this work, the experimental setup is referred to as CPOX 2 reformer. Details of CPOX 2 experimental setup can be found elsewhere [87]. The experimental set- up system is schematically depicted in Figure 3.1.

* Paragraphs taken from references [84, 86].

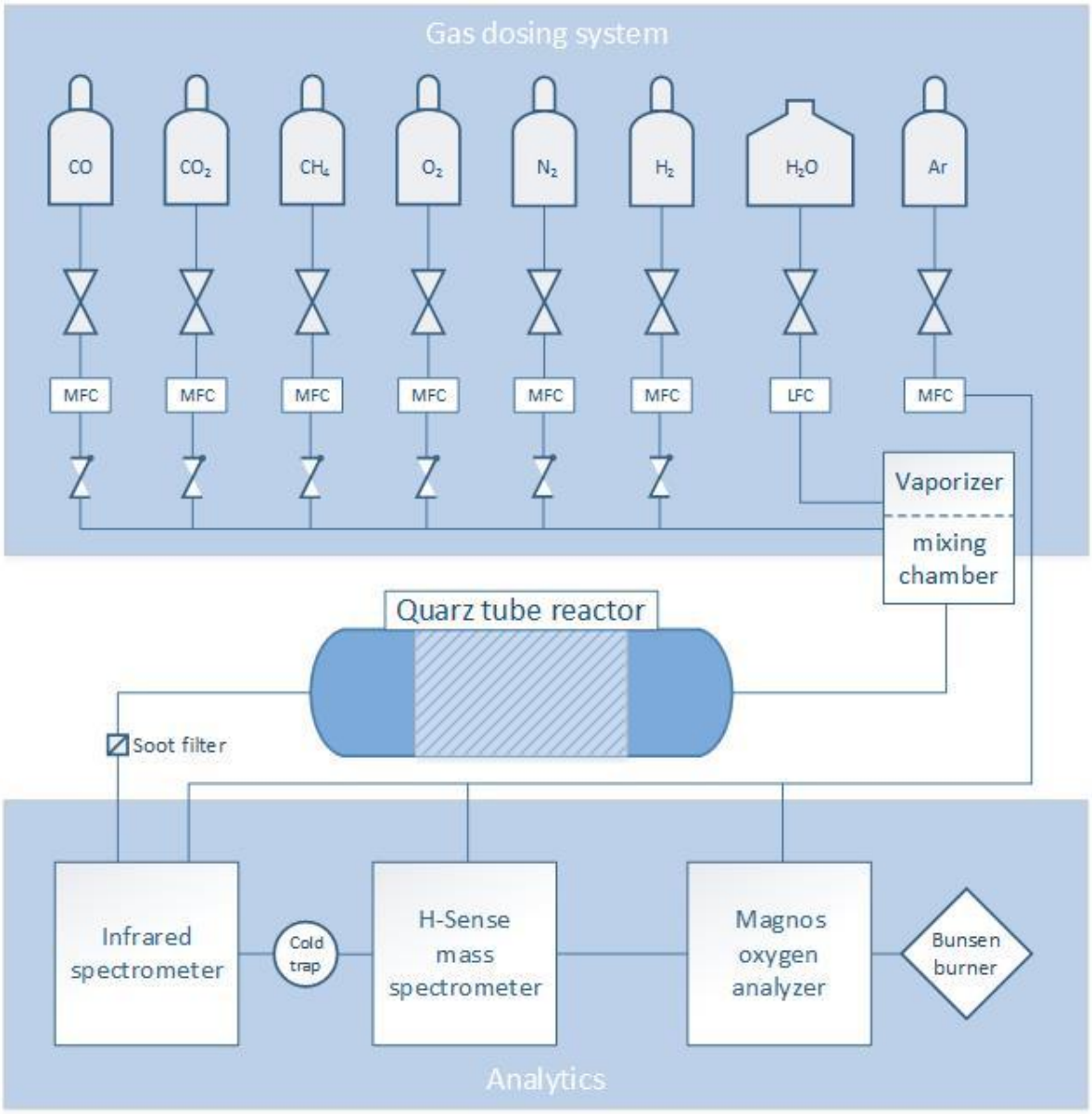

Figure 3.1 *Schematic diagram of the experimental setup used for catalytic oxidation and reforming experiments employing a nickel bed catalyst.*

The dosage of the gases (H_2, CO, O_2, CH_4, CO_2, and N_2) is controlled by mass flow controllers produced by Bronkhorst Hi-Tec. Water is provided by a liquid flow controller from a water reservoir. After evaporation the water steam is mixed directly into the reactant gas stream. Before entering the reactor the reactants gas stream is preheated to 463 K.

The reactor consisted of a quartz tube with an inner diameter of 10 mm filled with 10 mg to 20 mg of a nickel-based catalyst surrounded by a quartz frit and glass wool. Two separate thermocouples are used to measure the temperature of the gas phase during the reaction, type

K in front of the catalyst and type N behind the catalyst respectively. Figure 3.2 show the schematic drawing and photo of the catalytic bed.

a) **b)**

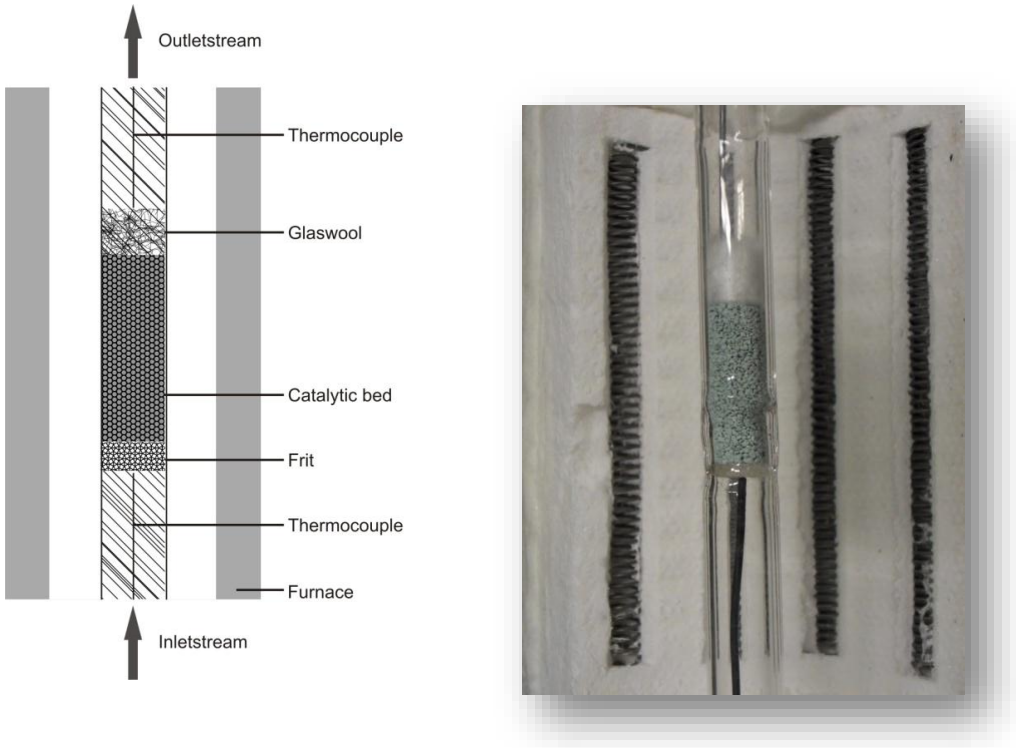

Figure 3.2 *Schematic drawing of the fixed bed reactor (a) and picture of the real catalytic bed (b).*

The complete reactor is surrounded by a furnace for heating and thermal insulation. The product composition is measured by means of online Fourier Transform Infrared Spectrometer (FT-IR), Mass spectrometer (H_2-MS) and paramagnetic oxygen detection (Magnos). Remaining water in the product stream is removed by a cold trap after passing the FT-IR to protect the following sensitive analytics. Argon is used as purifier gas for the analytics exclusively.

Figure 3.3 *Picture of the fully assembled reactor setup CPOX 2.*

3.1.2 Powdered nickel-based catalyst

Two nickel-based catalysts with different catalytic activity were synthesized and characterized in BASF laboratories as part of the DRYREF Project. The catalysts are used for the fixed bed experiments performed at KIT. Both catalysts have a particle size between 500-1000 µm. The powdered catalysts used in this work are named as: Fixedbed_Ni_BASF_Cat.1 and Fixedbed_Ni_BASF_Cat.2.

These catalysts are confidential and proprietary to BASF, therefore, further details about the catalyst cannot be disclosed.

Porosity of the catalytic bed

The porosity of the catalytic bed was not measured experimentally. Therefore, a statistical method proposed by Pushnov [88] is used to estimate the porosity of the catalytic bed.

The porosity of a fixed granular bed (FGB) will depend on the method of charging, the shape of the grains, and the ratio of the vessel diameter *D* to the grain diameter *d* [88]. The exact porosity value of the catalytic bed can only be determined experimentally by measuring the bulk density ρ_b of the bed and the density ρ_s of the grains of the solid phase:

$$\varepsilon = 1 - \left(\frac{\rho_b}{\rho_s}\right) \tag{3.1}$$

Pushnov [88] derived an empirical expression (Eq. 3.2) to estimate the average porosity of grains of different shape, which indicates that for cylindrical vessels with D/d>2 and FGB height H>20d:

$$\varepsilon = \frac{A}{(D/d)^n} + B \tag{3.2}$$

where A, B, and *n* are constants dependent on the shape of the grains (see Table 3.1).

Table 3.1 Constants dependent on the shape of the grains [88].

Shape of the grains	Coefficients		
	A	B	*n*
Spheres	1.0	0.375	2
Cylinders	0.9198	0.3414	2
Lumps of irregular shape	1.5	0.35	1
Rashing rings	0.349	0.5293	1

Table 3.2 shows the data used to calculate the porosity of the catalytic bed using the Eq. 3.2. The catalyst grains have an irregular shape with a particle size between 500-1000 µm. An intermediate size of the grain diameter of 750 µm is used to estimate the porosity of the catalytic bed. The vessel diameter *D* (10 mm) is the diameter of the reactor used in the laboratory from ITCP at KIT.

Table 3.2 Data used to estimate the porosity of the catalytic bed.

Vessel diameter *D* [m]	grain diameter *d* [m]	A	B	*n*	Estimate Porosity[ε]
0.01	7.5×10^{-4}	1.5	0.35	1	0.46

Catalyst pre-treatment

Before all experiments, the powdered nickel-based catalyst is conditioned with 20 vol.% O_2 diluted in nitrogen at 673 K (400 °C) for 30 min and then reduced with 10 vol.% H_2 diluted in nitrogen with a total flow of 4 SLPM at 873 K (600 °C), maintaining this temperature for 1 h as a regeneration procedure, after 1h the system is cooled down to room temperature.

3.1.3 Experimental conditions

The different reactants components are mixed at various gas compositions diluted in nitrogen. Typical operation conditions for the experiments are: flow velocity of 4 SLPM, total pressure of 1 bar and temperatures in the range of 393-1173 K (100-900 °C). A temperature ramp of 15 K/min is applied.

The following experiments are conducted in order to understand interactions between different gaseous species and the catalytic surface in the reaction system:

- Carbon monoxide oxidation (CO/O_2)
- Preferential oxidation of carbon monoxide ($CO/O_2/H_2$)
- Water Gas-Shift (CO/H_2O)
- Reverse Water Gas-Shift (CO/H_2O)
- Methane Partial and Total Oxidation (CH_4/O_2)
- Methane Steam Reforming (CH_4/H_2O)
- Methane Dry Reforming (CH_4/CO_2)

The experimental data are further used to develop the surface reaction mechanism over nickel. In Section 4 and Section 5, each experiment is explained in detailed.

3.2 Stagnation-flow reactor

The stagnation-flow reactor (SFR) offers a simple configuration to investigate heterogeneously catalyzed gas-phase reactions. Its fluid-mechanical properties enable measuring and modeling the gas-phase boundary layer adjacent to the zero-dimensional catalytic surface [63, 89].
The stagnation-flow experiments presented in Section 4.1 and Section 4.2 were performed by C. Karakaya [81, 90].

3.2.1 Experimental setup of the stagnation-flow reactor

A detailed explanation of the set-up design can be found elsewhere [90] and will only be described briefly here. The experimental set-up consists of a stagnation-flow reactor, a gas feeding system and analytics (Figure 3.4).The stagnation-flow reactor set-up enables working pressures between 100-1100 mbar; the pressure is controlled by a butterfly valve (MKS, T3BIA). The reactor can be operated at temperatures of 298-1173 K (25-900 °C). The inlet gases are dosed via mass flow controllers (MFC, Bronkhorst). The gases are premixed in a mixing unit before entering the reaction zone. A K-type thermocouple is embedded in the center of the mixing chamber to measure the inlet temperature of the gases.

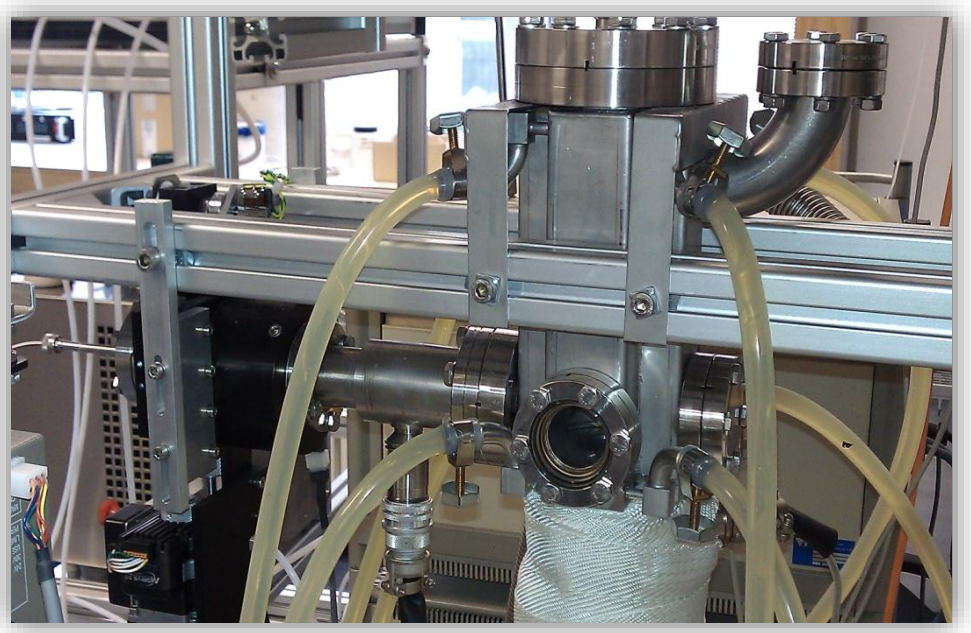

Figure 3.4 *Picture of the fully assembled stagnation-flow reactor setup. Figure taken from reference* [90].

3.2.2 Catalytic nickel surface - stagnation disk

A flat stagnation disk (55 mm diameter) is coated with a solution of Ni/Al_2O_3. Suitable amounts of an aqueous solution of nickel nitrate (99.99 %) and boehmite (AlOOH, 20 % boehmite) are mixed to obtain a 5 wt.% Ni/Al_2O_3. The nickel catalyst is prepared following the procedure described by Karakaya [81, 90].

Catalyst pre-treatment

Prior to the measurements, the coated stagnation disk is conditioned by 5 vol.% O_2 diluted in argon at 773 K for 2 h. The oxidized nickel catalyst is further reduced by 10 vol.% H_2 diluted in argon at 773 K for 2 h.

3.2.3 Experimental conditions

The experiments in the stagnation-flow reactor are carried out at 500 mbar total pressure and a total flow rate of 15 SLPM. The initial gas mixture and boundary-layer profiles of the species are measured at different steady state temperatures. The maximum boundary-layer thickness measured in the experiments is 7 mm. The concentration profiles of the species within the boundary-layer are measured by a microprobe sampling technique [90].

3.3 Continuous-flow reactor

A continuous- flow reactor is a device in which chemical reactions take place in channels. The reactors are typically tube-like and manufactured from different materials such as stainless steel, glass, and ceramics. This reactor type offers many advantages over conventional scale reactors, including good heat transfer, high energy efficiency, reaction speed and yield, safety, reliability, scalability.

3.3.1 Experimental Setup

The experiments over nickel catalyst are performed in a continuous-flow reactor. In this work, the experimental setup is referred to as CPOX 3 reformer (Figure 3.5). Details of CPOX 3 experimental setups can be found elsewhere [32].

The lab-scale reformer consists of a quartz tube placed in an oven for thermal insulation. The gaseous reactants and the evaporated fuel are mixed at the reactor inlet, which was designed to allow a rapid mixing. The dosing of the gases is controlled by mass flow controllers produced by Bronkhorst Hi-Tec. A thermocouple is used to measure the temperature of the gas phase during the reaction. Figure 3.5 shows the experimental continuous flow reactor used.

Figure 3.5 *Picture of the fully assembled reactor setup CPOX 3. Figure taken from* [32].

3.3.2 Ni/Al_2O_3 cordierite monolith catalyst

The kinetic studies are carried out using nickel/alumina-coated monoliths. The coated monoliths were prepared in cooperation with Verein des Gas- und Wasserfaches e.V (DVGW) test laboratory at the Engler-Bunte-Institut of the KIT. The nickel-based catalyst used for the wash coat of the monoliths is confidential. Therefore, further details about the catalyst cannot be disclosed.

The catalytic monolith was ~12 mm long and ~19 mm in diameter with 600 cpsi cell density (corresponding to a channel diameter of 880 μm). The catalyst is placed between two uncoated 600 cpsi cordierite honeycomb monoliths (same length and diameter as the catalytic module) to minimize axial heat losses. To prevent a gas by-pass between monoliths and quartz tube, the heat shields and the catalyst are wrapped with ~1 mm layer of ceramic fiber paper. Figure 3.6 shows the schematic drawing of the monoliths configuration inside the flow reactor.

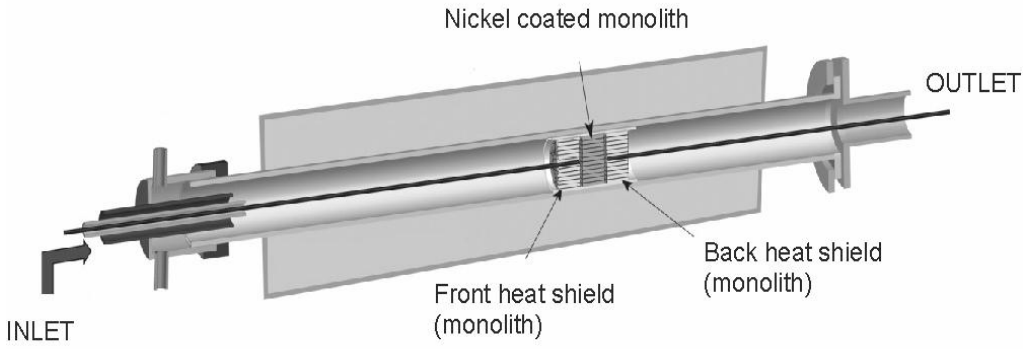

Figure 3.6 *Schematic drawing of the monoliths configuration inside the flow reactor. Figure adapted from reference* [91] .

Catalyst pre-treatment

Prior to the measurements, the coated cordierite monolith is conditioned by 20 vol.% O_2 diluted in nitrogen at 673 K (400 °C) for 30 min. The oxidized monolith nickel catalyst is further reduced by 10 vol.% H_2 diluted in nitrogen at 873 K for 1 h.

3.3.3 Experimental conditions

The experiments in the continuous flow reactor are carried out at 1bar total pressure and a total flow rate of 4 SLPM. The different reactants components are mixed to various inlet gas compositions. The experiments are performed at temperatures in the range of 373-1173 K (100-900 °C) and a temperature ramp of 15 K/min is applied.

4.Development of a Multi-Step Surface Reaction Mechanism

The development of the heterogeneous reaction kinetics is based on theoretical studies such as DFT, MC, semi-empirical calculations [11, 55, 57, 74, 92-96], as well as experimental kinetic studies.

In a unified surface reaction mechanism, all possible reactions paths and interactions between the chemical species under investigation have to be considered. A schematic diagram is shown in Figure 4.1 describing the hierarchical approach followed to establish the kinetic model for $CH_4/CO_2/H_2O/CO/O_2/H_2$ systems.

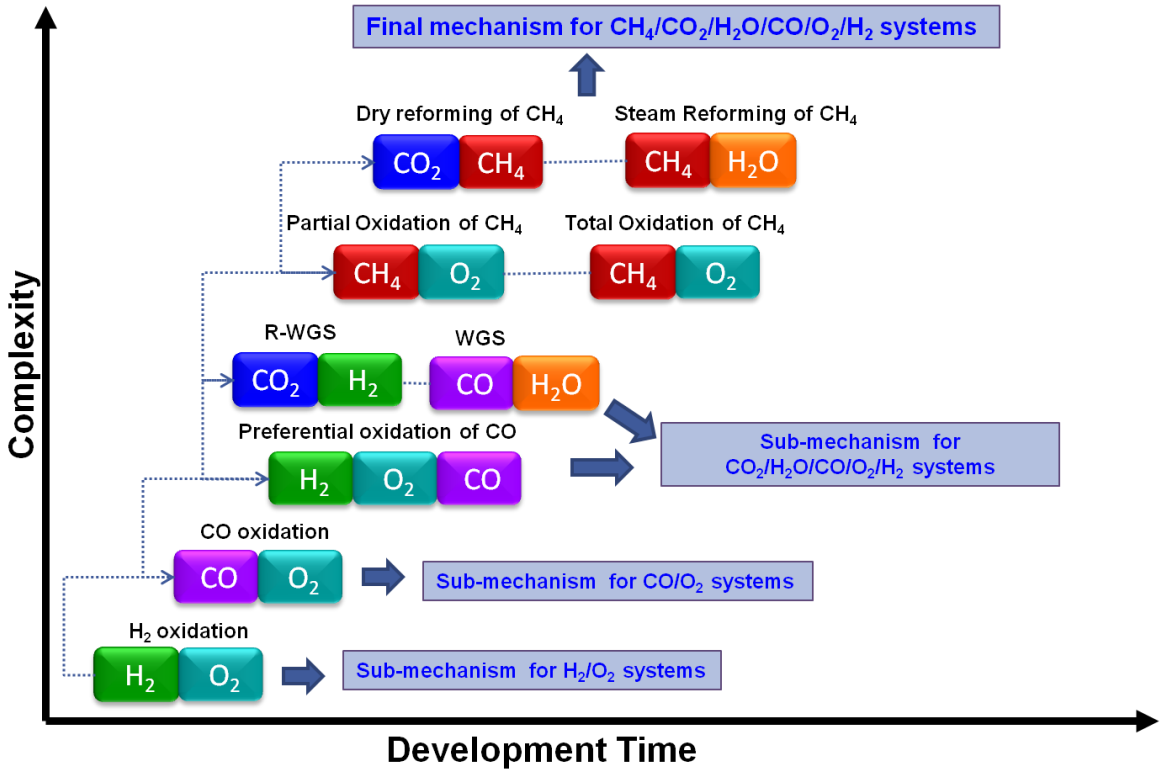

Figure 4.1 *Strategy for mechanism development: Hierarchical approach.*

A detailed multi-step heterogeneous reaction mechanism has been developed, which can reproduce conversion and selectivity for all systems under investigation. The reaction mechanism consists of 52 reactions with 6 gas-phase species and 13 surface species. The kinetic model also contains important intermediates such as adsorbed HCO and COOH species. The mechanism, without any modification, can be applied to $CH_4/CO_2/H_2O/CO/O_2/H_2$ systems operating in a wide range of external conditions. The mechanism also includes the formation of carbon monolayers and methanation reactions. A previous model developed in our group by Maier et al. [58], which serves as basis of the novel kinetic scheme, has already been successfully applied for steam reforming of methane at a wide range of temperatures and feed compositions. With the current mechanism extension, the experimental data for catalytic conversion of hydrogen, carbon monoxide, and methane under oxidative and reforming conditions can be modeled. The mechanism is evaluated against new experimental data at varying operating conditions. The overall thermodynamic consistency of the mechanism is ensured by a numerical approach, in which surface reaction rate parameters are adjusted to be thermodynamically consistent.

4.1 Kinetics of hydrogen oxidation (H_2/O_2)

The catalytic oxidation of hydrogen has always been a topic of technical interest, because it is one of the key reactions in many catalytic industrial processes.

The development of a detailed unified surface reaction mechanism for methane oxidation and reforming necessarily begins with the hydrogen/oxygen sub-mechanism. Therefore, the oxidation of H_2 on nickel-based catalysts has been investigated experimentally and numerically to achieve a better understanding of the kinetics behind this system. Experiments are carried out in the stagnation-flow reactor. The flow field of the entire reactor is two-dimensional. However, a potential flow can be established leading to a one–dimensional (1D) boundary-layer over the catalyst [97, 98]. Hence, most of the catalyst (except at the edges) is exposed to the identical gas-phase leading to no lateral variations of the catalyst surface coverage [63, 97].

The experimental results are used for developing an elementary step like sub-reaction mechanism for H_2/O_2. The validation of the resulting mechanisms is achieved by comparing the numerical results against the experimental data obtained.

4.1.1 Theoretical background

The catalytic oxidation of hydrogen on transition metals has been extensively investigated, the reaction is of a high technical interest, because is fundamental for some industrial catalytic processes [65, 99, 100].

$$H_2 + \frac{1}{2}O_2 \rightarrow H_2O, \quad \Delta H_{298}^0 = -482.0 \frac{\text{kJ}}{\text{mol}} \tag{4.1}$$

The use of hydrogen in petroleum refining has been growing in the last years due to a changes in crude production and environmental regulations, such as limits of sulfur in diesel, limits of NO, and SO, aromatic and light hydrocarbon concentrations in the gasoline [101, 102]. The prospect of a hydrogen-based economy has prompted increased interest in the use of hydrogen as a fuel given its high chemical energy per unit mass and cleanliness [103]*.

*Sentence taken from reference [103].

There is a considerable interest to understand the oxidation and reforming of hydrocarbon fuels over a wide range of operating conditions and reactor configurations. In particular, the water-formation rate determines the selectivity of the catalytic partial oxidation of methane to syngas. A detailed micro-kinetic model can be used to optimize and improve the efficiency of these processes. Thus, the development of a detailed kinetic mechanism for hydrocarbons oxidation and reforming necessarily begins with the hydrogen oxidation sub-mechanism. Experimental and theoretical studies of the interactions between O_2, H_2 and H_2O are carried out to clarify the kinetics of catalytic hydrogen oxidation [81, 103-105].

Larson and Smith [106] studied the nickel catalyzed hydrogen oxidation at 307-403 K and at oxygen concentrations up to 2 %. The authors suggested that at least two reactions take place, each reaction involving the formation of an oxide and its subsequent reduction by hydrogen. It has been reported that under certain conditions the catalytic oxidation of H_2 on Pt, Rh and Ni exhibits an oscillatory behavior [65, 100, 107-110]. Brown et al. [111] found during hydrogen oxidation on polycrystalline platinum that the reaction rate oscillations occurred due to the formation of hot spots. Wilke et al. [112] presented a theoretical investigation of the potential-energy diagram for water formation from adsorbed O and H species on Rh(111) and Pt(111) surfaces. Their study is based on first-principles calculations applying density-functional theory. Saranteas et al. [113] studied the catalytic oxidation of hydrogen at 513 K and 683 K on porous polycrystalline nickel films supported on stabilized zirconium, in order to elucidate the kinetics of the reaction. Studies on literature of hydrogen oxidation kinetics suggest that the reaction proceeds via a Langmuir–Hinshelwood mechanism [114, 115]. Mhadeshwar and Vlachos [116] studied the ignition of hydrogen on Rh foil, the experiments were conducted in a metallic micro-reactor at 1 atm. The results show a decrease in the ignition temperature of H_2/O_2 mixtures with the increase of H_2 in the inlet composition. The authors also developed a multiscale surface reaction mechanism for CO, H_2 oxidation, and CO-H coupling with water-gas shift (WGS) and preferential oxidation of CO on Rh, in their mechanism the activation energies for the desorption reactions are coverage dependent. Maestri et al. [117] performed H_2 and CO combustion experiments under rich conditions and high flow-rates in a isothermal annular reactor over Rh catalyst. The experimental results of H_2/O_2 system were compared with numerical predictions using and heterogeneous/homogeneous model. The model simulations underestimated the experimental results at temperatures between 573-923 K, but described well the measured conversion at high temperatures. Deutschmann [105, 118] studied the catalytic ignition of mixtures of H_2 and O_2 over platinum and palladium catalyst. The author proposed

two reaction mechanisms for catalytic oxidation of hydrogen over platinum and palladium respectively. The experimental results were simulated using the kinetic proposed models; both mechanisms were able to describe the main features of the system. Recently, Karakaya and Deutschmann [81] studied the kinetics of hydrogen oxidation on Rh/Al_2O_3 catalysts in a stagnation-flow reactor. The authors propose a thermodynamically consistent set of kinetic data for a 12-step surface reaction mechanism.

4.1.2 Experimental procedure

The oxidation of hydrogen on nickel is studied in the stagnation-flow reactor using a catalytic disk described in Section 3.2.2. The experiment is carried out at 500 mbar as total pressure with a total flow rate of 15 SLPM. The inlet gas mixture of 4.78 vol.% H_2 and 2.89 vol.% O_2 in argon dilution is fed into the system. The initial gas mixture and boundary-layer profiles of the species are measured at steady state temperature of 623 K. The maximum boundary-layer thickness measured in this experiment is 7 mm.

4.1.3 Kinetic parameters

The reaction mechanism developed by Maier et al. [58] is used as a reference for the reaction paths and enthalpy values. The new model involves adsorption and desorption steps of all reactants and products; surface elementary reaction steps are based on the mean-field approximation. The thermodynamically consistent surface reaction mechanism that is established on the base of the “source” surface reaction mechanism (Table 4.1) using an adjustment algorithm for the temperature interval 373-1273 K, the kinetic data of the mechanism presented in Table 4.1 are slightly modified by the adjustment procedure (Section 2.5). Sticking coefficients are used as kinetic data for the adsorption of reactants and products (H_2, O_2, and H_2O) represented in the reaction mechanism.

Table 4.1 Surface reaction mechanism for H_2 oxidation over nickel (thermodynamic-non-consistent version).

	REACTION	A[cm, mol, s]/S_0[-]	β [-]	E_a/[kJ/mol]
R1	H_2 + (Ni) + (Ni) → H(Ni) + H(Ni)	$3.000x10^{-02}$	0.000	5.00
R2	H(Ni) + H(Ni) → Ni(Ni) + Ni(Ni) + H_2	$2.545x10^{+20}$	0.000	95.21
R3	O_2 + (Ni) + Ni → O(Ni) + O(Ni)	$4.357x10^{-02}$	0.000	0.00
R4	O(Ni) + O(Ni) → (Ni) + (Ni) + O_2	$4.283x10^{+23}$	0.000	474.95
R5	H_2O + (Ni) → H_2O(Ni)	$1.000x10^{-01}$	0.000	0.00
R6	H_2O(Ni) → H_2O + (Ni)	$3.732x10^{+12}$	0.000	60.79
R7	H(Ni) + O(Ni) → OH(Ni) + (Ni)	$5.000x10^{+22}$	0.000	97.90
R8	OH(Ni) + (Ni) → H(Ni) + O(Ni)	$1.781x10^{+21}$	0.000	36.09
R9	H(Ni) + OH(Ni) → H_2O(Ni) + (Ni)	$3.000x10^{+20}$	0.000	42.70
R10	H_2O(Ni) + (Ni) → H(Ni) + OH(Ni)	$2.271x10^{+21}$	0.000	91.76
R11	OH(Ni) + OH(Ni) → H_2O(Ni) + O(Ni)	$3.000x10^{+21}$	0.000	100.00
R12	H_2O(Ni) + O(Ni) → OH(Ni) + OH(Ni)	$6.373x10^{+23}$	0.000	210.86

The proposed thermodynamically consistent surface reaction mechanism for H_2 oxidation is presented in Table 4.2. The model consists of 12 reactions with 3 gas-phase species and 6 surface species.

Table 4. 2 Thermodynamically consistent surface reaction mechanism for H_2 oxidation over nickel.

	REACTION	A[cm, mol, s]/S_0[-]	β [-]	E_a/[kJ/mol]
R1	H_2 + (Ni) + (Ni) → H(Ni) + H(Ni)	$3.000x10^{-02}$	0.000	5.00
R2	H(Ni) + H(Ni) → Ni(Ni) + Ni(Ni) + H_2	$2.544x10^{+20}$	0.000	95.21
R3	O_2 + (Ni) + Ni → O(Ni) + O(Ni)	$4.360x10^{-02}$	-0.206	1.51
R4	O(Ni) + O(Ni) → (Ni) + (Ni) + O_2	$1.188x10^{+21}$	0.823	468.91
R5	H_2O + (Ni) → H_2O(Ni)	$1.000x10^{-01}$	0.000	0.00
R6	H_2O(Ni) → H_2O + (Ni)	$3.734x10^{+12}$	0.000	60.79
R7	H(Ni) + O(Ni) → OH(Ni) + (Ni)	$3.951x10^{+23}$	-0.188	104.35
R8	OH(Ni) + (Ni) → H(Ni) + O(Ni)	$2.254x10^{+20}$	0.188	29.64
R9	H(Ni) + OH(Ni) → H_2O(Ni) + (Ni)	$1.854x10^{+20}$	0.086	41.52
R10	H_2O(Ni) + (Ni) → H(Ni) + OH(Ni)	$3.674x10^{+21}$	-0.086	92.94
R11	OH(Ni) + OH(Ni) → H_2O(Ni) + O(Ni)	$2.346x10^{+20}$	0.274	92.37
R12	H_2O(Ni) + O(Ni) → OH(Ni) + OH(Ni)	$8.148x10^{+24}$	-0.274	218.49

The rate coefficients are given in the form of $k=AT^{\beta}\exp(-E_a/RT)$; adsorption kinetics is given in form of sticking coefficients; the surface site density of Γ=2.66 x 10^{-9} mol cm^{-2} is calculated by assuming a site area of $6.5x10^{-2}$ nm^2 as observed for nickel [58, 119].

In the micro-kinetic model presented in Table 4.2, it is assumed that H_2 and O_2 dissociatively adsorb on the nickel surface with sticking coefficients of 0.03, and 0.0436 respectively.

Dissociation of water is found to be dependent on the crystal structure. Water on Ni(111) and Ni(100) adsorbed dissociatively but for Ni(110) the water can either chemisorb without clustering or dissociate, depending on the conditions [120-122].

Avaliable information for sticking coefficients of H_2 and O_2 vary in a wide range in the literature [11, 120, 123]. A summary of the literature values for sticking coefficients of H_2, O_2, and H_2O is given in Table 4. 3. Initial hydrogen sticking coefficients between 0.1 and 1 for nickel at gas temperatures of 373 K and 1073 K has been reported [120, 123-125]. Winkler and Rendulic [123] proposed that the reasons are the uncertainty in the measurement of the gas pressure and the differences in the surface structure and surface composition. The authors concluded that small changes in the surface structure or a very small amount of contaminant will considerably influence the adsorption kinetics of hydrogen on Ni(111). Bengaard et al. [120] assume a hydrogen sticking coefficient of 0.16 at a temperature of 623 K.

The sticking coefficient of 0.03 for hydrogen adsorption used in the micro-kinetic model presented in Table 4.2 is in agreement with the results reported by Rendulic et at. [126]. The authors measured an initial sticking coefficient of 0.02 and 0.03 for Ni(111) at room temperature.

The oxygen sticking probabilities depend linearly on the coverage. Stuckless et at. [127] shows initial values for sticking probability measurements for oxygen of 0.63, 0.78 and 0.23 for the Ni (100), Ni(110), and Ni(111) surface, respectively. Winker et at. [128] proposed that on very rough surfaces the value of the initial sticking coefficient is nearly 1, whereas on the flat Ni(111) plane it only reaches the value of 0.12, nevertheless, the adsorption probability on Ni(111) increases with increasing coverage up to 0.2 monolayers of oxygen. The sticking coefficient of water used in the current reaction mechanism is taken from the model developed by Maier et.al [58].

Table 4.3 Comparison of initial sticking coefficients of H_2, O_2, and H_2O on Ni active site.

Adsorbats	***Substrate***	***Sticking coefficient S_o***	***References***
	Ni(111)	≥0.01	[123, 126, 129-131]
H_2	Ni(100)	0.1-1	[11, 120, 123, 125]
	Ni(110)	0.96	[123]
O_2	Ni(111)	0.1-0.23	[127, 128]
	Ni(100)	0.63	[127]
	Ni(110)	0.75-1	[127]
H_2O	Value for Rh(111)	0.1-0.16	[33, 58]

Hydrogen desorption on nickel $\left(2H^* \rightarrow H_{2(g)} + 2*\right)$ has been studied by many authors, and is found to be an endothermic reaction with an activation energy for single crystal surface between 90-97 kJ/mol. Bartholomew [132] and Weatherbee [133] reported heats of adsorption in a range of approximately 82-89 kJ/mol. Katzer et al. [134] calculated a H_2 desorption energy of 96 kJ/mol. Chen et al. [11] estimated an activation energy of 97 kJ/mol by UBI-QEP method, this value is close to the results obtained by Zhu and White [135] on Ni (100) of 95 kJ/mol and 96 kJ/mol by Aparicio [53]. Bengaard et al. [120] determined the activation energies of desorption of H_2 from Ni(111), Ni(100), Ni(110) and Ni(445) to be 96, 90, 89, and 87 kJ/mol, respectively. Maier et al. [58] reported an activation energy for hydrogen desorption of 81 kJ/mol, this model is used as base line of the kinetic parameters. However, for the model in the presented in this study, the activation barrier of hydrogen desorption is estimated to be 95 kJ/mol, this valued is selected based on the literature studies, which is agreement with the results reported by the previous mentioned authors.

The interaction of oxygen on nickel has been subjected to a large number of surface science studies using a wide range of techniques. Stuckless et al. [127] listed the initial heats of adsorption of oxygen for the three low index crystal planes of Ni. The activation energy for the desorption process are 520 kJ/mol, 470 kJ/mol, and 485 kJ/mol for Ni(100), Ni(111) and Ni(110) respectively. These values are comparable with the *ab-initio* theoretical results obtained by Siegbahn and Wahlgren [136], in their work 540 kJ/mol is estimated for Ni(100) and 480 kJ/mol for Ni(111).

In the present work, the activation energy of oxygen desorption is 468.9 kJ/mol, which in is agreement with the values found it in the literature.

Stulen et al. [137] studied the desorption of H_2O at low temperature on clean Ni(111) using thermal desorption spectrometry (TDS) and electron-simulated desorption (ESD). They

reported an activation energy for H_2O desorption of 41 kJ/mol. Pache et al. [138] report an activation energy for H_2O desorption of 57±5 kJ/mol measured on clean Ni(111) surface. Chen et al. [11, 47] considered in their macro-kinetic model desorption energies for H_2O of 64.5-68.9 kJ/mol. Aparicio [53] performed detailed micro-kinetic studies of the hydrogen exchange reaction of H_2O with D_2 on $Ni/MgAl_2O_3$, the author reported an activation energy for H_2O desorption of 64.4 kJ/mol. Zakharov et al. [139] performed theoretical cluster calculations on Ni(111), the results show activation energies between 51.4 kJ/mol and 67.1 kJ/mol. The value of 60.79 kJ/mol used in the present work, is in the range of the experimental and theoretical values reported in the literature.

After the adsorption of H_2 and O_2, adsorbed O* and H* may react to produce the OH*. The activation energy of 104 kJ/mol used in this work is consistent with the barriers for Ni(111) of 96 kJ/mol and for Ni(211) of 114 kJ/mol surface determined by Bengaard et.al [120].

The formation of H_2O from absorbed OH* and H* is a fast step, the barrier for the reaction in this work is estimated to be 92 kJ/mol, which is in agreement with the value of 91 kJ/mol for Ni(111) calculated by Bengaard et.al [120] and the theoretical value of 89 kJ/mol calculated by Blaylock et al. [73] from DFT calculations.

4.1.4 Results and discussion

Hydrogen oxidation over nickel is studied in a stagnation-flow reactor. The experimental results and different theoretical data from the literature are used as a baseline to develop the detailed multi-step surface reaction mechanism presented in Table 4.2. The micro-kinetic model is thermodynamically consistent and is validated by comparison of the obtained experimental data and numerical results predicted.

The sensitivity analysis helps to identify which kinetic parameters are most influential to the simulation results. Sensitivity analysis of the reaction mechanism is performed at two temperatures: 373 K (low temperatures) and at 623 K (high temperature), with H_2/O_2=1.65 (92 % Ar), 500 mbar. The sensitivity of the exit molar fraction of H_2O is analyzed, by perturbing the pre-exponential of each reaction.

Results for water mole fraction at 373 K are presented in Figure 4.2, which show a high sensitivity to hydrogen adsorption (R1, Table 4.2) as well as to formation of OH* absorbed

species, which is a crucial reaction at this temperature (R7, Table 4.2) leading to water production on the surface (R8, Table 4.2).

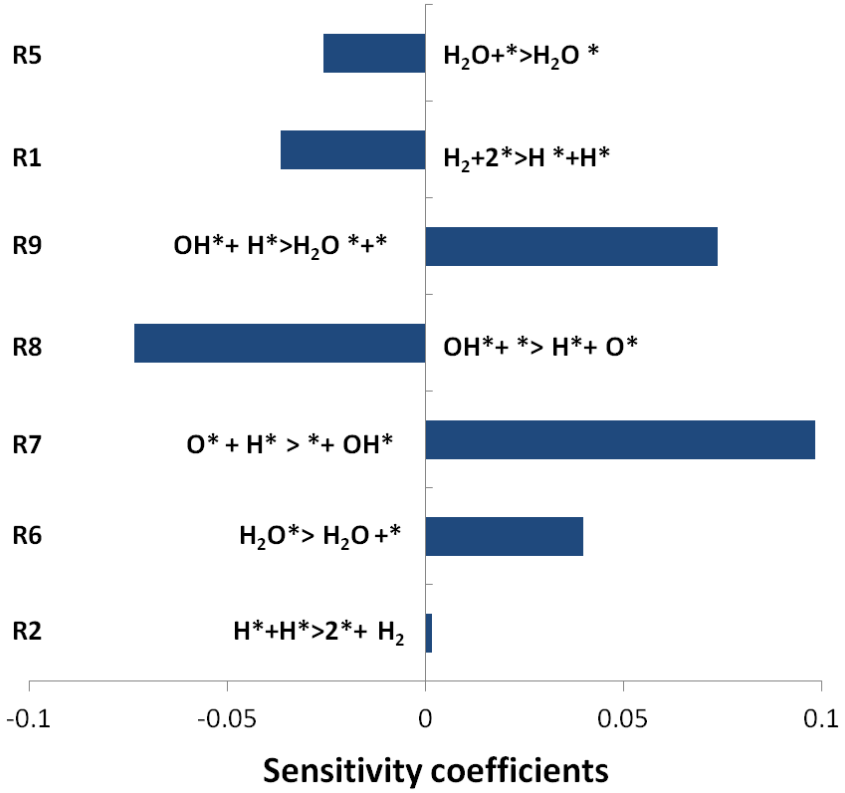

Figure 4.2 *Sensitivity coefficients for water mole fraction on the surface at 373 K for hydrogen oxidation, H_2/O_2=1.65 (92 % Ar).*

The sensitivity analysis performed at 623 K is presented in Figure 4.3. It shows that H_2 adsorption and desorption (R1, R2, Table 4.2), as well as OH* formation are crucial steps for the oxidation reaction. It can be also observed that the mechanism is highly sensitive to gas-phase H_2O, adsorbed H_2O, and as is expected, H_2O desorption (R6, Table 4.2) is the most sensitive reactions at such temperature.

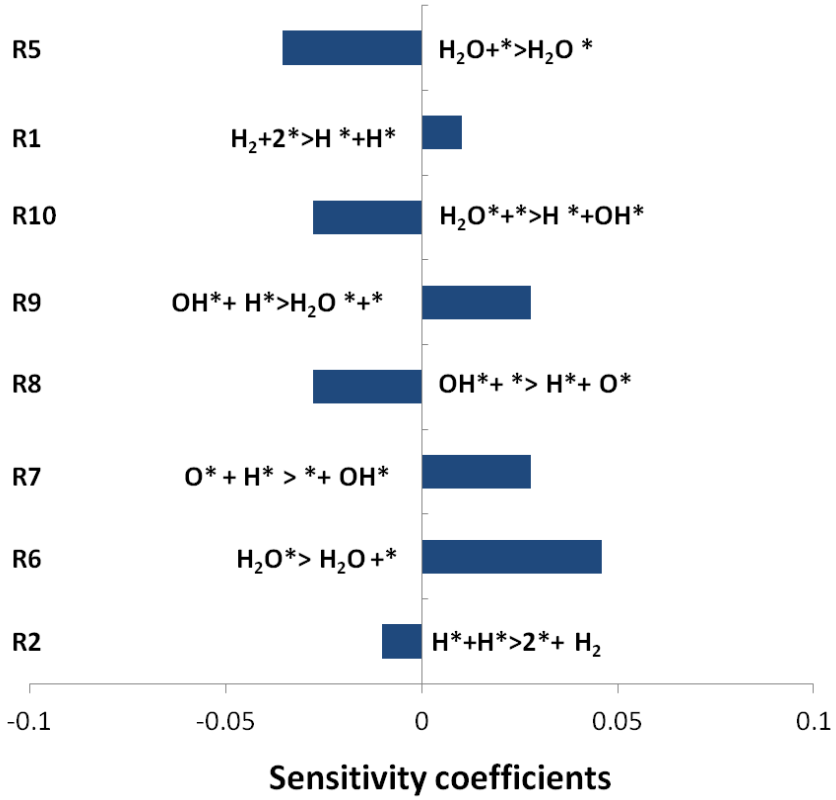

Figure 4.3 *Sensitivity coefficients for water mole fraction at 623 K for hydrogen oxidation, H_2/O_2=1.65 (92 % Ar).*

At low temperatures, the surface is almost fully covered by H_2. However, as the temperature increases the surface coverage of oxygen slightly increases and hydrogen coverage decreases letting a higher free nickel surface. The entire process is depicted in Figure 4.4.

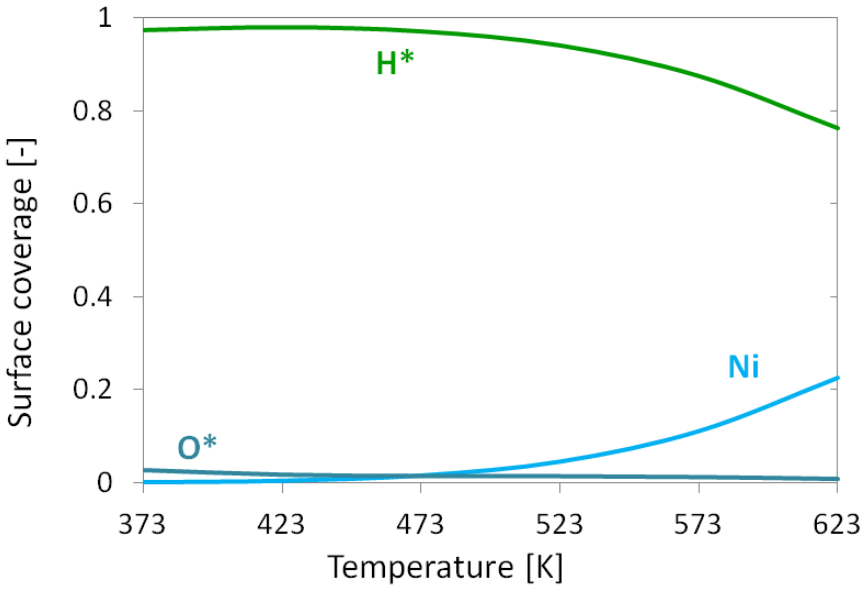

Figure 4.4 *Computed surface coverage of adsorbed species as function temperature for hydrogen.*

The stagnation-flow reactor experiment is carried out at steady state at 623 K with an inlet composition of 4.78 vol.% H_2 and 2.89 vol.% O_2 in argon dilution. The simulation is performed by using DETCHEM^{STAG} [77]. An effective $F_{cat/geo}$ =1.5 is used for the numerical simulation. The experimental concentration of H_2O is calculated by ensuring oxygen mass balance.

Figure 4.5 shows the catalytic oxidation of H_2 at steady state. Results from measurements (symbols) and simulation (lines) of H_2, and O_2 concentrations are depicted in the boundary-layer. According to the concentration profile, the reaction did not reach full conversion; oxygen and hydrogen are not fully consumed at the surface at 623 K (350 °C). The hydrogen results can be explained due to the high diffusion rate of H_2 in Ar compared to O_2. As long as H_2 is consumed on the surface, the high mass transport properties of H_2 result in a fast diffusion to the surface. The surface concentrations of H_2, O_2 as well as the production of H_2O are in agreement with the predicted numerical results. The difference between the hydrogen profile on the experiment and simulation can be attributed to the mass transport properties of H_2. As long as H_2 is consume on the surface, the high mass transport properties of H_2 result in a fast diffusion on the surface.

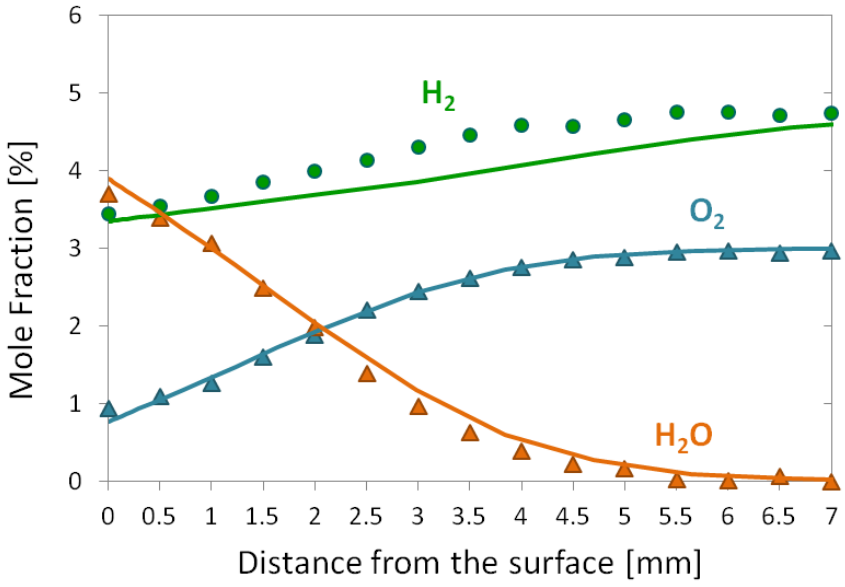

Figure 4.5 *Comparison of experimentally determined (symbols) and numerically predicted (lines) mole fractions as function of the temperature for catalytic oxidation of H_2 in a stagnation-flow reactor at 623 K; H_2/O_2=1.65 (92 % Ar) at 500 mbar; total flow rate of 15 SLPM.*

4.1.5 Summary

The oxidation of hydrogen over nickel has been experimentally studied in a stagnation-flow reactor. The reactor configuration facilitates computational modeling of heterogeneously catalyzed gas-phase reactions in a technical relevant flow regime.

An elementary-step like reaction mechanism for hydrogen oxidation is developed. The model is tested by using the numerical results performed in a stagnation flow reactor and data. A procedure has been applied throughout the development process to ensure the over-all thermodynamic consistency of the mechanism (Section 2.5).

Sensitivity analysis showed that hydrogen adsorption and desorption, as well as OH* formation are sensitive reactions, the mechanism is also highly sensitive to gas-phase H_2O, adsorbed H_2O*, and OH* species.

Experimentally measured concentrations are reproduced by numerical simulation using the developed reaction mechanism.

4.2 Kinetics of CO oxidation (CO/O_2)

Following the strategy diagram presented in Figure 4.1, the catalytic oxidation of CO over nickel is studied. Experiments are carried out in a fixed bed reactor and in a stagnation-flow reactor. The experimental results are used in the development of an elementary step-like sub-reaction mechanism for CO/O_2. The validation of the resulting mechanisms is achieved by comparing the numerical results with the experimental data obtained.

4.2.1 Theoretical background

The catalytic oxidation of CO on transition metals has been subject to many experimental and theoretical studies [116, 140-146]. The reaction is of high interest due to its technological importance, especially in the area of pollution control for combustion processes. Incomplete combustion processes can generate carbon monoxide, which is a harmful gas. Carbon monoxide can be oxidized by catalytic transition metals [147].

$$CO + O_2 \leftrightarrow CO_2, \qquad \Delta H_{298} = -283\ \mathrm{kJ/mol} \tag{4.2}$$

Currently, the removal of CO from automobile exhaust is accomplished by the oxidation of CO in catalytic converters using the three-way catalyst (TWC), which contains a mixture of Pt, Pd [148-150]. The CO oxidation has also attracted attention in fuel-cell technology as purification process, the proton exchange membrane in the fuel cells is very sensitive to impurities, it can just tolerate a few ppm of CO in the hydrogen stream, alkaline fuel cells require CO free hydrogen to avoid poisoning the fuel-cell catalyst [8, 151].

It is well known that nickel exhibit high reactivity for oxidation of CO, as well as oxidation and reforming methane [152-156]. It is important to investigate the mechanism of catalytic CO oxidation in order to developed catalysts able to preferentially oxidize CO for the production of CO-free hydrogen stream [140].

4.2.2 Experimental procedure

The kinetics of CO oxidation over nickel has been studied in a fixed bed reactor. The experiment is carried out using one of the powdered nickel-based catalyst developed by BASF (Fixedbed_Ni_BASF_Cat.1). The reactor tube is loaded with 1.03 g of catalyst. The catalyst pre-treatment is explained in the Section 3.1.2. Reactor operating pressure is selected to be 1 bar, and reaction temperatures in the range of 373 K to 673 K (100-400 °C). A temperature ramp of 15 K/min is applied. The inlet gas composition in Table 4.4 is fed into the reactor with a total flow rate of 2 SLPM, which results in a linear flow velocity of 0.984 m/s.

Table 4.4 Experimental conditions for the investigation of CO oxidation in a fixed bed reactor with Ni catalyst.

Temperature [K]	CO [vol.%]	O_2 [vol.%]	N_2 [vol.%]
373-673	2.0	4.0	94

4.2.3 Kinetic Parameters

The reaction mechanism presented in this section includes the reaction steps for direct catalytic oxidation of CO over nickel-based catalyst. The model consist of 10 reactions with 3 gas phase species and 4 surface species, the elementary-step like reaction model is based on the Langmuir-Hinshelwood mechanism (Table 4.5). The kinetic data for oxygen adsorption and desorption has been taken from the hydrogen oxidation mechanism presented in Table 4.2. The modeling approach is based on the mean field approximation. The thermodynamic consistency of the mechanism has been ensured for a temperature range of 373-1273 K.

Table 4.5 Surface reaction mechanism for CO oxidation over nickel.

	REACTION	A[cm, mol, s]/S_0[-]	β [-]	E_a/[kJ/mol]	ε_I [kJ/mol]
R1	O_2 + (Ni) + (Ni) → O(Ni) + O(Ni)	4.358×10^{-02}	-0.206	1.51	
R2	O(Ni) + O(Ni) → O_2 + (Ni) +(Ni)	$1.188 \times 10^{+21}$	0.823	468.91	
R3	CO + (Ni) → CO(Ni)	5.000×10^{-01}	0.00	0.00	
R4	CO(Ni) → CO + (Ni)	$3.566 \times 10^{+11}$	0.00	111.27	$-50\theta_{CO(Ni)}$
R5	CO_2 + (Ni) → CO_2(Ni)	7.000×10^{-06}	0.00	0.00	
R6	CO_2(Ni) → CO_2 + (Ni)	$6.442 \times 10^{+07}$	0.00	25.98	
R7	CO(Ni) + (Ni) → C(Ni) + O(Ni)	$1.758 \times 10^{+13}$	0.00	116.24	$-50\theta_{CO(Ni)}$
R8	C(Ni) + O(Ni) → CO(Ni) + (Ni)	$3.402 \times 10^{+23}$	0.00	148.00	
R9	CO(Ni) + O(Ni) → CO_2(Ni)	$2.002 \times 10^{+19}$	0.00	123.60	$-50\theta_{CO(Ni)}$
R10	CO_2(Ni) → CO(Ni) + O(Ni)	$4.648 \times 10^{+23}$	-1.00	89.32	

The rate coefficients are given in the form of $k=AT^{\beta} \exp(-E_a/RT)$; adsorption kinetics is given in form of sticking coefficients; the surface site density of $\Gamma=2.66 \times 10^{-9}$ mol cm^{-2} is calculated by assuming a site area of 6.5×10^{-2} nm^2 as observed for nickel [58, 119].

Sticking coefficients between 0.6-0.9 for CO on nickel are experimentally determined on single crystals [127]. However, the sticking coefficient is coverage dependent and it can drop if the coverage is increased from 0 to 0.5 monolayers [53, 157].

The reaction mechanism presented in Table 4.5 assumes a sticking coefficient of 0.5 for CO, which is in agreement with the value obtained by Aparicio [53] and Chen et al. [11]. The high sticking probability of CO on nickel can cause the blocking of the active sites, hindering the adsorption of other species [158]. Coverage dependency of 50 kJ/mol for CO is included into the model to describe the lateral interaction of adsorbed species. This value is estimated based in comparison of the model predictions and experimental results.

The adsorption and dissociation of CO on nickel surfaces is a particularly important heterogeneous reaction. The activation barrier for CO dissociation is coverage dependent, based on the CO coverage the activation energies varies in the literature from 100 to 200 kJ/mol [159]. An activation barrier for CO dissociation of 116 kJ/mol is used in this work to adjust the model with the experimental values.

Estimated values for CO desorption found in theoretical studies using DFT or UBI-QEP calculations are in the range of 120±10 kJ/mol [11, 55, 74, 94]. Using temperature-programmed desorption (TPD), Bjørgum et al. [159] derived a desorption energy of 119 kJ/mol for CO at low CO surface coverage. Al-Sarraf et al. [160] estimated an initial heat of CO adsorption of 122±4 kJ/mol for Ni(100) using a single crystal micro-calorimeter.

The heat of CO adsorption of 111 kJ/mol estimated in this wok, is close to the value of 115 kJ/mol reported by Aparicio [53] and the values calculated on Ni (100) by Benzinger et al. [161].

The initial sticking coefficient of $7.0x10^{-6}$ for CO_2 is based on the surface reaction mechanism for methane steam reforming developed by Maier et al. [58].

Nukolic et al.[162] and Rodes et al. [163] showed that CO_2 activation on transition metals surfaces is structure sensitive. CO_2 adsorption on nickel surface is also structure sensitive, dissociative on Ni(110), non dissociative on Ni(111), and both dissociative and non dissociative on Ni(100) [164]. Wang et al. [165] investigated theoretically the chemisorption on nickel surfaces using density functional theory. The authors reported the dissociative chemiesortion energies of 99.3 kJ/mol on Ni(111), 108.9 kJ/mol on Ni(111), and 13.5 kJ/mol on Ni(110), they also found that the ability of CO_2 chemisorption is in the order of Ni(110)>Ni(100)>Ni(111). In the kinetic model presented in this work, an activation energy of 89.32 kJ/mol for CO_2 dissociation (R10, Table 4.5) is used based on the kinetic data reported by Maier et al. [58].

The value of the activation energy for CO_2 desorption used for the model given in Table 4.5 is estimated to be 25 kJ/mol, which is comparable with the results of 28 kJ/mol calculated by Blaylok et al. [73] using density functional theory and the value of 27 kJ/mol reported by Chen et.al. [11].

4.2.4 Results and discussion

CO oxidation over nickel is studied in this work in a fixed bed reactor. Additionally data reported by Maier et al. [58] and from the literature [11, 47, 73] are used to develop the detailed multi-step surface reaction mechanism presented in Table 4.5. The thermodynamically consistent model is tested by comparison of the experimental results to the numerical predictions.

Experiments in a fixed bed reactor for CO oxidation

The experiment in the fixed bed reactor is carried out at temperatures between 373 K to 673 K, with an inlet gas composition of 2.0 vol.% CO and 4.0 vol.% O_2 in nitrogen dilution. The numerical simulation of the fixed bed is performed by using DETCHEM^{PACKEDBED} with an active catalytic surface area value of 1.14×10^5 m^{-1} (ratio between catalytic area and volume of the catalytic bed).

The numerical profiles presented in Figure 4.6 show agreement with the experimental results for all species in the range of temperatures studied, the ignition point is reached at 423 K, with full conversion at 573 K when the system reaches equilibrium.

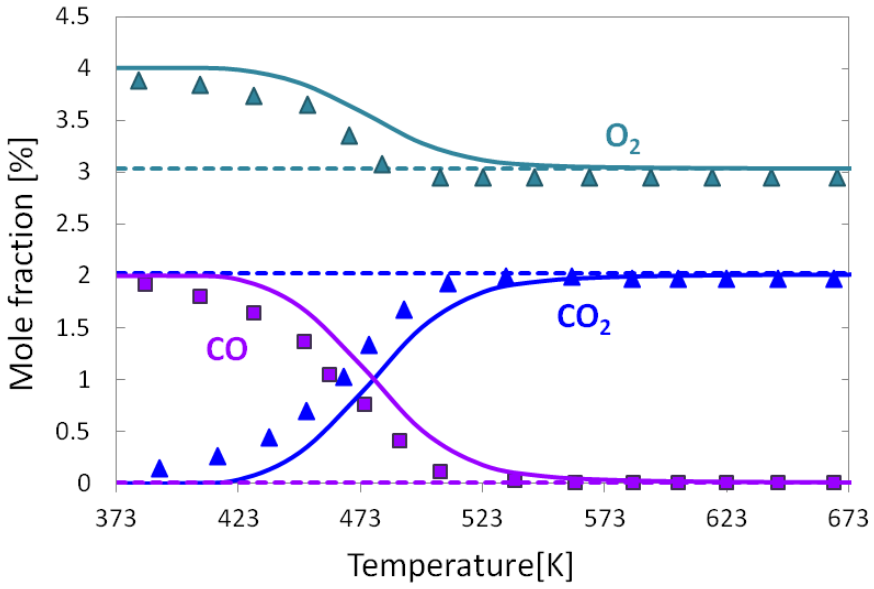

Figure 4.6 *Comparison of experimentally determined (symbols) and numerically predicted (lines) mol fractions as a function of the temperature for catalytic oxidation of CO in a fixed bed reactor; T_{inlet} =373 K; CO/O_2=0.5 (94 % N_2) at 1bar; total flow rate of 2 SLPM; dashed lines =equilibrium composition at given temperature.*

The computed surface coverage after ignition performed at steady state (673 K) is presented in Figure 4.7. It can be observed that before the reaction takes place, the surface is almost completely covered by CO* and less than 10% by O*. However, at higher temperatures, where the reaction reaches full conversion, the CO* is consumed leaving the surface covered by O*.

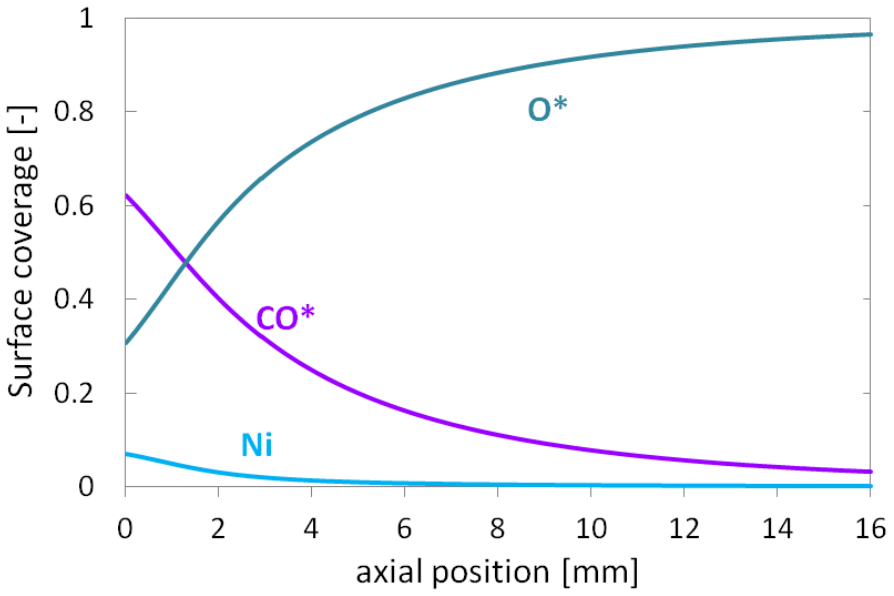

Figure 4.7 *Computed surface coverage of adsorbed species along the catalytic bed in CO oxidation after ignition (673 K).*

The reaction flow analysis of the CO oxidation mechanism is performed at 673 K, with CO/O_2=0.5 (94 % N_2), at 1bar. Figure 4.8 shows the reaction path for CO_2 formation, at this temperature, around 99.94 % of the CO absorbed on the surface is oxidized to CO_2, which desorbs readily due to its low sticking coefficient.

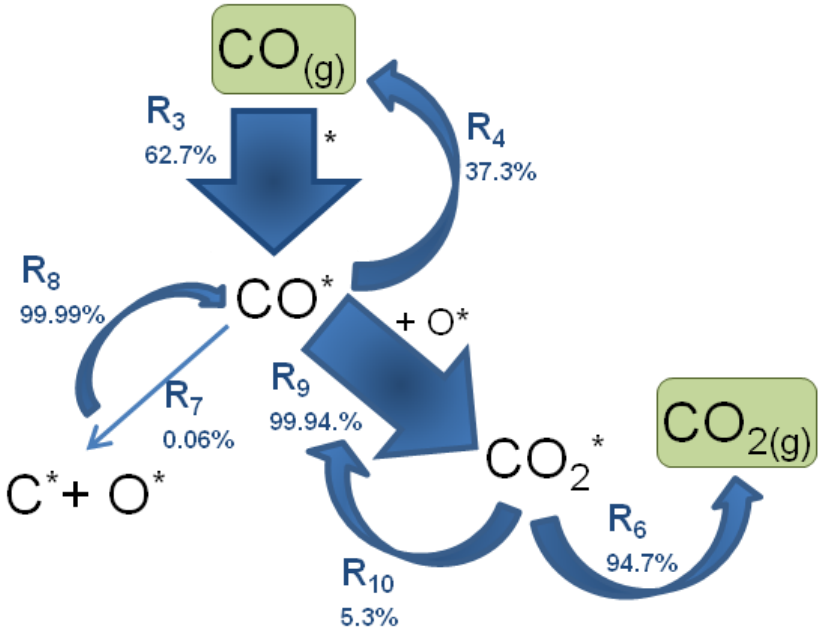

Figure 4.8 *Reaction flow analysis for CO oxidation on nickel at 623 K, 2 SLPM, CO/O_2=0.5 (94 % N_2), 1bar.*

Sensitivity analysis of the reaction mechanism is performed at three different temperatures: 473 K, 573 K, 673 K, with CO/O_2=0.5 (94 % N_2), at 1bar. CO oxidation depends on the CO adsorption (R3, Table 4.5) and desorption (R4, Table 4.5) equilibrium in all range of temperatures, and therefore on the CO concentration that dominates the catalytic surface, as shown in Figure 4.9.

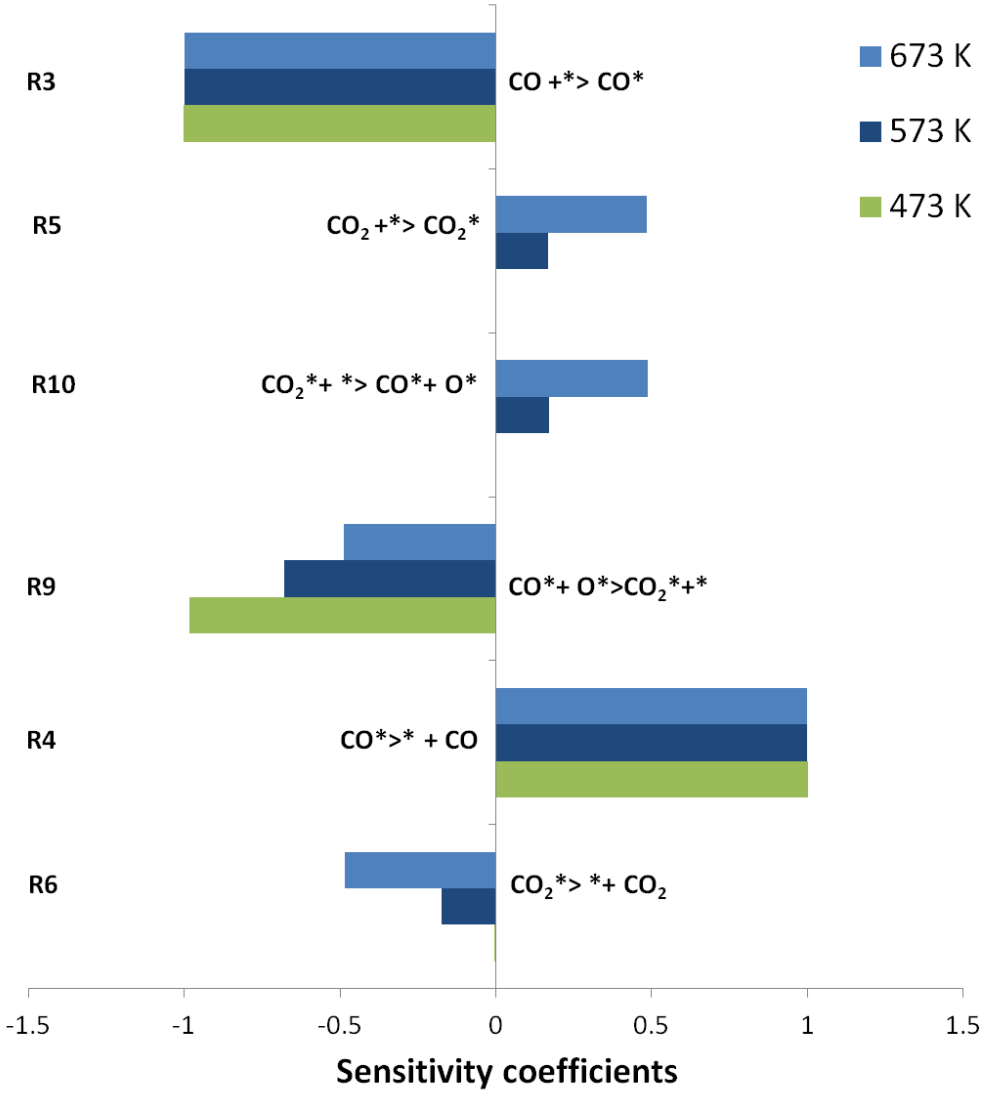

Figure 4.9 *Sensitivity coefficients for CO mole fraction at 473 K, 573 K, 673 K for CO oxidation, CO/O_2=0.5(94 % Ar).*

4.2.5 Stagnation flow reactor experiments

The reaction kinetic model is evaluated by comparison with the experimental results obtained in a stagnation-flow reactor for direct oxidation of CO on nickel. The experiments are carried out at 573 K, and 673 K. The inlet gas composition presented in Table 4.6 is fed into the reactor; the boundary-layer profiles of the species are measured at steady-state. Operating pressure is selected to be 500 mbar and a total flow rate of 15.5 SLPM. The maximum boundary-layer thickness measured is 6 mm.

Table 4.6 Experimental conditions for CO oxidation in a stagnation-flow reactor.

Test	CO [vol.%]	O_2 [vol.%]	Ar [vol.%]	Temperature [K]
1	2.78	2.22	95	573
2	2.77	2.23	95	673

The reaction kinetics is evaluated by comparison of the experimental results obtained in the stagnation-flow reactor and the numerical profiles derived from the simulations. The experimental and numerical boundary-layer concentration profiles of the species are compared in Figure 4.10, Figure 4.11.

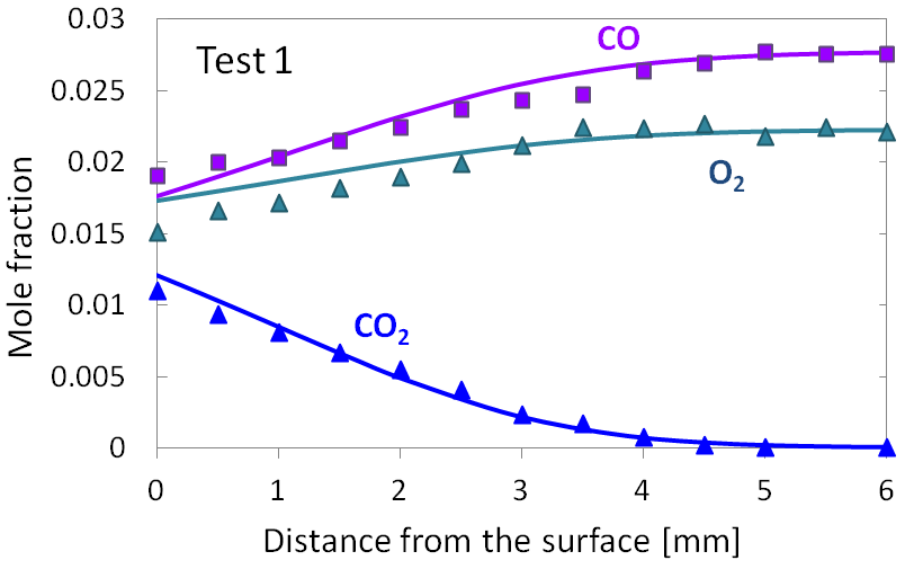

Figure 4.10 *Comparison of experimentally determined (symbols) and computed (lines) species profile in the stagnation-flow reactor for catalytic oxidation of CO at 573 K, 500 mbar, total flow rate of 15.5 SLPM.* $F_{cat/geo}$*=1.5 is used in the numerical simulation.*

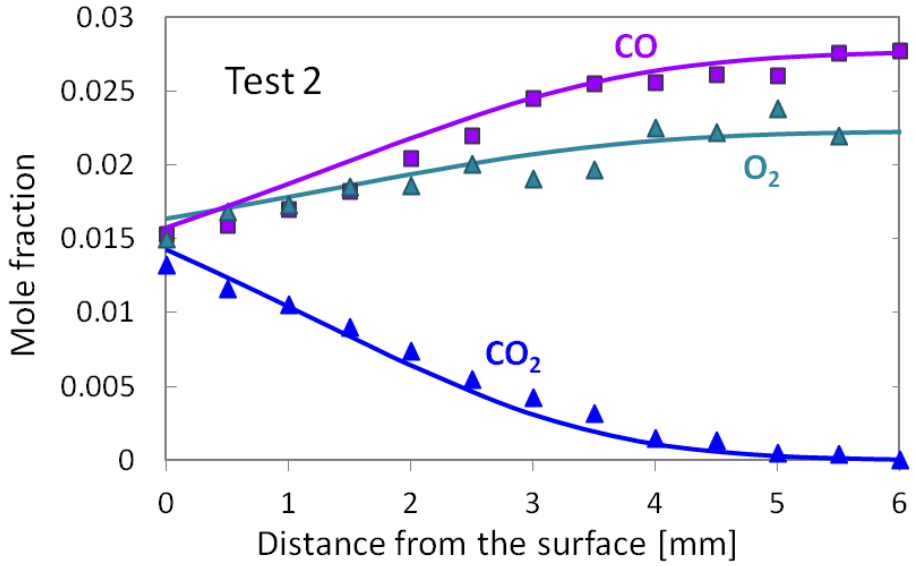

Figure 4.11 *Comparison of experimental (symbols) and computed (lines) species profile in the stagnation-flow reactor for catalytic oxidation of CO at 673 K; 500 mbar; total flow of 15.5 SLPM. $F_{cat/geo}$=1.5 is used in the numerical simulations.*

For the two systems investigated, the simulation results agree well with experimental data. At 573 K and 673 K the reaction is already ignited but the full conversion is not achieved. Closer examination performed after the experiments, confirmed that this was due to carbon formation covering the catalytic surface. The formation of coke on surface can block the active sites, which causes a decrease of the catalyst performance.

4.2.6 Summary

A heterogeneous surface reaction mechanism for the catalytic conversion of CO has been developed. Coverage dependency for CO is included into the model to describe the lateral interactions of adsorbed species. The results show that CO oxidation depends on the CO adsorption/desorption equilibrium, and therefore on the CO concentration that dominates the catalytic surface. Additionally, the surface reaction kinetics has been also evaluated by modeling the CO oxidation experiments performed in a stagnation-flow reactor at 573 K and 673 K. The nickel catalysts used for the experiments performed in the stagnation-flow reactor is more prone to produce coke on the surface than the powdered nickel based catalyst from BASF.

4.3 Kinetics of the water gas-shift reaction (WGS)

The kinetics of the water-gas shift (WGS), reverse water-gas shift (RWGS) and preferential oxidation of CO reaction in the presence of H_2 are studied experimentally and numerically. A thermodynamically consistent surface reaction mechanism is developed based on experimental results for WGS, RWGS, and preferential oxidation of CO. The experiments are carried out at laboratory scale in a flow reactor and in a fixed bed reactor using nickel/alumina-coated monoliths as catalyst (Section 3.3.2) and the nickel-based catalysts from BASF respectively (Section 3.1.2). The mechanism is a further extension of the elementary-step like reaction mechanism for H_2/O_2 and CO/O_2 presented in the previous sections (Section 4.1 and 4.2). The applicability of the reaction kinetics is validated against experimental data both from literature and experiments performed within this work.

4.3.1 Theoretical background

The conversion of carbon monoxide with water vapor called water-gas shift (WGS) reaction is crucial in the chemical industry for H_2 production from light hydrocarbons and CO purification [166, 167]. This reaction takes place in parallel to other chemical processes such as methane reforming, Fisher-Tropsh synthesis, methanol synthesis, etc. [1, 168].

$$CO + H_2O \leftrightarrow CO_2 + H_2 \qquad \Delta H_{298} = -41\ \mathrm{kJ/mol} \tag{4.3}$$

WGS reaction has also attracted interest in fuel cell technology. This reaction reduces the CO concentration while producing extra H_2. The reaction is slightly exothermic and reversible, and requires temperatures in the range of 200-450 °C in the presence of a catalyst for high equilibrium conversions [169]. The equilibrium constant of the reaction decreases with increasing temperature. WGS reaction is thermodynamically favored at low temperatures and kinetically favored at high temperatures.

The reaction can be catalyzed by both metal and metal oxides. The conventional water-gas shift catalysts for industrial applications are Fe-Cr at high temperatures and Cu-Zn-Al at low temperatures [166]. Cu-Zn-Al catalyst exhibits the highest rate per unit of volume. However, the catalyst is not stable under cyclic startup-shutdown conditions and at high temperatures. Several studies have been conducted on noble metal catalysts to overcome these problems [158, 170-173], but the activity is lower compared with the Cu-Zn-Al system. Ni based catalysts have

been also suggested as due to the high heat conductivity, that facilitates the control on the heat in exothermic reactions [174-176].

In the present study, the surface reaction mechanisms for H_2/O_2 and CO/O_2 are extended by C-OH species based on experimental results and data from the literature in order to describe the reactions of the $CO/CO_2/H_2/H_2O/O_2$ system over nickel catalyst.

4.3.2 Experimental Procedure

Fixed bed reactor experiments

The kinetics of WGS, R-WGS and preferential oxidation of CO with H_2 have been studied in a fixed bed reactor. The experiments are carried out using the nickel-based catalysts from BASF: Fixedbed_Ni_BASF_Cat.1 and Fixedbed_Ni_BASF_Cat.2. Between 1-1.77 g of catalyst is loaded into the reactor for the catalytic measurements. The catalyst pre-treatment is explained in the Section 3.1.2. Reactor operating pressure is selected to be 1bar, with total flow rates between 2-4 SLPM. The study is performed at temperatures in the range of 373-1073 K (100-800 °C). A temperature ramp of 15 K/min is applied.

Preferential oxidation of CO

The CO oxidation reaction in the presence of H_2 is performed in a fixed bed reactor at the operating conditions presented in Table 4.7. The reactor is loaded with 1.002 g of nickel catalyst (Fixedbed_Ni_BASF_Cat.1).The inlet gas composition presented in Table 4.7 is diluted in nitrogen and then fed into the reactor at 373 K with a total flow rate of 2 SLPM, which results in a linear flow velocity of 0.984 m/s.

Table 4.7 Experimental conditions for preferential oxidation of CO over Ni in a fixed bed reactor.

Temperature [K]	H_2 [vol.%]	CO [vol.%]	O_2 [vol.%]	N_2 [vol.%]
373-673	2.2	1.9	4.1	91.8

Water Gas-Shift Reaction (WGS) and Reverse Water Gas-Shift Reaction (RWGS)

The WGS reaction is carried out at a temperature range of 373-1073 K (100-800 °C) with different steam/carbon (S/C) ratios, the total flow rate is calculated to be 4 SLPM, which results in a linear flow velocity of 1.97 m/s. Table 4.8 shows the experimental inlet gas composition in nitrogen dilution, the gases are fed into the reactor at 373 K.

The reactor is loaded with 1 g of nickel catalyst (Fixedbed_Ni_BASF_Cat.1) for the experiment with a ratio S/C=3 and 1.51 g of the catalyst Fixedbed_Ni_BASF_Cat.2 is used for the experiment with an S/C= 1. The dosing of the gases is controlled by mass flow controllers, the steam is provided by a liquid flow controller from a water reservoir. After evaporation, the steam is mixed directly into the reactant gas stream. Equipment lines that carry steam must be preheated to 463 K before entering the reactor to avoid condensation through the lines.

Table 4.8 Experimental conditions for WGS reaction.

Temperature [K]	CO [vol.%]	H_2O [vol.%]	N_2 [vol.%]
373-1073	3.6	4.3	92.1
373-1073	4.0	12.7	83.3

Reverse water-gas shift reaction has been also evaluated in a temperature range of 373-1073 K (100-800 °C), with a total flow rate of 4 SLPM at 1bar. The reactor is loaded with 1.76 g of nickel catalyst (Fixedbed_Ni_BASF_Cat.2). The inlet gas composition diluted in nitrogen is presented in Table 4.9; the inlet mixture is fed into the reactor at 373 K.

Table 4.9 Experimental conditions for RWGS reaction.

Temperature [K]	CO_2 [vol.%]	H_2 [vol.%]	N_2 [vol.%]
373-1073	4.0	5.1	90.9

Continuous-flow reactor experiments with catalytic monoliths

The kinetics of R-WGS and preferential oxidation of CO with H_2 reaction have been also studied in a continuous flow reactor. The experiments are carried out using a nickel/alumina-coated monolith as catalyst. The catalyst structure and pre-treatment is explained in the Section 3.3.2. Reactor operating pressure is selected to be 1bar, with a flow rate of 4 SLPM, and reaction temperatures in the range of 373-973 K (100-700 °C). A temperature ramp of 15 K/min is applied.

Preferential oxidation of CO

Table 4.10 shows the experimental inlet gas composition in nitrogen dilution and the temperature range used for the preferential oxidation of CO in the presence of H_2 in a continuous-flow reactor.

Table 4.10 Experimental conditions for preferential oxidation of CO in H_2/O_2 in a continuous-flow reactor.

Temperature [K]	H_2 [vol.%]	CO [vol.%]	O_2 [vol.%]	N_2 [vol.%]
373-673	4.2	4.3	4.0	87.5

Reverse water gas-shift reaction (R-WGS)

Table 4.11 shows the experimental inlet mole fractions and the temperature range used for the reverse water gas-shift reaction in a continuous-flow reactor.

Table 4.11. Experimental conditions for R-WGS reaction.

Temperature [K]	CO_2 [vol.%]	H_2 [vol.%]	N_2 [vol.%]
373-1073	4.0	5.3	90.7

4.3.3 Kinetic Parameters

A detailed heterogeneous reaction mechanism for catalytic conversion of WGS, R-WGS and CO preferential oxidation over nickel-based catalyst has been developed. The model presented in this section is an extension of the previous mechanisms developed for H_2 and CO oxidation (Section 4.1 and Section 4.2). This kinetic model incorporates 10 more reactions, these reactions are presented in Table 4.12 highlighted in red. The reaction mechanism consists of 32 reactions with 5 gas phase species and 13 surface species. The kinetic model also contains important intermediates such as adsorbed HCO and COOH species. Reactions of CO and OH groups are introduced into the reaction steps as a WGS and consecutively R-WGS reaction steps. The overall thermodynamic consistency of the mechanism is ensured by a numerical approach, in which surface reaction rate parameters are slightly modified to be thermodynamically consistent.

Table 4.12 Propose surface reaction mechanism for WGS and RWGS.

	REACTION	A/[cm, mol, s]/S_0[-]	β [-]	E_a/[kJ/mol]	ε_1[kJ/mol]
R1	H_2 + (Ni) + (Ni) → H(Ni) + H(Ni)	$3.000 \cdot 10^{-02}$	0.000	0.00	
R2	H(Ni) + H(Ni) → Ni(Ni) + Ni(Ni) + H_2	$2.545 \cdot 10^{+20}$	0.000	95.21	
R3	O_2 + (Ni) + (Ni) → O(Ni) + O(Ni)	$4.358 \cdot 10^{-02}$	-0.206	0.00	
R4	O(Ni) + O(Ni) → (Ni) + (Ni) + O_2	$1.188 \cdot 10^{+21}$	0.823	468.91	
R5	H_2O + (Ni) → H_2O(Ni)	$1.000 \cdot 10^{-01}$	0.000	0.00	
R6	H_2O(Ni) → H_2O + (Ni)	$3.734 \cdot 10^{+12}$	0.000	60.79	
R7	CO_2 + (Ni) → CO_2(Ni)	$7.000 \cdot 10^{-06}$	0.000	0.00	
R8	CO_2(Ni) → CO_2 + (Ni)	$6.447 \cdot 10^{+07}$	0.000	25.98	
R9	CO + (Ni) → CO(Ni)	$5.000 \cdot 10^{-01}$	0.000	0.00	
R10	CO(Ni) → CO + (Ni)	$3.566 \cdot 10^{+11}$	0.000	111.27	-50.0 $\theta_{CO(Ni)}$
R11	H(Ni) + O(Ni) → OH(Ni) + (Ni)	$3.951 \cdot 10^{+23}$	-0.188	104.35	
R12	OH(Ni) +(Ni) →H(Ni) +O(Ni)	$2.254 \cdot 10^{+20}$	0.188	29.64	
R13	H(Ni) + OH(Ni) → H_2O(Ni) + (Ni)	$1.854 \cdot 10^{+20}$	0.086	41.52	
R14	H_2O(Ni) + (Ni) → H(Ni) + OH(Ni)	$3.674 \cdot 10^{+21}$	-0.086	92.94	
R15	OH(Ni) + OH(Ni) → H_2O(Ni) + O(Ni)	$2.346 \cdot 10^{+20}$	0.274	92.37	
R16	H_2O(Ni) + O(Ni) → OH(Ni) + OH(Ni)	$8.148 \cdot 10^{+23}$	-0.274	218.50	
R17	C(Ni) + O(Ni) → CO(Ni) + (Ni)	$3.402 \cdot 10^{+23}$	0.000	148.10	
R18	CO(Ni) + (Ni) → C(Ni) + O(Ni)	$1.758 \cdot 10^{+13}$	0.000	116.24	-50.0 $\theta_{CO(Ni)}$
R19	CO(Ni) + CO(Ni) → C(Ni) + CO_2(Ni)	$1.624 \cdot 10^{+14}$	0.500	241.76	-100.0 $\theta_{CO(Ni)}$

R20	$CO_2(Ni) + C(Ni) \rightarrow CO(Ni) + CO(Ni)$	$7.294 \cdot 10^{+28}$	-0.500	239.24	
R21	$CO(Ni) + O(Ni) \rightarrow CO_2(Ni) + (Ni)$	$2.002 \cdot 10^{+19}$	0.000	123.60	-50.0 $\theta_{CO(Ni)}$
R22	$CO_2(Ni) + (Ni) \rightarrow CO(Ni) + O(Ni)$	$4.648 \cdot 10^{+23}$	-1.000	89.32	
R23	$CO_2(Ni) + H(Ni) \rightarrow COOH(Ni) + (Ni)$	$6.250 \cdot 10^{+24}$	-0.475	117.24	
R24	$COOH(Ni) + (Ni) \rightarrow CO_2(Ni) + H(Ni)$	$3.737 \cdot 10^{+20}$	0.475	33.66	
R25	$COOH(Ni) + (Ni) \rightarrow CO(Ni) + OH(Ni)$	$1.461 \cdot 10^{+24}$	-0.213	54.37	
R26	$CO(Ni) + OH(Ni) \rightarrow COOH(Ni) + (Ni)$	$6.003 \cdot 10^{+20}$	0.213	97.63	-50.0 $\theta_{CO(Ni)}$
R27	$CO(Ni) + H(Ni) \rightarrow HCO(Ni) + (Ni)$	$4.019 \cdot 10^{+20}$	-1.000	132.23	
R28	$HCO(Ni) + (Ni) \rightarrow CO(Ni) + H(Ni)$	$3.700 \cdot 10^{+21}$	0.000	0.00	+50.0 $\theta_{CO(Ni)}$
R29	$COOH(Ni) + H(Ni) \rightarrow HCO(Ni) + OH(Ni)$	$6.000 \cdot 10^{+22}$	-1.163	104.88	
R30	$HCO(Ni) + OH(Ni) \rightarrow COOH(Ni) + H(Ni)$	$2.282 \cdot 10^{+20}$	0.263	15.92	
R31	$C(Ni) + OH(Ni) \rightarrow H(Ni) + CO(Ni)$	$3.888 \cdot 10^{+25}$	0.188	62.55	
R32	$H(Ni) + CO(Ni) \rightarrow C(Ni) + OH(Ni)$	$3.522 \cdot 10^{+18}$	-0.700	105.45	-50.0 $\theta_{CO(Ni)}$

The rate coefficients are given in the form of $k=AT^{\beta}\exp(-E_a/RT)$; adsorption kinetics is given in form of sticking coefficients; the surface site density of $\Gamma=2.66 \times 10^{-9}$ mol cm^{-2} is calculated by assuming a site area of 6.5×10^{-2} nm^2 as observed for nickel [58, 119].

Theoretical and experimental studies are conducted to elucidate the reaction mechanism for WGS. Two main mechanistic routes have been proposed to describe the WGS reaction, the regenerative mechanism also known as Redox mechanism and the associative mechanism [177-180]. According to the Redox mechanism, H_2O oxidize the active centers on the catalytic surface producing H_2 as by product

$$H_2O_{(g)} + * \rightarrow H^* + OH^* \tag{4.4}$$

$$OH^* + * \rightarrow H^* + O^* \tag{4.5}$$

followed by surface reduction to convert CO to CO_2.

$$CO + O^* \leftrightarrow CO_2 + * \tag{4.6}$$

Hilaire et al. [171] investigated the water-gas shift (WGS) reaction on various monometallic Pd, Ni, Fe, Co catalysts supported on ceria and Pd catalyst supported on silica. The authors assumed that the mechanism for the WGS reaction involves a Redox process.

The associative model assumes a reaction sequence to form intermediates including CO* and OH* that further decompose to produce H_2 and CO_2 [177, 181-183]. The intermediates are known as formate (HCOO*) or carboxyl species (COOH*)

$$CO + H_2O \leftrightarrow (\text{formate or carboxyl}) \leftrightarrow CO_2 + H_2 \tag{4.7}$$

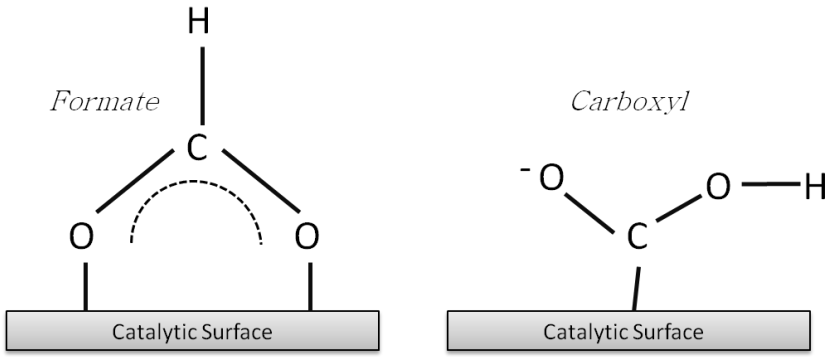

Figure 4.12 *Formate and carboxyl groups.*

The formation of formate and carboxyl surface species were detected experimentally using in-situ diffuse reflectance infrared Fourier transform spectroscopy (DRIFTS), steady-state IR measurements and steady-state isotopic transient kinetic analysis (SSITKA) technique [172, 184-186]. Jacobs et al. [172, 181, 187] studied the formation of formate species on reduced ceria and noble metal promoted ceria catalysts. Grenoble and Estadt [177] reported that WGS reaction occurred at two different sites, the metal centers activating carbon monoxide and the second principal sites situated on support material for water activation. The authors proposed a reaction sequence including formic acid as intermediate in order to account for the apparent bifunctionality of the supported catalyst systems. Tibiletti et al. [188] identified, formate, carbonate and carbonyl species at the surface of Pt/CeO_2 catalyst during the forward water-gas-shift (WGS) and the reverse reaction (RWGS). Shido and Iwasawa [189] also studied the formation of formate species on Rh/CeO_2 during WGS. The presence of formate on Ni (110) have been identified by Jones et al. [190] using high resolution electron energy loss spectrometers (HREELS). Ovesen et al. [191] found that water dissociation and carbon monoxide oxidation to be the rate determining steps. Their micro-kinetic model is based on the redox mechanism; the authors include more steps to account for the formate mechanism. Fishtik and Dutta [192] developed a micro-kinetic model that quantitatively describes the kinetics of the water-gas shift reaction on Cu(111). The authors concluded that both formate and Redox

mechanism may be important in different temperature ranges and for different feed composition.

Despite all studies carried out on WGS, there is still no convergence on the nature of the intermediate, as to whether it is a carboxyl or a formate species. Theoretical calculations favor the formation of the carboxyl species over formate species [193, 194]. Burch et al. [195] analyzed the evidence for and against a formate-base mechanism for the water-gas shift reaction, based on different published studies using metal supported and unsupported catalyst and concluded that the published results cannot be used to provide any mechanistic information either for or against a formate model.

The carboxyl mechanism is supported by Boisen et al. [158], they assumed that carboxyl species plays an important role specially on supports containing CeO_2, regardless of the metal type, the extraction of the first hydrogen from water is a slow step and the subsequent reaction of CO and OH results in a carboxyl (COOH) intermediate with decomposes into CO_2 and H_2. Grabow et al. [196] present a micro-kinetic model as well as experimental data for the low-temperature water-gas shift (WGS) reaction catalyzed by Pt at temperatures from 523 K to 573 K for various gas compositions at a pressure of 1 atm. The authors concluded that the most significant reaction channel proceeds via a carboxyl (COOH) intermediate and formate (HCOO) acts only as a spectator species. Gokhale et al. [193] used self-consistent density functional theory (DFT-GGA) calculations to investigate the water-gas shift reaction (WGS) mechanism on Cu(111). Through their calculations, they identify carboxyl, a new reactive intermediate, which plays a central role in WGS on Cu(111). In a recent study, Karakaya et al. [197] developed a kinetic model for water- gas shift reaction over Rh. In this model, the main path for CO_2 formation is concluded to be the direct oxidation of CO with O species at high temperatures, whereas the formation of the carboxyl group is significant a low temperatures.

In the surface mechanism presented in Table 4.12, the carboxyl (COOH) path is included and the formate species HCOO is ignored, because no concrete evidence of its existence has been found for nickel supported catalyst. The model developed by Blaylock et al. [55, 73] is used as a reference of the reaction paths and the enthalpy values in the reactions R23-R26 (Table 4.12). In this model, the formation of carboxyl (COOH) species proceeds as a reaction between the adsorbed CO and OH species derived from the dissociation of water (R26, Table 4.12)

$$CO^* + OH^* \leftrightarrow COOH^* + * \tag{4.8}$$

Adsorbed carboxyl (COOH) species can dissociate to form CO_2* and H* (R24, Table 4.12).

$$COOH^* + * \leftrightarrow CO_2{}^* + H^* \quad (4.9)$$

It has been proposed by several authors that the formyl HCO (also written as CHO) species coordinated over carbon is an important intermediate during the reforming and oxidation of methane over transition metals (Figure 4.13) [11, 47, 73, 93, 198, 199]. The implementation of the HCO* in the micro-kinetic model presented in this work is supported experimentally by TPRS and TR-FTIR experiments [200] and theoretically using UBI-QEP method [201, 202] and DFT studies [53, 55, 73, 93]. The reaction mechanism developed by Maier et al. [58] is used as a reference for the reaction paths and enthalpy values of the reactions R27 and R28 from Table 4.12.

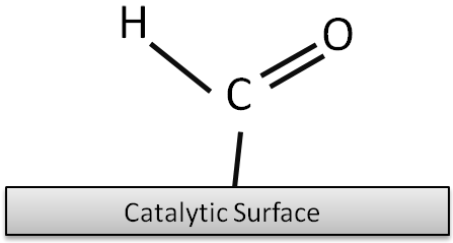

Figure 4.13 *Formyl species.*

4.3.4 Results and Discussion

Experiments in a fixed bed reactor for preferential oxidation of CO

Figure 4.14 shows a comparison of the experimental and the predicted results as a function of the temperature. An active catalytic surface area value of 1.14×10^5 m^{-1} is used for the simulation of the fixed bed reactor.

The model predicts the trend of the experimental data over the complete temperature range studied. The concentration profile of H_2 is under predicted in comparison with the experimental results. Experimentally, at rich oxygen concentrations the formation of CO_2 takes place first, living free active sites for hydrogen adsorption to produce H_2O. However, the model is not able to predict such results. The equilibrium of the reaction is reached after 573 K.

a)

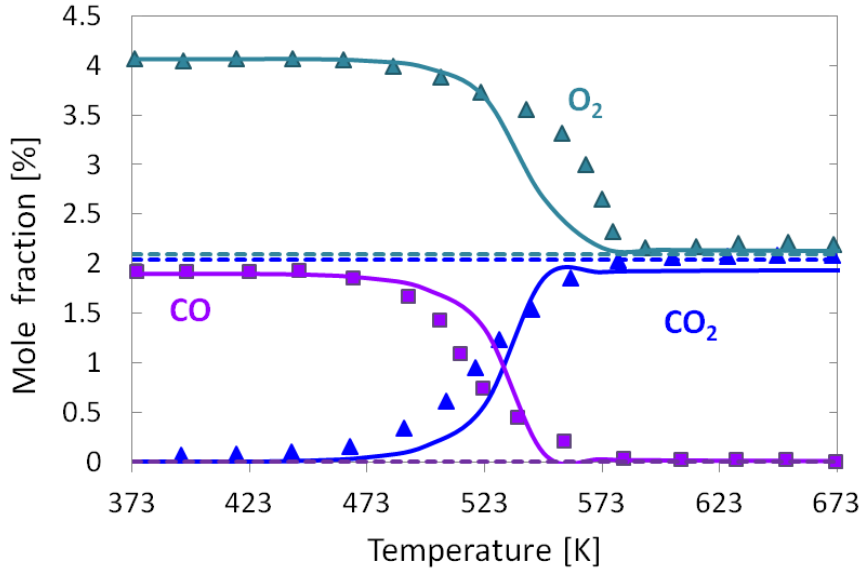

b)

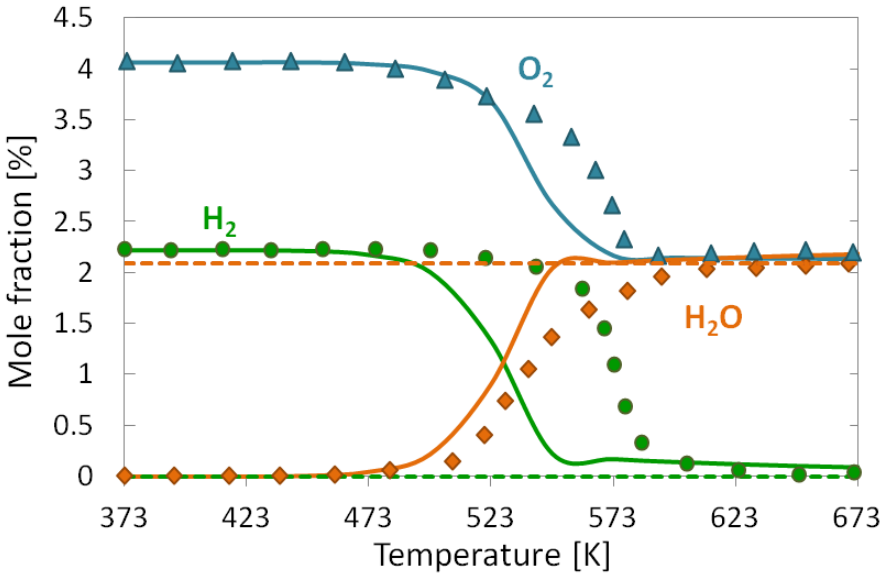

Figure 4.14. *Comparison of experimentally determined (symbols) and numerically predicted (lines) mole fractions as a function of temperature for preferential CO oxidation in a fixed bed reactor:* ***a)*** *CO, CO_2, and O_2;* ***b)*** *H_2, H_2O, and O_2; inlet gas composition of 2.22 vol.% CO, 1.90 vol.% H_2, 4.0 vol% O_2 in N_2; 1 bar; T_{inlet}= 373 K; total flow rate of 2 SLPM; dashed lines = equilibrium composition at given temperature.*

Figure 4.15 shows the computed mole fractions of the gas-phase species along the catalytic bed. It can be observed that water is produced before CO_2 which is the opposite result that should take place during CO preferential oxidation where CO_2 is produced first. In this case the mean field approximation does not work.

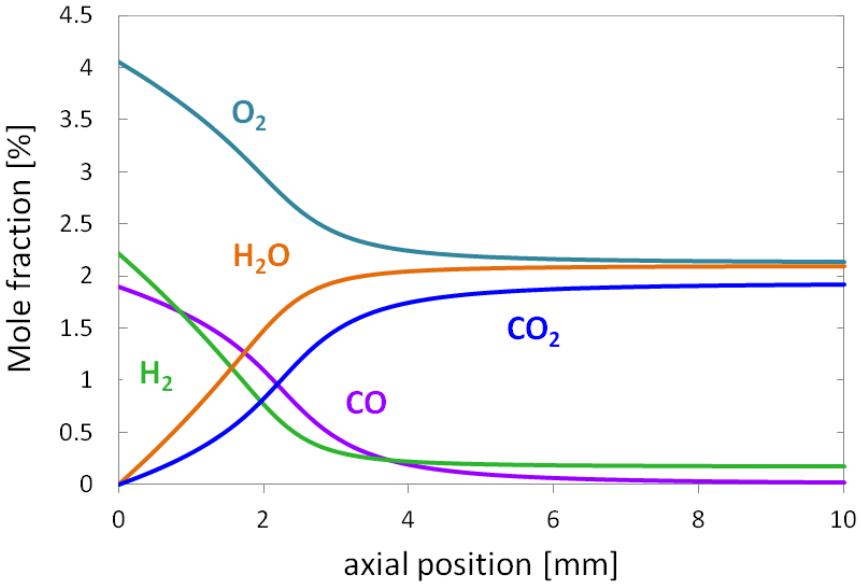

Figure 4.15. *Computed mole fraction of the gas-phase species along the catalytic bed for CO preferential oxidation at 573 K.*

In order to understand why the model does not reproduce the CO preferential oxidation, a reaction flow analysis of the reaction mechanism (Table 4.12) is performed. Figure 4.16 shows that reaction R11 ($O^* + H^* \rightarrow OH^* + *$) is too fast and the reaction R21 too slow ($O^* + CO^* \rightarrow CO_2^* + *$), which explains why the hydrogen oxidation take place first in the model. The kinetic parameters of these two reactions cannot be changed without affecting the other systems under study. Therefore, the reaction mechanism presented in this work is not able to reproduce CO preferential oxidation.

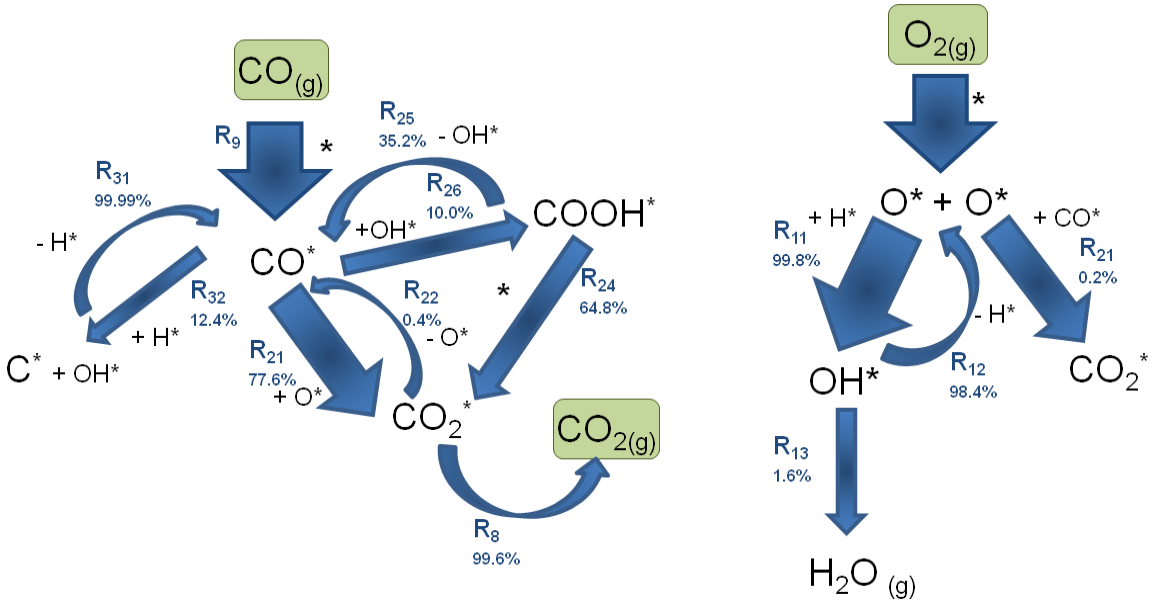

Figure 4.16 *Reaction flow analysis for CO preferential oxidation on nickel at 573 K, total flow rate of 2 SLPM, inlet gas composition of 2.22 vol.% CO, 1.90 vol.% H_2, 4.0 vol% O_2 in N_2 (94 % N_2), 1bar.*

Continuous-flow reactor results for preferential oxidation of CO

The preferential CO oxidation in the presence of H_2 is also studied in a continuous-flow reactor over a monolithic catalyst. An effective $F_{cat/geo}$ value 150 is used for the simulation. Figure 4.17 shows a comparison between the experimental data and the predicted results as a function of the temperature. As well as in the fixed reactor experiment, the model does not predict the experimental results of CO preferential oxidation over nickel. The experimental data obtained from the continuous-flow reactor exhibit the same results as the fixed bed reactor, in which at high oxygen concentrations, CO_2 and H_2O are ignited almost at the same temperature of approximately 473 K, reaching full conversion at 573 K.

a)

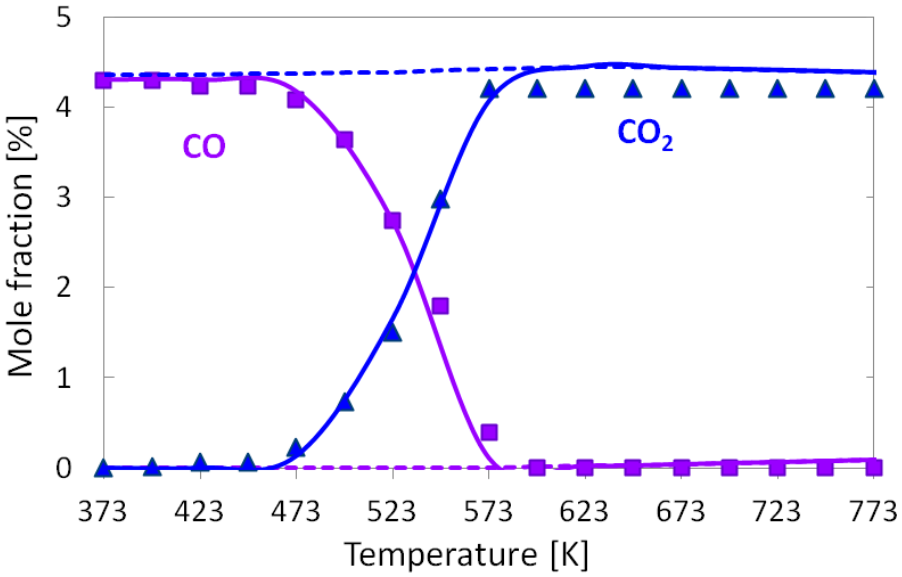

b)

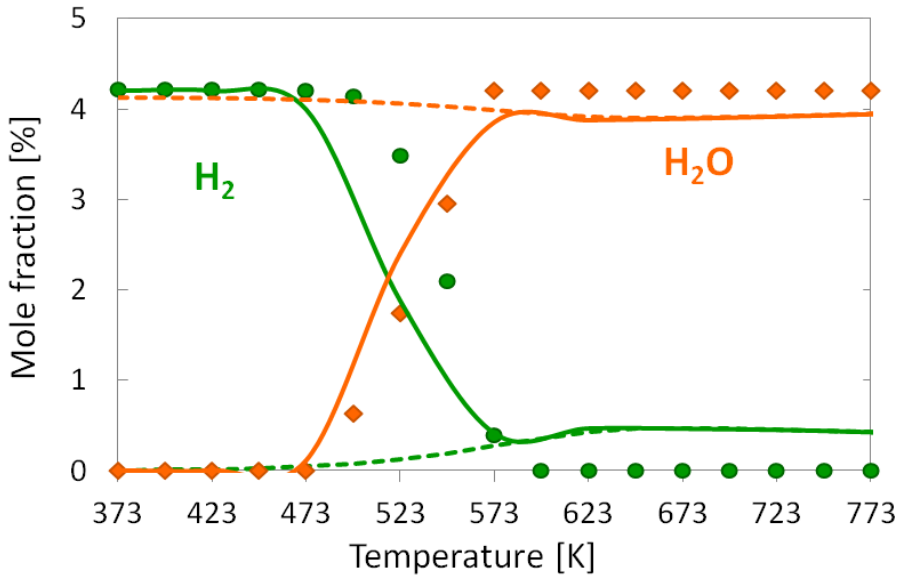

Figure 4.17 *Comparison of experimentally determined (symbols) and numerically predicted (lines) mole fractions as a function of temperature for preferential CO oxidation over a monolith catalyst:* ***a)*** *CO and CO_2;* ***b)*** *H_2 and H_2O; inlet gas composition of 4.3 vol.% CO, 4.2 vol.% H_2, 4.0 vol.% O_2 in N_2; 1 bar; T_{inlet}= 373 K; total flow rate of 4 SLPM; dashed lines = equilibrium composition at given temperature.*

Figure 4.18 shows the evolution of species surface coverage at the entrance of the monolith as a function of temperature. It can be observed that at low temperature the surface is mainly covered by CO*, but after 573 K when CO* and H* have been completely converted, nickel on the surface becomes free.

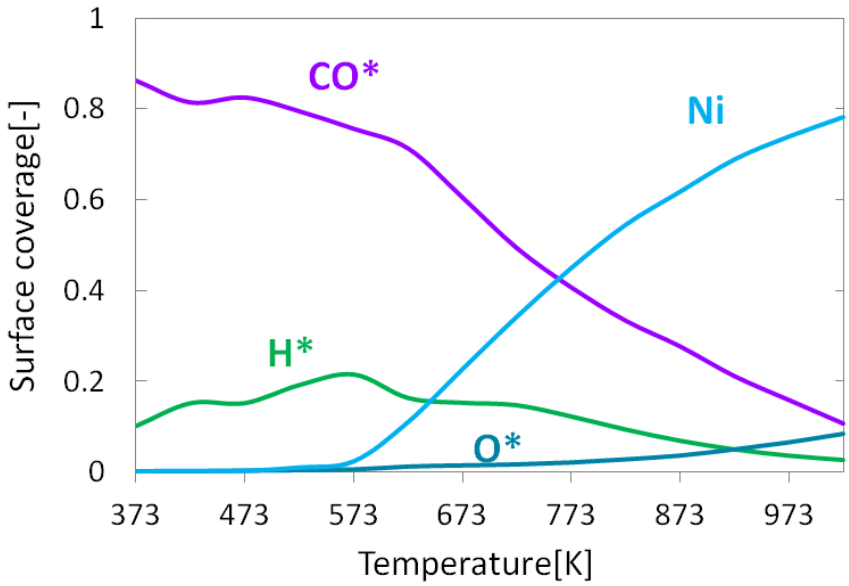

Figure 4.18 *Surface coverage as function of the temperature for preferential CO oxidation for an inlet mixture of 4.3 vol.% CO, 4.20 vol.% H_2, 4.0 vol.% O_2 in N_2; 1 bar; T_{inlet}= 373 K; 4 SLPM.*

Experiments in a fixed bed for Water-Gas Shift Reaction (WGS)

A sensitivity analysis of the reaction mechanism is performed for WGS reaction at temperatures between: 573-873 K (300-600 °C), with a ratio of CO/H_2O=1.65 (92 % N_2), at 1 bar. The sensitivity of CO_2 and H_2 molar fraction at the outlet are analyzed. Results for CO_2 mole fraction at different temperatures are presented in Figure 4.19. The analysis shows that at low temperature, the carboxyl (COOH*) species can dissociate to produce adsorbed CO_2* and H* ($COOH^* + * \rightarrow CO_2^* + H^*$) (R24, Table 4.12). However, at high temperatures, direct oxidation of CO by O* is favored ($CO^* + O^* \rightarrow CO_2^*$) (R21, Table 4.12). The analysis also indicates that the system is highly sensitive to C* formation (R32, Table 4.12) at low temperatures, which can lead to methane formation as secondary reaction. Methanation reactions will be analyzed in the Section 5.

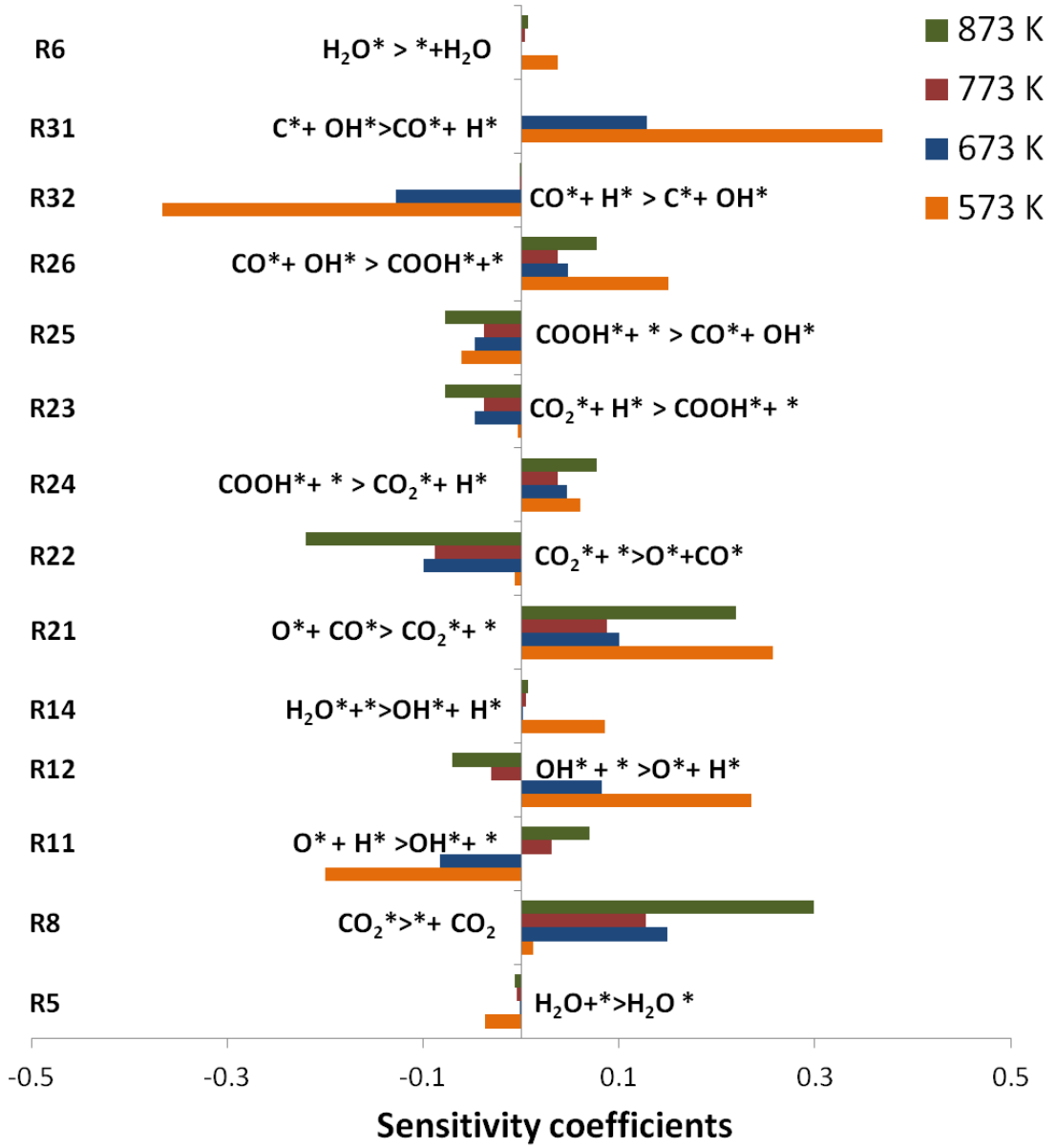

Figure 4.19 *Sensitivity analyses of CO_2 gas-phase concentration for WGS reaction at different temperature points. Inlet mole composition is chosen to be 3.6 vol.% CO and 4.3 vol.% H_2O in N_2 dilution.*

The sensitivity analysis for H_2 formation is presented in Figure 4.20, it indicates that hydrogen adsorption and desorption (R1 and R2, Table 4.12) are the most important reactions for hydrogen formation for the temperature range relevant to the analysis. Furthermore, it was also determined that H_2O dissociation to OH* and H* (R14, Table 4.12) is more sensitive at temperatures between 573 K and 673 K.

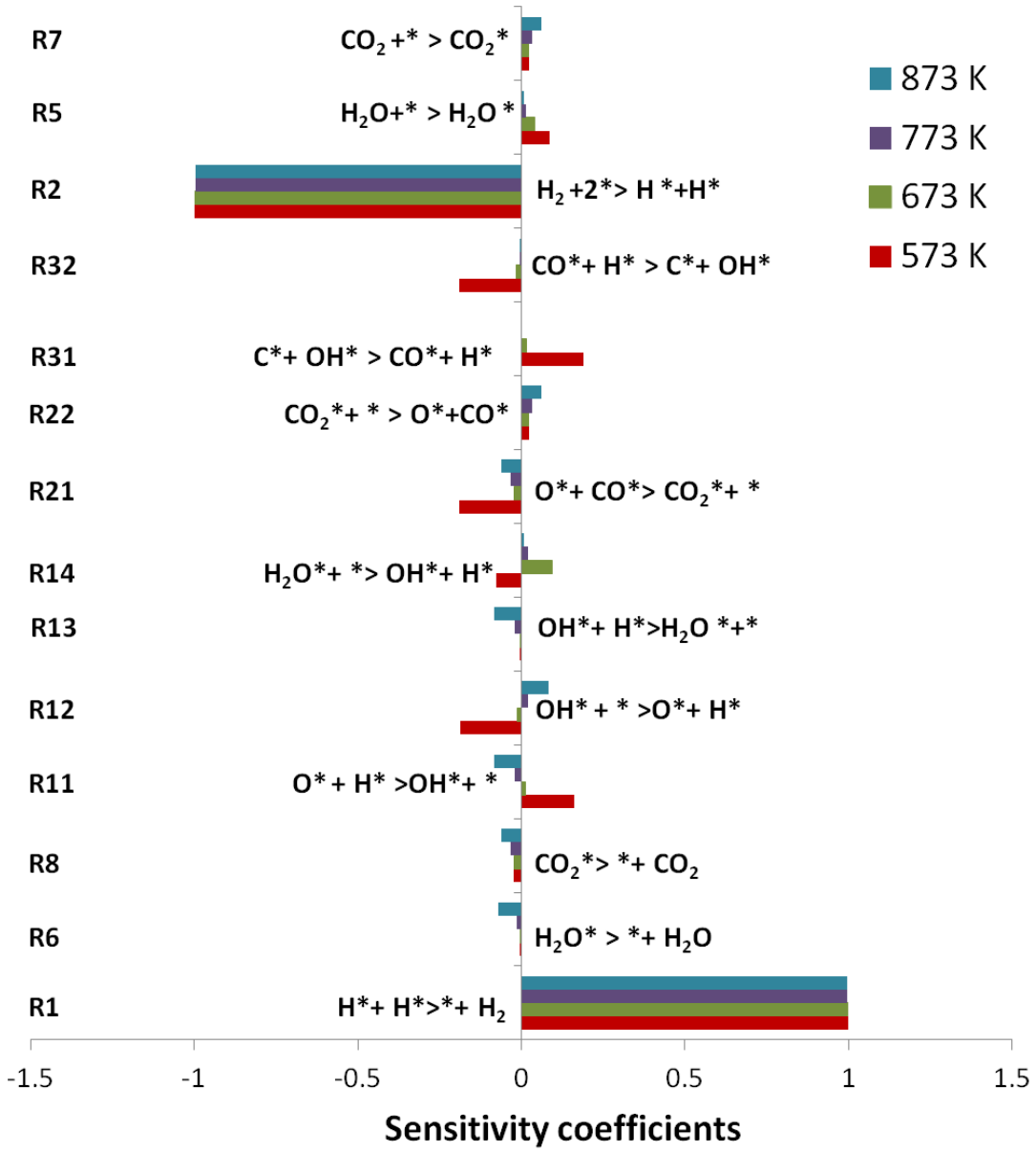

Figure 4.20 *Sensitivity analyses of H_2 gas-phase concentration for WGS reaction at different temperature points. Inlet gas composition is chosen to be 3.6 vol. % CO and 4.3 vol. % H_2O in N_2 dilution.*

The reaction flow analysis of the mechanism is performed at 673 K and 1 bar, with an inlet composition of 3.6 vol.% CO and 4.3 vol.% H_2O in nitrogen dilution. Figure 4.21 shows the reaction path for CO_2 and H_2 formation. The analysis shows that CO_2 is mainly produced by direct CO oxidation (R21, Table 4.12). However, it can also be originated through the carboxyl (COOH*) intermediate. The analysis also shows that water dissociate almost 100 % into OH* and H* (R14, Table 4.12).

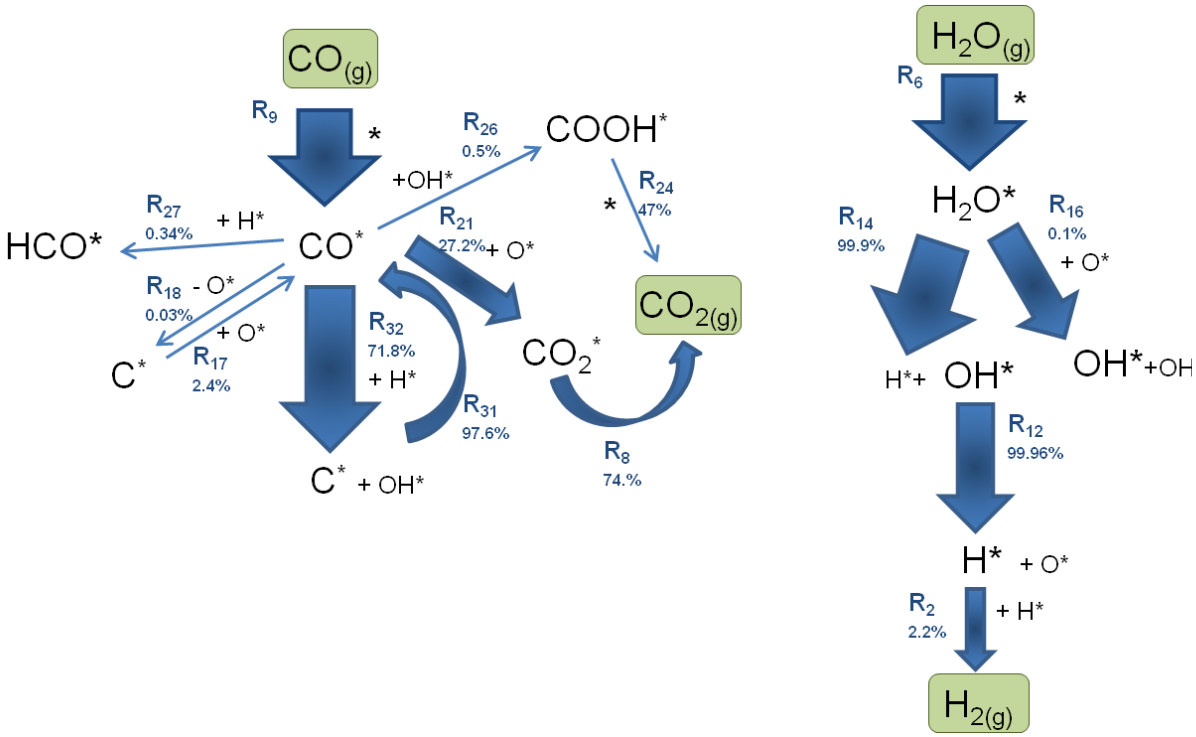

Figure 4.21 *Reaction flow analysis for WGS reaction on nickel at 673 K, 4 SLPM, inlet gas composition of 3.6 vol. % CO and 4.3 vol. % H_2O in N_2 dilution.*

An effective catalytic area of 9.85×10^6 m^{-1} is calculated for the powdered catalyst Fixedbed_Ni_BASF_Cat.2. However, this value has been adapted to 3.10×10^6 m^{-1} for the simulations of WGS and R-WGS experiments to fit the experimental results. It has been observed in several studies that CO activation is structure sensitive [52, 203, 204]. Szabo et al. [204] suggested that the elementary step producing CO_2 from adsorbed CO and oxygen on Pt (112) is structure sensitive, with a smaller activation energy on the terrace sites. Zafiris and Gorte [205] studied CO oxidation on Pt/α-Al_2O_3 (0001), the authors also observed structure sensitivity of CO that could be explained by changes in the desorption kinetics of CO with particle size. It has been also reported that CO_2 activation is structure sensitive [164, 206]. Nukolic et al.[162] reported that the reaction of CO_2 with H_2 is structure sensitive. These results are confirmed by Rodes et al. [163], which provide evidence that CO_2 reduction is on the surface defects.

Changes in the structure of the catalyst due to direct adsorption of CO or CO_2 cannot be described correctly using the mean field approximation applied in this work. Therefore, the effective catalytic area is adjusted to simulate such changes and fit the experimental data.

Figure 4.22 shows a comparison of the measured and the predicted concentration profiles of CO, H_2O, CO_2, H_2, and CH_4 species. The kinetic model is able to describe the experimental

results in the range of temperatures investigated. The reaction initiates at temperatures around 523 K (250 °C), reaching equilibrium at 723 K (450 °C). However, methane formation occurs at temperatures between 573-823 K, as shown by Figure 4.22b. Following the modeling approach presented in Figure 4.1, reactions for methane activation will be added in the Section 4.4. The kinetics of the methanation reactions will be analyzed in Section 5.

a)

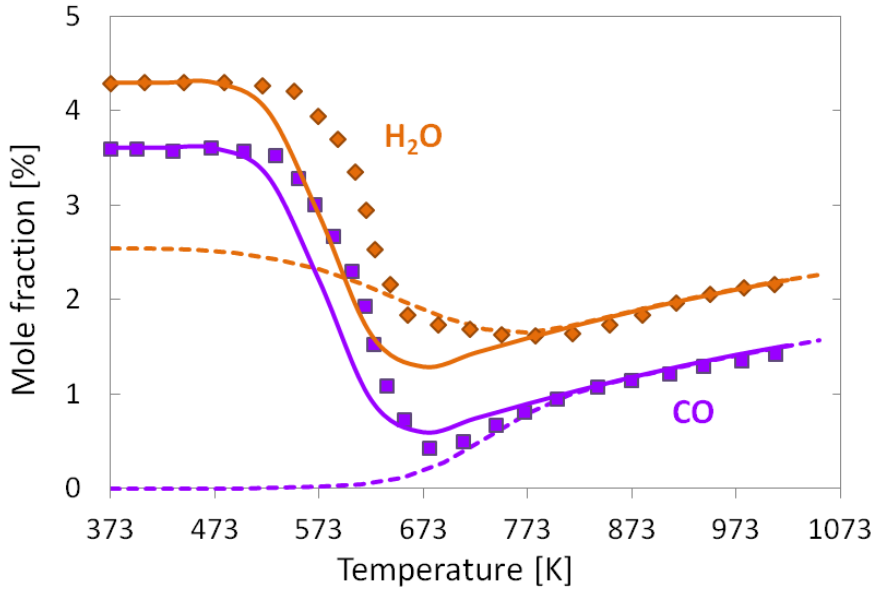

b)

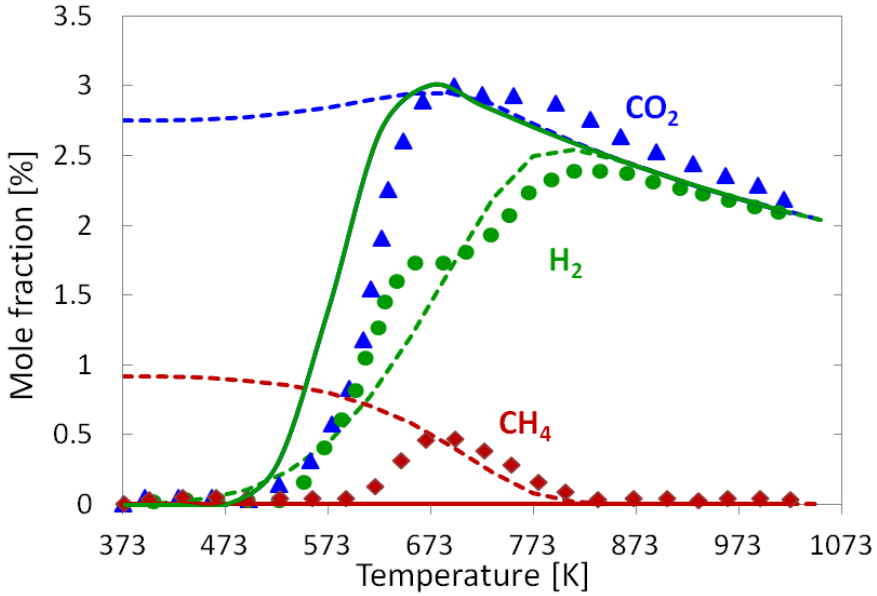

Figure 4.22 *Comparison of experimentally (symbols) and numerically predicted (lines) mole fractions as a function of temperature for WGS in a fixed bed reactor:* ***a)*** *CO and H_2O;* ***b)*** *CO_2, H_2, and CH_4, inlet gas composition of 3.6 vol.% CO, 4.3 vol. % H_2O in N_2; 1 bar; T_{inlet}= 373 K; 4 SLPM; dashed lines = equilibrium composition at given temperature.*

Figure 4.23 shows CO conversion as a function of the temperature during WGS reaction. It can be observed that CO conversion reaches the maximum at 676 K, beyond which the system reaches equilibrium.

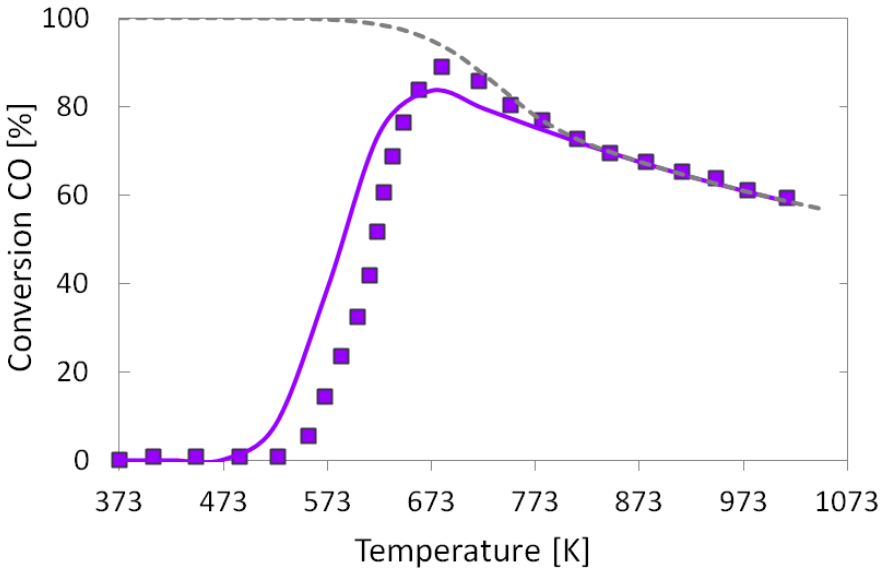

Figure 4.23 *CO conversion as a function of the temperature in water-gas shift reaction on Ni for an inlet gas composition of 3.6 vol. % CO, 4.3 vol. % H_2O in N_2; 1 bar; T_{inlet}= 373 K; 4 SLPM; symbols = experiment, lines = simulation, dashed lines = equilibrium composition at given temperature.*

Figure 4.24 shows a comparison of the measured and the predicted concentration profiles as a function of the temperature for an inlet mixture of 4.0 vol.% CO, 12.7 vol.% H_2O in nitrogen dilution. An active catalytic surface area value of 1.14×10^5 m^{-1} is used for the simulation. The kinetic model describes the experimental results with accuracy. The reaction initiates at temperatures above 573 K reaching equilibrium at 773 K. At high H_2O concentration in the inlet mixture, no methane is formation is observed.

It is well known that water inhibits the formation of carbon on the catalytic surface, without adsorbed carbon the methanation reactions cannot be initiated. As it was mentioned before the kinetics of the methanation reactions on nickel will be analyzed in the Section 5.

a)

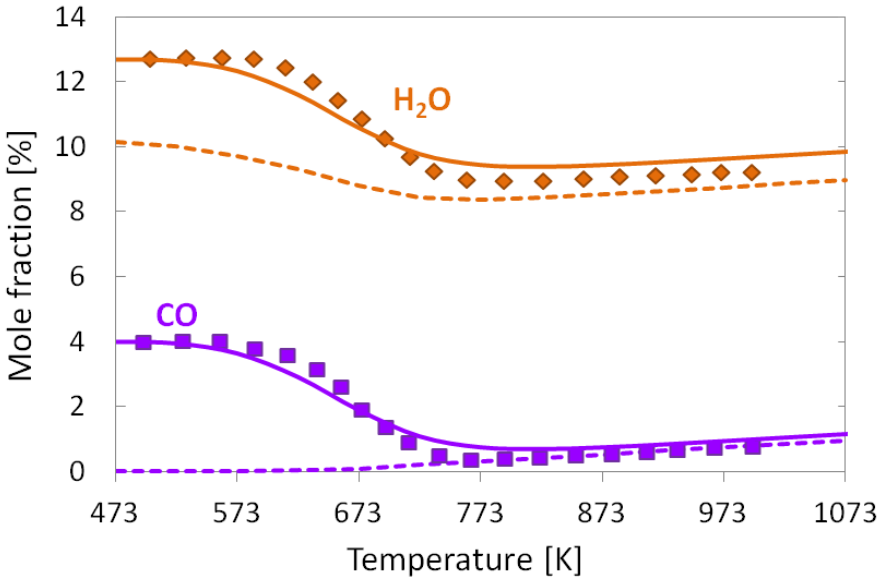

b)

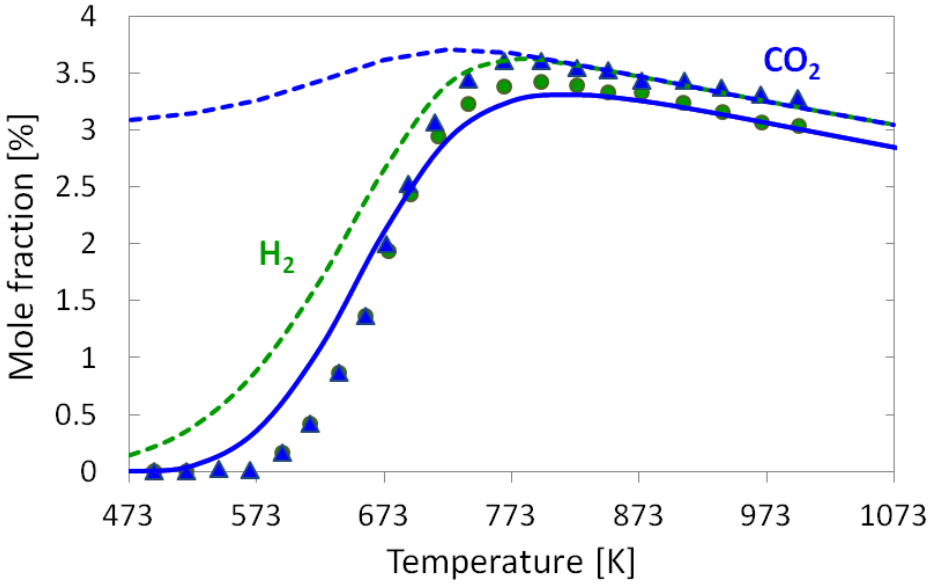

Figure 4.24 *Comparison of experimentally determined (symbols) and numerically predicted (lines) mole fractions as a function of temperature for WGS in a fixed reactor:* ***a)*** *CO and H_2O;* ***b)*** *CO_2, H_2, inlet gas composition of 4.0 vol. % CO, 12.7 vol.% H_2O in N_2; 1 bar; T_{inlet}= 373 K, 4 SLPM, dashed lines = equilibrium composition at given temperature.*

Experiments in a fixed bed for Reverse Water-Gas Shift Reaction (R-WGS)

A sensitivity analysis of the reaction mechanism is performed for the R-WGS reaction at temperatures between: 573-873 K (300-600 °C), with CO_2/H_2=0.78 in nitrogen dilution, at 1bar. The sensitivity of the exit molar fractions of the products CO and H_2O is analyzed. Results for CO mole fraction at different temperatures are presented in Figure 4.25. The analysis shows that CO adsorption (R9, Table 4.12) and desorption (R10, Table 4.12) are sensitive reactions in the range of temperatures investigated. The analysis also shows that CO* can be produced through the carboxyl intermediate (COOH*) at low temperature (R25, Table 4.12). However, at the temperatures higher than 673 K the CO* formation is favored via CO_2 decomposition (R22, Table 4.12).

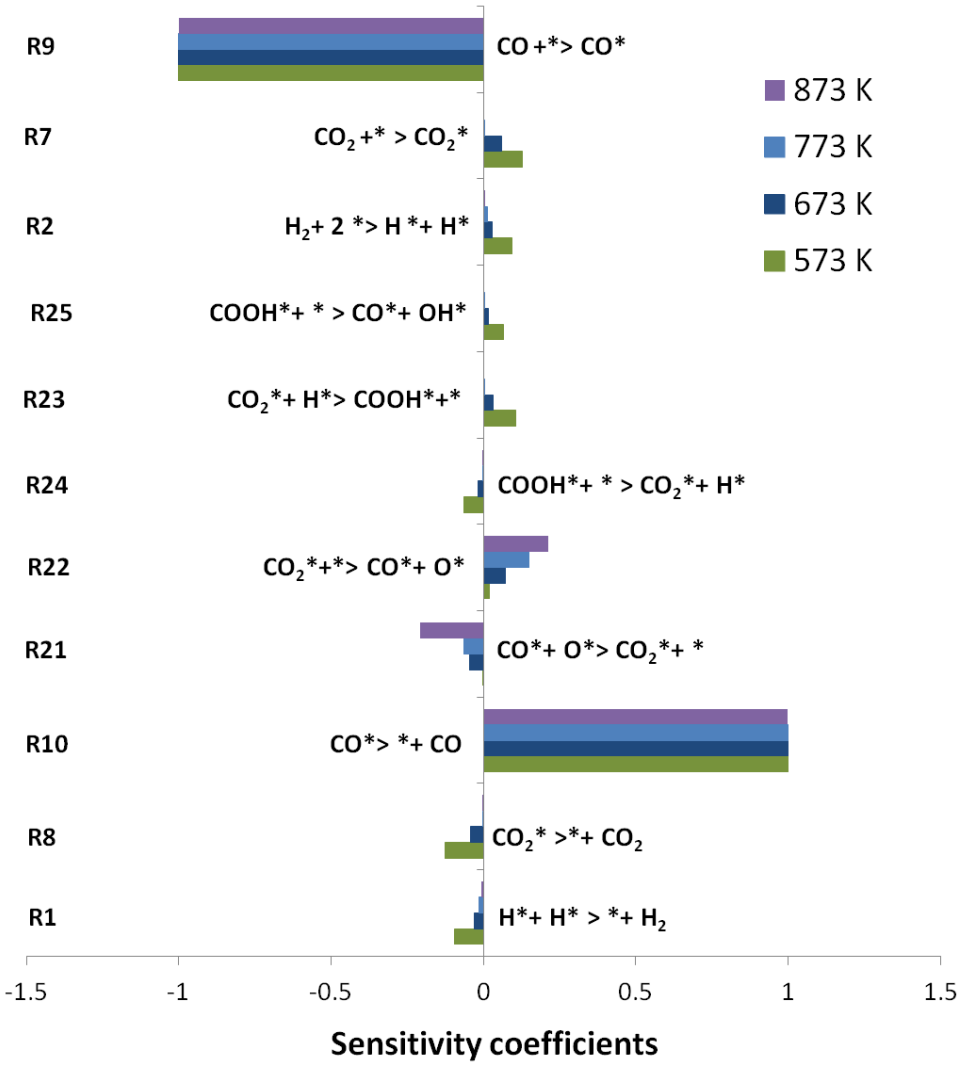

Figure 4.25 *Sensitivity analyses of CO gas-phase concentration for R-WGS reaction at different temperature points. Inlet gas composition is chosen to be 4.0 vol.% CO_2 and 5.1 vol.% H_2 in N_2 dilution.*

The sensitivity analysis for H_2O formation is presented in Figure 4.26. The analysis shows that CO_2 adsorption (R7, Table 4.12) and desorption (R8, Table 4.12) are dominant reactions at low temperatures. The analysis also indicates that at low temperatures formation of COOH* intermediate is favored (R23, Table 4.12), which further decomposes to CO* and OH* (R25, Table 4.12). The decomposition of CO_2* become more sensitive at higher temperatures (R22, Table 4.12). The reaction provides enough oxygen on the surface to form OH* (R12), which combines with H* to produce H_2O*, then consequently desorbs to the gas phase. The reactions R11, R12, R13, and R14 (Table 4.12) are highly dependent of the temperature.

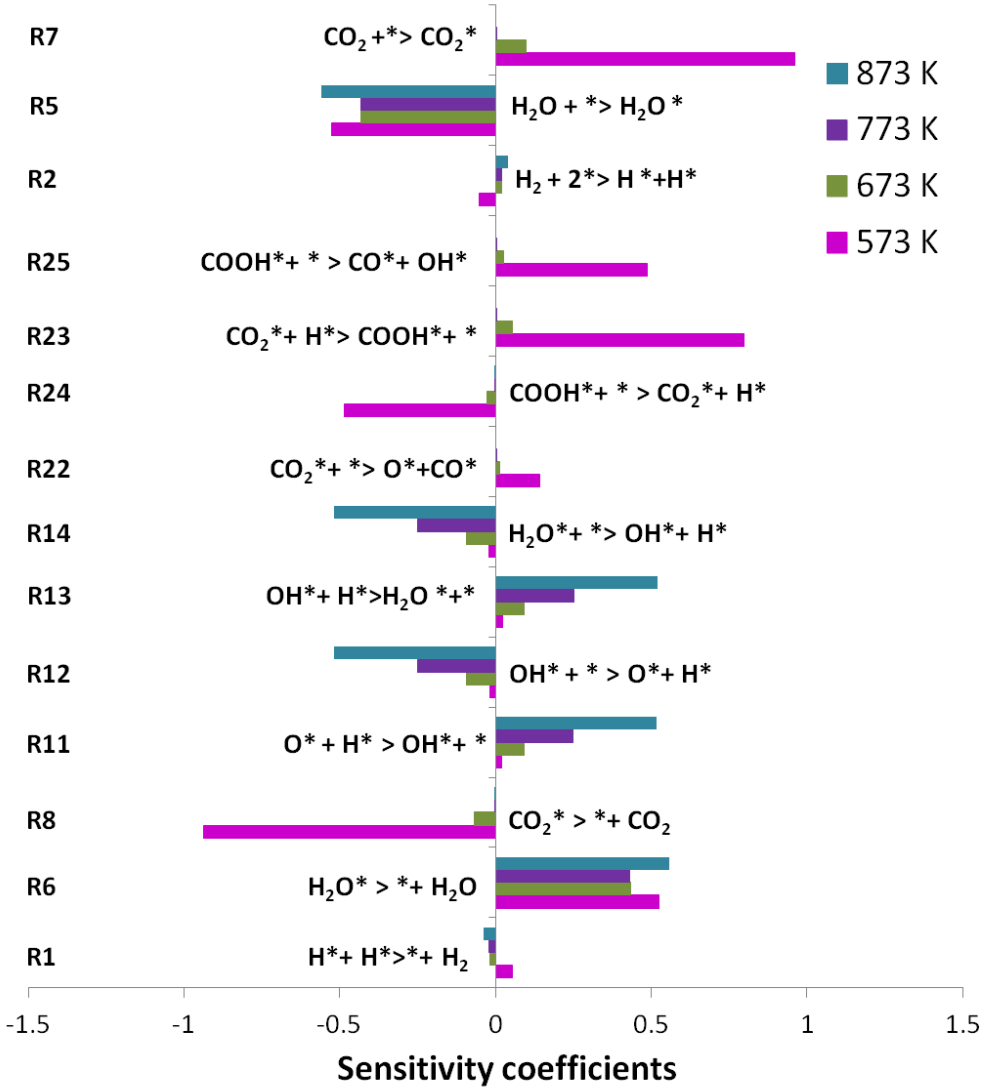

Figure 4.26 *Sensitivity analyses of H_2O gas-phase concentration for R-WGS reaction at different temperature points. Inlet gas composition is chose to be 4.0 vol.% CO_2 and 5.1 vol.% H_2 in N_2 dilution.*

The R-WGS reaction experiment is carried out in a fixed bed reactor at 1bar, with a total flow of 4 SLPM (1.97 m/s), in a temperature range between 373-1173 K (100-900 °C), with an inlet mole composition of 4.0 vol.% CO_2 and 5.1 vol.% H_2 in nitrogen dilution. An active catalytic surface area value of $3.10x10^6$ m^{-1} is used for the simulation. Figure 4.27 shows the comparison of the experimental measured and numerical simulated concentrations for R-WGS as a function of the temperature at the reactor outlet. During the experiment it is determined that the reaction initiates at temperatures above 523 K, producing methane and water first. It can be observed that the kinetic model produces the same trend as the experimental data at temperatures above 773 K. The methanation kinetics will be analyzed in the Section 5, where the same experiments are numerically simulated including methanation reactions in the kinetic model; the results are show in Figure 5.4.

a)

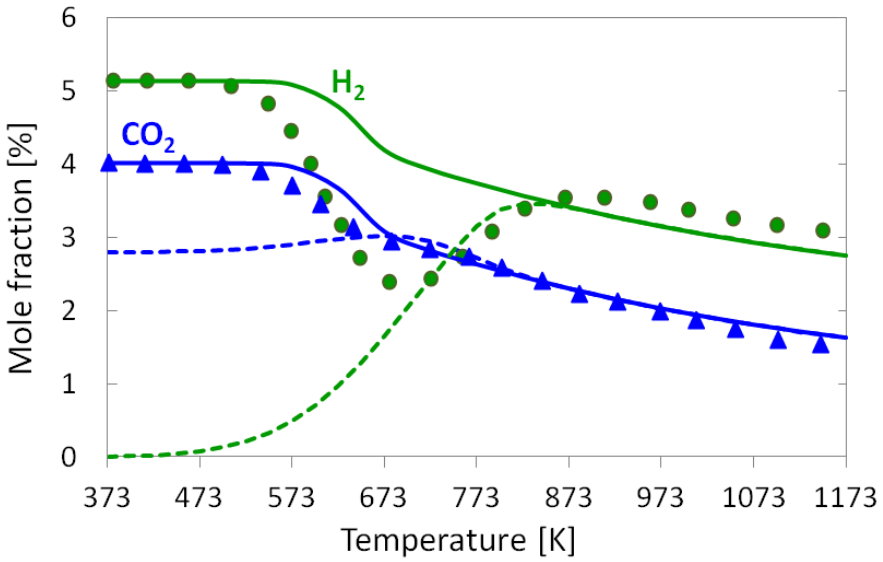

Figure 4.27 *Comparison of experimentally determined (symbols) and numerically predicted (lines) mole fractions as a function of temperature for R-WGS in a fixed bed reactor:* ***a)*** *CO_2 and H_2;* ***b)*** *CO, H_2O, and CH_4; inlet gas composition of 4.0 vol% CO_2 and 5.1 vol% H_2 in N_2 dilution; 1bar; T_{inlet}=373 K; 4SLPM; dashed lines =equilibrium composition at given temperature.*

b)

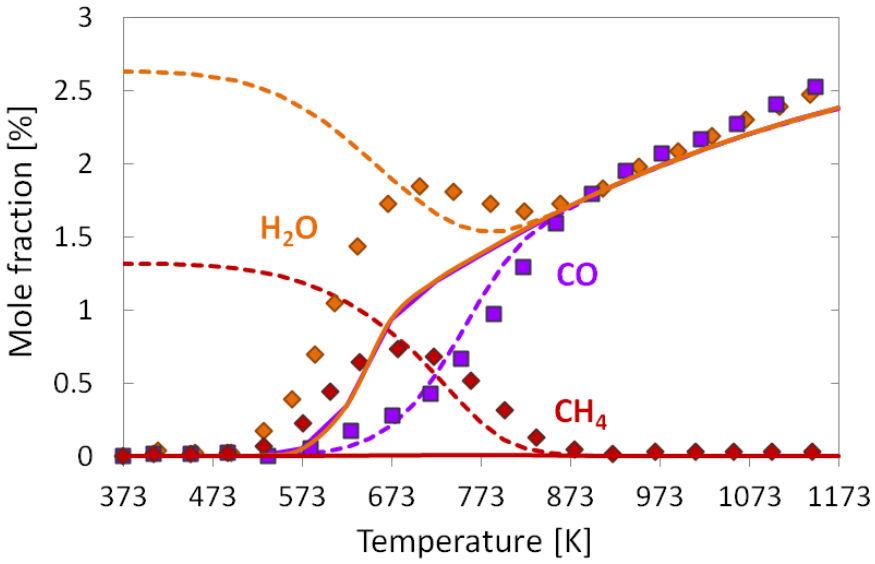

Figure 4.27: Continued

Continuous-flow reactor results for Reverse Water-Gas Shift Reaction (R-WGS)

The R-WGS reaction is also studied in a continuous-flow reactor at 1bar, total flow of 4 SLPM (0.514 m/s), in a temperature range between 373-973 K (100-700 °C), with an inlet gas composition of 4.0 vol.% CO_2 and 5.1 vol.% H_2 in nitrogen dilution. An effective $F_{cat/geo}$ value 150 is used for the simulation. Figure 4.28 shows a comparison of the experimental data and the predicted results as function of the temperature. During the experiment it is determined that the reaction initiates at temperatures above 573 K, but as for R-WGS performed in a fixed bed reactor, the kinetic model produces the same trend as the experimental data at temperatures starting above 773 K. The experimental results also show formation of methane at temperatures between 523-823 K (250-550 °C). The results confirmed the importance of including CH_4 and its reaction with other species, in order to correctly describe the kinetics during WGS and R-WGS reaction.

a)

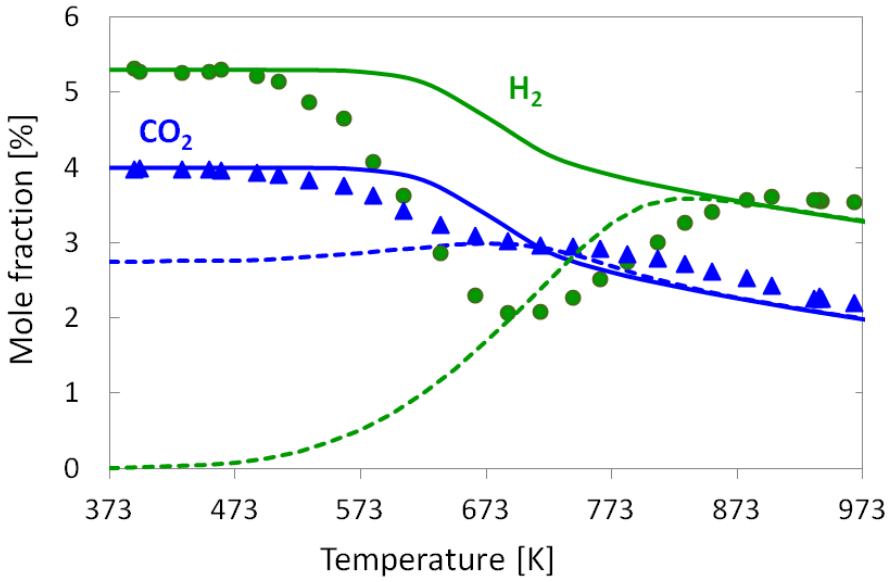

b)

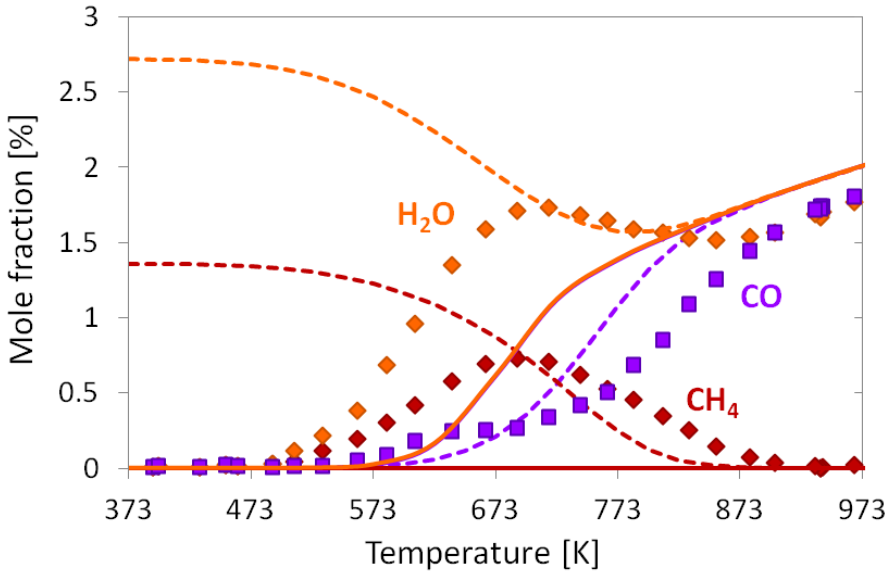

Figure 4.28 *Comparison of experimentally determined (symbols) and numerically predicted (lines) mole fractions as a function of temperature for R-WGS over a monolith catalyst:* ***a)*** *CO_2 and H_2;* ***b)*** *CO, H_2O, and CH_4; inlet gas composition of 4.0 vol.% CO_2 and 5.3 vol.% H_2 in N_2 dilution; 1 bar; T_{inlet}= 373 K, total flow rate of 4 SLPM, dashed lines = equilibrium composition at given temperature.*

4.3.5 Test of the reaction kinetics

The water-gas shift reaction at short contact times by Wheeler et.al. [207]

The reaction mechanism is also validated by numerically reproducing the experimental results performed by Wheeler et al. [207]. The experiment is carried out in a tube furnace controlled at temperatures up to 1473 K (1200 °C). Alumina ceramic foam monoliths are used as catalyst support containing 8 % silica with a nominal surface area of ~1.0 m^2/g. The monoliths had a diameter of 17 mm, 10 mm length, and a pore density of 80 pores per linear inch with a void fraction of 0.8. The monoliths are wash-coated on the support using a aqueous solution of $Ni(NO_3)_3$. A calculated amount of metal salt is used to ensure a 5 wt.% metal loading based on the mass of the monolith. An $F_{cat/geo}$ value of 90 is used to fit the experimental results presented by Wheeler et al. [207] . The monoliths are sealed into the reactor with alumina cloth. All measurements are carried out at atmospheric pressure with a feed composition of 1/2/4 for $CO/H_2/H_2O$ with 20 % nitrogen and a total flow rate of 3 SLPM, resulting in a contact time of ~13 ms at 773 K (500 °C). Detailed information about the catalyst preparation, experimental set-up and the reaction conditions are given elsewhere [207].

Figure 4.27 shows a comparison of the experimental values and model prediction. The numerical simulations are performed based on the 2D boundary-layer model of the channel with a hydraulic diameter of 0.5 mm and the 10 mm channel length by using DETCHEM^{CHANNEL} code [77]. Linear flow velocity was calculated to be 0.466 m/s in the channel.

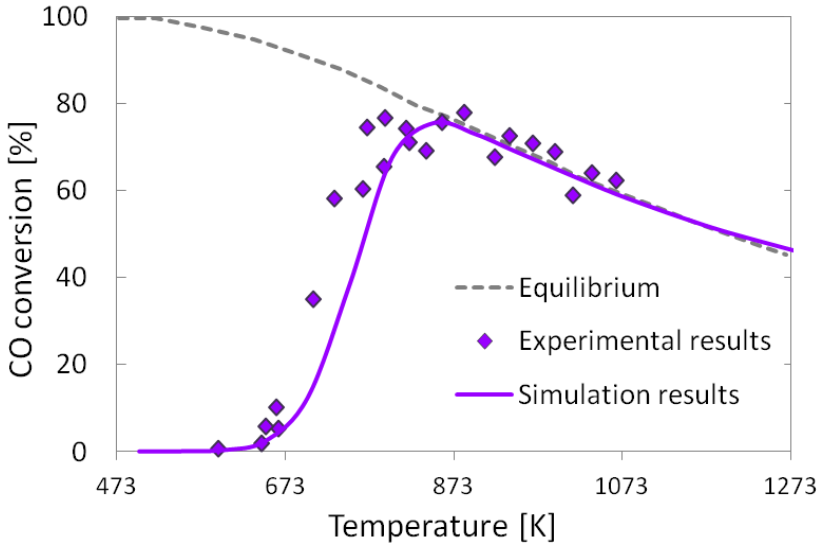

Figure 4.29 *CO conversion as function of the temperature in WGS on Ni supported on alumina foam monolith for a feed composition of 1/2/4 for $CO/H_2/H_2O$ with 20 % N_2 dilution.*

The WGS activity starts at 603 K, beyond 873 K the system reaches equilibrium at the given conditions. The model is able to simulate the experimental results with accuracy over a wide range of temperatures.

4.3.6 Summary

Preferential oxidation of CO, water-gas shift and reverse water-gas shift reaction kinetics over nickel-based catalyst are investigated experimentally and numerically. A heterogeneous surface reaction mechanism is proposed based on the experimental results and literature information. The reaction steps for the formation and decomposition of the intermediate carboxyl (COOH*) are included to enhance the reaction model at low temperatures. Sensitivity analysis shows that carboxyl species has major effect at low temperature. Whereas, the direct oxidation CO*and O* species on the surface is favored at high temperatures. Methane formation is obtained experimentally during WGS and R-WGS. It is found that methane formation exhibits a dependency on the inlet gas composition, e.g, at high H_2O concentration in the inlet mixture, no methane is formation is observed. The mechanism developed in this section is not yet able to be predicted the formation of methane during WGS and R-WGS reactions. The model cannot accurate preferential oxidation of CO. Additionally, the surface reaction kinetics has been also evaluated, by modeling experimental results from literature.

4.4 Kinetics of Catalytic Partial Oxidation and Reforming of Methane

The kinetics for catalytic partial oxidation (CPOX), steam reforming (SR), and dry reforming (DR) of methane are studied experimentally and numerically. Following a hierarchical approach (Figure 4.1), the reaction mechanism presented in Section 4.3 (Table 4.12) is extended by CH_x species. A thermodynamically consistent surface reaction mechanism is developed based on experimental and theoretical results for CPOX, SR, and DR of methane over nickel. The experiments are carried out at laboratory scale in a fixed bed reactor using the BASF nickel-based catalyst. The mechanism is evaluated against new data obtained from experiments conducted at varying operating conditions and also taken from literature.

4.4.1 Theoretical Background

The conversion of light hydrocarbons to produce hydrogen and syngas (H_2/CO) is still of great interest in research and technology. Syngas is widely used as a feedstock in the manufacture of valuable basic chemicals and synthetic fuels, via methanol, ammonia and Fischer-Tropsch synthesis [3, 208].

Processes such as steam reforming (SR), auto-thermal reforming (ATR), partial oxidation (CPOx) and dry reforming (DR) are the most common catalytic technologies for converting natural gas to synthesis [2].

The most important industrial method to produce syngas is the steam reforming of methane (Eq. 4.10) over nickel-based catalyst, which produces a H_2/CO ratio of 3:1. In this process, two stable molecules are converted into the more reactive synthesis gas; hence, the overall reaction is strongly exothermic, also the efficiency of the process is severely affected by the catalyst deactivation because of carbon formation.

$$CH_4 + H_2O \rightarrow CO + 3H_2, \quad \Delta H^0_{298} = 205.9 \frac{kJ}{mol} \tag{4.10}$$

Due to the increasing environmental concerns and oil depletion, methane dry reforming (Eq. 4.11) has gained considerable attention in the last year, because it offers the opportunity to convert these greenhouse gases (CH_4 and CO_2) into synthesis gas. The dry reforming of

methane has been proposed as an alternative process for SR, because produce H_2/CO with lower ratios, which is more suited for stream processes such as the oxo synthesis of the aldehydes or the syntheses of methanol, acetic acid, etc . However, one of the main challenges in dry reforming of methane, especially at industrial conditions, is also the formation of carbon, which causes the catalyst deactivation and in some cases the blocking of the reactor tubes.

$$CH_4 + CO_2 \rightarrow CO + H_2, \quad \Delta H_{298}^0 = 247.3 \frac{kJ}{mol} \tag{4.11}$$

The catalytic partial oxidation (Eq. 4.12) of methane over nickel-based catalyst has been deeply studied as a promising option to the endothermic reforming processes [16-21], because no additional steam or heat supplies are required.

$$CH_4 + \frac{1}{2}O_2 \rightarrow CO + 2H_2, \quad \Delta H_{298}^0 = -36.0 \frac{kJ}{mol} \tag{4.12}$$

Industrial practice would like to use Ni catalysts due the good availability and low costs compared with noble metals, although it is more sensitive to coke formation leading the catalyst deactivation [209]. Several methods and different nickel-based catalyst have been proposed for reducing the coke formation [48-50]. To improve the catalytic methane reforming processes it is necessary to gain a better understanding of the elementary steps of the reaction mechanism at a molecular level and the deactivation kinetics due to the coke formation. Therefore, the sequence and interaction of the reaction paths have to be analyzed for combined CPOX-steam-CO_2-reforming systems, because the conditions in any continuous-flow reactor vary along the flow directions, covering a wide range of mixture compositions and leading to quite different local reaction rate.

4.4.2 Experimental Procedure

The study of methane partial oxidation, steam and dry reforming is performed in a fixed reactor. The reactor is loaded with 2.0 g of the Fixedbed_Ni_BASF_Cat.2 powdered nickel-based catalyst from BASF for the catalytic measurements (Section 3.1.2). The different reactants components are mixed to various gas compositions in nitrogen dilution and preheated to 373 K before entering the reactor. The catalyst pretreatment is explained in Section 3.1.2. Reactor operating pressure is selected to be 1bar, flow rate of 4 SLPM, which results in a linear flow velocity of 1.97 m/s. The experiments are performed at temperatures in a range from 373 K to 1173 K. A temperature ramp of 15 K/min is used to heat up the catalytic bed, by increasing the temperature of the surrounding furnace.

Catalytic Partial Oxidation of CH_4 (CPOX)

The experimental conditions for the catalytic partial oxidation of methane are given in Table 4.13. The inlet gas composition of CH_4/O_2 is diluted in nitrogen and fed into the reactor at 373 K.

Table 4.13 Experimental conditions for catalytic partial oxidation of methane with a molar CH_4/O_2 ratio of 1.6 in nitrogen dilution.

Temperature [K]	CH_4 [vol.%]	O_2 [vol.%]	N_2 [vol.%]
373-1123	1.33	0.81	97.86

Steam Reforming of CH_4 (SR)

The experimental conditions for steam reforming of methane reaction are given in Table 4.14. The inlet gas composition of CH_4/H_2O is diluted in nitrogen and fed into the reactor at 373 K. The dosing of the gases is controlled by mass flow controller and the water is provided by a liquid flow controller from a water reservoir. After evaporation the steam is mixed directly into the reactant gas stream. Equipment lines that carry steam must be preheated to 463 K (190 °C) before entering the reactor to avoid condensation through the lines.

Table 4.14 Experimental conditions for steam reforming of methane.

Temperature [K]	CH_4 [vol.%]	H_2O [vol.%]	N_2 [vol.%]
373-1173	1.60	2.0	96.4

Experimental conditions for catalytic partial oxidation of methane with a molar CH_4/O_2 ratio of 1.6 in nitrogen dilution.

Dry Reforming (DR)

The reforming of methane with CO_2 reaction is studied with different inlet gas compositions in nitrogen dilution. The experimental conditions are given in Table 4.15.

Table 4.15 Experimental conditions for methane reforming with CO_2

	Temperature [K]	CH_4 [vol.%]	CO_2 [vol.%]	H_2 [vol.%]	H_2O [vol.%]	N_2 [vol.%]
CH_4/CO_2	373-1173	2.0	2.0	-	-	96
$CH_4/CO_2/H_2$	373-1173	1.6	2.1	1.8	-	94.5
$CH_4/CO_2/H_2O$	373-1173	1.7	2.1	-	2.1	94.1

4.4.3 Kinetic Parameters

The conversion of methane to syngas can be described as the combination of the following overall reactions (Table 4.16).

Table 4.16 Overall reactions in the methane reforming and oxidation system.

Methane steam reforming		
$CH_4 + H_2O \leftrightarrow CO + 3H_2$	ΔH^0_{298} = 205.9 kJ/mol	(4.13)
$CH_4 + 2H_2O \leftrightarrow CO_2 + 4H_2$	ΔH^0_{298} = 164.7 kJ/mol	(4.14)
Methane dry reforming		
$CH_4 + CO_2 \leftrightarrow 2CO + 2H_2$	ΔH^0_{298} = 247.3 kJ/mol	(4.15)
Methane partial oxidation		
$CH_4 + 1/2O_2 \leftrightarrow CO + 2H_2$	ΔH^0_{298} = -35.6 kJ/mol	(4.16)
Methane total oxidation		
$CH_4 + 2O_2 \leftrightarrow CO_2 + 2H_2O$	ΔH^0_{298} = -880 kJ/mol	(4.17)
Water-gas shift		
$CO + H_2O \leftrightarrow CO_2 + H_2$	ΔH^0_{298} = -41.2 kJ/mol	(4.18)
Methanation		
$CO + 3H_2 \leftrightarrow CH_4 + H_2O$	ΔH^0_{298} = -206 kJ/mol	(4.19)
$2CO + 2H_2 \leftrightarrow CH_4 + CO_2$	ΔH^0_{298} = -247 kJ/mol	(4.20)
Boudouard reaction		
$2CO \leftrightarrow C + CO_2$	ΔH^0_{298} = -172.4 kJ/mol	(4.21)
Methane cracking		
$CH_4 \leftrightarrow C + 2H_2$	ΔH^0_{298} = 74.9 kJ/mol	(4.22)
Gasification of carbon		
$C + H_2O \leftrightarrow CO + H_2$	ΔH^0_{298} = 131.3 kJ/mol	(4.23)
$C + O_2 \leftrightarrow CO_2$	ΔH^0_{298} = -393.5 kJ/mol	(4.24)

A detailed multi-step heterogeneous reaction mechanism has been developed based on theoretical and experimental studies. The mechanism is a further extension of the elementary-step-like reaction mechanism for $CO/CO_2/H_2/H_2O/O_2$ systems presented in Section 4.3. The model can predict conversion and selectivity for partial and total oxidation of methane as well as steam and dry reforming of methane over nickel. The reaction mechanism consists of 52

reactions with 6 gas phase species and 14 surface species and includes new reaction paths for carbon formation (Table 4.17). The modeling approach is based on the mean field approximation, i.e., the surface is assumed to be uniform and the adsorbates are randomly distributed on the surface. Temperature dependent activation energies are introduced to ensure thermodynamic consistency.

The mechanism involves adsorption and desorption steps of all reactants and products and surface elementary reaction steps. The reforming and oxidation processes on nickel catalyst are described as follows [58]:

Adsorption/desorption of reactants and products (R1-R12, Table 4.17).

Activation of methane without oxygen (R13-R20, Table 4.17)

$$CH_4(Ni) + (4-x)\,Ni \rightleftharpoons CH_x(Ni) + (4-x)\,H(Ni) \qquad 0 \le x \le 3 \qquad (4.25)$$

and oxygen assisted (R21-R28, Table 4.17)

$$CH_4(Ni) + (4-x)\,O(Ni) \rightleftharpoons CH_x(Ni) + (4-x)\,OH(Ni) \qquad 0 \le x \le 3 \qquad (4.26)$$

Dissociation of water (R29-R34, Table 4.17)

Dissociation of CO_2 (R35-R40, Table 4.17)

Reaction of the adsorbed species and production of CO and H_2 (R41-R52, Table 4.17)

The reaction mechanism developed comprises the reactions of partial and total oxidation, steam and dry reforming of methane and is based on the key reaction intermediate-adsorbed atomic oxygen O*, that is the common intermediate for these reactions, indicated by TPR and *in situ* isotope transient experiments [53]

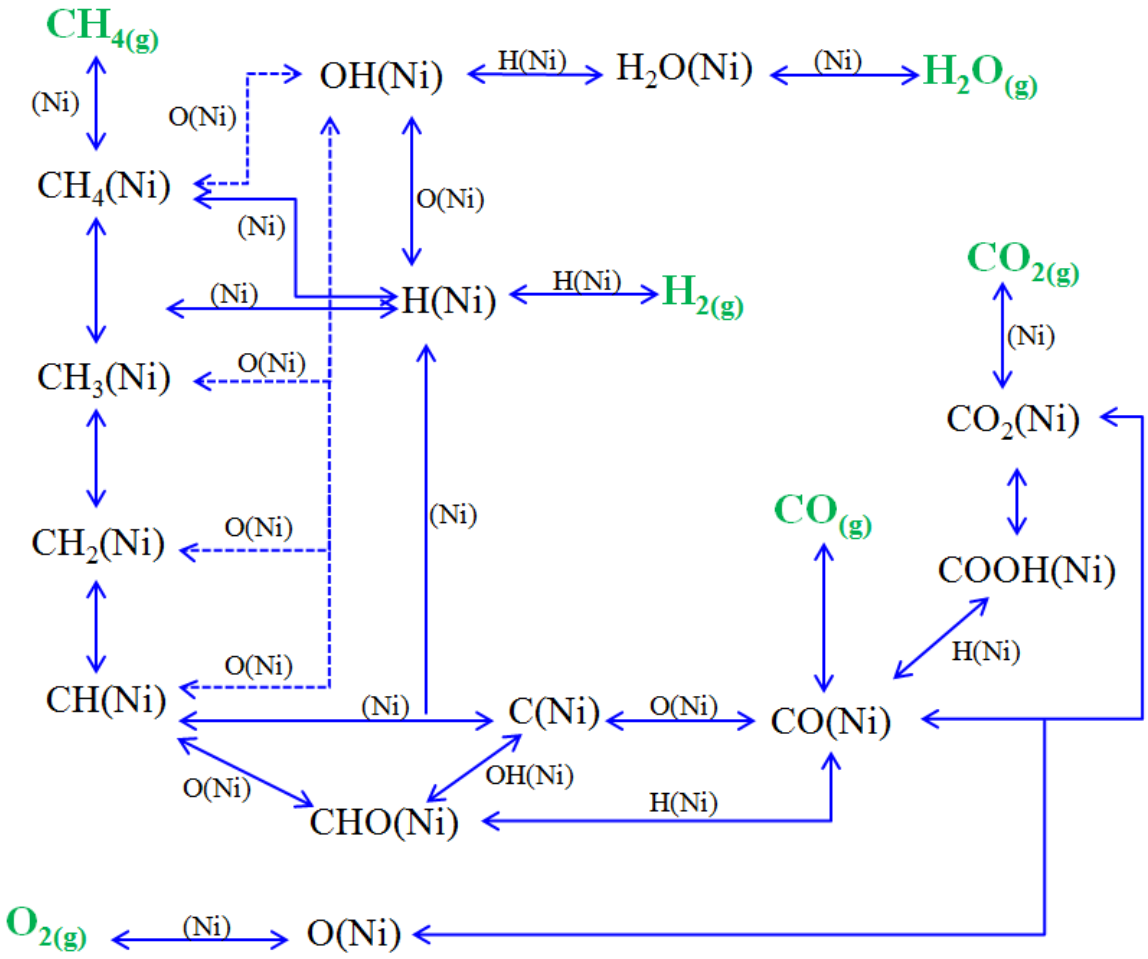

Figure 4.30 *Reaction mechanism scheme of methane under oxidation and reforming conditions over nickel catalyst.*

A previous model developed in our group [58], which serves as basis of the novel kinetics, has already been successfully applied for steam reforming of methane at a wide temperature range and feed compositions. In this model, unity bond index-quadratic exponential potential (UBI-QEP) approach [57, 201, 210] has been used to determine the heats of adsorption of species, reaction enthalpy changes, and the activation barriers for all relevant steps of the mechanism. The reaction steps of methane activation on nickel from the previous steam reforming model are used for the extension of the $CO/CO_2/H_2O/O_2/H_2$ mechanism presented in Section 4.3 (Table 4.12). The combine reaction steps are used to develop a new thermodynamically surface reaction mechanism for methane oxidation and reforming systems $CH_4/CO_2/H_2O/CO/O_2/H_2$ (Table 4.17). This new kinetic model incorporates 10 more reactions than the baseline model developed by Maier et at. [58], these reactions are presented in Table 4.17 highlighted in red.

Table 4.17 Thermodynamically consistent surface reaction mechanism for oxidation and reforming of methane over nickel.

	REACTION	A/[cm, mol, s]/S_0[-]	β [-]	E_a/[kJ/mol]	ε_I [kJ/mol]
R1	H_2 + (Ni) + (Ni) → H(Ni) + H(Ni)	$3.000 \cdot 10^{-02}$	0.000	5.00	
R2	H(Ni) + H(Ni) → Ni(Ni) + Ni(Ni) + H_2	$2.544 \cdot 10^{+20}$	0.000	95.21	
R3	O_2 + (Ni) + (Ni) → O(Ni) + O(Ni)	$4.358 \cdot 10^{-02}$	-0.206	1.51	
R4	O(Ni) + O(Ni) → (Ni) + (Ni) + O_2	$1.188 \cdot 10^{+21}$	0.823	468.91	
R5	CH_4 + (Ni) → CH_4(Ni)	$8.000 \cdot 10^{-03}$	0.000	0.0	
R6	CH_4(Ni) → CH_4 + Ni(Ni)	$8.705 \cdot 10^{+15}$	0.000	37.55	
R7	H_2O + (Ni) → H_2O(Ni)	$1.000 \cdot 10^{-01}$	0.000	0.0	
R8	H_2O(Ni) → H_2O + (Ni)	$3.732 \cdot 10^{+12}$	0.000	60.79	
R9	CO_2 + (Ni) → CO_2(Ni)	$7.001 \cdot 10^{-06}$	0.000	0.00	
R10	CO_2(Ni) → CO_2 + (Ni)	$6.442 \cdot 10^{+07}$	0.000	25.98	
R11	CO + (Ni) → CO(Ni)	$5.000 \cdot 10^{-01}$	0.000	0.00	
R12	CO(Ni) → CO + (Ni)	$3.566 \cdot 10^{+11}$	0.000	111.27	-50.0 $\theta_{CO(Ni)}$
R13	CH_4(Ni) + (Ni) → CH_3(Ni) + H(Ni)	$1.548 \cdot 10^{+21}$	0.087	55.83	
R14	CH_3(Ni) + H(Ni) → CH_4(Ni) + (Ni)	$1.443 \cdot 10^{+22}$	-0.087	63.45	
R15	CH_3(Ni) + (Ni) → CH_2(Ni) + H(Ni)	$1.548 \cdot 10^{+24}$	0.087	98.12	
R16	CH_2(Ni) + H(Ni) → CH_3(Ni) + (Ni)	$3.091 \cdot 10^{+23}$	-0.087	57.21	
R17	CH_2(Ni) + (Ni) → CH(Ni) + H(Ni)	$3.700 \cdot 10^{+24}$	0.087	95.23	
R18	CH(Ni) + H(Ni) → CH_2(Ni) + (Ni)	$9.774 \cdot 10^{+24}$	-0.087	81.05	
R19	CH(s) + (Ni) → C(Ni) + H(Ni)	$9.888 \cdot 10^{+20}$	0.500	21.99	
R20	C(Ni) + H(Ni) → CH(Ni) + (Ni)	$1.707 \cdot 10^{+24}$	-0.500	157.92	
R21	CH_4(Ni) + O(Ni) → CH_3(Ni) + OH(Ni)	$5.621 \cdot 10^{+24}$	-0.101	92.72	
R22	CH_3(Ni) + OH(Ni) → CH_4(Ni) + O(Ni)	$2.987 \cdot 10^{+22}$	0.101	25.80	
R23	CH_3(Ni) + O(Ni) → CH_2(Ni) + OH(Ni)	$1.223 \cdot 10^{+25}$	-0.101	134.67	
R24	CH_2(Ni) + OH(Ni) → CH_3(Ni) + O(Ni)	$1.393 \cdot 10^{+21}$	0.101	19.05	
R25	CH_2(Ni) + O(Ni) → CH(Ni) + OH(Ni)	$1.223 \cdot 10^{+25}$	-0.101	131.37	
R26	CH(Ni) + OH(Ni) → CH_2(Ni) + O(Ni)	$4.407 \cdot 10^{+22}$	0.101	42.45	
R27	CH(Ni) + O(Ni) → C(Ni) + OH(Ni)	$2.471 \cdot 10^{+21}$	0.312	57.74	
R28	C(Ni) + OH(Ni) → CH(Ni) + O(Ni)	$2.433 \cdot 10^{+21}$	-0.312	118.97	
R29	H(Ni) + O(Ni) → OH(Ni) + (Ni)	$3.951 \cdot 10^{+23}$	-0.188	104.35	
R30	OH(Ni) + (Ni) → H(Ni) + O(Ni)	$2.254 \cdot 10^{+20}$	0.188	29.64	
R31	H(Ni) + OH(Ni) → H_2O(Ni) + (Ni)	$1.854 \cdot 10^{+20}$	0.086	41.52	
R32	H_2O(Ni) + (Ni) → H(Ni) + OH(Ni)	$3.674 \cdot 10^{+21}$	-0.086	92.94	
R33	OH(Ni) + OH(Ni) → H_2O(Ni) + O(Ni)	$2.346 \cdot 10^{+20}$	0.274	92.37	

R34	$H_2O(Ni) + O(Ni) \rightarrow OH(Ni) + OH(Ni)$	$8.148 \cdot 10^{+24}$	-0.274	218.49	
R35	$C(Ni) + O(Ni) \rightarrow CO(Ni) + (Ni)$	$3.402 \cdot 10^{+23}$	0.000	148.10	
R36	$CO(Ni) + (Ni) \rightarrow C(Ni) + O(Ni)$	$1.758 \cdot 10^{+13}$	0.000	116.24	$-50.0\ \theta_{CO(Ni)}$
R37	$CO(Ni) + CO(Ni) \rightarrow C(Ni) + CO_2(Ni)$	$1.624 \cdot 10^{+14}$	0.500	241.76	$-100.0\ \theta_{CO(Ni)}$
R38	$CO_2(Ni) + C(Ni) \rightarrow CO(Ni) + CO(Ni)$	$7.294 \cdot 10^{+28}$	-0.500	239.24	
R39	$CO(Ni) + O(Ni) \rightarrow CO_2(Ni) + (Ni)$	$2.000 \cdot 10^{+19}$	0.000	123.60	$-50.0\ \theta_{CO(Ni)}$
R40	$CO_2(Ni) + (Ni) \rightarrow CO(Ni) + O(Ni)$	$4.648 \cdot 10^{+23}$	-1.000	89.32	
R41	$CO(Ni) + H(Ni) \rightarrow C(Ni) + OH(Ni)$	$3.522 \cdot 10^{+18}$	-0.188	105.45	$-50.0\ \theta_{CO(Ni)}$
R42	$C(Ni) + OH(Ni) \rightarrow H(Ni) + CO(Ni)$	$3.888 \cdot 10^{+25}$	0.188	62.55	
R43	$CO_2(Ni) + H(Ni) \rightarrow COOH(Ni) + (Ni)$	$6.250 \cdot 10^{+24}$	-0.475	117.24	
R44	$COOH(Ni) + (Ni) \rightarrow CO_2(Ni) + H(Ni)$	$3.737 \cdot 10^{+20}$	0.475	33.66	
R45	$COOH(Ni) + (Ni) \rightarrow CO(Ni) + OH(Ni)$	$1.461 \cdot 10^{+24}$	-0.213	54.37	
R46	$CO(Ni) + OH(Ni) \rightarrow COOH(Ni) + (Ni)$	$6.003 \cdot 10^{+21}$	0.213	97.63	$-50.0\ \theta_{CO(Ni)}$
R47	$CO(Ni) + H(Ni) \rightarrow HCO(Ni) + (Ni)$	$4.009 \cdot 10^{+20}$	-1.000	132.23	
R48	$HCO(Ni) + (Ni) \rightarrow CO(Ni) + H(Ni)$	$3.710 \cdot 10^{+21}$	0.000	0.0	$+50.0\theta_{CO(Ni)}$
R49	$HCO(Ni) + (Ni) \rightarrow CH(Ni) + O(Ni)$	$3.796 \cdot 10^{+14}$	0.000	81.91	
R50	$CH(Ni) + O(Ni) \rightarrow HCO(Ni) + (Ni)$	$4.599 \cdot 10^{+20}$	0.000	109.97	
R51	$H(Ni) + COOH(Ni) \rightarrow HCO(Ni) + OH(Ni)$	$6.000 \cdot 10^{+22}$	-1.163	104.88	
R52	$HCO(Ni) + OH(Ni) \rightarrow COOH(Ni) + H(Ni)$	$2.282 \cdot 10^{+20}$	0.263	15.92	

The rate coefficients are given in the form of $k=AT^{\beta}\exp(-E_a/RT)$; adsorption kinetics is given in form of sticking coefficients; the surface site density of Γ=2.66 x 10^{-9} mol cm^{-2} is calculated by assuming a site area of 6.5x10^{-2} nm^2 as observed for nickel [58, 119].

The activation energy for methane dissociation has been extensively studied using different experimental techniques. Broadly, the activation energy of methane dissociation from the gas phase ($CH_4^* \rightarrow CH_3^* + H^*$) is found in the range of 52-59 kJ/mol for Ni(111), Ni(100), and Ni(110) surfaces. Beebe et al. [211] investigated the kinetics of methane decomposition on Ni(111), Ni(110) and Ni(110) surfaces using high incident methane pressure (1 Torr) in the temperature range of 400-500 K (127-227 °C). The measured activation energies for methane decomposition were found to be 52.72 kJ/mol, 55.65 kJ/mol, and 26.78 kJ/mol for Ni(111), Ni(110) and Ni(110), respectively. Kinetic studies were also carried out by the same authors employing deuterated methane, the results showed a large kinetic isotopic effect for Ni(100), whereas no such effect was observed for the Ni(110) surface, the activation energies of deuterated methane measured on Ni(100) and Ni(110) were 62.64 kJ/mol and 52.3 kJ/mol respectively.

Using XPS surface techniques to monitor surface concentrations, Chorkendorff et al. [212] determined the sticking coefficient of CH_4 on Ni(100) as a function of coverage in the

temperature range 400-500 K (127-227 °C). The apparent activation energy of the initial sticking coefficient is found to be 50.24 kJ/mol. Aparicio [53] investigated the adsorption of methane and dehydrogenation, the reaction between CD_4 and H_2, the reported activation energy of methane on Ni/$MgAl_2O_4$-MgO was 54 kJ/mol. Chen et al. [11] founded that an activation energy of 58.6 kJ/mol is obtained, when the dissociation of methane was considered to proceed through dissociative adsorption of methane on the surface. Yang et al. [213] reported DFT results on the chemisorptions of hydrogen and CH_x and the dissociative chemisorptions of CH_4 on a Ni(111). The activation energy calculated for CH_4 to CH_3 and H is 71.2 kJ/mol. Katzer et al. [134] found a barrier about 100 kJ/mol using gradient-corrected density functional calculations for dissociative adsorption of CH_4 and a slab model on Ni(111). Bengaard et.al [120] used DFT to study methane steam reforming and the formation of graphite on Ni catalyst. The authors estimated a barrier of less than 97 kJ/mol for the first methane activation step from the gas-phase, which is in good agreement with the experimental value of 70-90 kJ/mol reported by Larsen and Chorkendorff [214]. Henkelman et al. [215] estimated a barrier energy of 77 kJ/mol for CH_4 dissociation using DFT calculations. Blaylock et at. [55] investigated the thermochemistry and kinetics of steam reforming on Ni(111) using plane wave density functional theory. The author obtained a barrier value of 129 kJ/mol for the dissociative adsorption of CH_4(g), such value is in agreement with the results estimated by Watwe et.al [216], where the activation energy was calculated to be 127 kJ/mol.

Accordingly, the barrier of 57.7 kJ/mol for methane activation on Ni(111) surface via dissociation of CH_4* to CH_3* and H* used in this model is in agreement with the data from thermal experimental results in the range of 52-59 kJ/mol. The activation barrier of adsorbed methyl dehydrogenation ($CH_3^* \rightarrow CH_2^* + H^*$) is derived from the previous model [58], where an UBI-QEP approach was used to estimate a barrier of 100 kJ/mol, which is in good agreement with DFT calculations on Ni(111) performed by Michaelides et al. [217] with a barrier of more than 100 kJ/mol and the results presented by Chen et al. [11] with an activation barrier of 99.9 kJ/mol.

As it is mentioned in Section 4.3.3, several studies propose that the HCO (CHO) species coordinated over carbon is an important intermediate during the reforming and oxidation of methane over transition metals [11, 47, 73, 93, 198, 199]. The reactions involving HCO* on Ni(111) have been studied by Pistonesi et al. [218], the authors conclude that HCO* species dissociation ($HCO^* \rightarrow CO^* + H^*$) is favorable for methane steam reforming on Ni(111). Zhou et al. [12] also concluded from DFT studies that HCO* species is a key intermediate during dry

reforming of methane to CO and H_2. Blaylock et at. [55] studied the kinetic of SR on Ni(111) based on DFT calculations, they calculated an activation energy of 150 kJ/mol for $(CH^* + O^* \rightarrow HCO^*)$ and proposed that HCO* decompose to form CO*. The authors also conclude that the formation of HCO* is a rate-limiting step during SR. Chen et al. [11] also include the HCO* surface species as intermediate in their micro-kinetic model for methane reforming.

The activation barrier for HCO* production from $(CH^* + O^* \rightarrow HCO^*)$ and $(CO^* + H^* \rightarrow HCO^*)$ in the current model are based on the data calculated from the previous model for SR developed by Maier et al. [58] using the UBI-QEP method.

Two possible reaction paths have been proposed for CO_2 dissociation. The first path is a direct dissociation of CO_2 on the catalytic surface to form CO* and O*. The second reaction pathway is the reaction of CO_2* with H* to produce COOH* carbonyl intermediate, which decomposes to produce CO* and OH* on the surface. The reaction paths including COOH* are explained in Section 4.3.3.

4.4.4 Results and Discussion

The catalytic partial oxidation and the reforming of methane reactions over nickel are studied in a fixed bed reactor using a powdered nickel based catalyst from BASF named in this work as Fixedbed_Ni_BASF_Cat.2 (Section 3.1.2). The thermodynamically consistent kinetic model is validated by comparison of the experimental results against numerical predictions.

Results for Catalytic Partial Oxidation of methane (CPOX)

The reaction mechanism of partial oxidation of methane to produce syngas is still controversial; two main paths have been suggested: the direct oxidation mechanisms were H_2 is directly originated from methane decomposition. Further interaction of adsorbed hydrocarbon species CH_x(x = 0, 1, 2, 3) with adsorbed atomic oxygen, produces carbon monoxide [5, 22, 23]. In the indirect route, methane is totally oxidized to CO_2 and H_2O, as long as oxygen is present close to the catalyst surface, and then the remaining CH_4 is reformed with steam or CO_2 to H_2 and CO [16, 24-27].

Reaction mechanisms and kinetic equations for some steps of the catalytic partial oxidation over nickel to syngas have been already published [22, 84, 219, 220]. A review on catalytic partial oxidation of methane to synthesis gas with emphasis on reaction mechanisms over transition metal catalysts was published by Holmen and co-workers [156]. De Groote and Froment [84] proposed a one-dimensional adiabatic model for POX to syngas in a fixed bed reactor on nickel catalyst. They considered the total oxidation of methane, total and partial steam reforming of methane and water-gas shift (WGS).

Figure 4.31 shows the experimental results in comparison with the simulation predictions as a function of the temperature. An active catalytic surface area of $9.85 \times 10^6\ m^{-1}$ is applied for the numerical simulation. It can be seen from Figure 4.31a, that methane is totally oxidized above 723 K (450 °C) leading to CO_2 and H_2O formation. No significant amounts of H_2 or CO are detected at this temperature. At temperatures above 873 K (600°C), reforming of methane is favored (Figure 4.31b), H_2 and CO formation increases while CO_2 and H_2O decreases quickly leading to the equilibrium composition at given operating conditions.

The experimental results presented in the Figure 4.31 are consistent with the indirect path were the total oxidation of methane takes place first producing CO_2 and H_2O, them being reformed to CO and H_2. Figure 4.31c shows a zoom-in of CO_2 and H_2O formation as a function of temperature, a decrease of CO_2 and H_2O can be clearly observed due to the reforming reactions with the residual CH_4 at temperatures above 873 K.

Numerically predicted O_2 and CH_4 conversion (Figure 4.31a) and the H_2 and CO selectivity (Figure 4.31b) agree the experimentally derived data in the whole temperature range under investigation.

a)

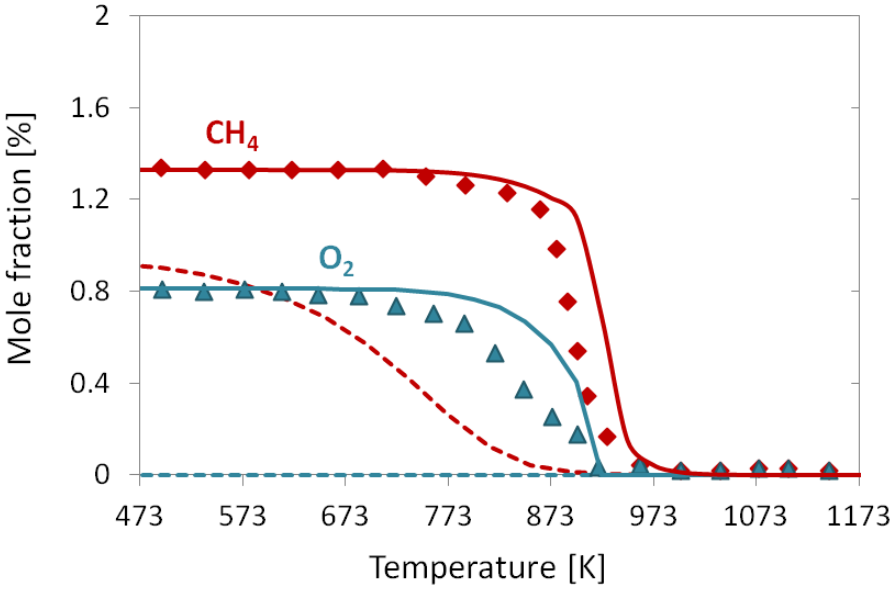

b)

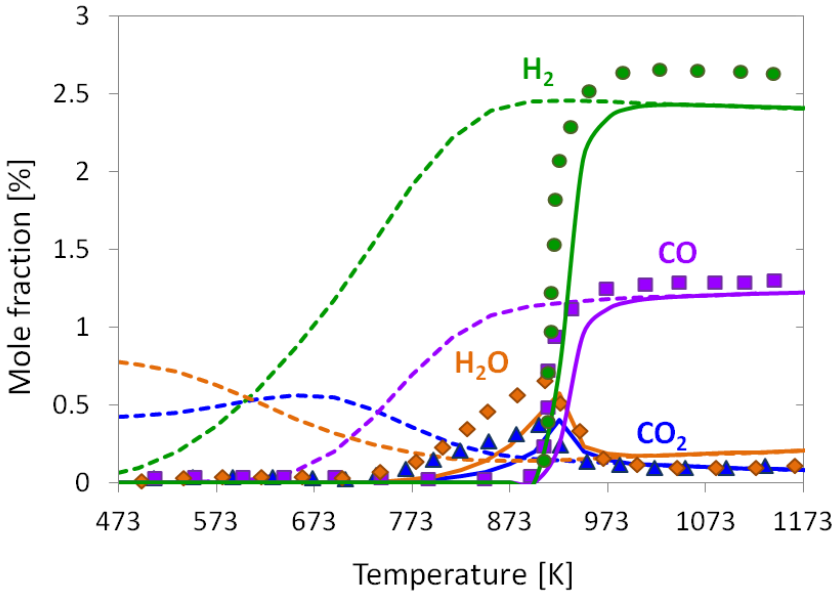

Figure 4.31 *Comparison of experimentally determined (symbols) and numerically predicted (lines) mole fractions as a function of temperature for catalytic partial oxidation of methane in a fixed bed reactor:* ***a)*** *CH_4 and O_2;* ***b)*** *CO_2, H_2O, CO, H_2;* ***c)*** *zoom-in of CO_2 and H_2O formation; inlet gas composition of CH_4/O_2 = 1.6 in N_2; 1 bar; T_{inlet}= 373 K; total flow rate of 4 SLPM; dashed lines =equilibrium composition at given temperature.*

c)

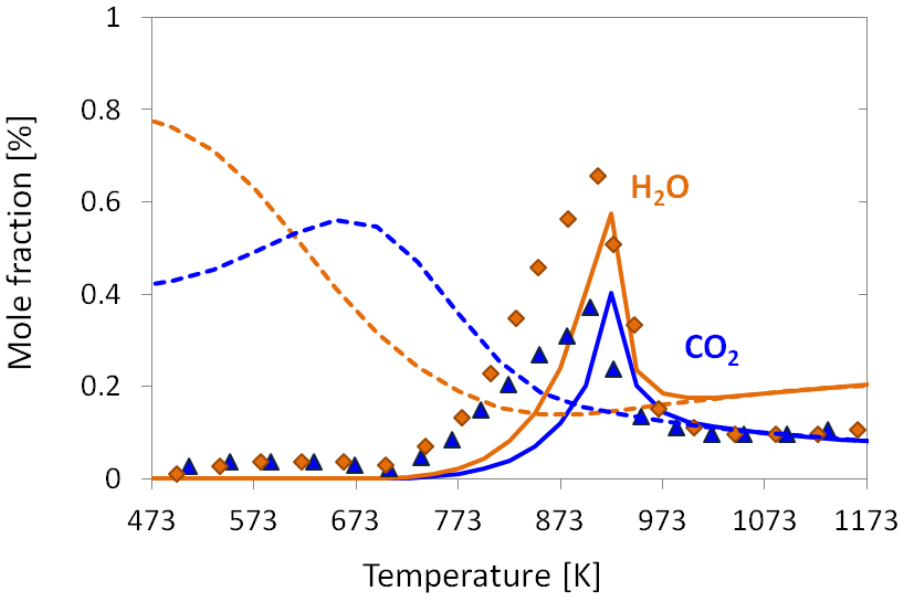

Figure 4.31: Continued

Figure 4.32 shows the computed mole fractions of the gas-phase species along the catalytic bed at 973 K (700°C) after ignition. It can be observed that CO_2 and H_2O are formed first by total oxidation of methane at the beginning of the catalytic bed, H_2 and CO are produce through reforming of methane.

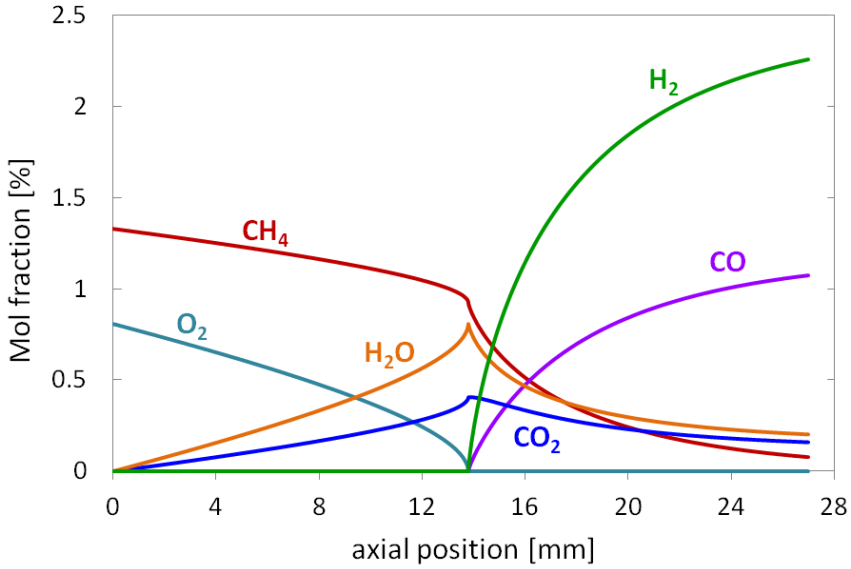

Figure 4.32 *Computed mole fraction of the gas-phase species: O_2, CH_4, H_2, H_2O, CO and CO_2 along the catalytic bed after the ignition for partial oxidation of methane over nickel at 973 K, CH_4/O_2=1.6.*

During the reaction, there is a competitive adsorption between CH_4 and O_2 on metallic Ni sites. However, the adsorption of O_2 is stronger than that of CH_4 [15]. Before ignition, the surface is mainly covered by oxygen; the system is controlled by surface reaction kinetics, in particular by the availability of adsorption sites of methane. The reversible adsorbed oxygen slowly shifts towards desorption with temperature rise, leading to vacancies on the surface. It explains the increase of the adsorption vacancies sites after the total oxidation. This highly exothermic reaction increases the temperature on the surface leading to further oxygen desorption, and hence, to more available adsorption sites that can be occupied by methane.

Figure 4.33 shows the computed surface coverage at 973 K (700 °C) after ignition. Significant oxygen coverage can be observed at the entrance of the catalytic bed. Further downstream, the oxygen coverage decreases fast producing free nickel sites together with carbon monoxide and hydrogen. Adsorbed OH* and H_2O* can also be found on the surface (Figure 4.33b). However, when the light-of takes place the amount of these species decreases and some coke is produced on the surface.

a)

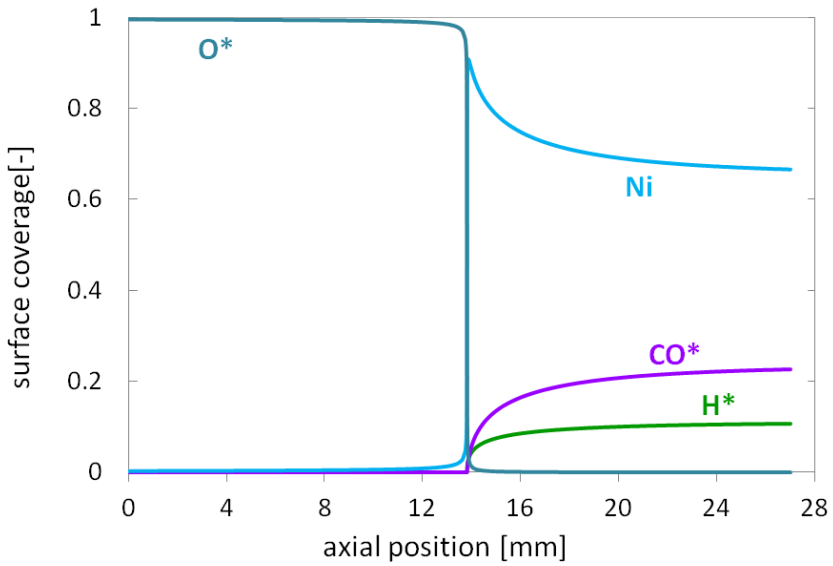

Figure 4.33 *Computed surface coverage of adsorbed species:* ***a)*** *O*, CO*, H*, Ni;* ***b)*** *OH*, H_2O*, CO_2*, and C* along the catalytic bed after the ignition for partial oxidation of methane over nickel at 973 K (700 °C), CH_4/O_2=1.6.*

* Sentence taken from reference [15].

b)

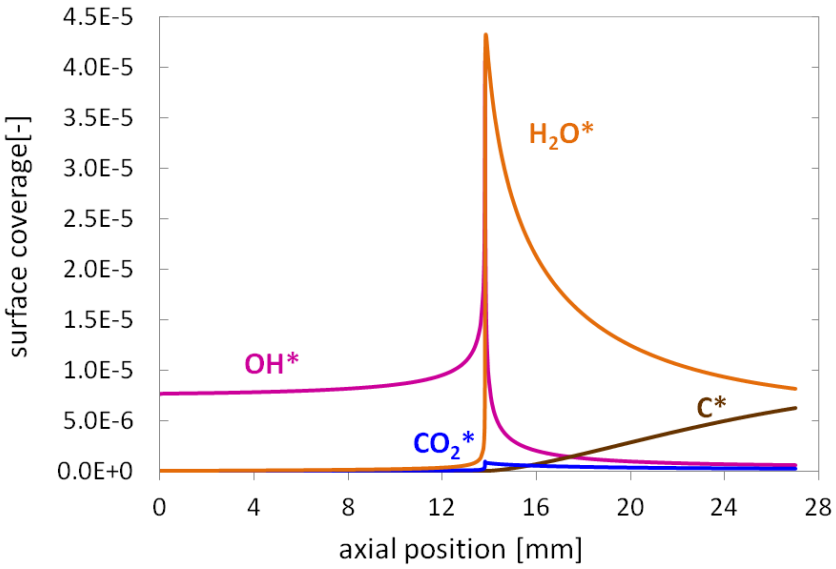

Figure 4.33: Continued

Figure 4.34 shows an infrared picture of the catalytic bed during partial oxidation of methane at high temperatures (>1048 K). Two zones are observed in the catalytic bed, an exothermic zone where the total oxidation of methane takes place first and an endothermic zone where the reforming reactions occur. These results are in agreement with the numerical predictions presented in the Figure 4.31 and Figure 4.32.

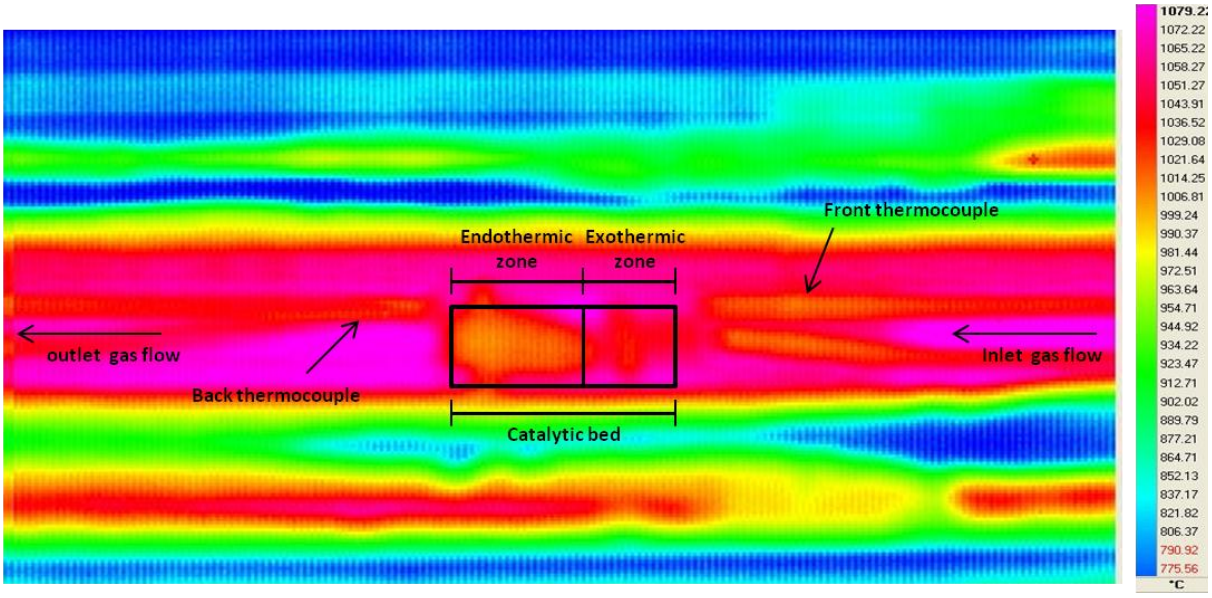

Figure 4.34 *Infrared picture of the catalytic bed during partial oxidation of methane (CPOx).*

Sensitivity analysis of the reaction mechanism is carried out at two different temperatures: 723 K (before ignition) and at 973 K (after ignition) with CH_4/O_2=1.6 in nitrogen dilution. The sensitivity of the exit gas-phase concentrations of CH_4, CO_2, H_2O, H_2 and CO is analyzed, by perturbing the pre-exponentials of each reaction. Results for the CO_2 mole fraction are presented Figure 4.35. These results show that the system is highly sensitive to methane adsorption and further dehydrogenation with oxygen assistance. It can be also observed that at 723 K, where the total oxidation takes place, the reactions to form OH, CO_2 and H_2O species are highly sensitive. However, at 973 K the sensitivity coefficients of these reactions decrease significantly.

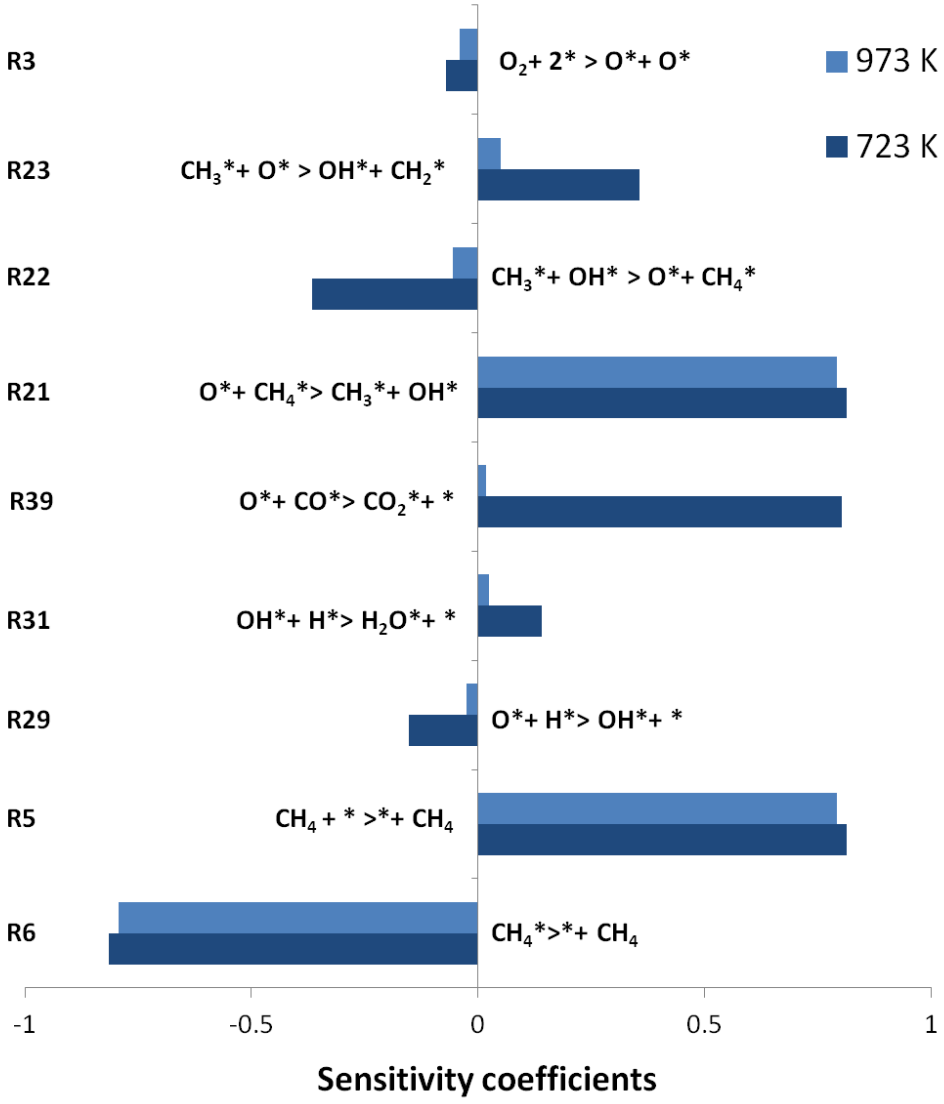

Figure 4. 35 *Sensitivity analysis of CO_2 gas phase concentration for CPOx reaction at 723 K and 948 K for CH_4/O_2 = 1.6 in N_2 dilution.*

Results for Steam Reforming of Methane (SR)

The overall mechanism performance is also evaluated for steam reforming. Experimental results conducted in a fixed reactor at atmospheric pressure are modeled. The catalytic bed temperature is varied between 473-1173 K (200-900 °C). The inlet gas composition of carbon/steam= 0.8 in nitrogen dilution is preheated at 373 K and continuously fed into the reactor. An active catalytic surface area of 9.85×10^6 m^{-1} is applied for the numerical simulation.

As is shown in Figure 4.36, the current mechanism extension is still able to predict the experimental results for methane steam reforming despite being adjusted for partial oxidation and dry reforming of methane. A small production of CO_2 is observed at temperatures between 623- 973 K (350-700 °C) due the availability of oxygen on the surface, which comes from added water (Figure 4.36c).

a)

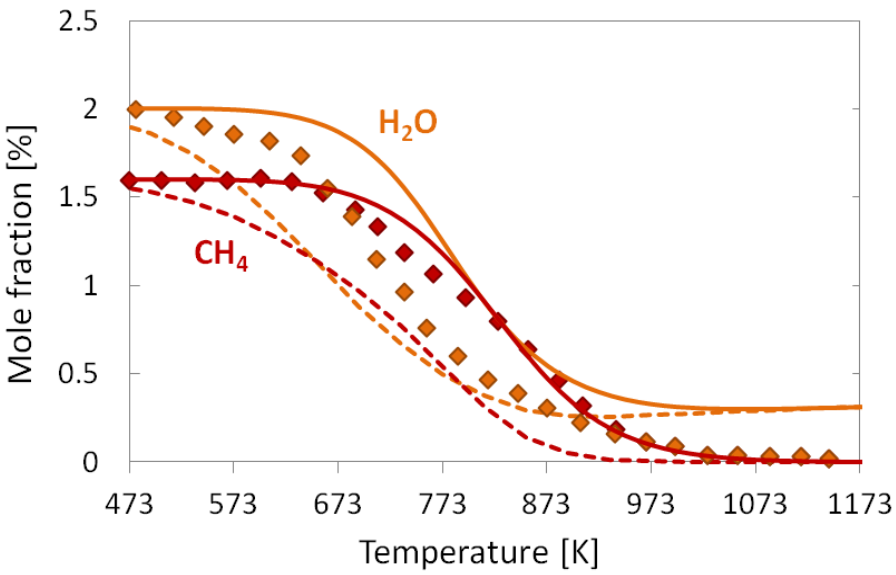

Figure 4.36 *Comparison of experimentally determined (symbols) and numerically predicted (lines) mole fractions as a function of temperature for catalytic steam reforming of methane in a fixed bed reactor:* ***a)*** *CH_4 and H_2O;* ***b)*** *CO_2, CO, H_2,* **c)** *zoom-in of CO_2 formation; inlet gas composition of C/S=0.8 in N_2, 1 bar; T_{inlet}= 373 K; total flow rate of 4 SLPM, dashed lines = equilibrium composition at given temperature.*

b)

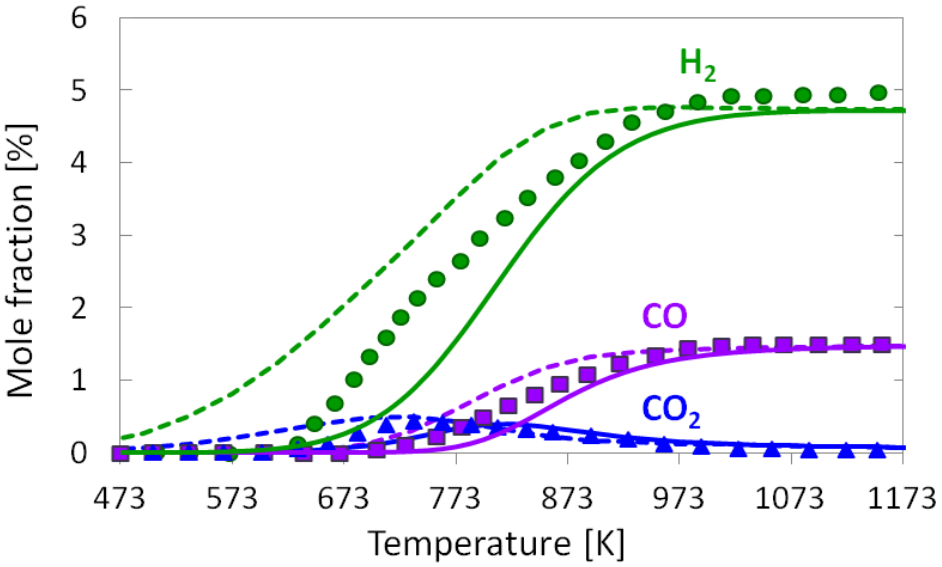

c)

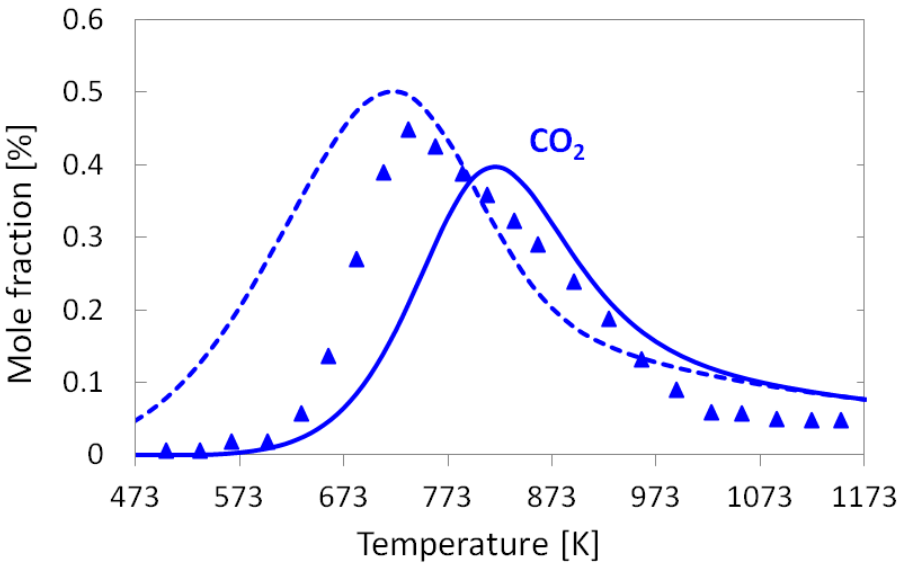

Figure 4.36: Continued

A sensitivity analysis of the reaction mechanism is carried out at three different temperatures 723 K, 923 K, and at 1123 K with CH_4/H_2O= 0.8 in nitrogen dilution. The sensitivity analysis for CO_2 mole fractions is presented in Figure 4.37. It can be seen that CO_2 is produced mainly via R39 ($CO^* + O^* \rightarrow CO_2{}^*$) at low temperature. It can be also observed that the system is sensitive to methane adsorption and to methane dehydrogenation with and without oxygen assistance.

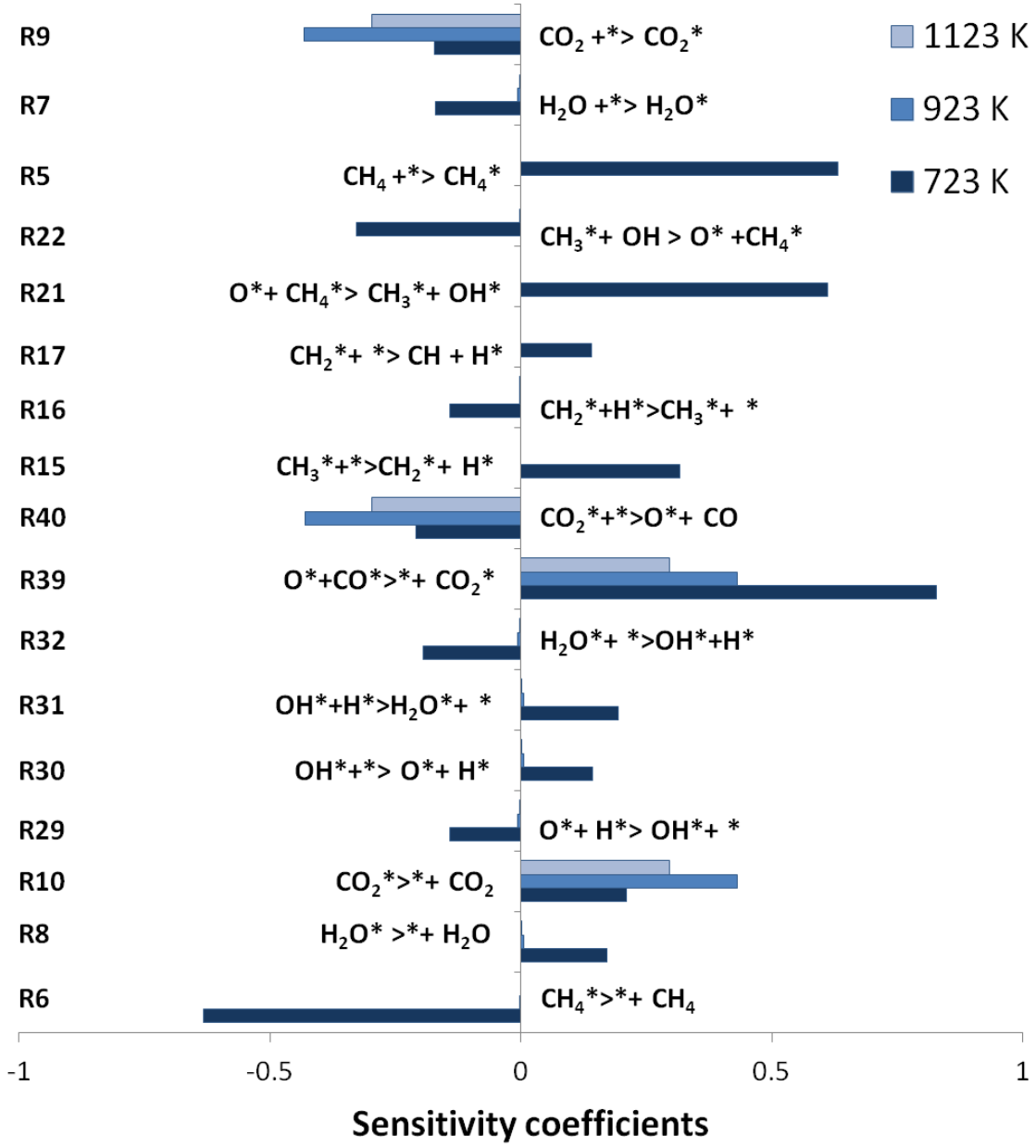

Figure 4.37 *Sensitivity analysis of CO_2 gas phase concentration for steam reforming methane at different temperatures points for CH_4/H_2O= 0.8 in N_2 dilution.*

Results for Dry Reforming of Methane (DR)

One of our main objectives of this study is to model the processes that take place during dry reforming of methane. The experiments for methane reforming with CO_2 are performed at the same pressure, flow velocity and temperature conditions as for methane partial oxidation and steam reforming experiments. An inlet CH_4/CO_2 mixture with a ratio of 1 in nitrogen dilution is continuously fed into the reactor. An active catalytic surface area of 9.85×10^6 m^{-1} is applied for all numerical simulations of methane reforming with CO_2 (Figure 4.38, Figure 4.41, and Figure 4.44).

Figure 4.38 shows the numerical simulation in comparison with the experimental results for methane dry reforming as function of the temperature. It can be observed that the kinetic model presented in Table 4.17 is able to reproduce conversion and selectivity, which are close to equilibrium for the whole temperature range.

a)

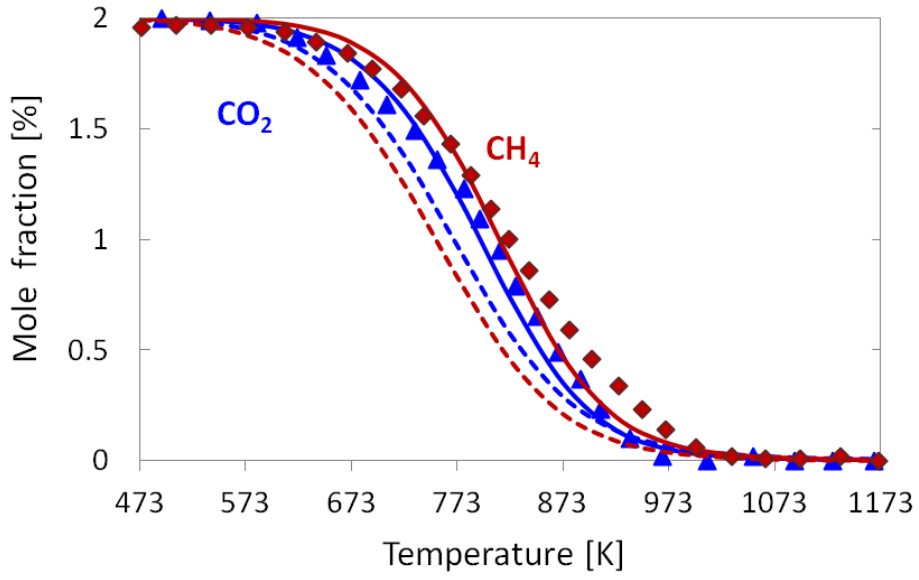

Figure 4.38 *Comparison of experimentally determined (symbols) and numerically predicted mole fractions (lines) as a function of temperature for catalytic reforming of methane with CO_2 in a fixed bed reactor:* ***a)*** *CH_4 and CO_2;* ***b)*** *CO, H_2, and H_2O;* ***c)*** *zoom-in H_2O formation; inlet gas composition of CH_4/CO_2=1 in N_2; 1 bar; T_{inlet}= 473 K; total flow rate of 4 SLPM, dashed lines = equilibrium composition at given temperature.*

b)

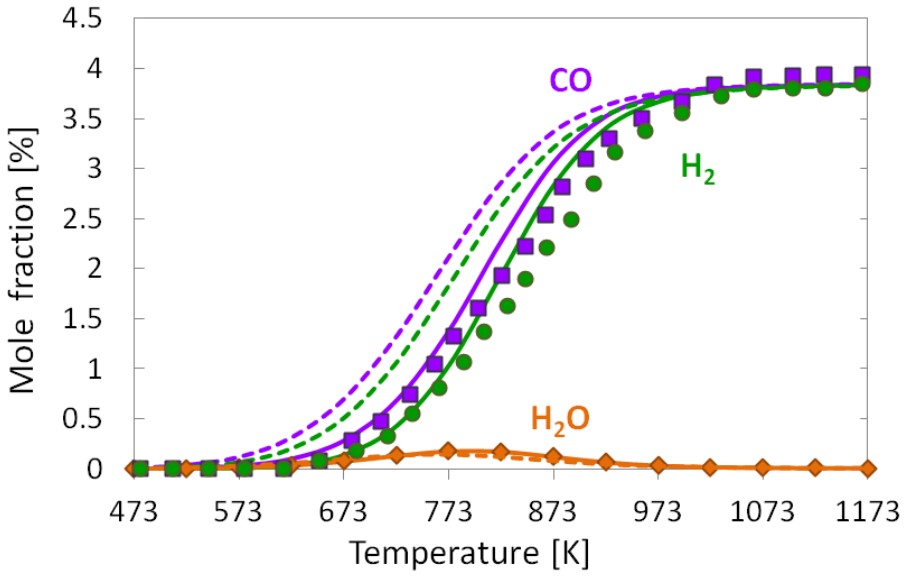

c)

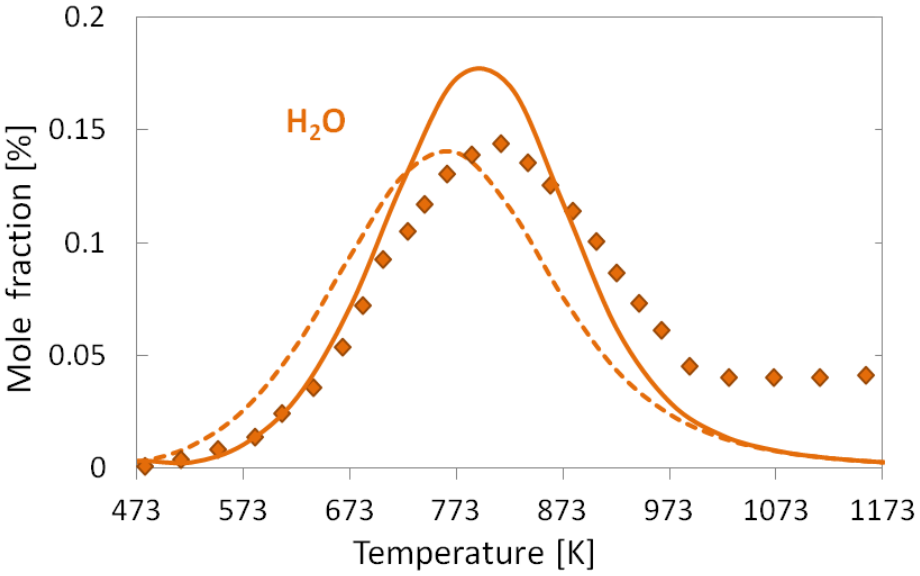

Figure 4.38: Continued

Figure 4.39 shows the computed surface coverage as a function of temperature for main absorbed species on the surface. It can be seen that at low temperatures, the surface is mainly covered by absorbed CO*, which is consumed as the temperature increases, leaving free nickel sites.

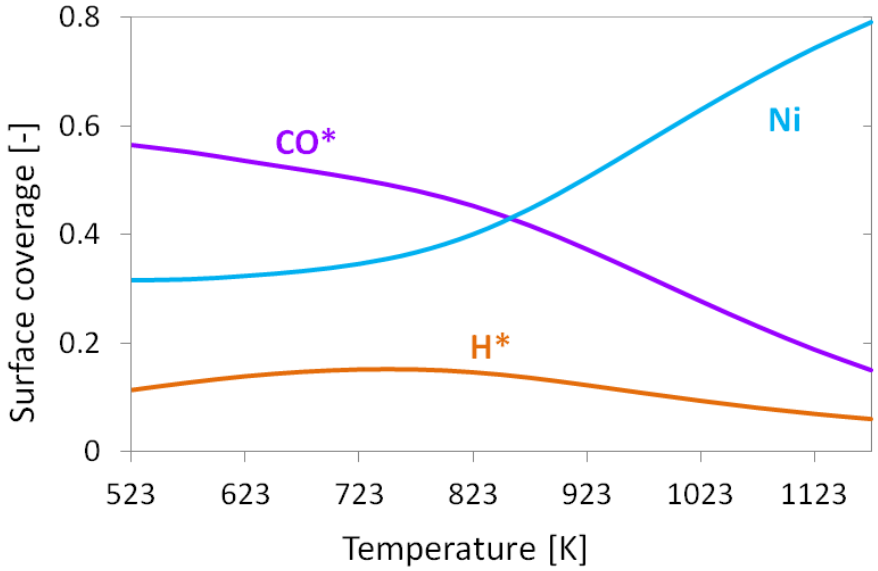

Figure 4.39 *Computed surface coverage of adsorbed species for methane dry reforming as a function of the temperature; CH_4/CO_2=1 in N_2; 1 bar; T_{inlet}= 473 K; total flow rate of 4 SLPM.*

Figure 4.40 shows the most sensitive kinetic parameters regarding to methane conversion for dry reforming, steam reforming, and partial oxidation. It indicates that simple dehydrogenation of methane is important for all processes, but for methane partial oxidation, the oxygen assisted dehydrogenation of methane is a preferable rate determining step at 1073 K (800°C).

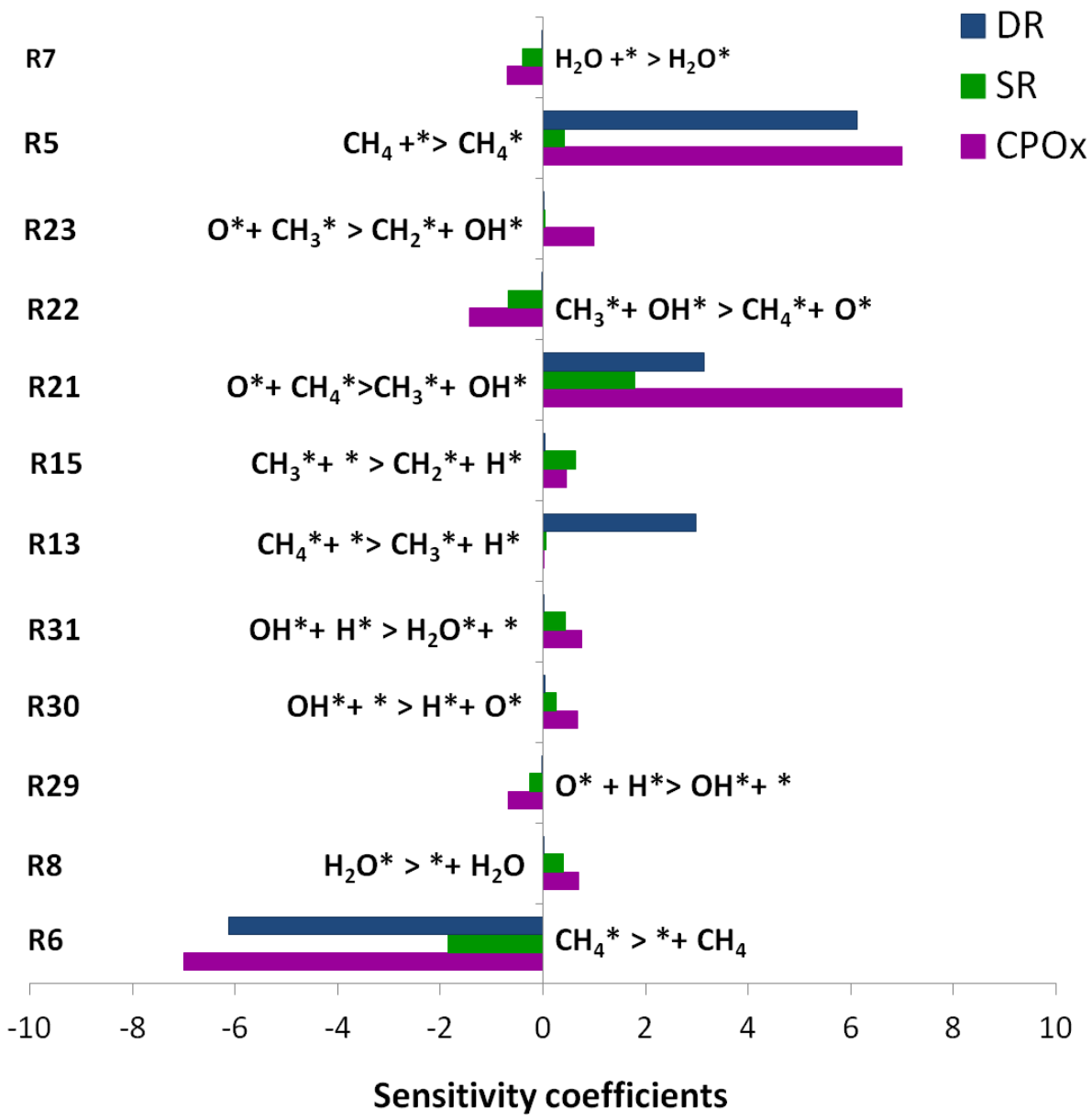

Figure 4.40 *Sensitivity coefficients for CH_4 consumption at 1073 K for DR, SR and CPOx.*

Influence of H_2 and H_2O on methane reforming with CO_2

Hydrogen and water have been recently studied as inhibitors of coal formation in the gas-phase during methane dry reforming at higher pressure and temperatures [42]. In order to study the influence of hydrogen and water on methane dry reforming, experiments using hydrogen and water as co-reactants are performed in a fixed bed reactor. The measurements are carried out at atmospheric pressure, with a total flow of 4 SLPM. Catalytic bed temperatures are varied from 373 K to 1173 K (100-900 °C). An inlet gas composition of 1.6 vol.% CH_4, 2.1 vol.% CO_2 and 1.8.vol% H_2 in nitrogen dilution is fed into the reactor at 373 K.

Figure 4.41 shows the experimental results in comparison with the numerical predictions as a function of the temperature. The remarkable effect of hydrogen at this experiment is the formation of water, probably produced through the R-WGS reaction. Then, water is consumed as temperature increases due to the steam reforming reaction with the remainder methane.

a)

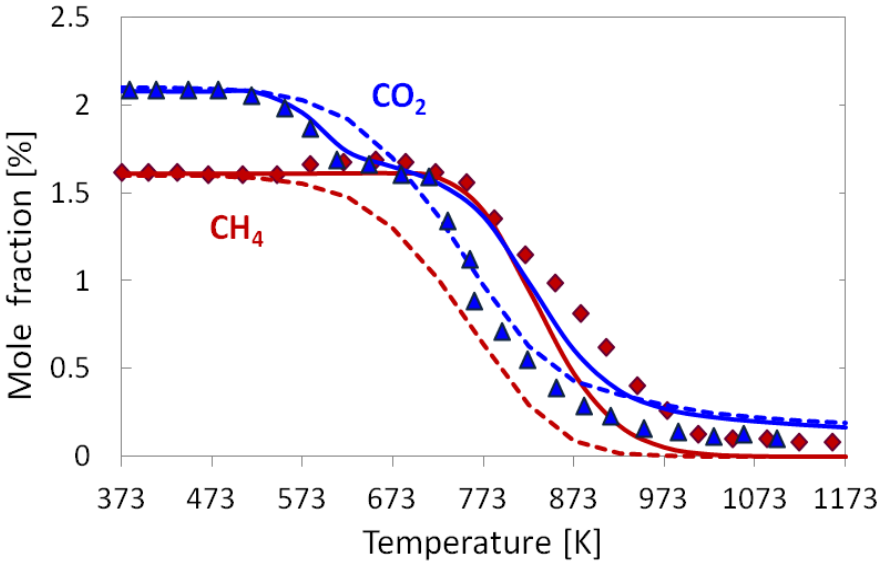

Figure 4.41 *Comparison of experimentally determined (symbols) and numerically predicted (lines) mole fractions as a function of temperature for catalytic dry reforming of methane with H_2:* ***a)*** *CH_4 and H_2O;* ***b)*** *CO_2, CO, H_2, inlet gas composition of 1.6 vol.% CH_4, 2.1 vol.% CO_2, 1.8 vol.% H_2 in N_2; 1 bar; T_{inlet}= 373 K; total flow rate of 4 SLPM; dashed lines = equilibrium composition at given temperature.*

b)

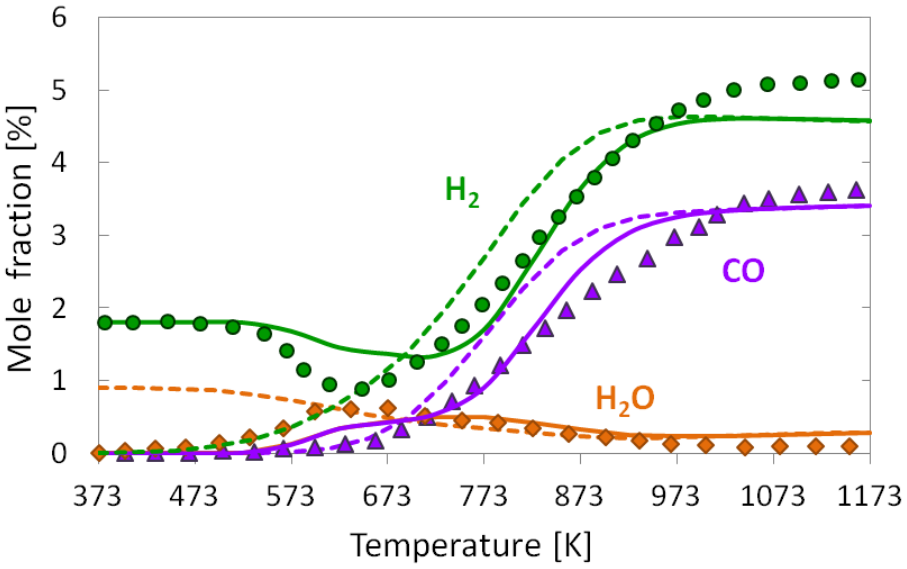

Figure 4.41: Continued

The computed surface coverage of main species absorbed is presented in the Figure 4.42. It can be observed that at low temperatures, the surface is completely covered by hydrogen which desorbs as the temperature increases. The maximum formation of carbon can be seen at temperatures between 373-573 K (100-300 °C); beyond these temperatures most carbon decreases with the increases of the temperature.

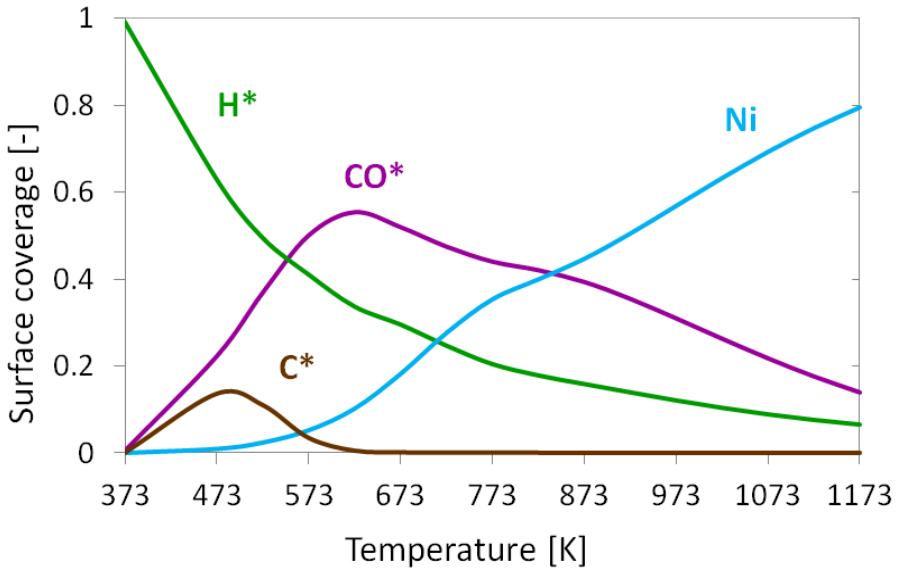

Figure 4.42 *Computed surface coverage of adsorbed species as function of the temperature for methane dry reforming with H_2 addition: inlet gas composition of 1.6 vol.% CH_4, 2.1 vol.% CO_2, 1.8 vol.% H_2 in N_2; 1 bar; T_{inlet}= 373 K; total flow rate 4 SLPM.*

Figure 4.43 shows the sensitivity analysis of the reaction mechanism at 473 K (200 °C) for C* species formation. It can be observed that gas-phase concentrations of CO_2 and H_2 are highly sensitive to adsorption and desorption steps as well as CO_2 and H_2O dissociation. The analysis also shows that reaction R41 (Table 4.17) is probably the main path for coke formation on the surface at low temperatures.

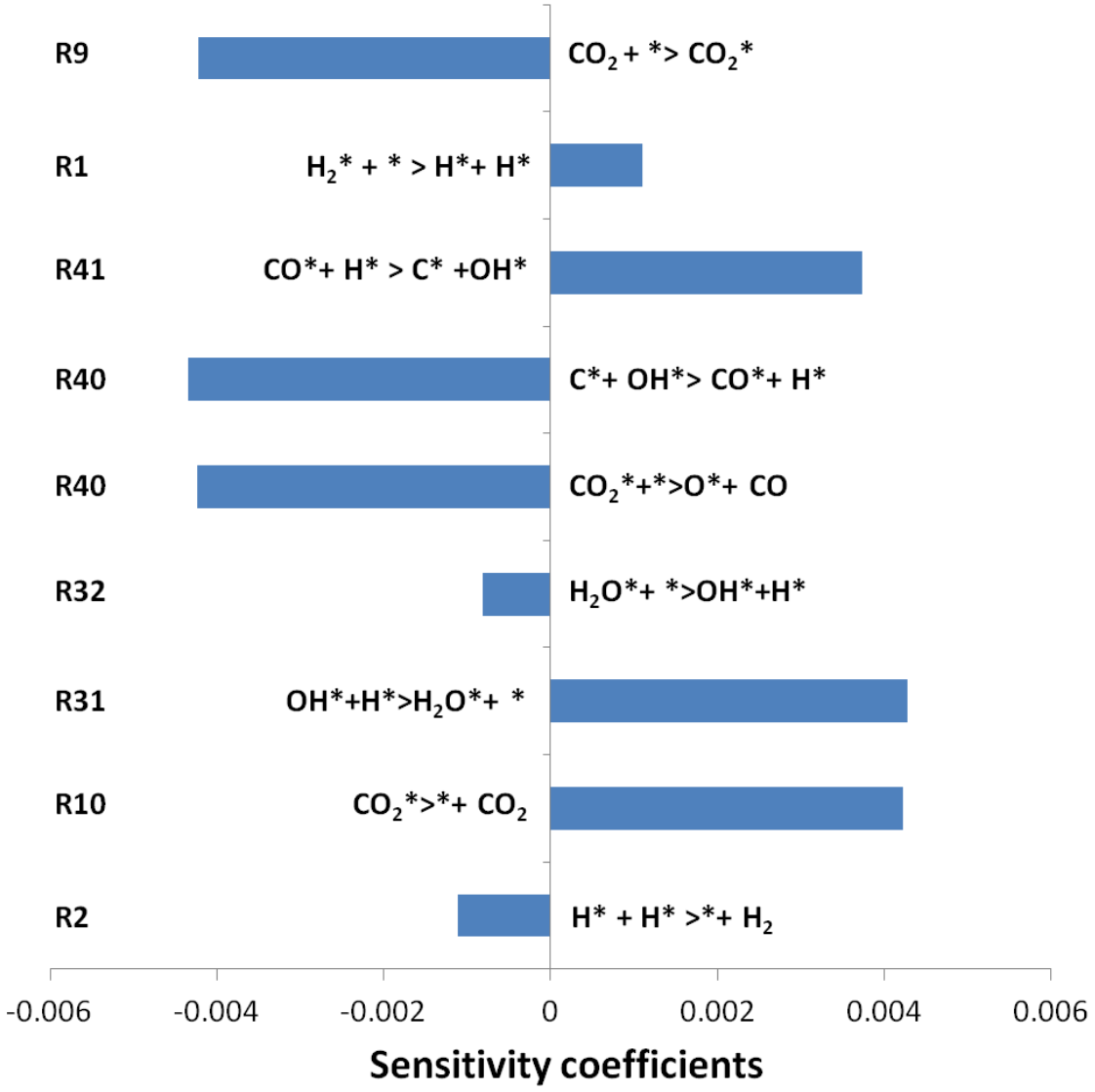

Figure 4.43 *Sensitivity analysis of absorbed C* for dry reforming of methane with H_2 at 473 K, inlet gas composition of 1.6 vol.% CH_4, 2.1 vol.% CO_2, 1.8 vol.% H_2 in N_2; 1 bar.*

Furthermore, the influence of water on methane reforming with CO_2 is also studied. Operating conditions are the same as in the previous experiment (Figure 4.44), except that water is added instead of H_2. An inlet mixture of 1.7 vol.% CH_4, 2.1 vol.% CO_2, and 2.1 vol.% H_2O in nitrogen dilution is fed into the reactor at 373 K.

Figure 4.44 compares the numerical and experimental results. It can be seen that at medium temperature, some CO_2 is produced probably by the WGS reaction. The equilibrium is reached at 973 K (700 °C) at the given conditions.

a)

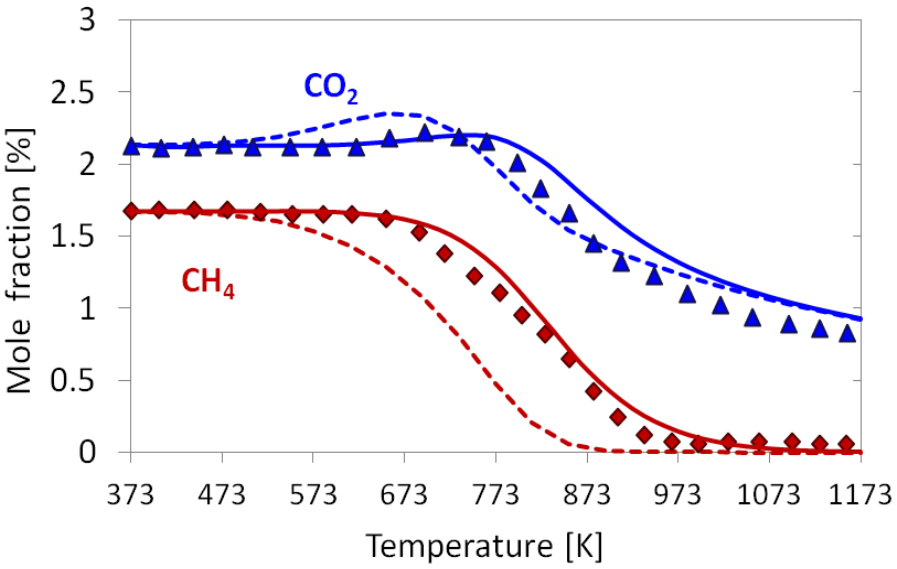

b)

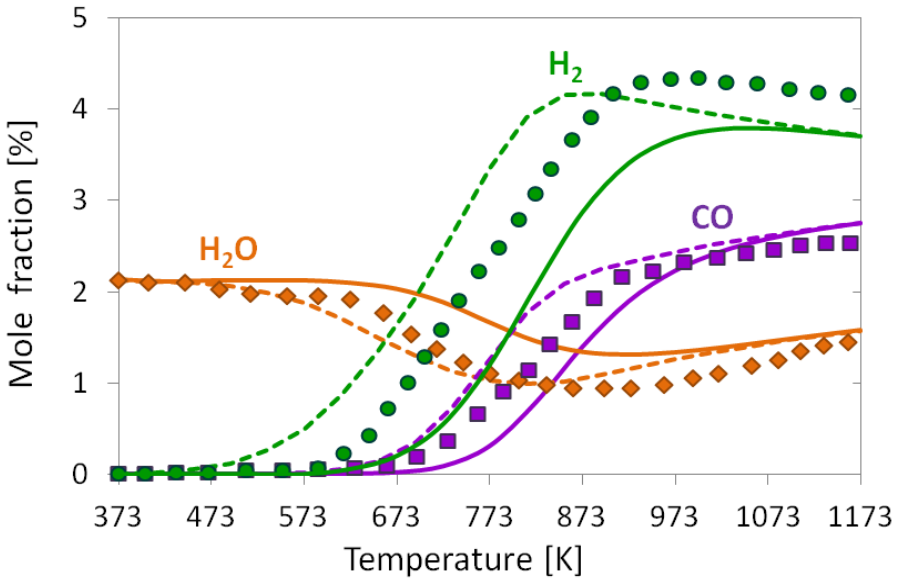

Figure 4.44 *Comparison of experimentally determined (symbols) and numerically predicted (lines) mole fractions as a function of temperature for catalytic dry reforming of methane with H_2O:* ***a)*** *CH_4, and CO_2;* ***b)*** *H_2O, CO, H_2; inlet gas composition of 1.7 vol.% CH_4, 2.1 vol.% CO_2, 2.1 vol.% H_2O in N_2; 1 bar; T_{inlet}= 373 K ,total flow rate of 4 SLPM, dashed lines = equilibrium composition at given temperature.*

Computed surface coverage of the main absorbed species at the catalytic surface is presented in Figure 4.45. It can be observed that at temperatures below 523 K (250 °C) the surface is mainly covered by oxygen coming from CO_2* and H_2O* dissociation, as the temperature increases the oxygen coverage decreases rapidly leading to free nickel sites, which catalyze the reaction producing H* and CO*. No significant amount of coke is obtained in comparison with the previous results by using H_2 as co-reactant (Figure 4.41).

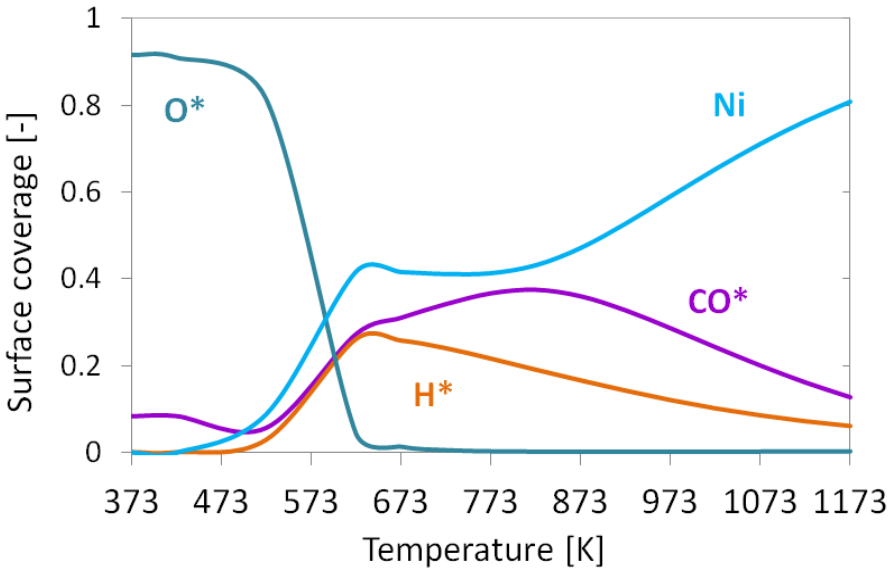

Figure 4.45 *Computed surface coverage of adsorbed species as function of the temperature for methane dry reforming with H_2O addition: 1.7 vol.% CH_4, 2.1 vol.% CO_2, 2.1 vol.% H_2O in N_2; 1 bar; T_{inlet}= 373 K; total flow rate of 4 SLPM.*

The nickel-base catalyst Fixedbed_Ni_BASF_Cat.2 from BASF used for the oxidation and reforming experiments axial does not produce significant amounts of coke on the surface at the working conditions in this study.

Figure 4.46 shows a comparison of the computed surface coverage of carbon at the three different conditions studied for reforming of methane with CO_2. It can be observed that dry reforming of methane produces the highest coverage of carbon at the surface (Figure 4.46a). Moreover, the results show that both H_2O and H_2 are inhibitors of coke deposition (Figure 4.46b). However, H_2O provides a better inhibition effect than H_2.

a)

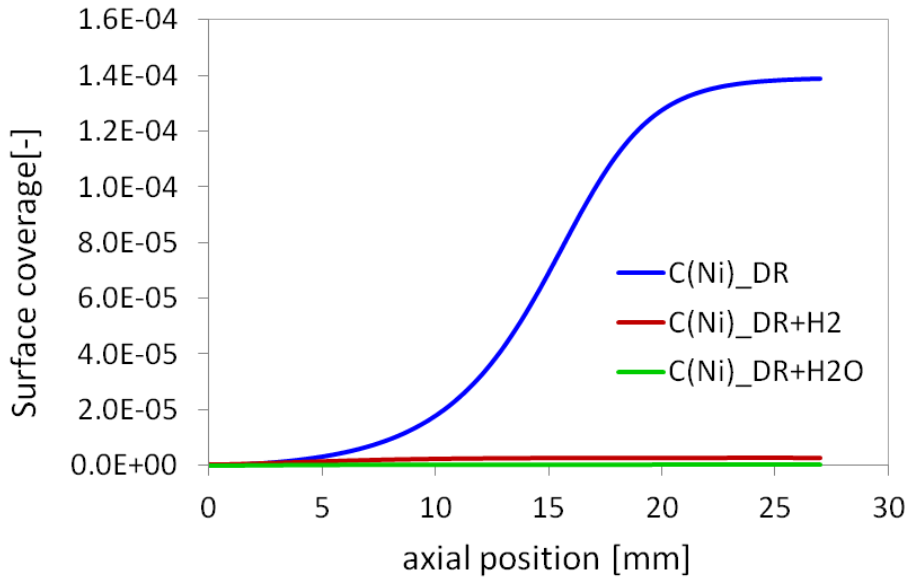

b)

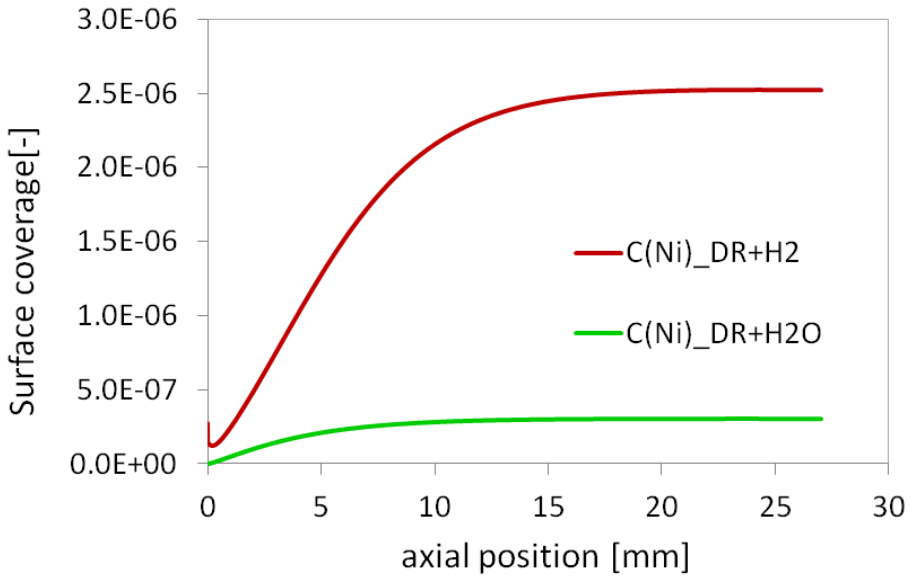

Figure 4.46 *Computed surface coverage for carbon along the catalytic bed for methane reforming with CO_2 at 1123 K:* ***a)*** *comparison of methane dry reforming between the cases with H_2 and steam addition,* ***b)*** *zoom-in of the surface coverage using H_2 and H_2O as co-reactant.*

4.4.5 Test of the Reaction Kinetics

Partial Oxidation of Methane to Carbon Monoxide and Hydrogen over a Ni/Al_2O_3 Catalyst. Dissanayake et al. [16].

The developed reaction mechanism in Table 4.17 is tested against experimental data provided by Dissanayake et.al. [16]. The experiment is carried out by using a tubular quartz reactor with an internal diameter of 2.5 mm depicted in Figure 4.47. The catalytic bed is 15 mm long for a 50 mg sample and it is preceded by a 15 mm preheating region containing 20-45 mesh quartz chips.

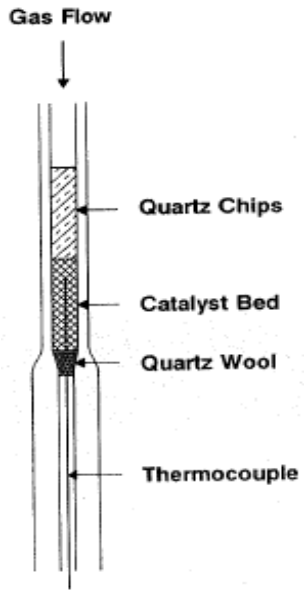

Figure 4.47 *Schematic representation of the continuous-flow reactor [16].*

A commercial nickel catalyst (C11-2S-06) with a Ni loading of 25 wt.% and a total BET-N_2 surface area of 22 m^2/g is used for the experimental study. The reaction is performed using a feed mixture of $CH_4/O_2/He$ = 1.78/1/25 at a total flow rate of 50 cm^3/min and total pressure of 1 atm, resulting in an effective contact time of ~0.09 s. Detailed information about the catalyst, experimental set-up and reaction conditions are given elsewhere [16].

Figure 4.48 shows a comparison of experimental values and model predictions. The numerical simulations are performed based on 1D model of the catalytic bed by using $DETCHEM^{PACKEDBED}$ code [77]. Linear flow velocity is calculated to be 0.00305 m/s and an active catalytic surface area of 4050 m^{-1} is applied for the numerical simulation to fit the experimental results.

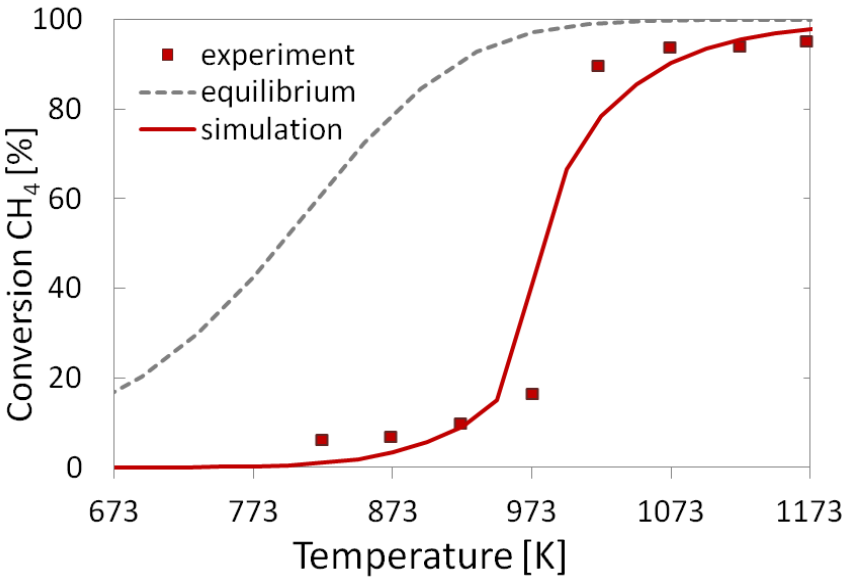

Figure 4.48 *Effect of the reaction temperature on conversion of CH_4 over pre-calcined Ni/Al_2O_3, CH_4/O_2=1.78, 1 bar; T_{range}= 673-1173 K; total flow rate of 50 cm^3/min [16].*

The authors [16] proposed a two step reaction mechanism, where total oxidation of methane is taking place first, and then followed by the reforming of the produced H_2O and CO_2 with residual CH_4 to form synthesis gas. Without any modification of the mechanism the light-off of the reaction can be reproduced.

Steam Reforming of CH_4 in a continuous-flow reactor using catalytic monoliths [58].

The experiment is performed using a tubular quartz reactor with an internal diameter of 18 mm depicted in Figure 4.49. Three cordierite honeycomb monoliths with a diameter of 1.5 cm are placed inside the ceramic tube. The monoliths, 10 mm in length, have 89 channels with an inner hydraulic diameter of 1.13mm. The monolith in the middle is coated with nickel by wet impregnation with a solution of $Ni_2(NO_3)_2*5H_2O$ (Alfa Aesar). The preparation procedure led to Ni loadings of 3 wt.% approximately. The catalysts do not carry a washcoat, the metal is spread on the blank cordierite surface to avoid any transport limitation within the catalyst layer. The experiment is carried out at constant S/C= 2.77 in 75% Ar dilution, at atmospheric pressure, the temperature is increased step-wise, and after the steady state is reached the exit concentration is analyzed. A constant flow rate of 593 ml/min is applied, resulting in a hydraulic flow velocity in the single channels of 0.056 m/s. Detailed information about the catalyst, experimental set-up and reaction conditions are given elsewhere [58].

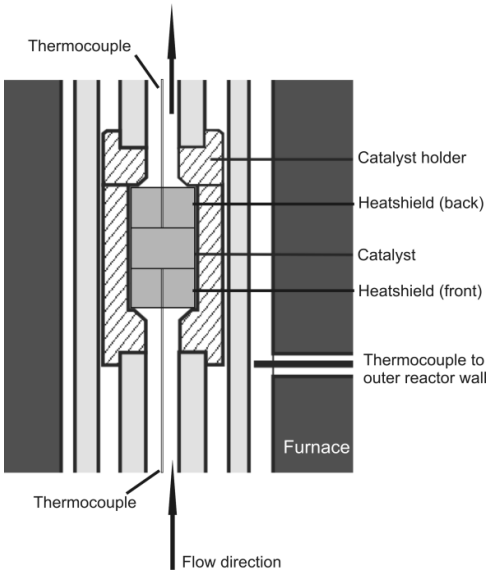

Figure 4.49 *Schematic representation of the experimental set-up used for catalytic reforming experiments employing Ni-coated monoliths [58].*

The numerical simulations are performed based on 2D model of the boundary-layer by using DETCHEM^{CHANNEL} code [77]. An $F_{cat/geo}$ of 60 is used in the simulation. A comparison of the experimental results and model predictions is presented in Figure 4.50. Both experimentally measured and numerical predicted results reveal that thermodynamic equilibrium is not reached at temperature below 1073 K (800 °C).

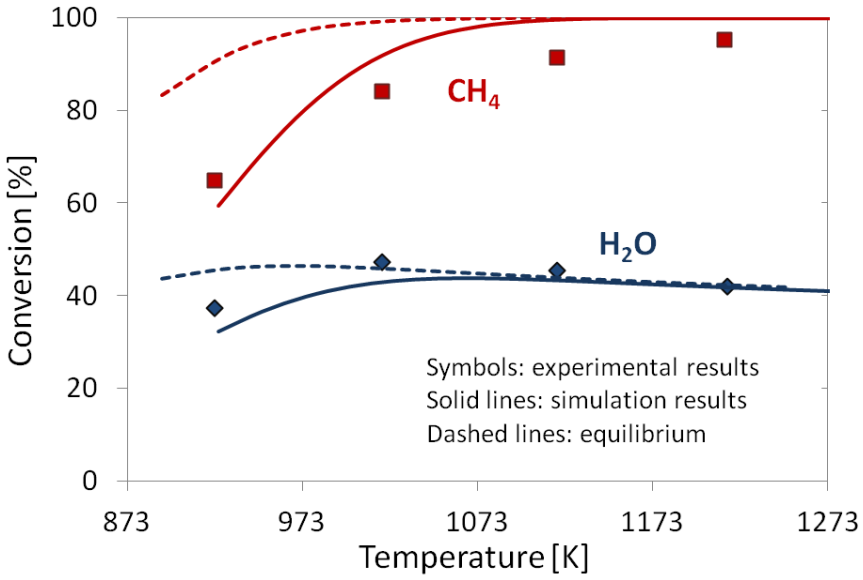

Figure 4.50 *Methane and water conversion as a function of temperature in methane steam reforming: S/C = 2.77, 75 % Ar; 1 bar; T_{range}= 923-1273 K; total flow rate of 593 ml/min [58].*

Figure 4.51 shows that the model predicts in agreement the experimentally determined H_2/CO ratio as function of temperature.

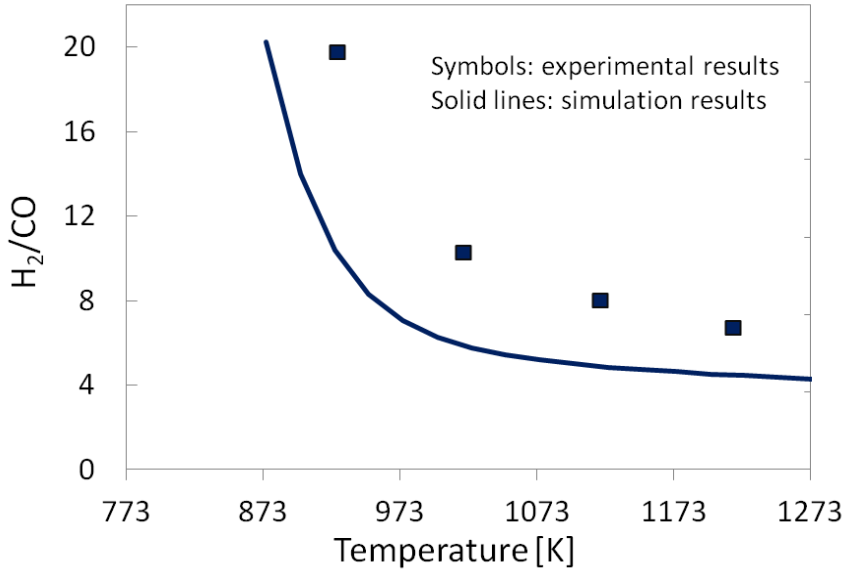

Figure 4.51 *Effect of temperature on H2/CO-ratio in methane steam reforming: S/C = 2.77, 75 % Ar; 1 bar; T_{range}= 923-1273 K; total flow rate of 593 mL/min [58].*

Ni catalyst wash-coated on metal monolith with enhanced heat-transfer capability for steam reforming, Ryu et al.[221].

To further evaluate the applicability of the developed surface reaction mechanism, experiments conducted by Ryu [221] are modeled. Steam reforming of methane is studied over two reduced nickel catalyst (21 wt.% Ni on MgO and Al_2O_3), packed into a quartz tube reactor. A mass of 3 g of nickel catalyst is used to make the wash-coat. The single monolith with a diameter of 22 mm being 20 mm in length consists of over 300 channels (640 cpsi) with an inner hydraulic diameter of 0.536 mm. The reactor is isothermally operated at atmospheric pressure at S/C = 3 without dilution, and a gas hourly space velocity (GHSV) of 9000 h^{-1}. More information about the catalyst preparation, experimental set-up and reaction conditions are given elsewhere [221, 222]. The numerical simulations are performed based on 1D and 2D model by using DETCHEM^{PACKEDBED} and DETCHEM^{CHANNEL} software [77]. An estimated dispersion of $9.5x10^{-3}$ is used to calculate the active surface area of both catalysts.

A ratio of the active to geometrical surface area of the channel wall ($F_{cat/geo}$) of 90 is used in the monolith simulation, whereas for the fixed bed simulations an active catalytic surface area of $1.45x10^{6}$ m^{-1} is used.

As is shown in Figure 4.52 and Figure 4.53, the reaction mechanism presented in Table 4.17 is able to reproduce the kinetics of the reaction, which is not in equilibrium up to a temperature of 1073 K (800 °C).

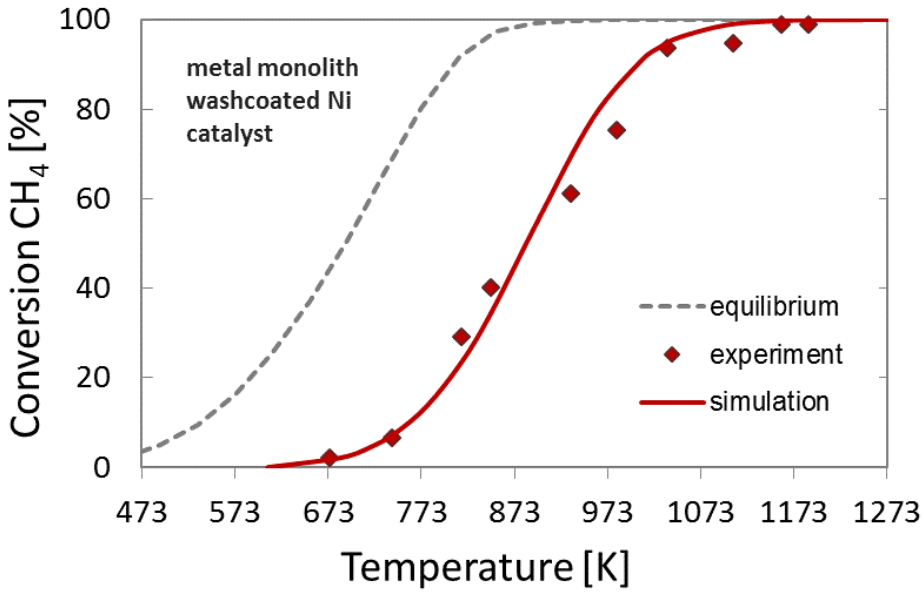

Figure 4.52 *Methane conversion as function of temperature over metal monolith wash-coated with Ni catalyst, S/C = 3; 1 bar; T_{range}= 400-1273 K; GHSV=9443 h^{-1} experimental data taken from Ryu [221].*

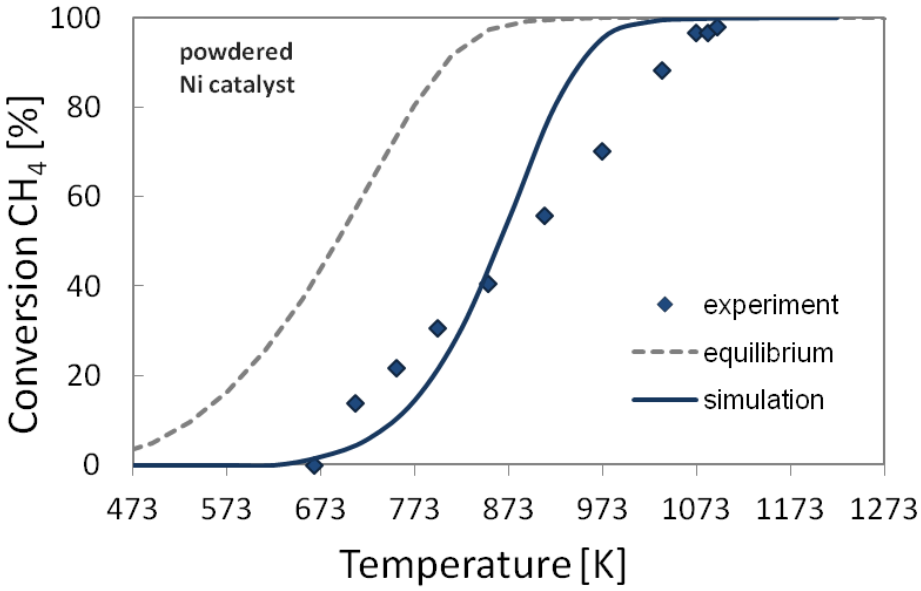

Figure 4.53 *Methane conversion as function of temperature over powdered Ni catalyst with Ni catalyst, S/C = 3; 1 bar; T_{range}= 473-1273 K; GHSV=9443 h^{-1} experimental data taken from Ryu [221].*

Mechanistic Study of Carbon Dioxide Reforming with Methane over Supported Nickel Catalysts, Yan et al. [223].

The studies performed Yan et al. [223] are modeled in order to further test the heterogeneous surface model developed in this work. The reforming reaction is carried out in a quartz fixed bed reactor (i.d.= 6 mm), the micro reactor is used to enhance the mass transfer between gas-phase and catalyst .The study is carried out using 40 mg of γ-Al_2O_3-supported catalyst with 8 wt.% Ni. The stoichiometric reforming reaction is conducted with CH_4/CO_2 =1, at atmospheric pressure and whit a volume flow of 180 cm^3/min. The numerical simulations are performed based on 1D model by using DETCHEM^{PACKEDBED} software [77]. An active catalytic surface area of 5.00x10^8 m^{-1} is used for the numerical modeling. The activity and selectivity of the Ni/Al_2O_3 catalyst is investigated at different temperatures, the variation of conversion and yields are compared with the numerical results in Figure 4.54.

a)

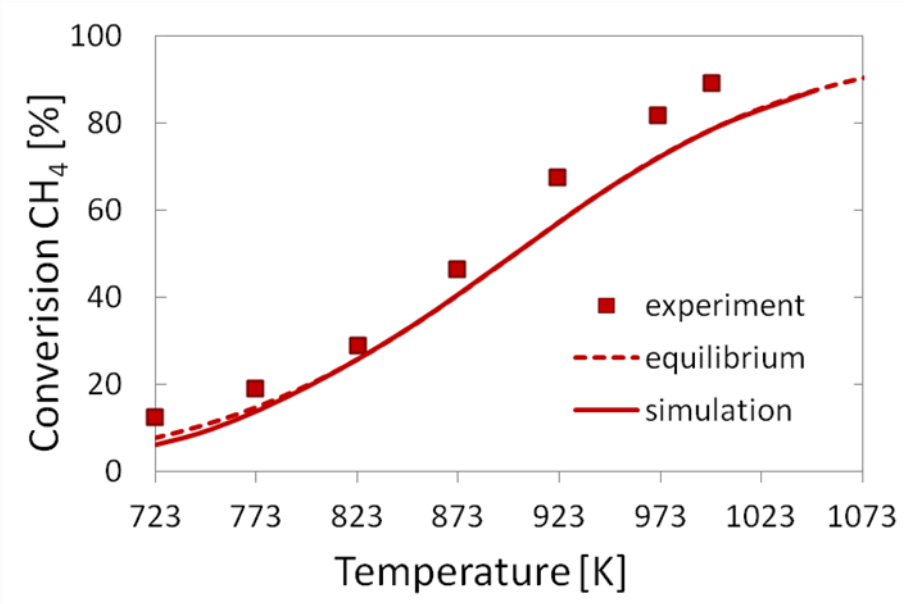

b)

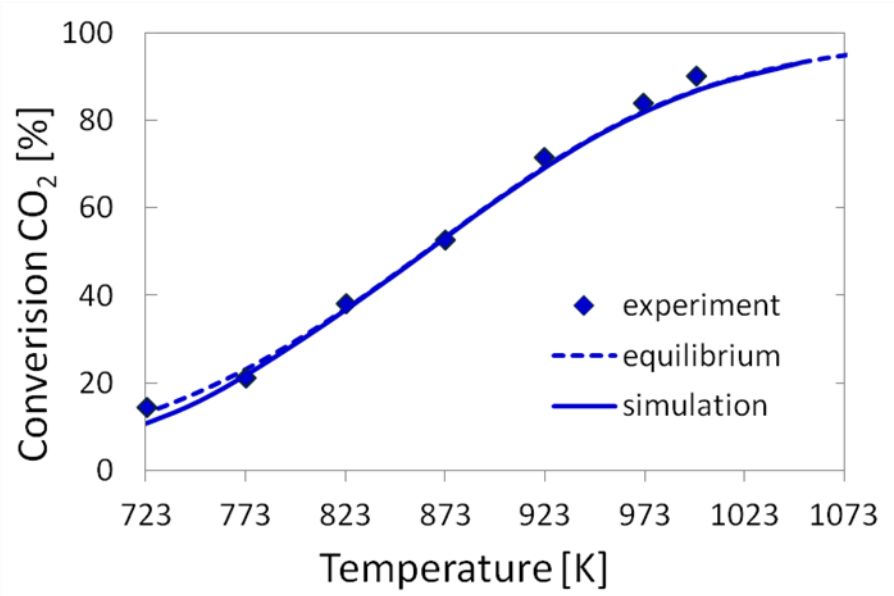

Figure 4.54 *Reactant conversions and product yields as a function of the temperature for DR:* ***a)*** *CH_4 conversion,* ***b)*** *CO_2 conversion, and* ***c)*** *CO and H_2 yields; for an inlet gas composition of CH_4/CO_2 = 1, temperature range 723-1073 K, and a volume flow of 180 cm^3/min [223].*

c)

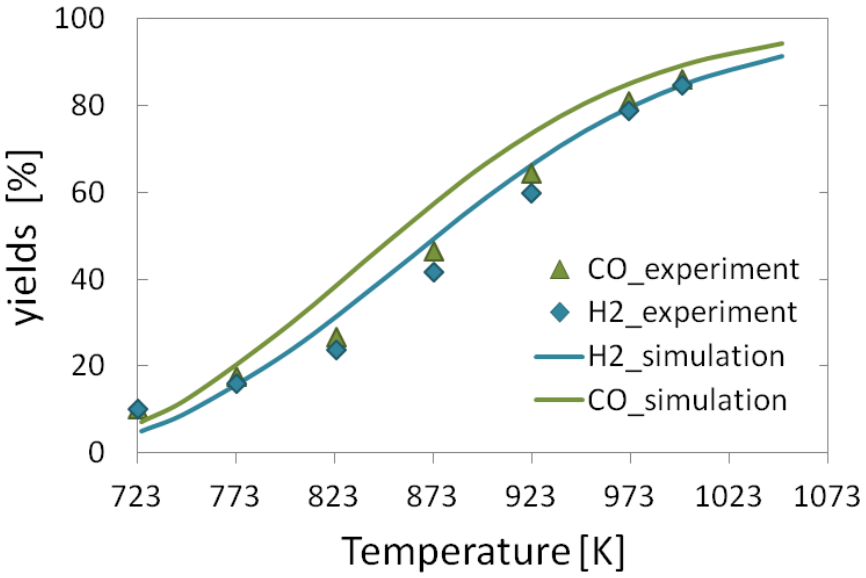

Figure 4.54: Continued

A comprehensive comparison of CH_4-CO_2 reforming activities of NiO/Al_2O_3 catalysts under fixed- and fluidized-bed operations, Chen et al.[224].

The experimental results performed by Chen et al. [224] are also modeled, these experimental results are chosen as an example for a case where the equilibrium is not reached even at high temperatures. A micro quartz reactor is used for the study. The size of its bed zone was designed to be 8 mm (i.d.) x 40 mm. The catalyst used is a γ-Al_2O_3-supported Ni catalyst (with 10.5 wt.% Ni and 150 m^2/g BET surface area). The reactor is isothermally operated at CH_4/CO_2 = 1.5, 1 bar, temperature range 973-1223 K (700-950 °C), and a volume flow of 125 cm^3/min. The simulation of a fixed bed is analyzed using a 1D model by using the software $DETCHEM^{PACKEDBED}$. An active catalytic surface area of $5.05x10^4\ m^{-1}$ is used for the numerical modeling to fit the experimental results.

Figure 4.55 illustrates a comparison of the experimental measured and numerical simulated conversion of CH_4 and CO_2 at different temperatures.

a)

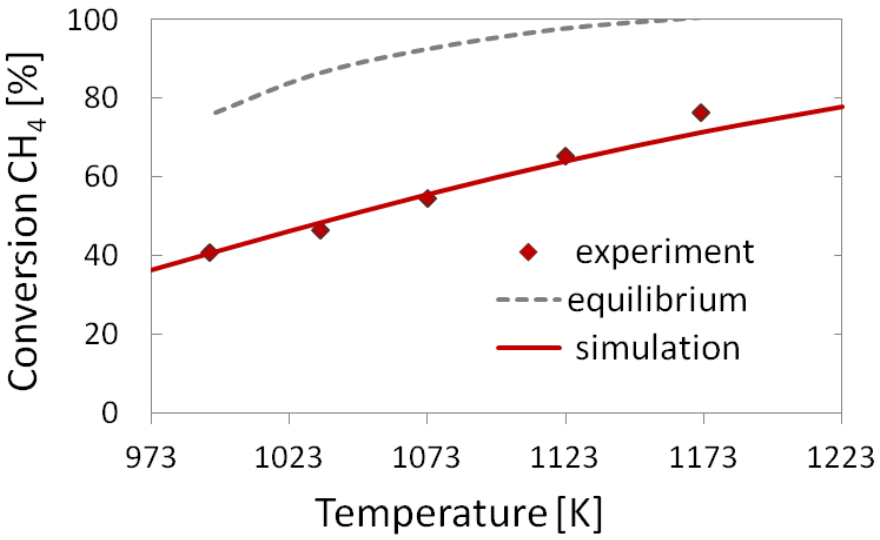

b)

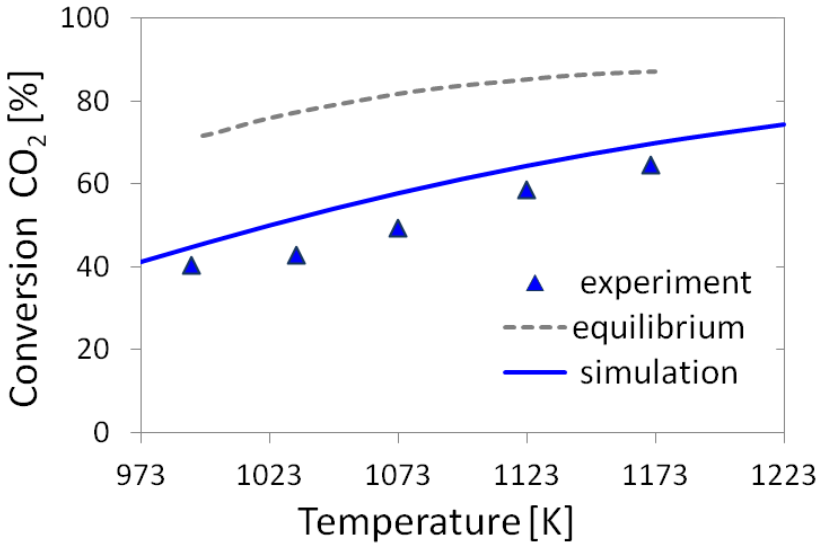

Figure 4.55 *Reactant conversions as function of the temperature for DR, CH_4/CO_2 = 1.5, temperature range* 973-1223 K*, and a volume flow of 125 cm^3/min [224].*

Dry Reforming Project:

Methane Reforming at High Temperature and Elevated Pressure

Dry reforming of methane at elevated pressures is of great interest in research and technology. The process offers the opportunity to use carbon dioxide as feed gas. The dry reforming reaction achieves lower H_2/CO ratios, which can be used directly in downstream chemistries that typically run in the range of H_2/CO ratios in between 1 and 2 [225].

The study of catalytic reforming of methane at high temperature and pressure is performed as part of the BMWI-Project DRYREF by employees from hte AG. The studies are carried out in an experimental test unit constituted of a 6-fold reactor with dimensions similar to industrially-used reformer tubes (Figure 4.56).

Figure 4.56 *Pilot plant from the AG. Figure taken from reference [76].*

In the laboratory pilot plant the inside vertical flow reactor consists of a ceramic tube, 12 mm in inner diameter and 1400 mm in length. The experiments are carried out using the Fixedbed_Ni_BASF_Cat.1 nickel-based catalyst synthesized and characterized by BASF (Section 3.1.2). In the tubular reactor, a volume of 20 ml catalytic bed of the nickel-based catalyst is placed in the primary tube and maintained in the isothermal zone of the furnace The porosity of the catalytic bed $\varepsilon = 0.44$ is calculated using Eq. 3.2 (Section 3.1.2). An active catalytic surface area of 1.54×10^5 m^{-1} is used for the numerical simulation. The reactor setup used for the measurements is shown in Figure 4.57. The reactor configuration is numerically

modeled using a one-dimensional description of the reactive flow. DETCHEM software package are couple to simulate the different setup sections [77]. DETCHEM^{PLUG} is used for the gas phase simulations of the reactor section 1 and 3, and DETCHEM^{PACKEDBED} for section 2, which correspond to the catalytic bed.

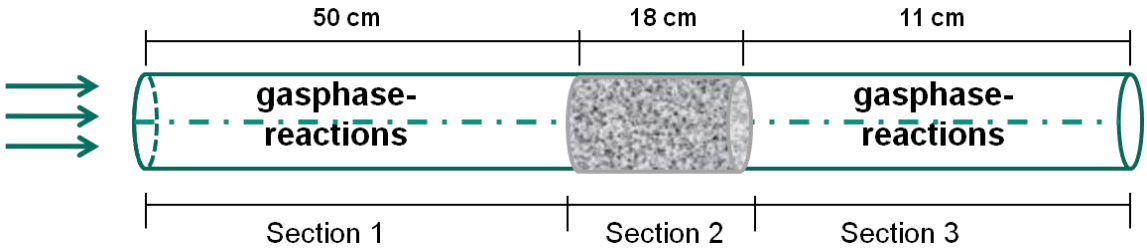

Figure 4.57 *Schematic diagram of the experimental reactor setup.*

Experimentally-obtained temperature profiles along the reactor at two different operating temperatures of the quasi-isothermal zone are shown in Figure 4.58. These profiles are used for the numerical simulations.

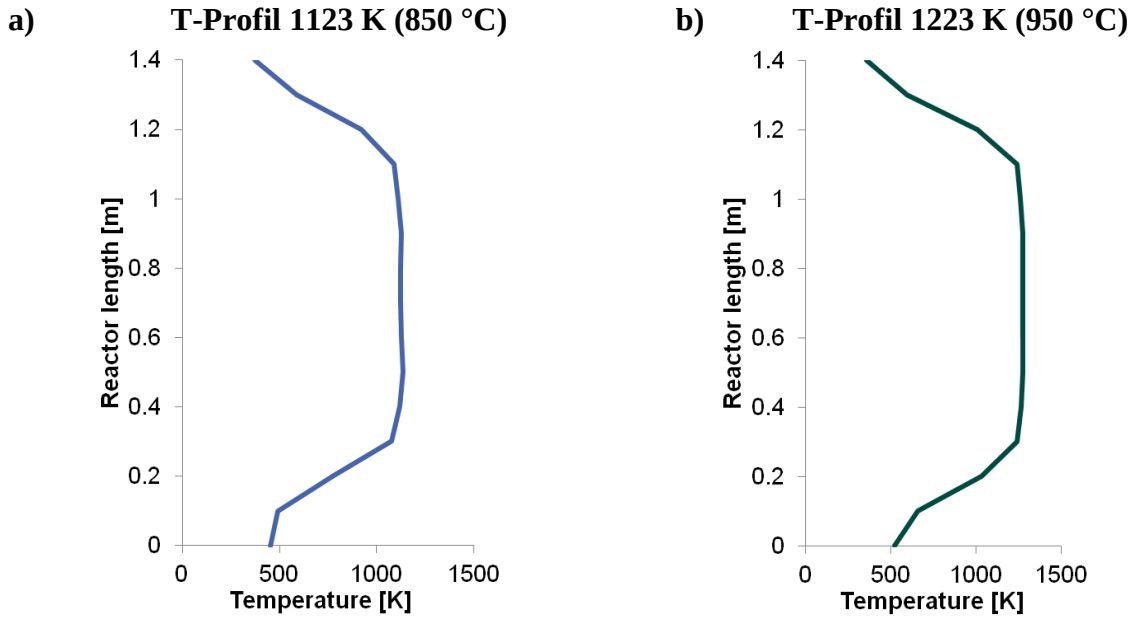

Figure 4.58 *Experimentally obtained temperature profiles along the reactor length at two temperatures of the quasi-isothermal zone: 1123 K and 1223 K.*

The catalytic tests are conducted following the protocol presented in Table 4.18 to fulfil industrially relevant conditions.

The experiments are carried out with a CH_4/CO_2 =0.9 in Ar dilution, at temperatures of 1123 K (850 °C) and 1223 K (950 °C), 20 bar, and a residence time of τ=0.947 s, which corresponds to a gas hourly space velocity of GHSV=3800 m^{-1} referring to standard conditions (25 °C, 1013.25 mbar).

Table 4.18 Inlet compositions given in mole fractions in 5 vol.% Ar dilution gas.

	Inlet gas composition [vol.%]				
Phase	CH_4	CO_2	H_2O	H_2	T [K]
1	0.475	-	0.475	-	1123
2	0.250	0.300	0.40		1123
3	0.250	0.300	-	0.40	1123
4	0.295	0.355	-	0.30	1123
5	0.295	0.354	-	0.30	1223
6	0.341	0.409	-	0.20	1223
7	0.386	0.464	-	0.1	1223
8	0.386	0.465	0.05	0.05	1223
9	0.386	0.464	0.1	-	1223

At high temperatures and elevated pressure, non-catalytic reactions in the gas-phase play an important role in the formation of higher hydrocarbons. The energy barrier a gas-phase reaction is higher than its equivalent in the catalytic surface, thus favoring the formation of radicals, which ignite gas-phase reactions.

During the experiments, coke formation at the entrance of the catalytic bed is observed at different carbon to steam (C/S) ratios and temperatures. Therefore, the numerical simulations are carried out taking into account possible gas-phase reactions, in order to understand the formation of coke from homogeneous reactions. An elementary-step gas-phase reaction mechanism [226] is coupled with the heterogeneous surface reaction model presented in Table 4.17 to numerically predict species profiles and product composition at different temperatures. Several elementary reaction mechanisms for oxidation and pyrolysis of hydrocarbons are available in the literature for modeling homogeneous gas-phase systems [227-231]. The gas phase mechanism developed by Golovitchev group [226] is used for the numerical modeling in this work. The homogeneous model consists of 690 reactions among 130 species from C1 through C8 and is applicable for a wide range of conditions (640-1760 K; 1-55 bar) [42].

A comparison of the experimental data and simulation results is presented in Figure 4.59. For all 9 phases, the results show agreement between the calculated and the experimental conversion during the reforming reactions for all experimental conditions studied. Phase 9 is slightly under predicted by the mechanism due to the formation of carbon on the catalyst during the experiment.

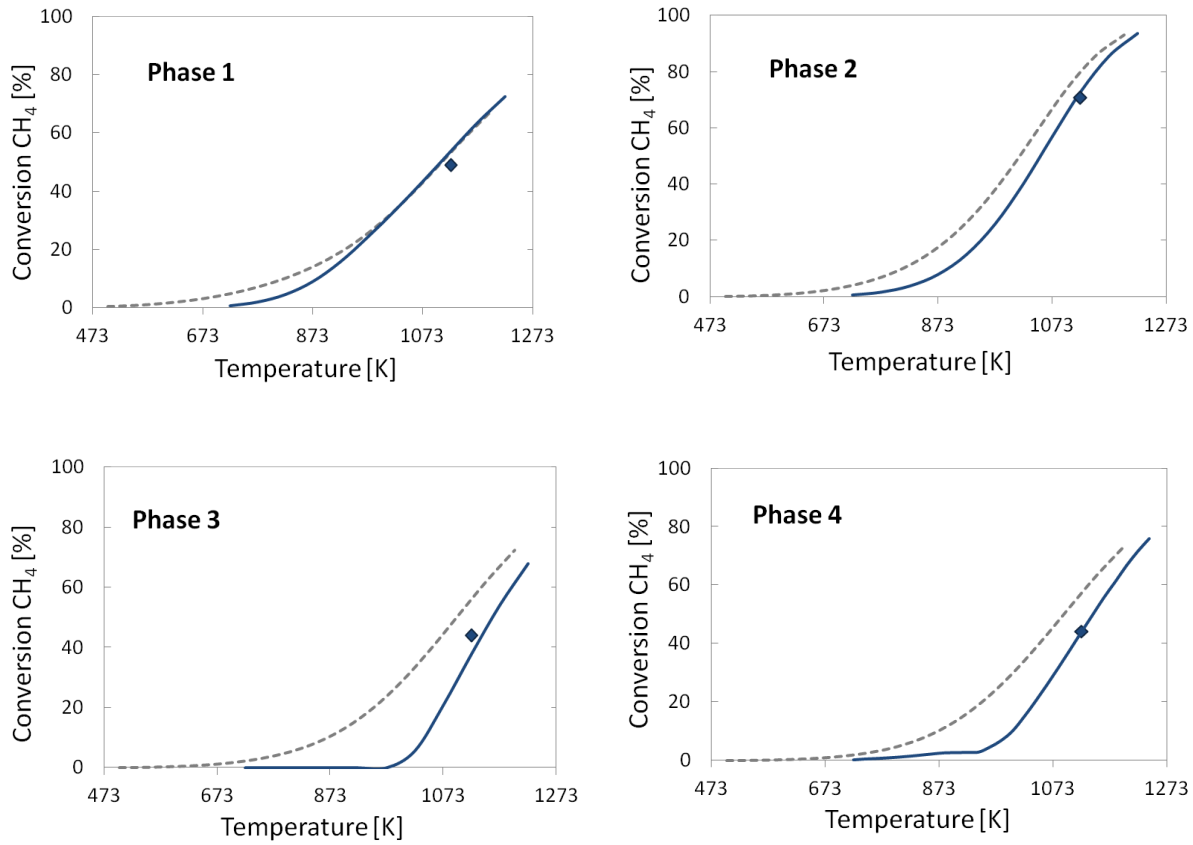

Figure 4.59 *Comparison of the experimental and numerical results for methane conversion as a function of temperature, Phase 1- 9, 20 bar; symbols = experiment, lines = simulation, dashed lines = equilibrium composition.*

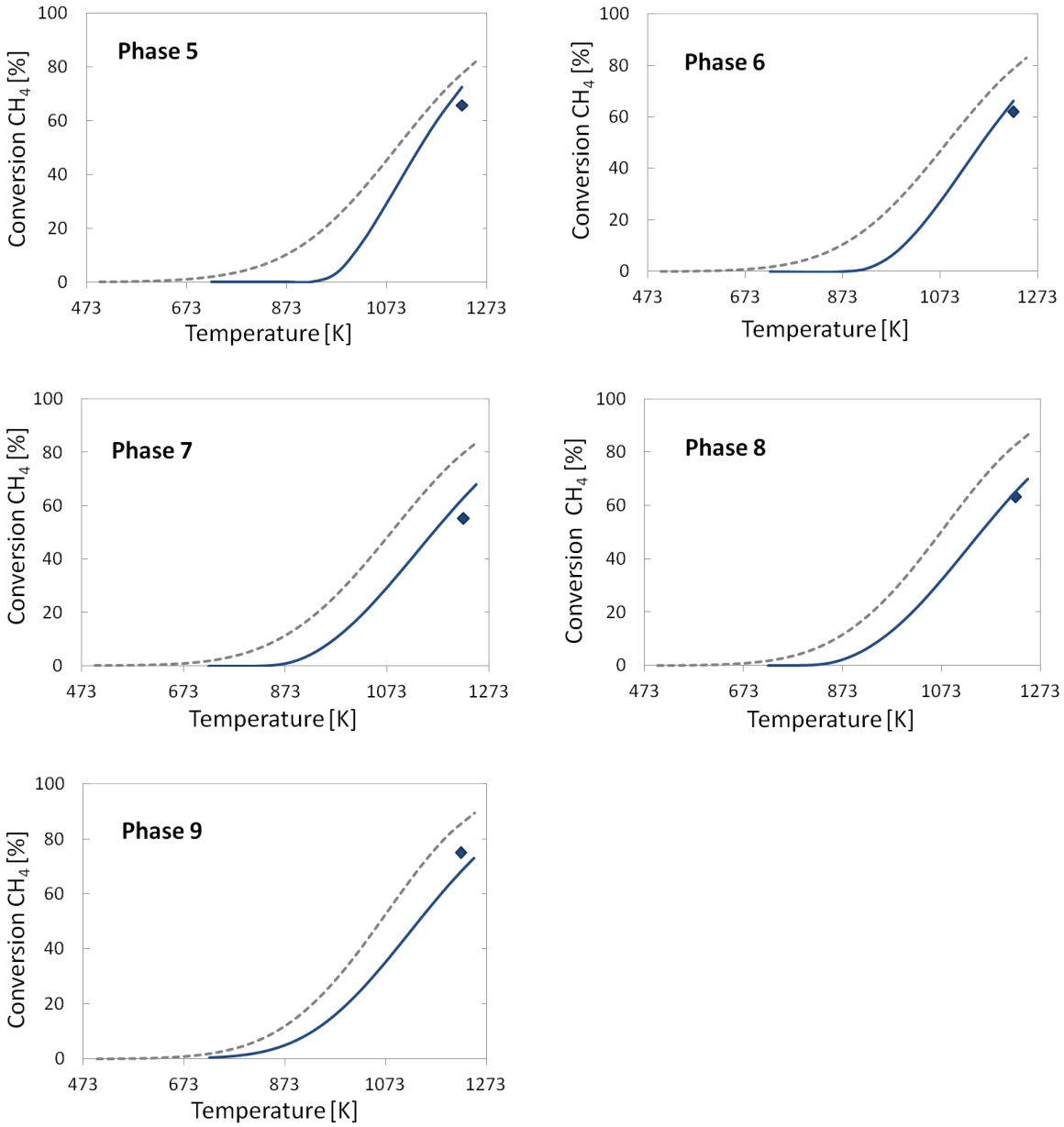

Figure 4.59: Continued

One of the main problems in many industrial reactors that involve methane as fuel, especially at elevated pressure and temperature, is coke deposition on catalysts and the reactor pipes walls. The coke can be a source for catalyst deactivation and in some cases lead to blocking of reactor tubes as well as physical disintegration of the catalyst support structure, and bring about process shut down all within a few hours [38-42].

Noble metals are less prone to coke formation under reforming conditions [43]. However, due to the high price its use in industrial processes is economically unsustainable. Industrially, Ni

based catalysts are preferred due to the lower cost and high activity, but the use is limited by higher proneness to coke formation than noble metals [44-47].

Some authors like Solymosi et al. [232] and Kaltschmitt et al. [233] reported the presence of coke precursors in the gas-phase under dry reforming and oxidation conditions at high temperatures. Kahle et al. [42] studied both experimentally and numerically, the impact of gas-phase reactions during dry reforming of methane over platinum- based catalyst at high temperature and elevated pressure.

Methane can be converted directly to hydrocarbons by thermally induced coupling reactions at high temperatures [39, 234-238]. The stepwise dehydrogenation of methane can be explained by free radical mechanisms [234]. Figure 4.60 shows the main path for carbon deposition from methane proposed by Becker and Hüttinger [239, 240].

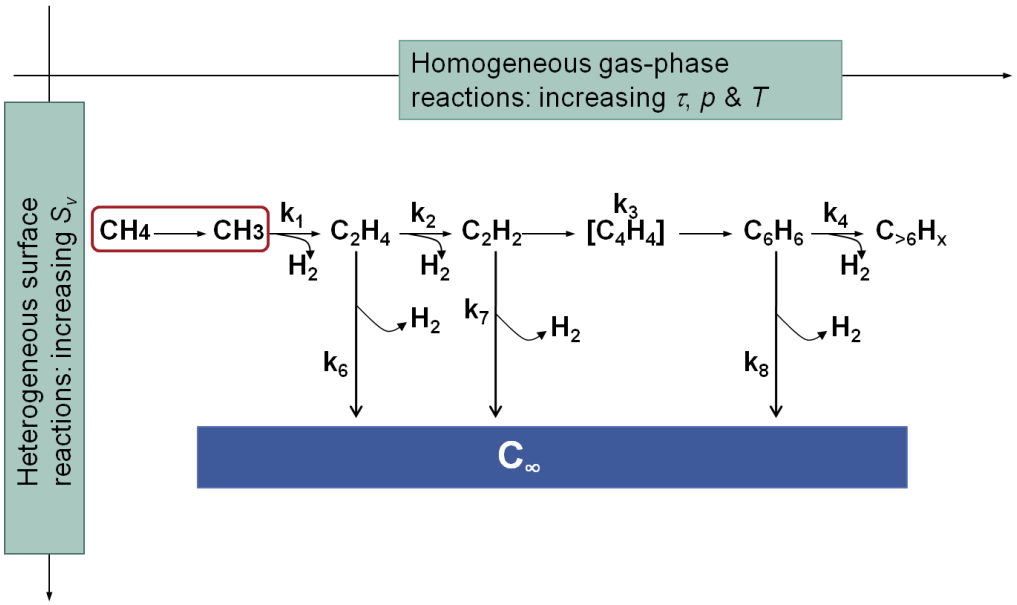

Figure 4.60 *Model of pyrocarbon deposition from methane* [239, 240].

Carbon can be deposited by means of surface reactions of these coke precursors on a carbon surface by condensation of small hydrocarbons to larger entities and assemblies (macro molecules) in the gas-phase [241].

Numerical simulations indicate that coke precursors can be formed to appreciable extent in the gas phase. Typical coke precursors would be ethylene (C_2H_4), acetylene (C_2H_2) and benzene (C_6H_6).

$$C_2H_4 + 6* > 4H* + 2C* \quad (4.27)$$

$$C_2H_2 + 4* > 2H* + 2C* \quad (4.28)$$

$$C_6H_6 + 12* > 6H* + 6C* \quad (4.29)$$

The numerical results presented in Figures 4.61 and 4.62 show that significant amounts of coke precursors are formed as result of methane pyrolysis in front and after the catalytic bed. The combination of acetylene and aromatic hydrocarbons may lead to the formation of polycyclic aromatic hydrocarbons, such as naphthalene, anthracene, and pyrene, all of which are potent precursors for carbon formation and deposition [42, 233].

The conversion of CH_4 and CO_2 increases with the temperature, and therefore, the mole fractions of the hydrocarbons also rise significantly above 1223 K (Phase 5 to 9). These results are supported by the work of Norinaga et al. [242]. The authors showed the chemical kinetics of ethylene pyrolysis at temperatures between 1073-1373 K (800-1100 °C). They found that higher temperatures favor H-abstraction, thus enhancing the formation of the highly-unsaturated hydrocarbons acetylene, diacetylene, and benzene.

The numerically predicted profiles show no significant formation of hydrocarbons in Phase 3 and 4, where high concentrations of hydrogen were added in the feed composition. Phases 2 and 3 have the same inlet concentrations of CH_4 and CO_2, with the difference that Phase 2 has 40 % H_2O in the feeding composition and Phase 3 has 40 % H_2 in instead of water. It can be observed that Phase 2 present higher amounts of coke precursors from the gas-phase than Phase 3, which indicates that hydrogen has higher effect in the inhibition of precursors from the gas-phase. These results are supported by the pyrolysis studies performed by Kahle et al. [42]. The authors conclude that hydrogen has a higher inhibition effect than water on the gas-phase at high temperatures and pressure.

The results also show no significant formation of precursors in Phase 3 and 4 with a rich inlet hydrogen composition. Phase 5 is also carried out in the presence of a high inlet concentration of H_2. However, the rise of the temperature promotes the formation of ethylene.

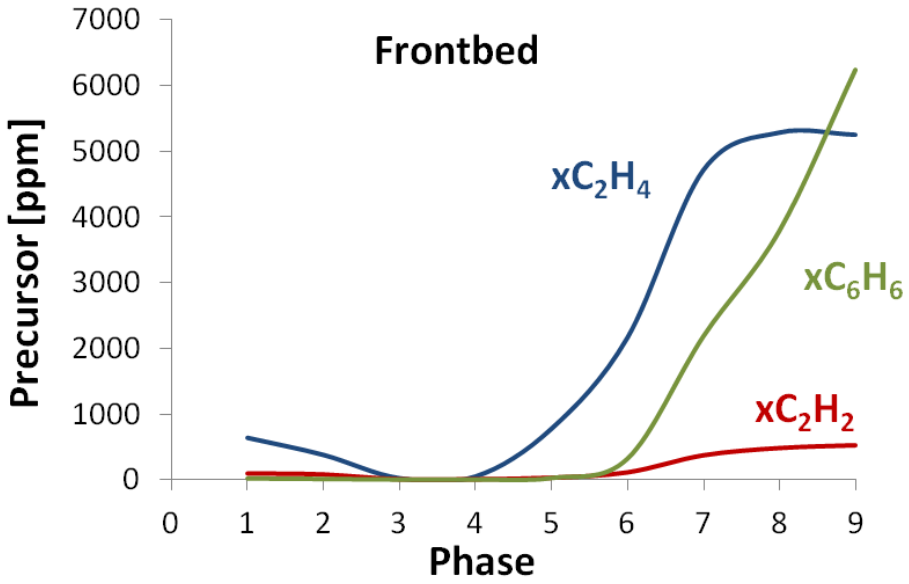

Figure 4. 61 *Numerically predicted profiles of coke precursors of the 9 Phases in front of the catalytic bed.*

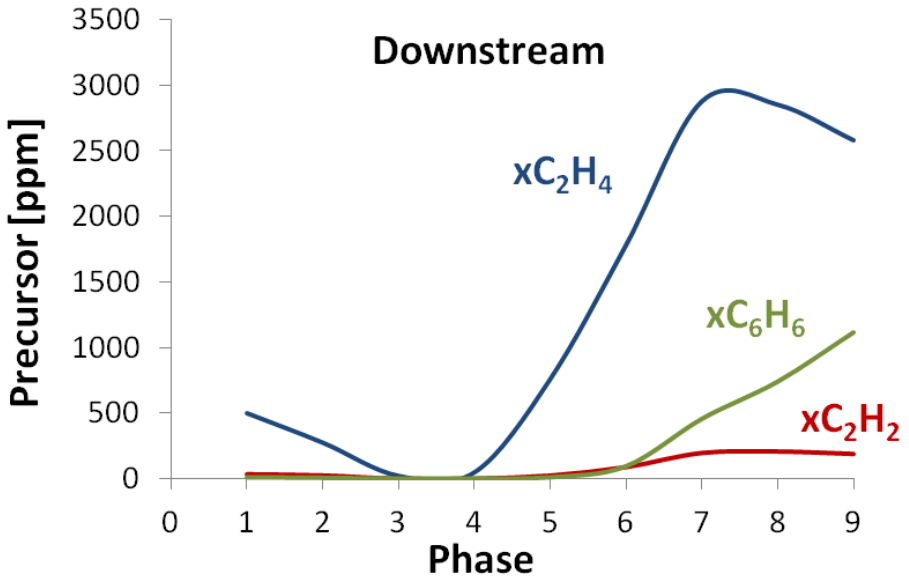

Figure 4.62 *Numerically predicted profiles of coke precursors of the 9 Phases in after of the catalytic bed.*

The coke precursor formation is experimentally measured using the same inlet conditions as Phase 1, CH_4/H_2O=1, 20 bar, 1123 K. The precursor's formation is monitored for 125 h. The results are compared with the numerical predictions using the gas-phase and surface reaction mechanisms. Table 4.19 shows the methane conversion and selectivity obtained experimentally in comparison with the simulation results. The model over predict the H_2/CO ratio, which may

be due to higher formation of carbon during the experiment and the fact that the model is only able to predict one single carbon monolayer.

Table 4.19 Methane conversion and selectivity for $CH4/H_2O=1$

	CH_4 conversion[%]	**H_2/CO**
Experiment	38.7	3.9
Simulation	38.0	4.6

The experimental results show the formation ethylene and ethane, however, no acetylene (C_2H_2) and benzene (C_6H_6) are detected in significant amount at the studied conditions. Table 4.20 contains the numerical results for the three reactor sections in comparison with the precursors measured experimentally.

It can be observed that the simulation results obtained by coupling of the gas-phase and surface models are able to describe the experimental results.

Table 4.20 Precursors formation for Phase 1, with an inlet ratio of $CH_4/H_2O=1$, 20 bar, 1123 K for 125 h.

Section	C_2H_4	C_2H_6	C_6H_6
1	$1.28x10^{-4}$	$8.84x10^{-5}$	$2.18x10^{-7}$
2	$6.54x10^{-5}$	$1.59x10^{-4}$	$2.02x10^{-7}$
3	$4.86x10^{-5}$	$1.95x10^{-4}$	$7.55x10^{-8}$
Simulation	**48.6 ppm**	**195 ppm**	**0.075 ppm**
Experiment	**50.0 ppm**	**250 ppm**	**No detected**

No experimental data for precursor's formation are measured for the rest of the Phases. Therefore, the comparison with the simulations is not possible.

One of the main objectives of this study is to understand the reaction paths that take place during the reforming of methane with CO_2 at high pressure and temperature. Using reaction flow analysis is possible determine the main path of production and consumption of the species within the catalytic cycle. Hence, a reaction flow analysis of the surface model here developed (Table 4.17) is carried out at dry reforming conditions. A ratio $CH_4/CO_2=1$ in 5 vol.% Ar dilution is used, with a reaction temperature of 1123 K, at 20 bar and a gas hourly space velocity of GHSV=3800 m^{-1}.

The reaction flow analysis presented in Figure 4.63 shows that at high temperature approximately 90 % of the absorbed CO_2 dissociate CO* and O*, which is consistent with the results obtained for WGS, where the reactions involving the COOH* intermediate take place mainly at low temperature and the dissociation of CO_2 to CO* and O* at high temperatures. The results also show that nearly 99% of the produced CO* desorbs to gas phase. However, the remaining 1% leads to coke formation.

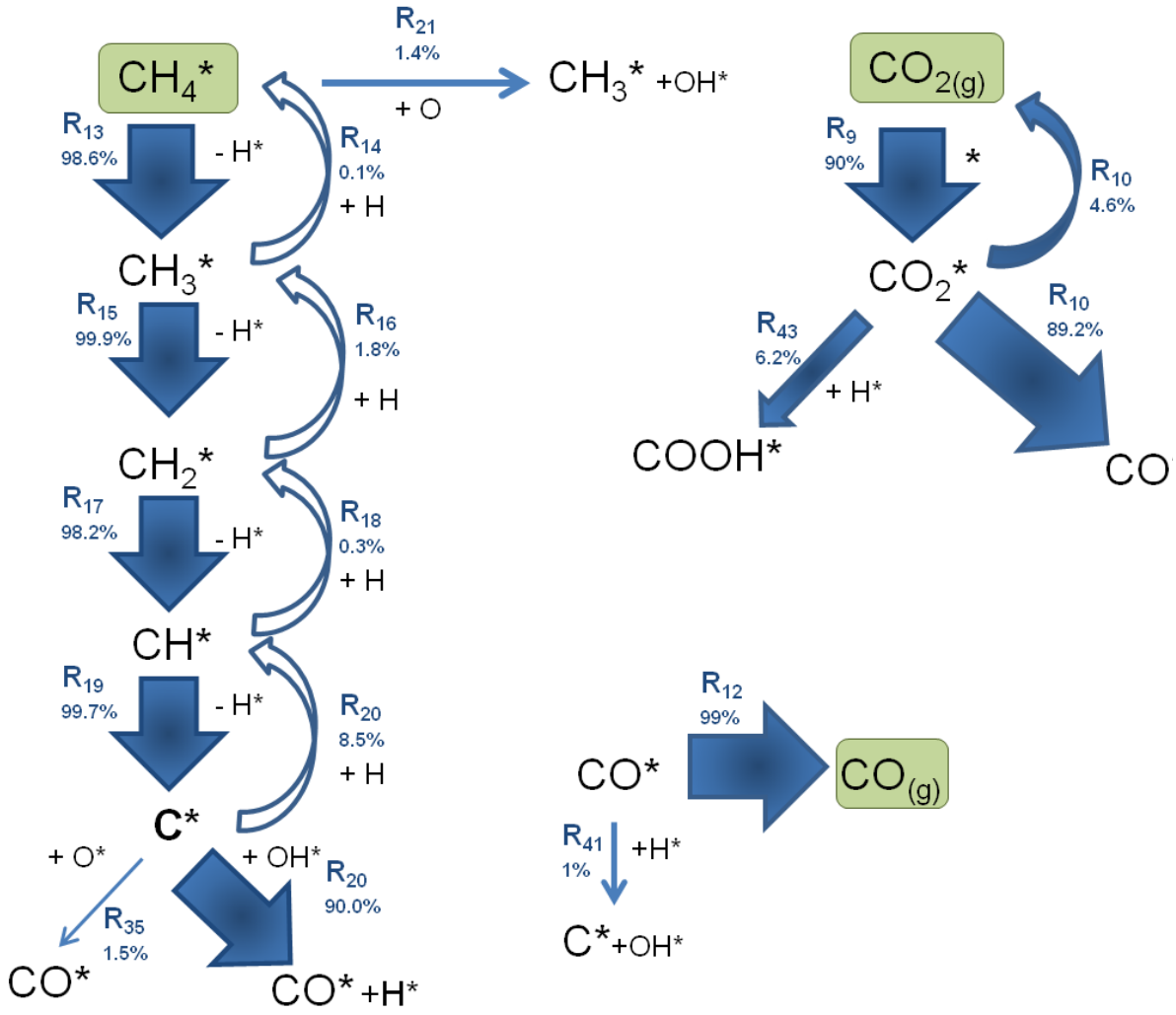

Figure 4.63 *Reaction flow analysis for dry reforming of methane on nickel at 1123 K, 20bar, ratio of CH4/CO_2=1 in 5% Ar dilution.*

4.4.6 Summary

Partial oxidation and reforming of methane over nickel-based catalyst have been experimentally studied in a fixed reactor. The reactions steps of methane activation on nickel from a previous model are used to extend the mechanism for WGS and R-WGS. The combined reaction steps are used to develop a new kinetic model for catalytic partial oxidation and reforming of methane. Kinetic parameters are enhanced based using experimental data here presented and from the literature. The introduction of new reaction paths together with adjustments of the kinetic parameters, make the new mechanism capable to predict conversion and selectivity for partial oxidation and reforming of methane as well as the sub-systems involved in these processes over a wide range of experimental conditions.

The overall thermodynamic consistency of the reactions mechanism is ensured by a numerically approach, in which the surface reaction rate parameters are slightly modified to be thermodynamically consistent.

The mechanism is evaluated against new experimental data at varying operating conditions and reactor configurations, as well experimental results from literature.

The experimental results for synthesis gas production via partial oxidation of methane (CPOX) are consistent with the indirect path, were the total oxidation of methane takes place first producing CO_2 and H_2O, which react with the remaining methane through reforming reactions to produce H_2 and CO.

The overall mechanism performance is also validated for steam and dry reforming of methane. The results show that the current mechanism is able to predict the experimental results for steam reforming despite being adjusted for CPOx and DR. Results for dry reforming show that the model can reproduce conversion and selectivity, which are close to the equilibrium.

The simulation results of methane reforming in the presence of H_2O and H_2 show that both components are good inhibitors of coke deposition at the catalytic surface. However, H_2O present a higher inhibition effect than H_2.

Sensitivity and reaction flow analyses support the mechanism development. The sensitivity analysis for DR, SR and CPOX indicates that the simple dehydrogenation of methane is important for all processes, but for methane partial oxidation, the oxygen assisted dehydrogenation of CH_4 is a preferable rate determining step at 800 °C.

The heterogeneous model is successfully applied at 1 bar; but the application to higher pressures is also possible. The amounts of coke precursors obtained numerically as result of methane

pyrolysis are consistent with the results obtained from experiments performed by project parents from hte AG. The reaction flow analysis at high temperature and pressure for dry reforming of methane indicates that nearly 1% of the CO* produced leads to coke formation. Experimentally measured conversion and selectivity as well as results from the literature are predicted by numerical simulations based on the developed reaction mechanism and appropriate models for mass and heat transport.

5.Kinetic Study of CO Methanation

Formation of methane is detected during the WGS and RWGS experiments presented in Section 4.3. In order to explain such observations, CO methanation is studied experimentally and numerically.

The experiments are carried out at laboratory scale in a fixed bed reactor and in a continuous-flow reactor. The reaction mechanism is a modification of the elementary-step-like thermodynamically consistent reaction mechanism for $CH_4/CO_2/H_2O/CO/H_2/O_2$ systems (Section 4.4). The evaluation of the reaction kinetics is tested with new experimental data.

5.1 Theoretical Background

Nickel-based catalysts are active for water-gas shift reaction (WGS), but not selective. Methanation reactions can also take place during WGS and R-WGS, depending on the conditions [175]. In the methanation reaction, CO (Eq. 5.1) or CO_2 (Eq. 5.2) react with H_2 to produce methane and steam:

$$CO + 3H_2 \leftrightarrow CH_4 + H_2O \qquad \Delta H_{298} = -206.2\ \mathrm{kJ/mol} \qquad (5.1)$$

$$CO_2 + 4H_2 \leftrightarrow CH_4 + 2H_2O \qquad \Delta H_{298} = -165.5\ \mathrm{kJ/mol} \qquad (5.2)$$

The CO methanation is the reverse methane steam reforming reaction, which generally proceeds over nickel catalysts. Therefore, nickel has been investigated as an effective catalyst for CO methanation [243]. The synthesis gas methanation generally takes place at high feed H_2/CO ratio ≥ 3, and in the temperature range of 573- 873 K (300-600 °C) [244]. At temperatures above 450 K, the chemisorbed CO* on nickel dissociated into chemisorbed C* and O* species ($CO^* \rightarrow C^* + O^*$) [245]; at higher temperature 623 K (350 °C), the absorbed carbon (C*) converts to graphite.

The CO methanation reaction has been intensively studied since its discovery by Sabatier and Senderens in 1902 [246]. The reaction is subject of a number of studies due to the renewed interest in industrial applications and it has been proposed as an alternative process to remove carbon monoxide from hydrogen rich syngas (H_2/CO).

During the 1970s it was believed that the methanation reaction proceeds via CH_xO intermediate. However, the experimental results failed to show the presence of such an intermediate. Coenen et al. [247] studied the dynamics of methanation of carbon monoxide on different nickel catalysts. Using $^{13}C^{16}O$ and $^{12}C^{18}O$ together with hydrogen as feed gas, the experimental results did not show isotopic scrambling, suggesting that CO dissociation is the rate-determining step with or without hydrogen assistance.

Alstrup [248] gave a summary of the kinetic models for CO methanation over nickel. The author proposed a micro-kinetic model for CO methanation on nickel, based on CO dissociation and stepwise hydrogenation on surface carbon.

Many kinetic studies have been carried out and several kinetic Langmuir-Hinshelwood (LH) models have been suggested for CO methanation [249-252]. However, the results showed large differences between measured and calculated rates. *Generally, the catalytic performance of a metal-supported catalyst depends on the nature of the metal and support, surface structure and composition, and the physical/chemical interactions between the active metal and support [253]*. The variability of the parameters mentioned above explains why some models cannot accurately reproduce the measured experimental data.

Goodman et al. [254] made the first comparisons between the kinetic behavior of single crystal surfaces and supported Ni catalysts. They found that the turnover frequencies on Ni(111) and Ni(100), as well as on supported Ni catalysts are comparable. In a further work, the authors found that the effective activation energy and the turnover numbers obtained for single crystals are comparable with the methanation rates obtained on alumina supported catalyst [255]. Sehested et al. [243] studied the steady-state CO methanation kinetics over nickel at low CO concentrations and at hydrogen pressures slightly above ambient pressure. The authors proposed the kinetics of the reaction by a first-order expression with CO dissociation at the nickel surface as the rate-determining step.

The objective of this section is the development a reaction model to describe the kinetics of methanation during the WGS and RWGS. The mechanism can be potentially extended for application in CO and CO_2 methanation processes.

*Paragraph taken from reference [253]

5.2 Experimental Procedure

CO methanation reaction is studied in a fixed bed reactor and in a continuous-flow reactor. The experimental conditions for methanation during WGS and RWGS are explained in detail in Section 4.3.2. The fixed bed experiments are carried out using the Fixedbed_Ni_BASF_Cat.2 nickel-based catalyst from BASF; the catalyst pre-treatment is explained in the Section 3.1.2.

The CO methanation reaction is also studied in the continuous-flow reactor using a nickel/alumina-coated monolith as catalyst. The catalyst geometry and pre-treatment are explained in Section 3.3.2.

The operating pressure in both reactors is selected to be 1 bar, with a flow rate of 4 SLPM and reaction temperatures in the range of 373-973 K (100-700 °C). A temperature ramp of 15 K/min is applied.

The Table 5.1 shows the experimental inlet gas composition in nitrogen dilution and the temperature range used for the CO methanation experiment in a continuous-flow reactor.

Table 5.1 Experimental conditions for CO methanation in a continuous-flow reactor

Temperature [K]	CO [vol.%]	H_2 [vol.%]	N_2 [vol.%]
373-973	2.04	7.0	90.96

5.3 Kinetics of CO Methanation

Formation of methane is detected in some of the experiments presented in the Section 4.3 for WGS and RWGS. The proposed thermodynamically consistent reaction mechanism for CH_4/ CO_2/H_2O/CO/O_2/H_2 systems (Section 4.4, Table 4.17) is slightly modified in order to predict the methane formation presented in the experiments of Section 4.3.

It has been reported that the rate of the methanation reaction depends on the previous history of the surface [256]. Kim et.al [174] studied the effect of pretreatment on the activity of nickel catalyst for WGS and methanation. In their experiments the nickel catalyst is pretreated by oxidation and reduction processes. The authors proposed the associative mechanism for WGS reaction on Ni catalyst, water dissociate on the nickel surface providing the initial step $H_2O^* \rightarrow OH^* + H^*$ producing hydroxyl species and atomic hydrogen on the surface. The hydroxyl group

reacts with adsorbed carbon monoxide to form a COOH* intermediate ($CO^* + OH^* \rightarrow COOH^*$) which eventually decomposes into carbon dioxide and hydrogen ($COOH^* \rightarrow CO_2^* + H^*$). The XRD results performed by Kim et al. [174] show the presence of NiO on a pretreated catalyst, which weakens the CO* bond. Before absorbed CO* and OH* reacts, the CO* bond is weakened by the active oxygen on Ni, facilitating the formation of surface carbon intermediates, which can be hydrogenated to produce methane. Grosvenor et at. [257] and Roberts et al. [258] expected that NiO to have an effect on WGS and methanation. Oxygen tends to form OH species on the nickel surface [220, 259] which is proposed to be the active site in the WGS mechanism [187, 189]. However, since absorbed O* species are more reactive than the OH species on the nickel catalyst, the presence of the O* on the surface may promote the methanation reaction during water-gas shift reaction [259]. Weeler et at. [207] concluded that the highest CO conversion over a Ni catalyst also resulted in the undesired promotion of carbon formation which then facilitate the formation of methane.

The dependence of the catalytic activity on the crystal structure may explain the lack of accurate reproducibility of some the experimental results reported [252, 260]. Berkó et al.[256, 261] studied the methanation reaction on nickel single crystal surfaces. The authors demonstrated that the methanation rate on nickel has very high structure sensitivity. Microscopic scale restructuring of the surface is responsible for the increase of the reactivity for methanation on Ni surfaces. Kelly and Semancik [262] deduce from auger electron spectroscopy measurements at 350 °C (623 K), that there is a relationship between the methanation rate and the coverage of carbon at this temperature. Using isotopic transient experiments Biloen et al. [263] conclude that a large carbidic overlayer is developed during the steady-state reaction, but only a small part participates directly in the methanation reaction.

Micro-kinetic modeling grounded on information from surface science studies is relevant to understand and identify important elementary steps during CO methanation. However, the dependence of the history of the sample and the formation of multiple monolayers of carbon, which does not participate directly in the processes, represent a challenge to establishing a micro-kinetic model [248].

* This paragraph has been taken from reference [248].

Alstrup [248] developed a model based on a set of elementary steps, where the concentration of reactive carbon is assumed to be constant, based on the observations and experimental results obtained by some of the above-mentioned authors [158, 254, 264]. In Alstrup´s model, the rate-controlling step is the hydrogenation of surface methylidyne (CH*), and the coverage of reactive carbon (θc) is treated as a constant parameter independent of the reaction conditions. Alstrup´s [248] approximations seem to have good agreement with the methanation rates measured on Ni(100) by Goodman et al. [254] and on nickel policristaline foils by Polizzotti and Schwarz [264]. Both experimental studies are carried out in batch reactors at different inlet gas compositions and working conditions.

In this work, the previous reaction mechanism developed for $CH_4/CO_2/H_2O/CO/O_2/H_2$ systems (Table 4.17) is slightly modified to fit the experimental results. These modifications are based on the literature results discussed above, especially the results reported by Alstrup [248], and by comparison with the experimental results here presented.

Carbon coverage dependency is included as parameter in the reaction R20 ($C^* + H^* \rightarrow CH^* + *$), which is believed to be the rate determining step of the methanation reaction based on the sensitivity analyses (Figure 5.1 and Figure 5.3). A reduced activation energy of 120kJ/mol ($\theta_{C(Ni)}$) in case of carbon coverage is estimated for R20 ($C^* + H^* \rightarrow CH^* + *$) on the basis of the fixed bed and the continuous-flow reactor experimental data and from literature information [90]. The pre-exponential factor in reaction R42 is decreased to $3.888x10^{+23}$ in order to get consistency with the experimental results performed in this study. Due to these modifications the reaction mechanism presented in Table 5.2 is not thermodynamically consistent.

Table 5.2 Surface reaction mechanism for CO methanation over nickel-based catalyst.

	REACTION	A/[cm, mol, s]/S_0[-]	β [-]	E_a/[kJ/mol]	ε_1 [kJ/mol]
R1	H_2 + (Ni) + (Ni) → H(Ni) + H(Ni)	$3.000 \cdot 10^{-02}$	0.000	5.00	
R2	H(Ni) + H(Ni) → Ni(Ni) + Ni(Ni) + H_2	$2.544 \cdot 10^{+20}$	0.000	95.21	
R3	O_2 + (Ni) + (Ni) → O(Ni) + O(Ni)	$4.358 \cdot 10^{-02}$	-0.206	1.51	
R4	O(Ni) + O(Ni) → (Ni) + (Ni) + O_2	$1.188 \cdot 10^{+21}$	0.823	468.91	
R5	CH_4 + (Ni) → CH_4(Ni)	$8.000 \cdot 10^{-03}$	0.000	0.00	
R6	CH_4(Ni) → CH_4 + Ni(Ni)	$8.705 \cdot 10^{+15}$	0.000	37.55	
R7	H_2O + (Ni) → H_2O(Ni)	$1.000 \cdot 10^{-01}$	0.000	0.00	
R8	H_2O(Ni) → H_2O + (Ni)	$3.732 \cdot 10^{+12}$	0.000	60.79	
R9	CO_2 + (Ni) → CO_2(Ni)	$7.001 \cdot 10^{-06}$	0.000	0.00	
R10	CO_2(Ni) → CO_2 + (Ni)	$6.442 \cdot 10^{+07}$	0.000	25.98	
R11	CO + (Ni) → CO(Ni)	$5.000 \cdot 10^{-01}$	0.000	0.00	
R12	CO(Ni) → CO + (Ni)	$3.566 \cdot 10^{+11}$	0.000	111.27	-50.0 $\theta_{CO(Ni)}$
R13	CH_4(Ni) + (Ni) → CH_3(Ni) + H(Ni)	$1.548 \cdot 10^{+21}$	0.087	55.83	
R14	CH_3(Ni) + H(Ni) → CH_4(Ni) + (Ni)	$1.443 \cdot 10^{+22}$	-0.087	63.45	
R15	CH_3(Ni) + (Ni) → CH_2(Ni) + H(Ni)	$1.548 \cdot 10^{+24}$	0.087	98.12	
R16	CH_2(Ni) + H(Ni) → CH_3(Ni) + (Ni)	$3.091 \cdot 10^{+23}$	-0.087	57.21	
R17	CH_2(Ni) + (Ni) → CH(Ni) + H(Ni)	$3.700 \cdot 10^{+24}$	0.087	95.23	
R18	CH(Ni) + H(Ni) → CH_2(Ni) + (Ni)	$9.774 \cdot 10^{+24}$	-0.087	81.05	
R19	CH(s) + (Ni) → C(Ni) + H(Ni)	$9.888 \cdot 10^{+20}$	0.500	21.99	
R20	C(Ni) + H(Ni) → CH(Ni) + (Ni)	$1.707 \cdot 10^{+24}$	-0.500	157.92	**-120.0 $\theta_{C(Ni)}$**
R21	CH_4(Ni) + O(Ni) → CH_3(Ni) + OH(Ni)	$5.621 \cdot 10^{+24}$	-0.101	92.72	
R22	CH_3(Ni) + OH(Ni) → CH_4(Ni) + O(Ni)	$2.987 \cdot 10^{+22}$	0.101	25.80	
R23	CH_3(Ni) + O(Ni) → CH_2(Ni) + OH(Ni)	$1.223 \cdot 10^{+25}$	-0.101	134.67	
R24	CH_2(Ni) + OH(Ni) → CH_3(Ni) + O(Ni)	$1.393 \cdot 10^{+21}$	0.101	19.05	
R25	CH_2(Ni) + O(Ni) → CH(Ni) + OH(Ni)	$1.223 \cdot 10^{+25}$	-0.101	131.37	
R26	CH(Ni) + OH(Ni) → CH_2(Ni) + O(Ni)	$4.407 \cdot 10^{+22}$	0.101	42.45	
R27	CH(Ni) + O(Ni) → C(Ni) + OH(Ni)	$2.471 \cdot 10^{+21}$	0.312	57.74	
R28	C(Ni) + OH(Ni) → CH(Ni) + O(Ni)	$2.433 \cdot 10^{+21}$	-0.312	118.97	
R29	H(Ni) + O(Ni) → OH(Ni) + (Ni)	$3.951 \cdot 10^{+23}$	-0.188	104.35	
R30	OH(Ni) + (Ni) → H(Ni) + O(Ni)	$2.254 \cdot 10^{+20}$	0.188	29.64	
R31	H(Ni) + OH(Ni) → H_2O(Ni) + (Ni)	$1.854 \cdot 10^{+20}$	0.086	41.52	
R32	H_2O(Ni) + (Ni) → H(Ni) + OH(Ni)	$3.674 \cdot 10^{+21}$	-0.086	92.94	
R33	OH(Ni) + OH(Ni) → H_2O(Ni) + O(Ni)	$2.346 \cdot 10^{+20}$	0.274	92.37	
R34	H_2O(Ni) + O(Ni) → OH(Ni) + OH(Ni)	$8.148 \cdot 10^{+24}$	-0.274	218.49	

R35	C(Ni) + O(Ni) → CO(Ni) + (Ni)	$3.402 \cdot 10^{+23}$	0.000	148.10	
R36	CO(Ni) + (Ni) → C(Ni) + O(Ni)	$1.758 \cdot 10^{+13}$	0.000	116.24	-50.0 $\theta_{CO(Ni)}$
R37	CO(Ni) + CO(Ni) → C(Ni) + CO_2(Ni)	$1.624 \cdot 10^{+14}$	0.500	241.76	-100.0 $\theta_{CO(Ni)}$
R38	CO_2(Ni) + C(Ni) → CO(Ni) + CO(Ni)	$7.294 \cdot 10^{+28}$	-0.500	239.24	
R39	CO(Ni) + O(Ni) → CO_2(Ni) + (Ni)	$2.000 \cdot 10^{+19}$	0.000	123.60	-50.0 $\theta_{CO(Ni)}$
R40	CO_2(Ni) + (Ni) → CO(Ni) + O(Ni)	$4.648 \cdot 10^{+23}$	-1.000	89.32	
R41	CO(Ni) + H(Ni) → C(Ni) + OH(Ni)	$3.522 \cdot 10^{+18}$	-0.188	105.45	-50.0 $\theta_{CO(Ni)}$
R42	C(Ni) + OH(Ni) → H(Ni) + CO(Ni)	**$3.888 \cdot 10^{+23}$**	0.188	62.55	
R43	CO_2(Ni) + H(Ni) → COOH(Ni) + (Ni)	$6.250 \cdot 10^{+24}$	-0.475	117.24	
R44	COOH(Ni) + (Ni) → CO_2(Ni) + H(Ni)	$3.737 \cdot 10^{+20}$	0.475	33.66	
R45	COOH(Ni) + (Ni) → CO(Ni) + OH(Ni)	$1.461 \cdot 10^{+24}$	-0.213	54.37	
R46	CO(Ni) + OH(Ni) → COOH(Ni) + (Ni)	$6.003 \cdot 10^{+21}$	0.213	97.63	-50.0 $\theta_{CO(Ni)}$
R47	CO(Ni) + H(Ni) → HCO(Ni) + (Ni)	$4.009 \cdot 10^{+20}$	-1.000	132.23	
R48	HCO(Ni) + (Ni) → CO(Ni) + H(Ni)	$3.710 \cdot 10^{+21}$	0.000	0.00	+50.0 $\theta_{CO(Ni)}$
R49	HCO(Ni) + (Ni) → CH(Ni) + O(Ni)	$3.796 \cdot 10^{+14}$	0.000	81.91	
R50	CH(Ni) + O(Ni) → HCO(Ni) + (Ni)	$4.599 \cdot 10^{+20}$	0.000	109.97	
R51	H(Ni) + COOH(Ni) → HCO(Ni) + OH(Ni)	$6.000 \cdot 10^{+22}$	-1.163	104.88	
R52	HCO(Ni) + OH (Ni) → COOH(Ni) + H(Ni)	$2.282 \cdot 10^{+20}$	0.263	15.92	

The rate coefficients are given in the form of $k=AT^{\beta}\exp(-E_a/RT)$; adsorption kinetics is given in form of sticking coefficients; the surface site density of Γ=2.66 x 10^{-9} mol cm^{-2} is calculated by assuming a site area of 6.5x10^{-2} nm^2 as observed for nickel [58, 119].

5.4 Results and Discussion

Formation of methane during WGS and R-WGS as well as CO methanation have been studied in a fixed bed and continuous-flow reactor (Section 4.3). The experiments are carried out using the powdered catalyst from BASF (Section 3.1.2) and a nickel/alumina-coated monolith (Section 3.3.2). The modified micro-kinetic model is validated by comparison of the experimental data and numerical results predicted.

Results for Water Gas-Shift Reaction (WGS)

Sensitivity analysis of the reaction mechanism is performed for R-WGS reaction at 1 bar and four different temperatures: 573 K, 673 K, 773 K, and 873 K, with an inlet gas composition of 3.6 vol.% CO, 4.3 vol.% H_2O in nitrogen dilution. The sensitivity coefficients for CH_4 mole fraction at different temperatures are presented in Figure 5.1.

From Figure 5.1, it can be seen that the gas-phase methane concentration is sensitive to the reaction R20 (Table 5.2) for all temperatures studied, in this reaction surface carbon reacts with hydrogen to produce the methylidyne species (CH*). The analysis also shows that hydrogenation of surface methylidyne to CH_2* is also a sensitive step (R18, Table 5.2), which is consistent with the model presented by Alstrup [248] that assumes this reaction as the rate–controlling step.

In the proposed mechanism presented in this study, the main path to produce carbon on the surface is through hydrogen-assisted CO dissociation R41($CO^* + H^* \rightarrow C^* + OH^*$) and not by CO dissociation ($CO^* \rightarrow C^* + O^*$), as is suggested by some authors [265, 266]. Hydrogen-assisted CO dissociation reaction is supported by Van Ho and Harriott [251]. They proposed a model where the rate limiting step (RLS) may be the surface reaction between adsorbed carbon monoxide and hydrogen atoms to form carbon and water this model is in agreement the experimental data.

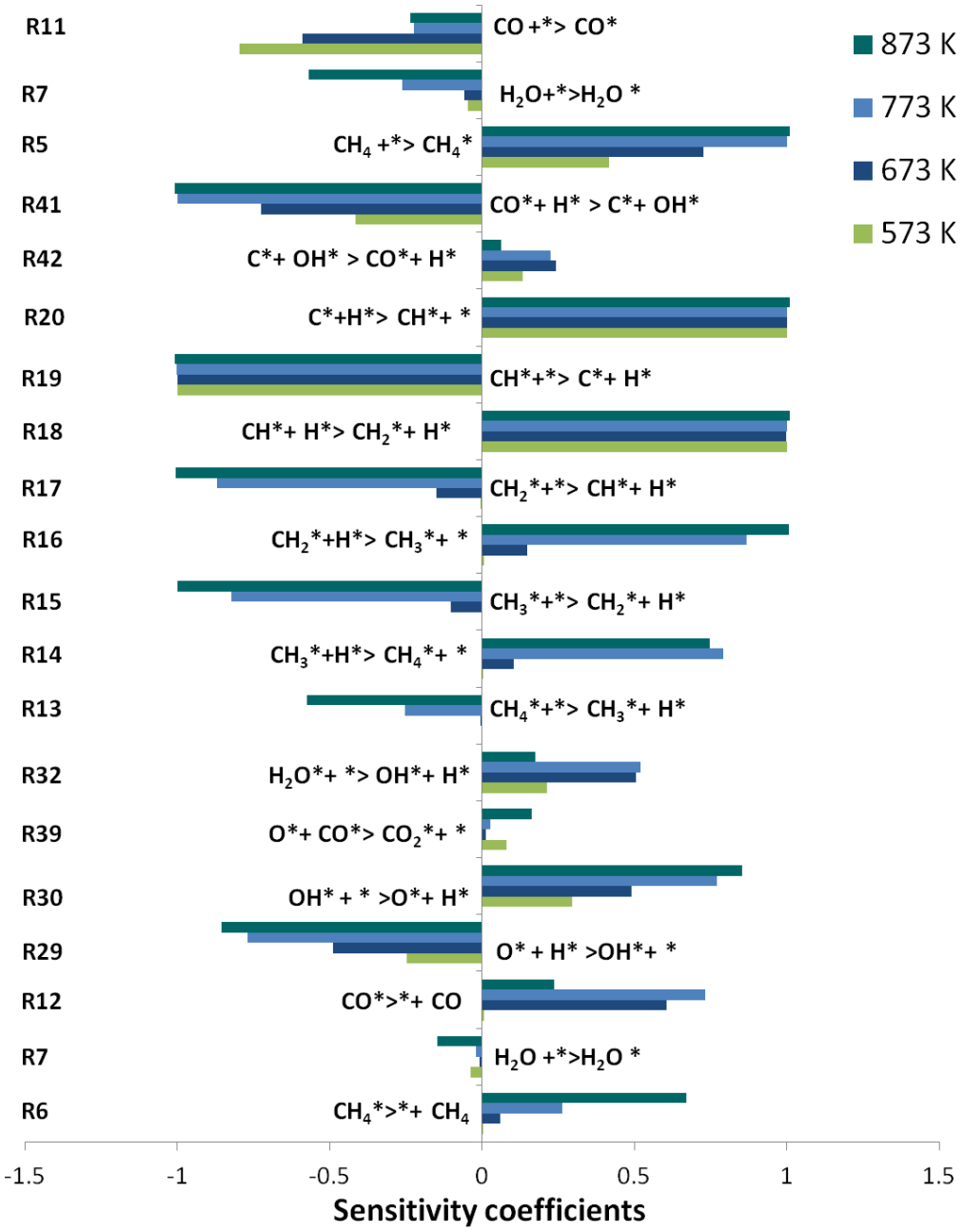

Figure 5.1 *Sensitivity analysis of CH_4 gas-phase concentration for WGS reaction at different temperature points. Inlet gas composition is chose to be 3.6 vol.% CO, 4.3 vol.% H_2O in N_2 dilution; 4 SLPM; at 1bar.*

The WGS reaction study is carried out in a fixed bed reactor, with an inlet gas composition of 3.6 vol.% CO and 4.3 vol% H_2O in nitrogen dilution, at 1bar, total flow rate of 4 SLPM, and a temperature range from 373 K to 1073 K (100-800 °C). More information about the experiment can be found in Section 4.3.

Figure 5.2 shows a comparison of the measured and predicted concentration profiles as function of the temperature. An active catalytic surface area of $3.10x10^6$ m^{-1} is used for the simulation. It can be observed that the modified kinetic model (Table 5.2) predicts with good agreement the experimental results of reactants and products, including methane formation. The produced methane is consumed at high temperatures via reforming reactions.

a)

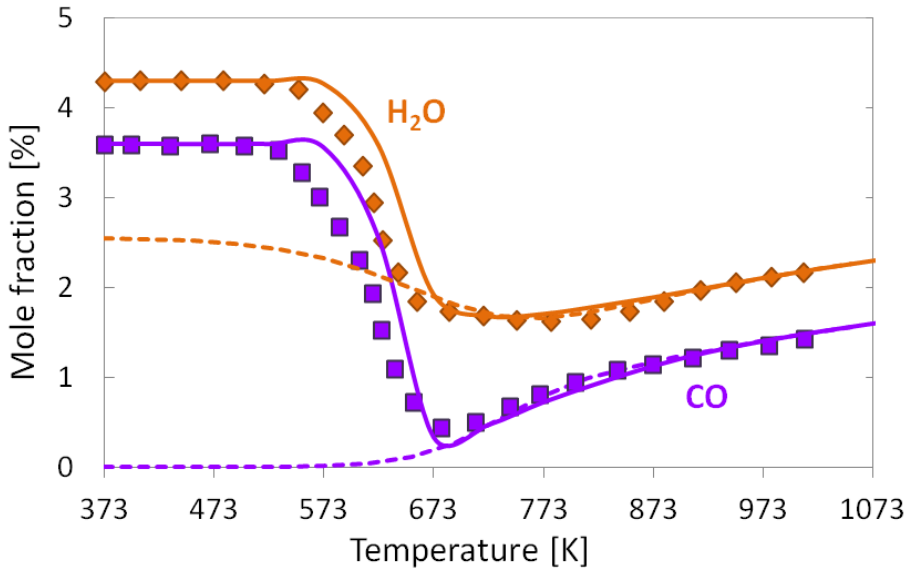

Figure 5.2 *Comparison of experimentally determined (symbols) and numerically predicted (lines) mole fractions as a function of temperature for WGS in a fixed bed reactor:* ***a)*** *CO and H_2O;* ***b)*** *CO_2, H_2, and CH_4, inlet gas composition of 3.6 vol.% CO, 4.3 vol. % H_2O in N_2; 1 bar; T_{inlet}= 373 K; 4 SLPM; dashed lines = equilibrium composition at given temperature.*

b)

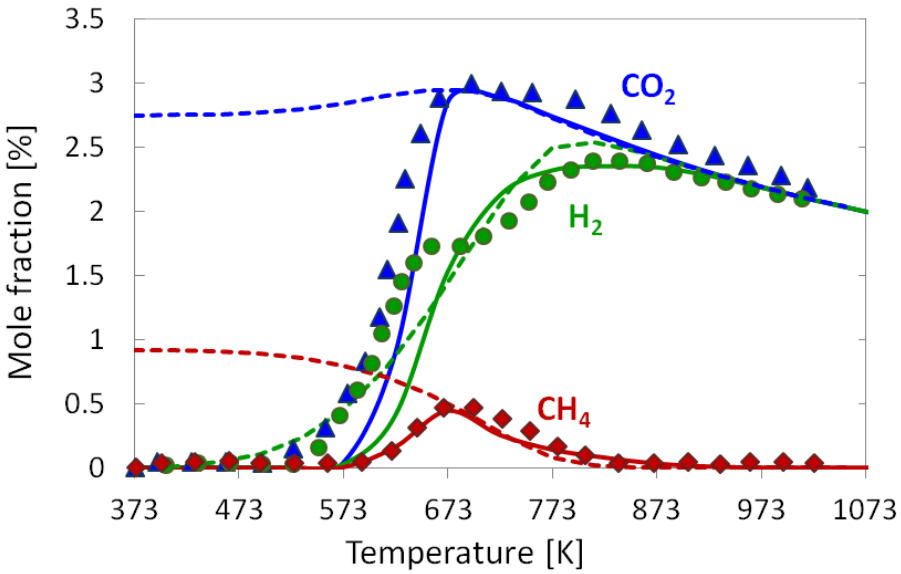

c)

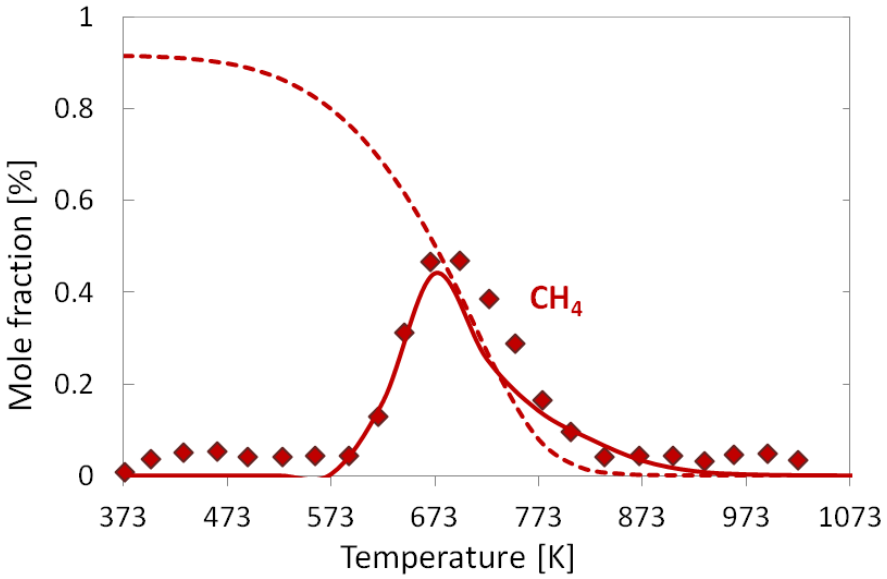

Figure 5.2: Continued

Results for Reverse Water-Gas Shift Reaction (R-WGS)

Sensitivity analysis of the reaction mechanism is performed for R-WGS reaction at 1 bar and four different temperatures: 573 K, 673 K, 773 K, and 873 K, with an inlet gas composition of 4.0 vol.% CO_2 and 5.1 vol.% H_2 in nitrogen dilution.

Figure 5.3 shows the normalized sensitivity coefficients for CH_4 mole fractions at the selected temperatures. The sensitivity analysis shows that at high temperature the main carbon source is CO*, which is formed by the CO_2 dissociation (R40, Table 5.2) and through the carboxyl (COOH*) intermediate (R45, Table 5.2). It can also be observed that formation of methylidyne species (CH*), followed by the formation of the CH_2* are highly sensitive reactions for all studied temperatures, which agree to the results presented in Figure 5.1 for methane formation during water-gas shift reaction. Figure 5.3 also indicates, that the oxygen on the surface coming from CO_2 dissociation reacts with hydrogen (R29, Table 5.2) to produce hydroxyl species (OH)*, which further react with the methyl species (CH_3*) to produce methane on the surface.

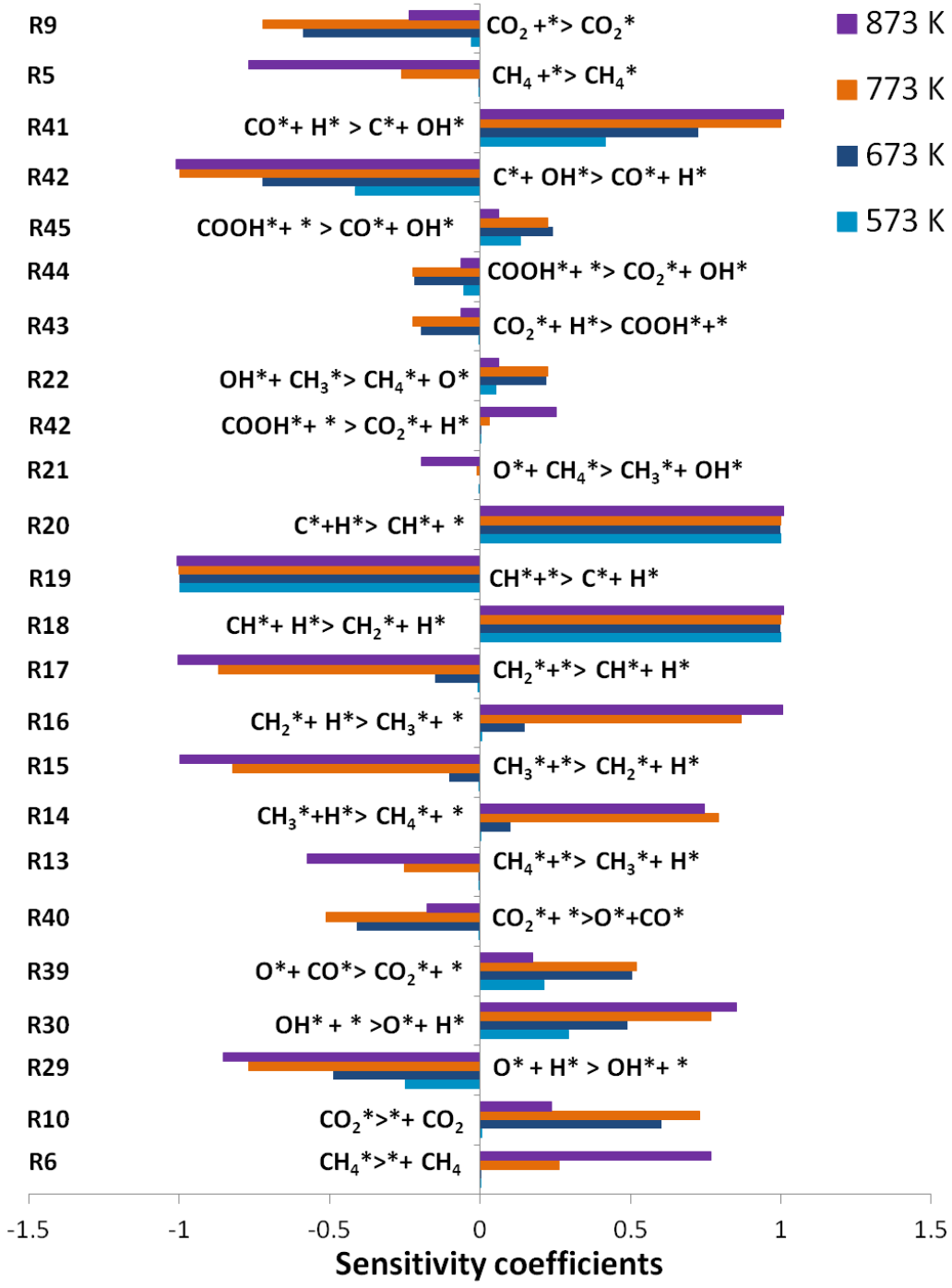

Figure 5.3 *Sensitivity analysis of CH_4 gas-phase concentration for R-WGS reaction at different temperature points. Inlet mole composition is chose to be 4.0 vol.% CO_2, 5.1 vol.% H_2O in N_2 dilution, at 1 bar.*

The R-WGS reaction experiment is carried out in a fixed bed reactor at 1 bar, total flow of 4 SLPM, in a temperature range between 373-1073 K (100-900 °C), with a inlet gas composition of 4.0 vol.% CO_2 and 5.1 vol. % H_2 in nitrogen dilution (Section 4.3). An active catalytic surface area of $3.10x10^6$ m^{-1} is used for the simulation.

Figure 5.4 shows the comparison of the experimental measured and numerical simulated concentrations of CO_2, CO, H_2, H_2O, and CH_4 during R-WGS reaction at the reactor outlet at different temperatures. It can be observed that the numerical predications based on the kinetic modified model are in accordance with the experimental data in the range of temperatures. The experimental formation of methane at temperatures between 523-823 K (250-550 °C) is also predicted by the kinetic model presented in Table 5.2.

a)

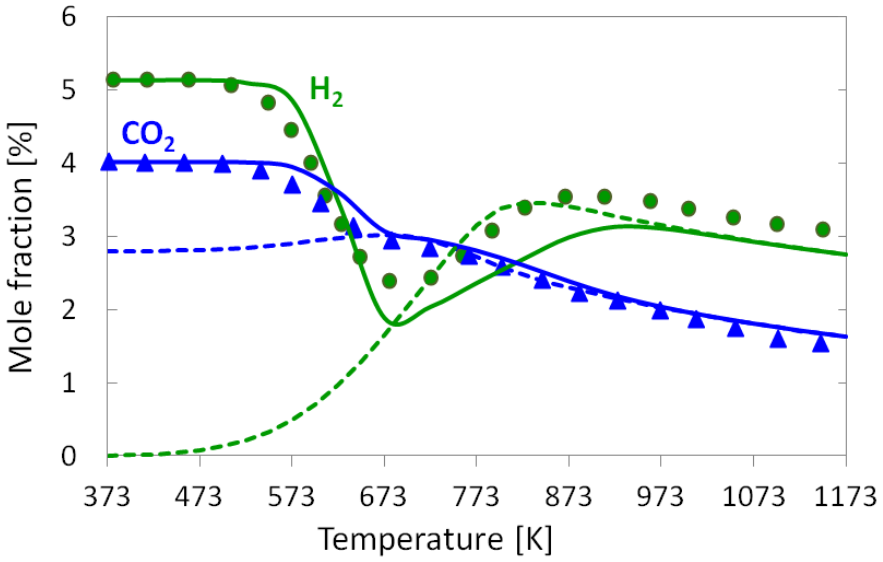

Figure 5.4 *Comparison of experimentally determined (symbols) and numerically predicted (lines) mole fractions as a function of temperature for R-WGS in a fixed bed reactor:* ***a)*** *CO_2 and H_2;* ***b)*** *CO, H_2O, and CH_4,* ***c)*** *CH_4 formation; inlet gas composition of 4.0 vol% CO_2 and 5.1 vol% H_2 in N_2 dilution; 1bar; T_{inlet}=373 K; total flow rate of 4SLPM; dashed lines =equilibrium composition at given temperature.*

b)

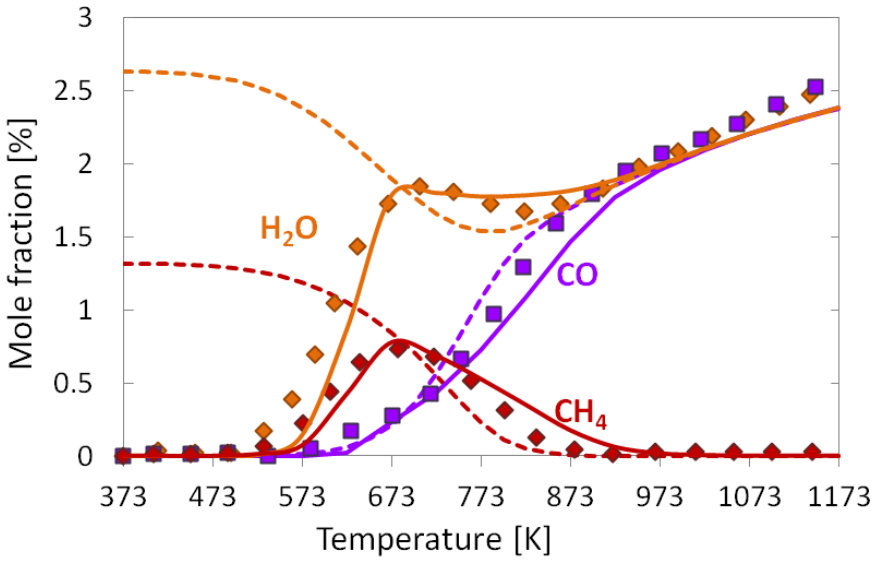

c)

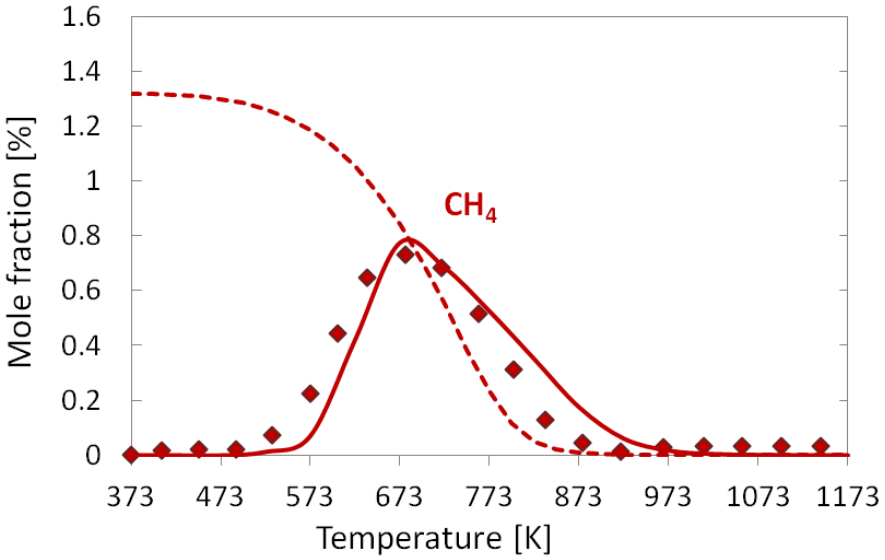

Figure 5.4: Continued

The R-WGS reaction is also studied in a continuous-flow reactor at 1bar, 4 SLPM (0.5138 m/s), in a temperature range between 373-973 K (100-700 °C), with an inlet gas composition of 4.0 vol.% CO_2 and 5.1 vol.% H_2 in nitrogen dilution. Detailed information about the experimental conditions can be found in Section 4.3. An effective $F_{cat\ /geo}$ value of 150 is used for the simulation. Figure 5.5 shows the comparison of the experimental results and the predicted mole fraction of reactants and products as function of the temperature. The current model is able to predict the experimental data in the range of temperatures, including the formation of methane and its consumption through reforming reactions at high temperatures.

a)

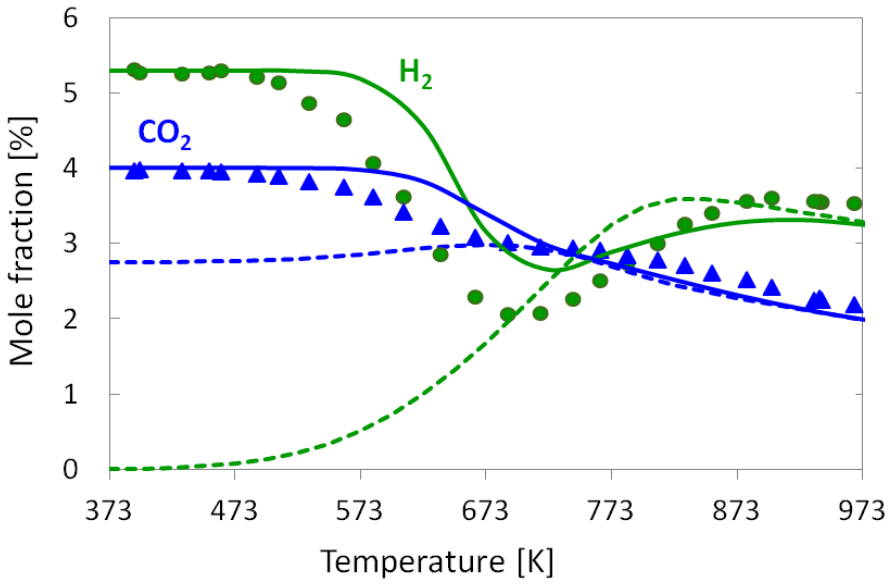

Figure 5.5 *Comparison of experimentally determined (symbols) and numerically predicted (lines) mole fractions as a function of temperature for R-WGS in a continuous-flow reactor:* ***a)*** *CO_2 and H_2;* ***b)*** *CO, H_2O, and CH_4,* ***c)*** *CH_4 formation; inlet gas composition of 4.0 vol.% CO_2 and 5.3 vol.% H_2 in N_2 dilution; 1 bar; T_{inlet}= 373 K, total flow rate of 4 SLPM, dashed lines = equilibrium composition at given temperature.*

b)

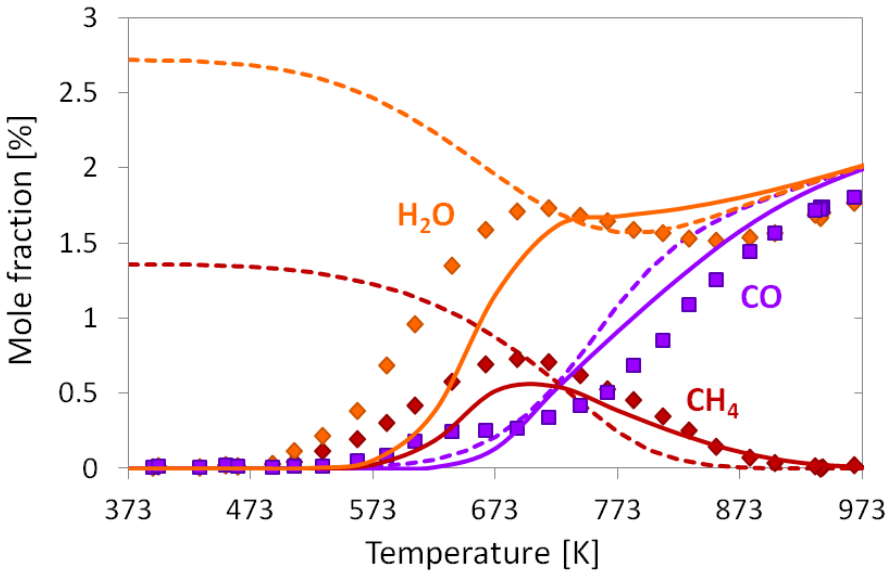

c)

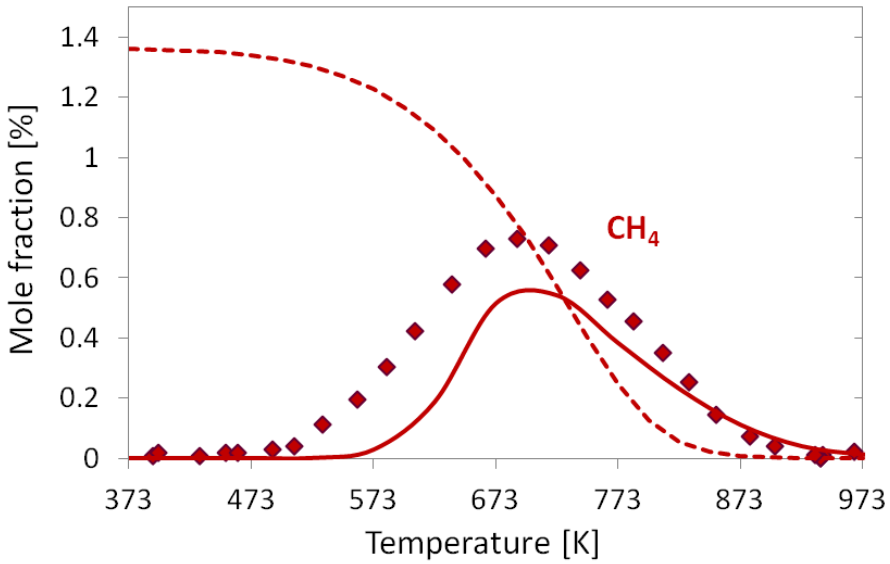

Figure 5.5: Continued

Results for CO methanation (CO/H_2)

It has been shown that the modified mechanism presented in Table 5.2 is able to reproduce the formation of methane during WGS and R-WGS reactions. In order to further evaluate the applicability of the heterogeneous surface model developed, CO methanation results conducted in a continuous-flow reactor are also modeled.

The CO methanation reaction is studied using a monolith catalysts (Section 3.3.2). The experiment is carried out at 1bar, 4 SLPM which corresponds to a linear flow velocity of 0.5138 m/s, in a temperature range from 373 K to 973 K, with an inlet gas composition of 2.04 vol.% CO and 7.0 vol.% H_2 in nitrogen dilution.

A reaction flow analysis of the kinetic model is performed for CO methanation at 673 K (400 °C). Figure 5.6 shows the main path for CO consumption and methane production within the catalytic cycle. It can be observed that carbon is mainly produced by the reaction between CO* and H* (R41, Table 5.2), however, this path is not unique for these conditions, as absorbed CO* can also dissociate on the surface to produce C* and O*. The absorbed carbon reacts with H* to produce the methylidyne (CH*) species, which is considered the rate-determine step in this model.

These results are in agreement with the work presented by Coenen et al. [267], who extensively studied the methanation reaction and evaluated several mechanisms. They found an excellent description by a model in which CH_x hydrogenation is assumed to be the rate-limiting step (RLS).

As it was suggested by Mills et al. [249, 268], the methanation process can also proceed through a CH_xO intermediate. However, IR studies at reaction conditions failed to show the presence of this intermediate. Anderson et al. [269] studied of the dissociation mechanism of CO on Ni surfaces by combined extensive density functional theory calculations, ultra-high vacuum experiments on well-defined single crystals, and catalytic activity measurements on supported catalysts. The authors considered an additional type of mechanism in which the transition stated for CO dissociation is stabilized by hydrogen, forming intermediates (HCO and COH).

The mechanism presented in this work, also considers the formation of CH* through HCO intermediate. However, just 0.5% of CO is converted to HCO*, which is a very low percentage in comparison with the reactions R41 and R36 (Table 5.2).

Once the methylidyne has been produced, the hydrogenation takes place and produces CH_4*, which further desorbs to the gas-phase.

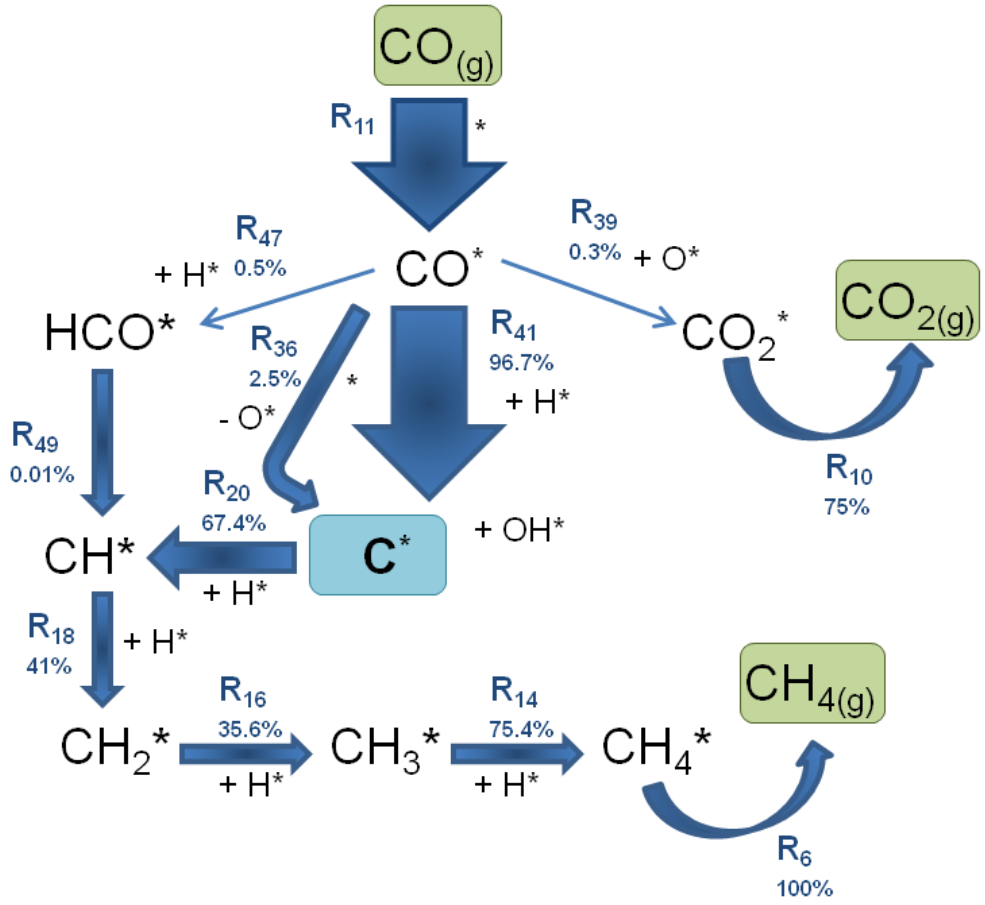

Figure 5.6 *Reaction flow analysis for CO methanation on nickel at 673K (400°C), 1bar, with an inlet mole composition of 2.0.vol% CO and 7.0.vol % H_2 in N_2 dilution.*

Figure 5.7 shows the experimental results in comparison with the numerical predictions for CO methanation on a nickel-based catalyst as function of the temperature.

At the experimental working conditions presented here, the catalyst suffered severe coke formation, which explains the differences between the numerical profiles and the experimental results in Figure 5.7b. It can be observed that water formation is over-predicted. Nevertheless, the model can match the measured trends of all gas-phase species involved. The surface reaction mechanism proposed in this study is only able to describe the formation of one carbon monolayer, but not the transient carbon deposition on the surface in form of carbon film with different morphology, which is a limitation of the model.

a)

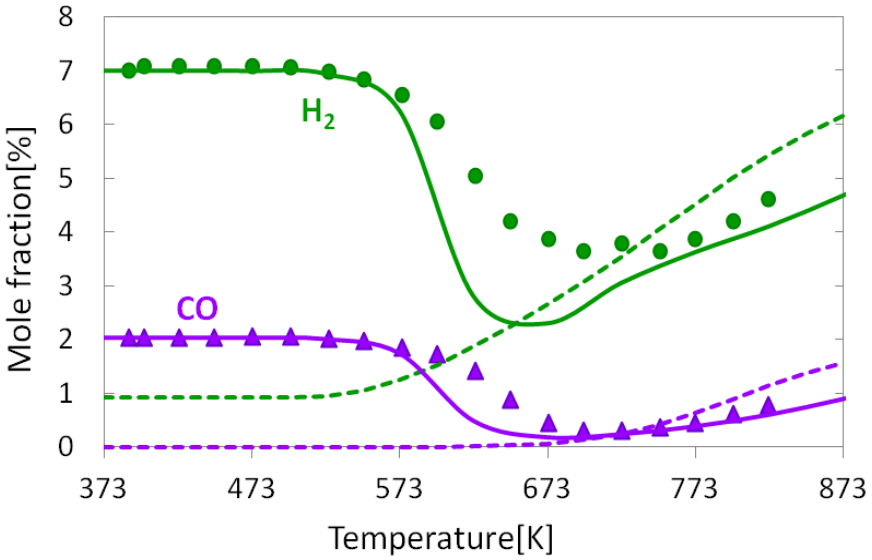

b)

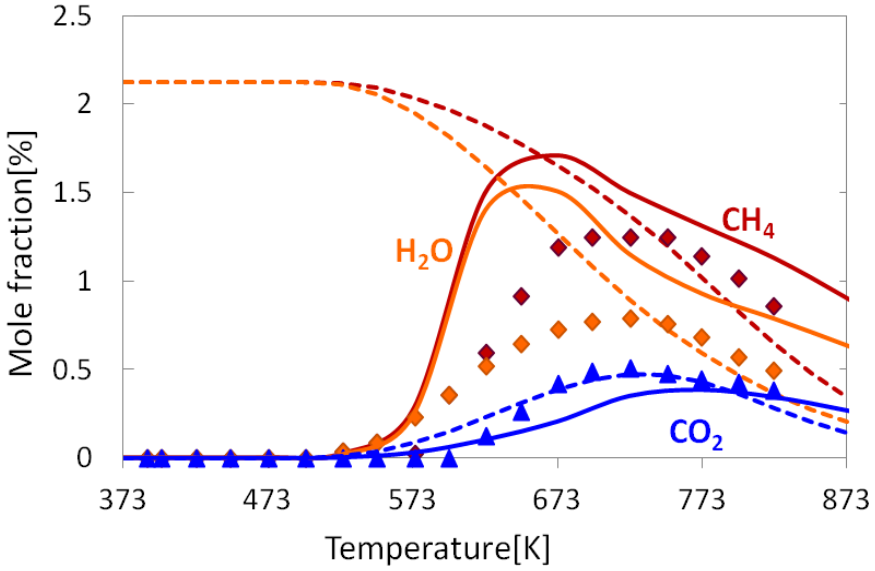

Figure 5.7 *Comparison of experimentally determined (symbols) and numerically predicted (lines) mole fractions as function of temperature for CO methanation:* ***a)*** *CO and H_2;* ***b)*** *CO_2, CH_4, and H_2O; inlet gas composition of = 2.04 vol.% CO and 7.0 vol.% H_2 in N_2 dilution; 1bar; T_{inlet}=373 K; total flow rate of 4 SLPM; dashed lines =equilibrium composition at given temperature.*

Figure 5.8 shows the numerical surface coverage of the absorbed species as function of the temperature for CO methanation. It can be observed that at low temperatures the surface is mainly covered by CO* and C*. As the temperature increase, carbon is gasified with hydrogen producing methane. Nakano et al. [270] studied the dissociation of CO on several stepped Ni(111) using scanning tunneling microscopy (STM); they found that CO dissociated readily at 400 K (127 °C), which explains the high carbon coverage at low temperatures indicated in Figure 5.8.

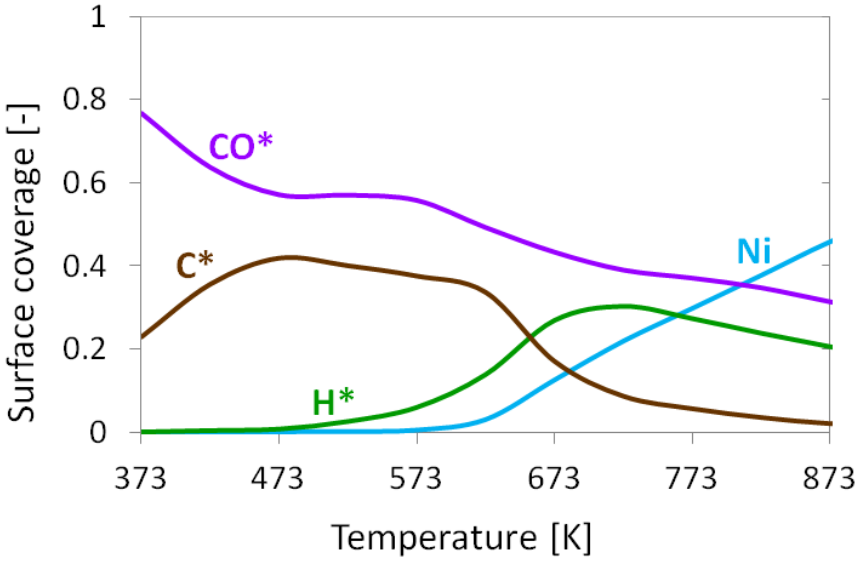

Figure 5.8 *Computed surface coverage of adsorbed species as function of the temperature for CO methanation at 1 bar, inlet gas composition of 2.04 vol.% CO and 7.0 vol.% H_2 in N_2 dilution; 1bar; T_{inlet}=373 K; total flow rate of 4 SLPM.*

The deactivation of the catalyst during CO methanation is explained by Pedersen and Rostrup-Nielsen [271]. At high CO partial pressures and low temperatures (below 503 K), there is a high risk that carbon monoxide reacts with nickel, forming nickel carbonyl [$Ni(CO)_4$]. The formation of nickel carbonyl results in a drastic growth of the nickel crystals, which then resulted in a breakdown of the catalyst [271]. Shen et al. [272] also found that Ni/Al_2O_3 methanation catalysts deactivate rapidly during methanation at high partial pressures of CO (>20 kPa) and temperatures below 698 K (425 °C) due to [$Ni(CO)_4$] formation.

Nickel tetracarbonyl [$Ni(CO)_4$] is usually produced at low temperatures and it has a great effect on the surface reactivity [273]. Goodmann et al. [274, 275], suggested that the measured rate depends on a delicate balance between carbide formation and carbide hydrogenation on the surface. Bartholomew [276] proposed different paths for coke formation from CO on a supported metal catalyst (Figure 5.9). The author describes different kinds of carbon and coke

which vary in morphology and reactivity, and which are formed in these reactions. For example, CO dissociates on metals to form C_α (473-673 K), an adsorbed atomic carbon; C_α can react to C_β (523-773 K), a polymeric carbon film. The more reactive, amorphous forms of carbons formed at low temperatures (e.g. C_α and C_β) are converted at high temperatures over a period of time to less reactive, graphitic forms such as carbon whiskers (C_v, 573–1273 K) and graphitic carbon (C_c, 773–823 K) [276, 277].

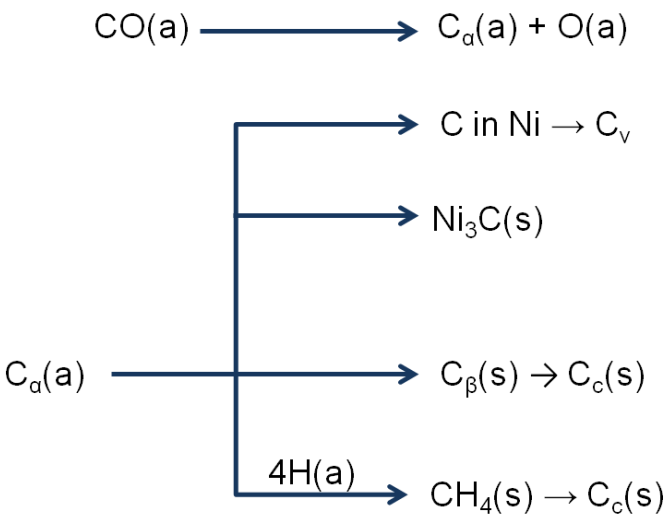

Figure 5.9 *Formation, transformation and gasification of carbon on nickel, as proposed by Bartholomew (a, g, s refer to adsorbed, gaseous and solid states, respectively) [276].*

The loss of the catalytic activity is inevitable, but if the processes is well-controlled this lost occurs slowly [276]. Agnelli et al. [278] investigated kinetics of sintering due to formation and migration of nickel carbonyl species. The authors proposed two solutions for reducing catalyst deactivation: (i) increasing reaction temperature and decreasing CO partial pressure in order to lower the rate of carbonyl formation, and (ii) changing catalyst composition, e.g., alloying nickel with copper or adding alkali to inhibit carbonyl species migration.

Future work will focus on the implementation of a coking model into the surface reaction scheme, to describe transient carbon formation on the surface.

5.5 Test of the Reaction Kinetics

The reaction mechanism presented in Table 5.2 is also tested, by simulating the methanation experiment performed in cooperation with Verein des Gas- und Wasserfaches e.V (DVGW) test laboratory at the Engler-Bunte-Institut of the KIT.

A manufactured Ni/Al_2O_3 metal monolith (200 channels per square inch (cpsi), length = 100 mm, and a diameter of 33mm) is positioned inside a flow reactor. The reaction is studied in a range of temperatures from 503 K to 573 K (230-300 °C), at 1.8 bar.

The residence time is defined in terms of mass of catalyst over CO inlet molar rate and is called modified residence time (τ_{mod}).

$$\tau_{mod} = \frac{m_{cat}}{\dot{N}co, in} \tag{5.3}$$

The volumetric flow rate is set in the mass flow controllers (MFC) according to $\tau_{mod} = 76$ kg*s/mol, which corresponds to a linear flow velocity of 0.0134m/s at 453 K (180 °C). Inlet gas composition is presented in Table 5.3; such mixture is selected due to its similarity with biogas composition. An $F_{cat/geo}$ value of 195 is used for the simulation. More details about the experimental conditions and reactor configuration can be found elsewhere [279].

Table 5.3 Experimental inlet mole fractions for CO methanation reaction.

H_2 [vol.%]	O_2 [vol.%]	N_2 [vol.%]	CH_4 [vol.%]	CO [vol.%]	CO_2 [vol.%]
35.52	0.0059	30.32	4.06	11.75	17.56

The numerical and experimental results are presented in Figure 5.10. It can be observed that the conversion of syngas increases with the temperature, reaching complete CO conversion at temperatures above 533 K (260 °C). The model predicts the experimental data well over a wide range of temperatures. At temperatures above 563 K (290 °C), all species in the experimental data and the model reach the equilibrium at the given conditions. Under the operating conditions in this experiment the formation of nickel carbonyl is not expected.

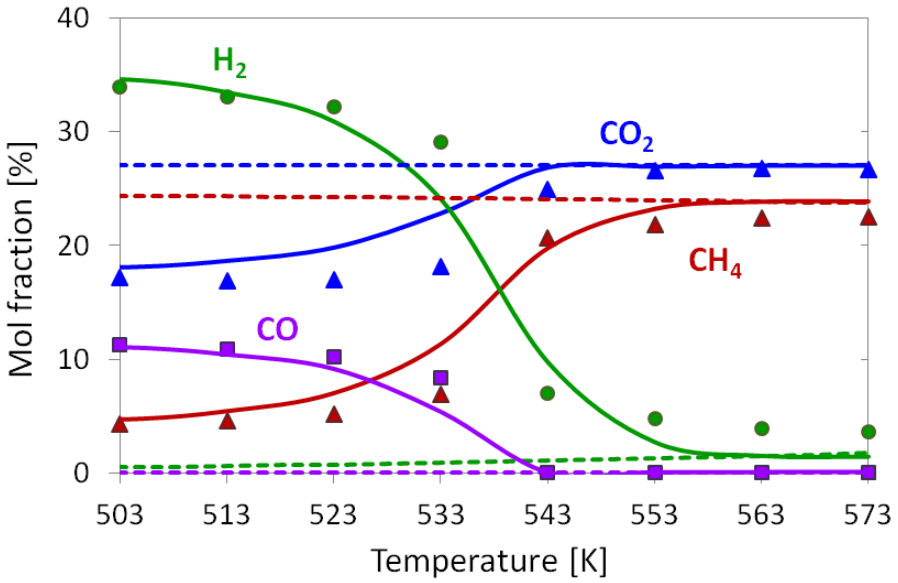

Figure 5.10 *Comparison of experimentally determined (symbols) and numerically predicted (lines) mole fractions as function of temperature for CO methanation: inlet gas composition of 11.75 vol.% CO, 35.52 vol.% H_2, 0.0059 vo.l% O_2, 4.06 vol.% CH_4 and 17.56 vol.% CO_2 in N_2 dilution; 1.8bar; T_{inlet}=453 K; $\tau_{mod,CO}$=76 kg*s/mol; dashed lines =equilibrium composition at given temperature.*

5.6 Summary

CO methanation has been experimentally and numerically studied. Experiments are carried out in a packed be reactor and in a continuous-flow reactor. The experimental data are used to model 1D and 2D solution of the reactive flow respectively.

The reaction mechanism for catalytic oxidation and reforming of methane presented in Table 4.16 (Section 4.4) has been modified in order to model the formation of methane measured during the WGS and R-WGS experiments (Section 4.3). These modifications are based on methanation studies from the literature and by comparison with the experimental data from this work. The methanation model is based on the formation of reactive surface carbon by the reaction R41($CO^* + H^* \rightarrow C^* + OH^*$) and stepwise hydrogenation of surface carbon, R20 ($C^* + H^* \rightarrow CH^* + *$). Carbon coverage dependency ($\theta_{CO(Ni)}$) is included as a constant parameter in the reaction R41 (Table 5.2).

Methane formation during WGS and R-WGS experiments (Section 4.3) is attributed to changes in the structure of the catalyst; this assumption is based on both experimental results and theoretical analysis from literature.

At the experimental working conditions for CO methanation used in this work, the catalyst suffered severe coke formation, that diminished its performance by blocking the active sites.

Appropriated conditions have to be selected during the methanation of CO, in order to reduce the formation of nickel tetracarbonyl [$Ni(CO)_4$], which is believed to be the main cause of catalyst deactivation at low temperatures. The development of a model for description of coke formation exceeding one mono-layer is still pending. The proposed mechanism is further tested by using the experimental data carried out in this work and derived experimental results performed in DVGW test laboratory at the Engler-Bunte-Institut of the KIT.

6.Summary and Outlook

Scope of this work

The conversion of natural gas to hydrogen and syngas plays a key role in many catalytic processes in the chemical industry. Processes such as steam reforming (SR), catalytic partial oxidation (CPOx) and methane dry reforming (DR) are widely used for converting natural gas to synthesis gas and hydrogen.

Micro-kinetic modeling based on fundamental studies plays an important role in the development of technically relevant catalytic systems. The models provide a deeper understanding of the catalytic processes at molecular level. Therefore, the numerical-based prediction of the reactor behavior becomes a useful diagnostic tool to enhance the processes efficiency.

The scope of this work is the development of surface reaction kinetics to describe the following catalytic processes over a nickel based catalyst: hydrogen oxidation (H_2/O_2), CO oxidation (CO/O_2), preferential CO oxidation ($CO/H_2/O_2$), water-gas shift (CO/H_2O), reverse water-gas shift (CO_2/H_2), partial oxidation of methane (CH_4/O_2), steam reforming of methane (CH_4/H_2O) and dry reforming of methane (CH_4/CO_2).

Modeling approach

An elementary surface reaction mechanism is developed to describe the catalytic conversion of methane under oxidative and reforming conditions over a wide range of temperature, pressure, and residence time. The modeling approach is based on the mean field approximation, i.e., the surface is assumed to be uniform and the adsorbates are randomly distributed on the surface. A previously established model for steam reforming on nickel developed in our group [58] serves as basis of the novel kinetics derived for the $CH_4/CO_2/H_2O/CO/O_2/H_2$ systems. The introduction of new reaction paths together with adjustments of the kinetic parameters, make it possible to predict conversion and selectivity for partial oxidation and reforming of methane as well as the sub-systems involved in these processes over a wide range of experimental conditions with the newly mechanism developed.

The methodology presented in Figure 6.1 is applied to develop the reaction kinetics presented in this work. It starts with the simplest reactions using a single fuel such H_2 or CO, the complexity of the system is augmented by increasing the number of components in the reactive gas mixture. This hierarchical approach is an effective method for the development of complex kinetic models. The same approach can be also used to extent the current kinetic model for higher hydrocarbons.

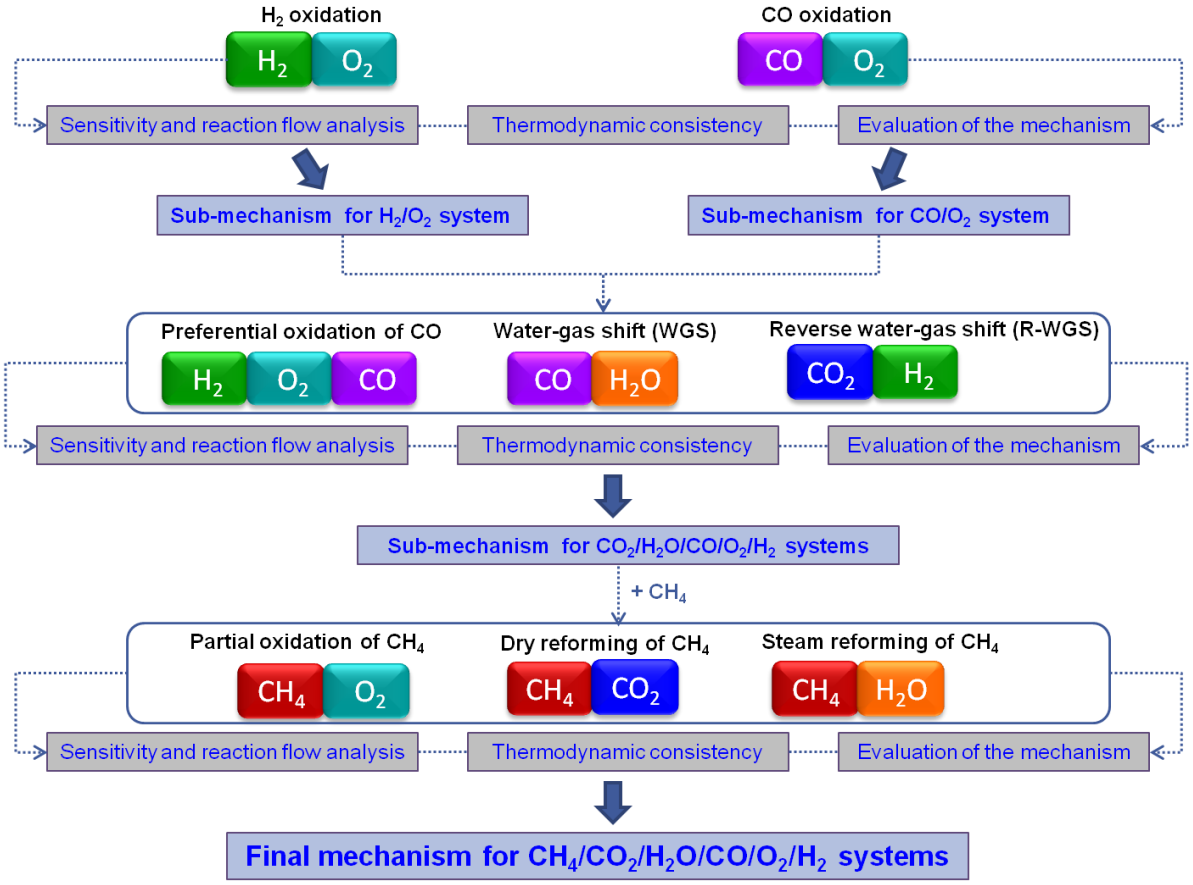

Figure 6.1 *Hierarchical approach used for the development of the surface reaction kinetics presented in this work.*

Sensitivity analyses are carried out to evaluate crucial parameters and determine the most important reactions in the mechanism for the conversion and production of individual species at different inlet conditions. Reaction flow analyses are also performed to determine the main path of production and consumption of the species within the catalytic cycle. A mathematical approach has been applied through the development process to ensure the over-all thermodynamic consistency of the mechanism. The surface reaction kinetics developed in each step presented in Table 6.1 need to be evaluated by modeling many experiments using different

nickel-based catalyst, experimental conditions, i.e., fuel compositions, flow rates and reactor configurations.

Evaluation of the reaction kinetics

The purpose of the experiments performed in this work is to assess the accuracy of the kinetic models for each of the reaction systems shown in Figure 6.1.

The experiments are conducted in three different reactor configurations, a continuous flow reactor with a wash-coated honeycomb nickel monolith as catalyst, a stagnation-flow reactor with a catalytic disk, and a fixed bed reactor loaded with powdered nickel-based catalysts developed by BASF. Fixed bed and continuous-flow reactor configurations are selected because of their common use in laboratory experiments. The stagnation-flow reactor is chosen because it offers a simple configuration to investigate heterogeneously catalyzed gas-phase reactions. The technique enable measuring and modeling of well-defined flow field with a zero-dimensional catalytic surface.

The product stream for all cases is analyzed by FT-IR and MS, which allow time-resolved monitoring. Table 6.1 shows an overview of the reactor types, and catalysts used for the experimental study, as well as the corresponding $F_{cat/geo}$ and active surface area used for the numerical simulations.

Table 6.1 Reactor types and catalysts used in this work for the experiments and numerical simulations.

Reactor Type	**Catalyst**	**$F_{cat/geo}$**	**Active surface area (m^{-1})**
Stagnation-flow	catalytic disk 5wt.% Ni/Al_2O_3	1.5	-
Continuous-flow	wash-coated monolith Ni/Al_2O_3	150	-
Fixed bed	Fixedbed_Ni_BASF_Cat.1	1	$1.14x10^5$
	Fixedbed_Ni_BASF_Cat.2	1	$9.85x10^6$

Table 6.2 summarizes the simulation results of the experiments performed in this work as well as from literature using different nickel supported catalysts. These experiments can be simulated using a unique micro-kinetic model (Table 4.17) without modifications. For all the conditions hereby studied, the support has no significant impact on the reaction kinetics. Therefore, nickel dominates the results, in spite of the support used.

A color code is used to classify the deviation between numerical results and experiments performed. Table 6.2 shows a good agreement between the calculated and experimental conversion, selectivity of the products for the most of the experimental conditions studied.

Table 6.2 Summary of all experiments numerically simulated in this work using the $CH_4/CO_2/H_2O/CO/O_2/H_2$ mechanism.

Reactor type and catalyst	H_2/O_2	CO/O_2	$CO/O_2/H_2$	CO/H_2O (WGS)	CO_2/H_2 (R-WGS)	CH_4/O_2 (CPOx)	CH_4/H_2O (SR)	CH_4/CO_2 (DR)	$CH_4/CO_2/H_2$ ($DR+H_2$)	$CH_4/CO_2/H_2O$ ($DR+H_2O$)
Performed Experiments										
Stagnation-flow 5 wt.% Ni/Al_2O_3 catalytic disk										
Continuous-flow Ni/Al_2O_3 wash-coated monolith										
Fixed bed Fixedbed_Ni_BASF_Cat.1										
Fixed bed Fixedbed_Ni_BASF_Cat.2										
Literature Experiments										
Continuous-flow wash-coated monolith 5 wt.% Ni/Al_2O_3 [197]										
Fixed bed Commercial Ni catalyst 25 wt.% Ni (C11-2S-06) [16]										
Continuous-flow wash-coated monolith 3 wt.% Ni/Al_2O_3 [57]										
Fixed bed 21 wt.% $Ni/MgO/Al_2O_3$ [211]										
Continuous-flow wash-coated monolith 21 wt.% $Ni/MgO/Al_2O_3$ [211]										
Fixed bed 8 wt.% $Ni/\gamma\text{-}Al_2O_3$ [213]										
Fixed bed 10.5 wt.% $Ni/\gamma\text{-}Al_2O_3$ [214]										
Experiments from hte AG project partners										
Fixed bed Fixedbed_Ni_BASF_Cat.1										

Color code	Deviation between experiment and model [%]
Green	0-10
Yellow	11-20
Red	>20

Hydrogen oxidation (H_2/O_2)

The first system investigated in this work is the catalytic oxidation of hydrogen over nickel. An elementary-step like surface reaction mechanism for hydrogen oxidation has been developed using the experimental results from experiments performed during this work in a stagnation-flow reactor.

Sensitivity analysis of the kinetic model indicates that hydrogen adsorption is sensitive at 373 K before the ignition of the reaction, after ignition the mechanism becomes more sensitive to

gas-phase and adsorbed water. Formation of OH* species seems to be the rate determining step, since the reaction is highly sensitive in the all range of temperatures.
The developed surface reaction mechanism is able to reproduce the experimentally measured concentrations for hydrogen oxidation in a stagnation flow reactor. DETCHEM^{STAG} software is used for the numerical simulations.
The newly reactions kinetics serves as a fundamental model to described the H_2/O_2 reactions that take place in more complex systems such as water–gas-shift and partial and total oxidation as well as steam and dry reforming over nickel-based catalyst.

CO oxidation (CO/O_2)

CO total oxidation is also investigated under varying CO/oxygen composition over a wide temperature range. A heterogeneous surface reaction mechanism for the catalytic oxidation of CO has been developed using the experimental results performed during this work in a fixed bed and in a stagnation-flow reactor. Simulation results show that CO oxidation depends on the CO adsorption/desorption equilibrium, and therefore on the CO concentration on the catalytic surface. A high CO concentration in the inlet gas composition leads to full CO-covered surfaces that inhibit oxygen adsorption. Therefore, coverage dependency for CO is included to in the mechanism to describe the lateral interactions of adsorbed species.
For all cases investigated, the simulation results agree well with the experimental results.

Preferential CO oxidation, water-gas shift and reverse water-gas shift ($CO/CO_2/H_2O/O_2/H_2$)

The complexity of the system is increased by coupling the previously established reaction kinetics for H_2/O_2 and CO/O_2 systems with new CO-H reactions.
A thermodynamically consistent multi-step surface reaction mechanism with the associated rate expressions is developed for preferential CO oxidation, water-gas shift and reverse water-gas shift reactions using the experimental results from experiments performed in fixed and a continuous flow reactor.
The kinetic model for the $CO/CO_2/H_2O/O_2/H_2$ systems contains important intermediates such as adsorbed HCO* and COOH* species. Sensitivity analysis shows that the carboxyl species

has a major effect at low temperature. Whereas at high temperatures, the direct oxidation of CO* with O* species on the surface is favored.

Methane formation is observed in R-WGS experiments and in one of the experiments performed for WGS. Following the modeling approach presented in Figure 6.1, reactions for methane activation are not included yet. Therefore, it becomes necessary to follow the next step of the hierarchical approach, where methane reactions are included in order to properly describe the kinetics of WGS and R-WGS.

Experimentally, it is found that methane formation during WGS exhibits a dependency on the inlet gas composition, e.g, at high H_2O concentration in the inlet mixture, no methane formation is observed.

The experimental results obtained for preferential CO oxidation over nickel-based catalyst are also simulated using the kinetic model developed for the $CO/CO_2/H_2O/O_2/H_2$ system. However, the mechanism cannot accurately represent preferential CO oxidation. Numerical results show that hydrogen is consumed before CO is oxidized, whereas, experimentally the formation of CO oxidation takes place first, leaving free actives sites for hydrogen adsorption to produce water. In the case of preferential CO oxidation, the mean field approximation does not seem to work. The kinetic data cannot be further adjusted to predict the preferential CO oxidation due to the sensitivity of the reactions involved. Slight changes to these data will produce inaccurate results for the other systems, which need to be covered by this mechanism.

Oxidation and reforming of methane ($CH_4/CO_2/H_2O/CO/O_2/H_2$)

Catalytic partial oxidation as well as steam and dry reforming of methane over nickel-based catalyst have been studied in a fixed bed reactor. The reactions steps of methane activation on nickel from a former kinetic model developed in our group [58] are used to extend the previously established $CO/CO_2/H_2O/O_2/H_2$ mechanism. The combined reaction steps are used to develop a new thermodynamically consistent surface reaction mechanism for $CH_4/CO_2/H_2O/CO/O_2/H_2$ systems. The introduction of new reaction paths, together with adjustments of the kinetic parameters, make it possible to predict with the new mechanism the conversion and selectivity for partial oxidation and reforming of methane as well as the sub-systems involved in these processes over a wide range of experimental conditions.

A sensitivity analysis regarding to methane conversion for dry reforming, steam reforming, and partial oxidation is performed at 1073 K. It indicates that simple dehydrogenation of methane

is important for all processes. However, for methane partial oxidation, the oxygen assisted dehydrogenation of methane is a preferred rate determining step.

The mechanism is evaluated against new experimental data, as well as experimental results from literature at varying operating conditions and reactor configurations.

Both experimental and numerical results for synthesis gas production via partial oxidation of methane (CPOX) are consistent with the indirect path. Here total oxidation of methane takes place first producing CO_2 and H_2O at temperatures above 773 K. The residual CH_4 is reformed to produce CO and H_2 at temperatures above 873 K; below this temperature no H_2 or CO is observed.

The results for dry and steam reforming show that the kinetic model is able to reproduce conversion and selectivity, which are close to equilibrium, for the whole temperature range.

The influence of hydrogen and water as co-reactants on methane dry reforming is also studied in a fixed bed reactor. The effect of hydrogen on the experiment is the formation of water at temperatures between 573 K-673 K, produced through the R-WGS reaction. Then, water is consumed as temperature increases due to the steam reforming reaction with the remaining methane. When water is added instead of H_2 as co-reactant, it can be seen that at medium temperature some CO_2 is produced by the WGS reaction.

The nickel-based catalyst from BASF (Fixedbed_Ni_BASF_Cat.2) used for the oxidation and reforming experiments does not produce significant amounts of coke on the surface at the working conditions relevant for this study. Therefore, the amount of coke on the surface could not be measured. Nevertheless, a comparison between the computed surface coverage of carbon for the three CO_2 reforming conditions studied (DR, DR+H_2, and DR+H_2O) show that dry reforming of methane (DR) produces the highest coverage of carbon at the surface. Moreover, the numerical results show that both H_2O and H_2 are inhibitors of coke deposition. However, H_2O provides a higher inhibition effect than H_2 at the studied conditions.

Table 6.2 Summarizes all experiments numerically simulated in this work using the $CH_4/CO_2/H_2O/CO/O_2/H_2$ mechanism. The model shows good agreement between the calculated experimental conversion, and selectivity during reforming and oxidation of methane for all experimental conditions studied.

Reforming of methane at high pressure and temperature

Reforming processes to produce syngas performed at high pressure have gained considerable attention in the field of catalysis, as it offers the opportunity to easily integrate the product stream with H_2/CO suitable ratios in downstream processes (e.g. petrochemical processes) commonly conducted at high pressures.

The heterogeneous model developed for $CH_4/CO_2/H_2O/CO/O_2/H_2$ systems is successfully applied at 1 bar; application at higher pressures (e.g. up to 30 bar) is also possible. Experiments performed by project partners from hte AG show that at high temperatures and pressure (20 bar), non-catalytic reactions in the gas-phase play an important role in the formation of higher hydrocarbons, which are potential coke precursors during the reforming reaction. Therefore, the numerical simulations are carried out taking into account possible gas-phase reactions by coupling an elementary-step gas-phase reaction mechanism with the surface model developed for $CH_4/CO_2/H_2O/CO/O_2/H_2$ systems. Numerical results show that significant amounts of coke precursors are formed as result of methane pyrolysis in front and after the catalytic bed; this is consistent with results obtained from experimental data. Reaction flow analysis of the mechanism at high temperature and pressure for dry reforming of methane indicates that nearly 99% of CO* produced on the surface desorbs to the gas phase. However, the remaining 1% leads to coke formation.

CO methanation

Formation of methane as a by-product is detected during the WGS and R-WGS experiments. In order to explain such observations, methanation reactions are also studied. It has been reported [174] that the rate of the methanation reaction is structure sensitivity. Structural changes in the catalyst cannot be simulated by the reaction mechanism developed in Section 4 (Table 4.17) due the mean field approximation method used in this work. Therefore, the reaction mechanism for $CH_4/CO_2/H_2O/CO/O_2/H_2$ systems has been slightly modified in order to simulate the methanation reactions. A significant improvement is observed in the simulation results of WGS and R-WGS experiments by using the modified mechanism. The new kinetic model for methanation is based on the formation of reactive surface carbon from the reaction between absorbed CO* and H* and stepwise hydrogenation of C* to produce CH*, which is considered to be the rate limiting step. Carbon coverage dependency (θ_{CO}) is also included as a

constant parameter in this reaction. However, by making these changes the kinetic model is not longer thermodynamically consistent.

The modified mechanism is further tested for CO methanation by modeling experimental results, which are obtained using a continuous-flow reactor with a monolithic catalyst. The model predicts the experimental results with a deviation higher than 20%. At the experimental operating conditions for CO methanation used in this work, the catalyst suffered severe coke formation. This carbon deposition diminished its performance by blocking the active sites, which explains the differences between the numerical profiles and the experimental results. The surface reaction mechanism proposed in this study is only able to describe the formation of one carbon monolayer, but not the transient carbon deposition on the surface, which is a limitation of the model. Nevertheless, the model can match the measured trends of all gas-phase species involved.

The modified mechanism is also evaluated by using results obtained from CO methanation experiments performed in DVGW test laboratory at KIT's Engler-Bunte-Institut. In this experiment, an inlet mixture similar to biogas composition is selected. The modified micro-kinetic model is able to reproduce the experimental results with good agreement. A summary of the simulation results obtained using the modified mechanism is presented in Table 6.3.

Table 6.3 Summary of all experiments numerically simulated in this work using the modified $CH_4/CO_2/H_2O/CO/O_2/H_2$ mechanism.

In this study	**Experiments**		
Reactor type and catalyst	CO/H_2O (WGS)	CO_2/H_2 (R-WGS)	CO/H_2
In this study			
Continuous-flow Ni/Al_2O_3 wash-coated monolith			
Fixed bed Fixedbed_Ni_BASF_Cat.2			
From DVGW			
Continuous-flow wash-coated monolith			

Color code	**Deviation between experiment and model [%]**
Green	0-10
Yellow	11-20
Red	>20

Outlook

By using the model developed in this work and by following the same hierarchical approach presented here, the reaction mechanism can be extended to be applied to process aimed at higher hydrocarbons, such as ethanol, methanol and propane.

The surface reaction mechanism proposed in this study is able to describe the formation of one carbon monolayer. Therefore, a detailed investigation of carbon formation over nickel is necessary to understand the deactivation process and its effect on the catalyst performance. Future work will focus on the implementation of a coking model into the surface reaction scheme, to describe transient carbon deposition on the surface in form of carbon film with different morphology.

Appendix

Table 1. Developed surface reaction mechanism over nickel for $CH_4/CO_2/H_2O/CO/O_2/H_2$ systems.

	REACTION	A/[cm, mol, s]/S_0[-]	β [-]	E_a/[kJ/mol]	ε_1 [kJ/mol]
R1	$H_2 + (Ni) + (Ni) \rightarrow H(Ni) + H(Ni)$	$3.000 \cdot 10^{-02}$	0.0	5.00	
R2	$H(Ni) + H(Ni) \rightarrow Ni(Ni) + Ni(Ni) + H_2$	$2.544 \cdot 10^{+20}$	0.0	95.21	
R3	$O_2 + (Ni) + (Ni) \rightarrow O(Ni) + O(Ni)$	$4.358 \cdot 10^{-02}$	-0.206	1.51	
R4	$O(Ni) + O(Ni) \rightarrow (Ni) + (Ni) + O_2$	$1.188 \cdot 10^{+21}$	0.823	468.91	
R5	$CH_4 + (Ni) \rightarrow CH_4(Ni)$	$8.000 \cdot 10^{-03}$	0.0	0.0	
R6	$CH_4(Ni) \rightarrow CH_4 + Ni(Ni)$	$8.705 \cdot 10^{+15}$	0.0	37.55	
R7	$H_2O + (Ni) \rightarrow H_2O(Ni)$	$1.000 \cdot 10^{-01}$	0.0	0.0	
R8	$H_2O(Ni) \rightarrow H_2O + (Ni)$	$3.732 \cdot 10^{+12}$	0.0	60.79	
R9	$CO_2 + (Ni) \rightarrow CO_2(Ni)$	$7.001 \cdot 10^{-06}$	0.0	0.00	
R10	$CO_2(Ni) \rightarrow CO_2 + (Ni)$	$6.442 \cdot 10^{+07}$	0.0	25.98	
R11	$CO + (Ni) \rightarrow CO(Ni)$	$5.000 \cdot 10^{-01}$	0.0	0.0	
R12	$CO(Ni) \rightarrow CO + (Ni)$	$3.566 \cdot 10^{+11}$	0.0	111.27	$-50\theta_{CO(s)}$
R13	$CH_4(Ni) + (Ni) \rightarrow CH_3(Ni) + H(Ni)$	$1.548 \cdot 10^{+21}$	0.087	55.83	
R14	$CH_3(Ni) + H(Ni) \rightarrow CH_4(Ni) + (Ni)$	$1.443 \cdot 10^{+22}$	-0.087	63.45	
R15	$CH_3(Ni) + (Ni) \rightarrow CH_2(Ni) + H(Ni)$	$1.548 \cdot 10^{+24}$	0.087	98.12	
R16	$CH_2(Ni) + H(Ni) \rightarrow CH_3(Ni) + (Ni)$	$3.091 \cdot 10^{+23}$	-0.087	57.21	
R17	$CH_2(Ni) + (Ni) \rightarrow CH(Ni) + H(Ni)$	$3.700 \cdot 10^{+24}$	0.087	95.23	
R18	$CH(Ni) + H(Ni) \rightarrow CH_2(Ni) + (Ni)$	$9.774 \cdot 10^{+24}$	-0.087	81.05	
R19	$CH(s) + (Ni) \rightarrow C(Ni) + H(Ni)$	$9.888 \cdot 10^{+20}$	0.50	21.99	
R20	$C(Ni) + H(Ni) \rightarrow CH(Ni) + (Ni)$	$1.707 \cdot 10^{+24}$	-0.50	157.92	
R21	$CH_4(Ni) + O(Ni) \rightarrow CH_3(Ni) + OH(Ni)$	$5.621 \cdot 10^{+24}$	-0.101	92.72	
R22	$CH_3(Ni) + OH(Ni) \rightarrow CH_4(Ni) + O(Ni)$	$2.987 \cdot 10^{+22}$	0.101	25.80	
R23	$CH_3(Ni) + O(Ni) \rightarrow CH_2(Ni) + OH(Ni)$	$1.223 \cdot 10^{+25}$	-0.101	134.67	
R24	$CH_2(Ni) + OH(Ni) \rightarrow CH_3(Ni) + O(Ni)$	$1.393 \cdot 10^{+21}$	0.101	19.05	
R25	$CH_2(Ni) + O(Ni) \rightarrow CH(Ni) + OH(Ni)$	$1.223 \cdot 10^{+25}$	-0.101	131.37	
R26	$CH(Ni) + OH(Ni) \rightarrow CH_2(Ni) + O(Ni)$	$4.407 \cdot 10^{+22}$	0.101	42.45	
R27	$CH(Ni) + O(Ni) \rightarrow C(Ni) + OH(Ni)$	$2.471 \cdot 10^{+21}$	0.312	57.74	
R28	$C(Ni) + OH(Ni) \rightarrow CH(Ni) + O(Ni)$	$2.433 \cdot 10^{+21}$	-0.312	118.97	
R29	$H(Ni) + O(Ni) \rightarrow OH(Ni) + (Ni)$	$3.951 \cdot 10^{+23}$	-0.188	104.35	
R30	$OH(Ni) + (Ni) \rightarrow H(Ni) + O(Ni)$	$2.254 \cdot 10^{+20}$	0.188	29.64	
R31	$H(Ni) + OH(Ni) \rightarrow H_2O(Ni) + (Ni)$	$1.854 \cdot 10^{+20}$	0.086	41.52	

R32	$H_2O(Ni) + (Ni) \rightarrow H(Ni) + OH(Ni)$	$3.674 \cdot 10^{+21}$	-0.086	92.94	
R33	$OH(Ni) + OH(Ni) \rightarrow H_2O(Ni) + O(Ni)$	$2.346 \cdot 10^{+20}$	0.274	92.37	
R34	$H_2O(Ni) + O(Ni) \rightarrow OH(Ni) + OH(Ni)$	$8.148 \cdot 10^{+24}$	-0.274	218.49	
R35	$C(Ni) + O(Ni) \rightarrow CO(Ni) + (Ni)$	$3.402 \cdot 10^{+23}$	0.0	148.10	
R36	$CO(Ni) + (Ni) \rightarrow C(Ni) + O(Ni)$	$1.758 \cdot 10^{+13}$	0.0	116.24	$-50.0\ \theta_{CO(s)}$
R37	$CO(Ni) + CO(Ni) \rightarrow C(Ni) + CO_2(Ni)$	$1.624 \cdot 10^{+14}$	0.5	241.76	$-100.0\ \theta_{CO(s)}$
R38	$CO_2(Ni) + C(Ni) \rightarrow CO(Ni) + CO(Ni)$	$7.294 \cdot 10^{+28}$	-0.5	239.24	
R39	$CO(Ni) + O(Ni) \rightarrow CO_2(Ni) + (Ni)$	$2.000 \cdot 10^{+19}$	0.0	123.60	$-50.0\ \theta_{CO(s)}$
R40	$CO_2(Ni) + (Ni) \rightarrow CO(Ni) + O(Ni)$	$4.648 \cdot 10^{+23}$	-1.0	89.32	
R41	$CO(Ni) + H(Ni) \rightarrow C(Ni) + OH(Ni)$	$3.522 \cdot 10^{+18}$	-0.188	105.45	$-50.0\ \theta_{CO(s)}$
R42	$C(Ni) + OH(Ni) \rightarrow H(Ni) + CO(Ni)$	$3.888 \cdot 10^{+25}$	0.188	62.55	
R43	$CO_2(Ni) + H(Ni) \rightarrow COOH(Ni) + (Ni)$	$6.250 \cdot 10^{+24}$	-0.475	117.24	
R44	$COOH(Ni) + (Ni) \rightarrow CO_2(Ni) + H(Ni)$	$3.737 \cdot 10^{+20}$	0.475	33.66	
R45	$COOH(Ni) + (Ni) \rightarrow CO(Ni) + OH(Ni)$	$1.461 \cdot 10^{+24}$	-0.213	54.37	
R46	$CO(Ni) + OH(Ni) \rightarrow COOH(Ni) + (Ni)$	$6.003 \cdot 10^{+21}$	0.213	97.63	$-50.0\ \theta_{CO(s)}$
R47	$CO(Ni) + H(Ni) \rightarrow HCO(Ni) + (Ni)$	$4.009 \cdot 10^{+20}$	-1.0	132.23	
R48	$HCO(Ni) + (Ni) \rightarrow CO(Ni) + H(Ni)$	$3.710 \cdot 10^{+21}$	0.0	0.0	$+50.0\theta_{CO(s)}$
R49	$HCO(Ni) + (Ni) \rightarrow CH(Ni) + O(Ni)$	$3.796 \cdot 10^{+14}$	0.0	81.91	
R50	$CH(Ni) + O(Ni) \rightarrow HCO(Ni) + (Ni)$	$4.599 \cdot 10^{+20}$	0.0	109.97	
R51	$H(Ni) + COOH(Ni) \rightarrow HCO(Ni) + OH(Ni)$	$6.000 \cdot 10^{+22}$	-1.163	104.88	
R52	$HCO(Ni) + OH(Ni) \rightarrow COOH(Ni) + H(Ni)$	$2.282 \cdot 10^{+20}$	0.263	15.92	

Table 2. Modified surface reaction mechanism over nickel for CO methanation.

	REACTION	A/[cm, mol, s]/S_0[-]	β [-]	E_a/[kJ/mol]	ε_I [kJ/mol]
R1	H_2 + (Ni) + (Ni) → H(Ni) + H(Ni)	$3.000 \cdot 10^{-02}$	0.000	5.00	
R2	H(Ni) + H(Ni) → Ni(Ni) + Ni(Ni) + H_2	$2.544 \cdot 10^{+20}$	0.000	95.21	
R3	O_2 + (Ni) + (Ni) → O(Ni) + O(Ni)	$4.358 \cdot 10^{-02}$	-0.206	1.51	
R4	O(Ni) + O(Ni) → (Ni) + (Ni) + O_2	$1.188 \cdot 10^{+21}$	0.823	468.91	
R5	CH_4 + (Ni) → CH_4(Ni)	$8.000 \cdot 10^{-03}$	0.000	0.00	
R6	CH_4(Ni) → CH_4 + Ni(Ni)	$8.705 \cdot 10^{+15}$	0.000	37.55	
R7	H_2O + (Ni) → H_2O(Ni)	$1.000 \cdot 10^{-01}$	0.000	0.00	
R8	H_2O(Ni) → H_2O + (Ni)	$3.732 \cdot 10^{+12}$	0.000	60.79	
R9	CO_2 + (Ni) → CO_2(Ni)	$7.001 \cdot 10^{-06}$	0.000	0.00	
R10	CO_2(Ni) → CO_2 + (Ni)	$6.442 \cdot 10^{+07}$	0.000	25.98	
R11	CO + (Ni) → CO(Ni)	$5.000 \cdot 10^{-01}$	0.000	0.00	
R12	CO(Ni) → CO + (Ni)	$3.566 \cdot 10^{+11}$	0.000	111.27	-50.0 $\theta_{CO(Ni)}$
R13	CH_4(Ni) + (Ni) → CH_3(Ni) + H(Ni)	$1.548 \cdot 10^{+21}$	0.087	55.83	
R14	CH_3(Ni) + H(Ni) → CH_4(Ni) + (Ni)	$1.443 \cdot 10^{+22}$	-0.087	63.45	
R15	CH_3(Ni) + (Ni) → CH_2(Ni) + H(Ni)	$1.548 \cdot 10^{+24}$	0.087	98.12	
R16	CH_2(Ni) + H(Ni) → CH_3(Ni) + (Ni)	$3.091 \cdot 10^{+23}$	-0.087	57.21	
R17	CH_2(Ni) + (Ni) → CH(Ni) + H(Ni)	$3.700 \cdot 10^{+24}$	0.087	95.23	
R18	CH(Ni) + H(Ni) → CH_2(Ni) + (Ni)	$9.774 \cdot 10^{+24}$	-0.087	81.05	
R19	CH(s) + (Ni) → C(Ni) + H(Ni)	$9.888 \cdot 10^{+20}$	0.500	21.99	
R20	C(Ni) + H(Ni) → CH(Ni) + (Ni)	$1.707 \cdot 10^{+24}$	-0.500	157.92	**-120.0 $\theta_{C(Ni)}$**
R21	CH_4(Ni) + O(Ni) → CH_3(Ni) + OH(Ni)	$5.621 \cdot 10^{+24}$	-0.101	92.72	
R22	CH_3(Ni) + OH(Ni) → CH_4(Ni) + O(Ni)	$2.987 \cdot 10^{+22}$	0.101	25.80	
R23	CH_3(Ni) + O(Ni) → CH_2(Ni) + OH(Ni)	$1.223 \cdot 10^{+25}$	-0.101	134.67	
R24	CH_2(Ni) + OH(Ni) → CH_3(Ni) + O(Ni)	$1.393 \cdot 10^{+21}$	0.101	19.05	
R25	CH_2(Ni) + O(Ni) → CH(Ni) + OH(Ni)	$1.223 \cdot 10^{+25}$	-0.101	131.37	
R26	CH(Ni) + OH(Ni) → CH_2(Ni) + O(Ni)	$4.407 \cdot 10^{+22}$	0.101	42.45	
R27	CH(Ni) + O(Ni) → C(Ni) + OH(Ni)	$2.471 \cdot 10^{+21}$	0.312	57.74	
R28	C(Ni) + OH(Ni) → CH(Ni) + O(Ni)	$2.433 \cdot 10^{+21}$	-0.312	118.97	
R29	H(Ni) + O(Ni) → OH(Ni) + (Ni)	$3.951 \cdot 10^{+23}$	-0.188	104.35	
R30	OH(Ni) + (Ni) → H(Ni) + O(Ni)	$2.254 \cdot 10^{+20}$	0.188	29.64	
R31	H(Ni) + OH(Ni) → H_2O(Ni) + (Ni)	$1.854 \cdot 10^{+20}$	0.086	41.52	
R32	H_2O(Ni) + (Ni) → H(Ni) + OH(Ni)	$3.674 \cdot 10^{+21}$	-0.086	92.94	
R33	OH(Ni) + OH(Ni) → H_2O(Ni) + O(Ni)	$2.346 \cdot 10^{+20}$	0.274	92.37	
R34	H_2O(Ni) + O(Ni) → OH(Ni) + OH(Ni)	$8.148 \cdot 10^{+24}$	-0.274	218.49	
R35	C(Ni) + O(Ni) → CO(Ni) + (Ni)	$3.402 \cdot 10^{+23}$	0.000	148.10	

R36	$CO(Ni) + (Ni) \rightarrow C(Ni) + O(Ni)$	$1.758 \cdot 10^{+13}$	0.000	116.24	-50.0 $\theta_{CO(Ni)}$
R37	$CO(Ni) + CO(Ni) \rightarrow C(Ni) + CO_2(Ni)$	$1.624 \cdot 10^{+14}$	0.500	241.76	-100.0 $\theta_{CO(Ni)}$
R38	$CO_2(Ni) + C(Ni) \rightarrow CO(Ni) + CO(Ni)$	$7.294 \cdot 10^{+28}$	-0.500	239.24	
R39	$CO(Ni) + O(Ni) \rightarrow CO_2(Ni) + (Ni)$	$2.000 \cdot 10^{+19}$	0.000	123.60	-50.0 $\theta_{CO(Ni)}$
R40	$CO_2(Ni) + (Ni) \rightarrow CO(Ni) + O(Ni)$	$4.648 \cdot 10^{+23}$	-1.000	89.32	
R41	$CO(Ni) + H(Ni) \rightarrow C(Ni) + OH(Ni)$	$3.522 \cdot 10^{+18}$	-0.188	105.45	-50.0 $\theta_{CO(Ni)}$
R42	$C(Ni) + OH(Ni) \rightarrow H(Ni) + CO(Ni)$	**$3.888 \cdot 10^{+23}$**	0.188	62.55	
R43	$CO_2(Ni) + H(Ni) \rightarrow COOH(Ni) + (Ni)$	$6.250 \cdot 10^{+24}$	-0.475	117.24	
R44	$COOH(Ni) + (Ni) \rightarrow CO_2(Ni) + H(Ni)$	$3.737 \cdot 10^{+20}$	0.475	33.66	
R45	$COOH(Ni) + (Ni) \rightarrow CO(Ni) + OH(Ni)$	$1.461 \cdot 10^{+24}$	-0.213	54.37	
R46	$CO(Ni) + OH(Ni) \rightarrow COOH(Ni) + (Ni)$	$6.003 \cdot 10^{+21}$	0.213	97.63	-50.0 $\theta_{CO(Ni)}$
R47	$CO(Ni) + H(Ni) \rightarrow HCO(Ni) + (Ni)$	$4.009 \cdot 10^{+20}$	-1.000	132.23	
R48	$HCO(Ni) + (Ni) \rightarrow CO(Ni) + H(Ni)$	$3.710 \cdot 10^{+21}$	0.000	0.00	+50.0 $\theta_{CO(Ni)}$
R49	$HCO(Ni) + (Ni) \rightarrow CH(Ni) + O(Ni)$	$3.796 \cdot 10^{+14}$	0.000	81.91	
R50	$CH(Ni) + O(Ni) \rightarrow HCO(Ni) + (Ni)$	$4.599 \cdot 10^{+20}$	0.000	109.97	
R51	$H(Ni) + COOH(Ni) \rightarrow HCO(Ni) + OH(Ni)$	$6.000 \cdot 10^{+22}$	-1.163	104.88	
R52	$HCO(Ni) + OH(Ni) \rightarrow COOH(Ni) + H(Ni)$	$2.282 \cdot 10^{+20}$	0.263	15.92	

Table 3. Thermodynamic data surface and gas- phase species

```
CH4                     C   1H   4    0    0      300.00   5000.00 1000.00       1
 0.16834788E+01  0.10237236E-01 -0.38751286E-05 0.67855849E-09  -0.45034231E-13   2
-0.10080787E+05  0.96233950E+01  0.77874148E+00 0.17476683E-01  -0.27834090E-04   3
 0.30497080E-07 -0.12239307E-10 -0.98252285E+04 0.13722195E+02                    4
O2                      O   2    0    0    0      300.00   5000.00 1000.00       1
 0.36122139E+01  0.74853166E-03 -0.19820647E-06  0.33749008E-10 -0.23907374E-14   2
-0.11978151E+04  0.36703307E+01  0.37837135E+01 -0.30233634E-02  0.99492751E-05   3
-0.98189101E-08  0.33031825E-11 -0.10638107E+04  0.36416345E+01                   4
CO                      C   1O   1    0    0      300.00    5000.00 1000.00      1
 0.30250781E+01  0.14426885E-02 -0.56308278E-06  0.10185813E-09 -0.69109516E-14   2
-0.14268350E+05  0.61082177E+01  0.32624517E+01  0.15119409E-02 -0.38817552E-05   3
 0.55819442E-08 -0.24749512E-11 -0.14310539E+05  0.48488970E+01                   4
CO2                     C   1O   2    0    0      300.00    5000.00 1000.00      1
 0.44536228E+01  0.31401687E-02 -0.12784105E-05  0.23939967E-09 -0.16690332E-13   2
-0.48966961E+05 -0.95539588E+00  0.22757246E+01  0.99220723E-02 -0.10409113E-04   3
 0.68666868E-08 -0.21172801E-11 -0.48373141E+05  0.10188488E+02                   4
H2                      H   2    0    0    0      300.00    5000.00 1000.00      1
 0.30667095E+01  0.57473755E-03  0.13938319E-07 -0.25483518E-10  0.29098574E-14   2
-0.86547412E+03 -0.17798424E+01  0.33553514E+01  0.50136144E-03 -0.23006908E-06   3
-0.47905324E-09  0.48522585E-12 -0.10191626E+04 -0.35477228E+01                   4
H2O                     H   2O   1    0    0      300.00    5000.00 1000.00      1
 0.26110472E+01  0.31563130E-02 -0.92985438E-06  0.13331538E-09 -0.74689351E-14   2
-0.29868167E+05  0.72091268E+01  0.41677234E+01 -0.18114970E-02  0.59471288E-05   3
-0.48692021E-08  0.15291991E-11 -0.30289969E+05 -0.73135474E+00                   4
AR                      AR  1    0    0    0      300.00   5000.00 1000.00       1
 0.25000000E+01  0.00000000E+00  0.00000000E+00  0.00000000E+00  0.00000000E+00   2
-0.74537502E+03  0.43660006E+01  0.25000000E+01  0.00000000E+00  .00000000E+00    3
 0.00000000E+00  0.00000000E+00 -0.74537498E+03  0.43660006E+01                   4
N2                      N   2    0    0    0      300.00   5000.00 1000.00       1
 0.28532899E+01  0.16022128E-02 -0.62936893E-06  0.11441022E-09 -0.78057465E-14   2
-0.89008093E+03  0.63964897E+01  0.37044177E+01 -0.14218753E-02  0.28670392E-05   3
-0.12028885E-08 -0.13954677E-13 -0.10640795E+04  0.22336285E+01                   4
H(Ni)                   H   1Ni  1    0    0      500.00   2000.00 2000.00       1
 0.13852235E+01 -0.36029151E-04  0.10148288E-05 -0.63923405E-09  0.12606464E-12   2
-0.54588657E+04 -0.50426290E+01  0.13852235E+01 -0.36029151E-04  0.10148288E-05   3
-0.63923405E-09  0.12606464E-12 -0.54588657E+04 -0.50426290E+01                   4
O(Ni)                   O   1Ni  1    0    0      500.00   2000.00 2000.00       1
 0.93388577E+00  0.14928749E-02 -0.15115381E-05  0.76013345E-09 -0.14249939E-12   2
-0.28801188E+05 -0.34724750E+01  0.93388577E+00  0.14928749E-02 -0.15115381E-05   3
 0.76013345E-09 -0.14249939E-12 -0.28801188E+05 -0.34724750E+01                   4
CH4(Ni)                 C   1H   4Ni  1    0      500.00   2000.00 2000.00       1
 0.34765146E+00  0.99227736E-02 -0.20174749E-05 -0.10640458E-08  0.41875938E -12  2
-0.13899727E+05 -0.46164625E+01  0.34765146E+00  0.99227736E-02 -0.20174749E-05   3
-0.10640458E-08  0.41875938E-12 -0.13899727E+05 -0.46164625E+01                   4
(Ni)                    Ni  1    0    0    0      300.00   3000.00 1000.00       1
 0.00000000E+00  0.00000000E+00  0.00000000E+00  0.00000000E+00  0.00000000E+00   2
 0.00000000E+00  0.00000000E+00  0.00000000E+00  0.00000000E+00  0.00000000E+00   3
 0.00000000E+00  0.00000000E+00  0.00000000E+00  0.00000000E+00                   4
H2O(Ni)                 H   2O   1Ni  1    0      500.00   2000.00 2000.00       1
 0.35042138E+01  0.66859484E-03  0.17626874E-05 -0.11703015E-08  0.22618536E-12   2
-0.37912917E+05 -0.10558253E+02  0.35042138E+01  0.66859484E-03  0.17626874E-05   3
-0.11703015E-08  0.22618536E-12 -0.37912917E+05 -0.10558253E+02                   4
CO2(Ni)                 C   1O   2Ni  1    0      500.00   2000.00 2000.00       1
 0.21578208E+01  0.88579810E-02 -0.73329557E-05  0.30145547E-08 -0.48361741E-12   2
-0.51721137E+05 -0.39677820E+00  0.21578208E+01  0.88579810E-02 -0.73329557E-05   3
 0.30145547E-08 -0.48361741E-12 -0.51721137E+05 -0.39677820E+00                   4
CO(Ni)                  C   1O   1Ni  1    0      500.00   2000.00 2000.00       1
 0.10495840E+01  0.53782555E-02 -0.35189591E-05  0.10632343E-08 -0.11268924E-12   2
-0.27374439E+05  0.76055902E+01  0.10495840E+01  0.53782555E-02 -0.35189591E-05   3
 0.10632343E-08 -0.11268924E-12 -0.27374439E+05  0.76055902E+01                   4
OH(Ni)                  H   1O   1Ni  1    0      500.00   2000.00 2000.00       1
 0.20890550E+01  0.17144390E-02 -0.42783855E-06  0.91121141E-11  0.11376037E-13   2
-0.26733430E+05 -0.38613884E+01  0.20890550E+01  0.17144390E-02 -0.42783855E-06   3
 0.91121141E-11  0.11376037E-13 -0.26733430E+05 -0.38613884E+01                   4
```

```
C(Ni)                    C   1Ni  1    0    0      500.00   2000.00 2000.00       1
-0.34933091E+01  0.52352469E-02 -0.30330892E-05  0.65561104E-09 -0.14096655E-13   2
-0.22312473E+04  0.76842124E+01 -0.34933091E+01  0.52352469E-02 -0.30330892E-05   3
 0.65561104E-09 -0.14096655E-13 -0.22312473E+04  0.76842124E+01                   4
HCO(Ni)                  C   1H   1O   1Ni  1      500.00   2000.00 2000.00       1
 0.14205486E+01  0.64189860E-02 -0.32561122E-05  0.66040647E-09 -0.12595880E-13   2
-0.17229959E+05 -0.13406041E+01  0.14205486E+01  0.64189860E-02 -0.32561122E-05   3
 0.66040647E-09 -0.12595880E-13 -0.17229959E+05 -0.13406041E+01                   4
CH3(Ni)                  C   1H   3Ni  1    0      500.00   2000.00 2000.00       1
-0.61076060E+00  0.86161251E-02 -0.21771493E-05 -0.66381529E-09  0.31381932E-12   2
-0.88979208E+04 -0.20082870E+01 -0.61076060E+00  0.86161251E-02 -0.21771493E-05   3
-0.66381529E-09  0.31381932E-12 -0.88979208E+04 -0.20082870E+01                   4
CH2(Ni)                  C   1H   2Ni  1    0      500.00   2000.00 2000.00       1
-0.15691759E+01  0.73094888E-02 -0.23368400E-05 -0.26357539E-09  0.20887732E-12   2
 0.19430750E+04  0.44426598E+01 -0.15691759E+01  0.73094888E-02 -0.23368400E-05   3
-0.26357539E-09  0.20887732E-12  0.19430750E+04  0.44426598E+01                   4
CH(Ni)                   C   1H   1Ni  1    0      500.00   2000.00 2000.00       1
-0.25276235E+01  0.60029740E-02 -0.24966946E-05  0.13675870E-09  0.10391580E-12   2
 0.95668107E+04  0.74401015E+01 -0.25276235E+01  0.60029740E-02 -0.24966946E-05   3
 0.13675870E-09  0.10391580E-12  0.95668107E+04  0.74401015E+01                   4
COOH(Ni)                 C   1H   1O   2Ni  1      200.00      0.00    0.00       1
 0.30016165E+01  0.54084505E-02 -0.40538058E-06 -0.53422466E-09  0.11451887E-12   2
-0.32752722E+04 -0.10965984E+02  0.12919217E+01  0.72675603E-02  0.98179476E-06   3
-0.20471294E-08  0.90832717E-13 -0.25745610E+04 -0.11983037E+01                   4
```

Symbol	Description	Unit
A_{cat}	catalytic surface area	m^2
A_{geo}	gerometrical surface area	m^2
A_c	Area of cross section of the channel	
A_k	pre-exponential factor	cm, mol, s
a_{jk}	order of reaction *k* of species *j*	
c_i	concentration of species i	$mol.m^{-3}$
c_p	specific heat capacity	$J.kg^{-1}K^{-1}$
E_a	activation energy	$kJ.mol^{-1}$
$F_{cat/geo}$	surface scaling factor	-
G_i	Gibb free energy of species i	$kJmol^{-1}$
h_i	specific enthalpy of species *i*	
J_i	diffusion velocity of species *i*	
k_{fk}	reaction rate coefficient	mol, m,s
k_B	Boltzmann constant	$1.38064x10^{-23}$ J K^{-1}
k^{th}	reaction	
M_i	molecular weight of species *i*	$kg.mol^{-1}$
n_i	number of moles of species *i*	mol
N_A	Avogadro´s number	$6.02x10^{23}$ mol^{-1}
N_g	number of gas-phase species	-
N_s	number of surface species	-
N_b	number of bulk species	*
p	pressure	Pa
r	radius	m
R	gas constant	8.314 $J.(mol.K)^{-1}$
$\dot{s}_i$	molar reaction rate of species *i*	$mol.m^{-2}.s^{-1}$
T	temperature	K
T_w	Temperature of the wall	K
t	time	s
u	axial velocity	$m.s^{-1}$
v	radial velocity	$m.s^{-1}$
V_i	diffusion velocity of species *i*	$m.s^{-1}$
V	normalized velocity	$m.s^{-1}$
x_i	mole fraction of species *i*	-
X_i	conversion of species *i*	-
t	time	s
Y_i	mass fraction of species *i*	$m.s^{-1}$
v_{ik}	stoichiometric coefficients	-

Greek Symbols

Symbol	Description	Unit
Γ	surface site density	$mol.m^{2}$
β_k	temperature exponent	-
ε_i	coverage dependent activation energy	$kJmol^{-1}$
θ_i	surface coverage of species i	-
λ	thermal conductivity	$W.(m.K)_{-1}$
μ	viscosity	$kg.(m.s)^{-1}$
ρ	density	$kg.\ m^{-3}$
$\dot{\omega}_\iota$	molar reaction rate of gas-phase reaction of species i	$mol.m^{-3}.s^{-1}$
$\wedge$	eigenvalue of the momentum	-
$\mathcal{E}$	porosity	-

Abbreviations

AES	Auger Electron Spectroscopy
ATR	Auto-thermal Reforming
C/O	Carbon to Oxygen
C/S	Carbon to Steam
cpsi	Cell Per Square Inch
CPOx	Catalytic Partical Oxidation
DFT	Density Functional Theory
DR	Dry Reforming
DRIFTS	Diffuse reflectance infrared Fourier transform spectroscopy
ESD	Electron-simulated desorption
FTIR	Fourier Transform Infrared Spectroscopy
FGB	Fixed granular bed
GHSV	Gas Hourly Space Velocity (T= 298 K, *p*= 1.013 bar)
HREELS	High-resolution electron energy loss spectroscopy
IR	Infrared
MS	Mass Spectrometer
MC	Monte Carlo simulations
RLS	Rate limiting step
R-WGS	Reverse Water-Gas Shift
SEM	Scanning Electron Microscopy
SLPM	Standard Liter Per Minute (T= 298 K, *p*= 1.013 bar)
SR	Steam Reforming
SFR	Stagnation-flow reactor
SSITKA	Steady-state isotopic transient kinetic analysis
TDS	Thermal desorption spectrometry
TEM	Transmission Electron Miscroscopy
UBI-QUEP	Unit Bond Index-Quadratic Exponential Potential
WGS	Water-Gas Shift
XRD	X-Ray Diffraction

References

[1] J. Rostrup-Nielsen, I. Dybkjaer, K. Aasberg-Petersen, Synthesis gas for large scale Fischer-Tropsch synthesis, American Chemical Society, Division of Petroleum Chemistry, Preprints, 45 (2000) 186-189.

[2] J.R. Rostrup-Nielsen, J. Sehested, J.K. Nørskov, Hydrogen and synthesis gas by steam- and CO_2 reforming, in: Advances in Catalysis, Academic Press, 2002, pp. 65-139.

[3] E. Iglesia, Design, synthesis, and use of cobalt-based Fischer-Tropsch synthesis catalysts, Applied Catalysis A: General, 161 (1997) 59-78.

[4] J.R. Rostrup-Nielsen, New aspects of syngas production and use, Catalysis Today, 63 (2000) 159-164.

[5] D.A. Hickman, L.D. Schmidt, Production of Syngas by Direct Catalytic Oxidation of Methane, Science, 259 (1993) 343-346.

[6] M.A. Pen˜a, J.P. Gómez, J.L.G. Fierro, New catalytic routes for syngas and hydrogen production, Applied Catalysis A: General, 144 (1996) 7-57.

[7] Z. Shao, S.M. Haile, A high-performance cathode for the next generation of solid-oxide fuel cells, Nature, 431 (2004) 170-173.

[8] S. Park, J.M. Vohs, R.J. Gorte, Direct oxidation of hydrocarbons in a solid-oxide fuel cell, Nature, 404 (2000) 265-267.

[9] S.C. Singhal, Advances in solid oxide fuel cell technology, Solid State Ionics, 135 (2000) 305-313.

[10] B.C. Michael, A. Donazzi, L.D. Schmidt, Effects of H_2O and CO_2 addition in catalytic partial oxidation of methane on Rh, Journal of Catalysis, 265 (2009) 117-129.

[11] D. Chen, R. Lødeng, H. Svendsen, A. Holmen, Hierarchical Multiscale Modeling of Methane Steam Reforming Reactions, Industrial & Engineering Chemistry Research, 50 (2010) 2600-2612.

[12] Y.-A. Zhu, D. Chen, X.-G. Zhou, W.-K. Yuan, DFT studies of dry reforming of methane on Ni catalyst, Catalysis Today, 148 (2009) 260-267.

[13] J. Xu, Y. Yang, Y.-W. Li, Fischer–Tropsch synthesis process development: steps from fundamentals to industrial practices, Current Opinion in Chemical Engineering, 2 (2013) 354-362.

[14] D.A. Hickman, L.D. Schmidt, Synthesis gas formation by direct oxidation of methane over Pt monoliths, Journal of Catalysis, 138 (1992) 267-282.

[15] C. Li, C. Yu, S. Shen, Role of the surface state of Ni/Al_2O_3 in partial oxidation of CH_4, Catalysis Letters, 67 (2000) 139-145.

[16] D. Dissanayake, M.P. Rosynek, K.C.C. Kharas, J.H. Lunsford, Partial oxidation of methane to carbon monoxide and hydrogen over a Ni/Al_2O_3 catalyst, Journal of Catalysis, 132 (1991) 117-127.

[17] T. Zhu, M. Flytzani-Stephanopoulos, Catalytic partial oxidation of methane to synthesis gas over $Ni–CeO_2$, Applied Catalysis A: General, 208 (2001) 403-417.

[18] S. Tang, J. Lin, K.L. Tan, Partial oxidation of methane to syngas over Ni/MgO, Ni/CaO and Ni/CeO_2, Catalysis Letters, 51 (1998) 169-175.

[19] M.A. Goula, A.A. Lemonidou, W. Grünert, M. Baerns, Methane partial oxidation to synthesis gas using nickel on calcium aluminate catalysts, Catalysis Today, 32 (1996) 149-156.

[20] Z.-W. Liu, K.-W. Jun, H.-S. Roh, S.-E. Park, Y.-S. Oh, Partial oxidation of methane over nickel catalysts supported on various aluminas, Korean J. Chem. Eng., 19 (2002) 735-741.

[21] P.F. Vernon, M.H. Green, A. Cheetham, A. Ashcroft, Partial oxidation of methane to synthesis gas, Catalysis Letters, 6 (1990) 181-186.

[22] C. Li, C. Yu, S. Shen, Isotopic Studies on the Mechanism of Partial Oxidation of CH_4 to Syngas over a Ni/Al_2O_3 Catalyst, Catalysis Letters, 75 (2001) 183-189.

[23] S. Tang, J. Lin, K.L. Tan, Pulse-MS studies on CH_4/CD_4 isotope effect in the partial oxidation of methane to syngas over $Pt/\alpha\text{-}Al_2O_3$, Catalysis Letters, 55 (1998) 83-86.

[24] R. Schwiedernoch, S. Tischer, C. Correa, O. Deutschmann, Experimental and numerical study on the transient behavior of partial oxidation of methane in a catalytic monolith, Chemical Engineering Science, 58 (2003) 633-642.

[25] H.Y. Wang, E. Ruckenstein, Catalytic partial oxidation of methane to synthesis gas over $\gamma\text{-}Al_2O_2$-supported rhodium catalysts, Catalysis Letters, 59 (1999) 121-127.

[26] S.-B. Kim, Y.-K. Kim, Y.-S. Lim, M.-S. Kim, H.-S. Hahm, Reaction mechanism of partial oxidation of methane to synthesis gas over supported ni catalysts, Korean J. Chem. Eng., 20 (2003) 1023-1025.

[27] V.R. Choudhary, A.M. Rajput, B. Prabhakar, Nonequilibrium Oxidative Conversion of Methane to CO and H_2 with High Selectivity and Productivity over Ni/Al_2O_3 at Low Temperatures, Journal of Catalysis, 139 (1993) 326-328.

[28] R. Schwiedernoch, S. Tischer, C. Correa, O. Deutschmann, Experimental and numerical study on the transient behavior of partial oxidation of methane in a catalytic, monolith, Chemical Engineering Science, 58 (2003) 633-642.

[29] M. Bizzi, G. Saracco, R. Schwiedernoch, O. Deutschmann, Modeling the partial oxidation of methane in a fixed bed with detailed chemistry, Aiche Journal, 50 (2004) 1289-1299.

[30] R. Schwiedernoch, S. Tischer, H.R. Volpp, O. Deutschmann, Towards a better understanding of transient processes in catalytic oxidation reactors, in: X. Bao, Y. Xu (Eds.) Natural Gas Conversion Vii, 2004, pp. 511-516.

[31] J.N. Bär, C. Karakaya, O. Deutschmann, Catalytic ignition of light hydrocarbons over Rh/Al_2O_3 studied in a stagnation-point flow reactor, Proceedings of the Combustion Institute, 34 (2013) 2313-2320.

[32] C. Diehm, Catalytic Reforming of Fuels over Noble Metal-Coated Honeycomb Monoliths: Capillary-Based In-Situ Sampling Technique
in: Institute for Chemical Technology and Polymer Chemistry, Fakultät für Chemie und Biowissenschaften, Karlsruhe Institute of Technology 2013.

[33] O. Deutschmann, L.D. Schmidt, Modeling the partial oxidation of methane in a short-contact-time reactor, AIChE Journal, 44 (1998) 2465-2477.

[34] F. Behrendt, O. Deutschmann, U. Maas, J. Warnatz, Simulation and sensitivity analysis of the heterogeneous oxidation of methane on a platinum foil, Journal of Vacuum Science & Technology A, 13 (1995) 1373-1377.

[35] O. Deutschmann, L.D. Schmidt, Two-dimensional modeling of partial oxidation of methane on rhodium in a short contact time reactor, Symposium (International) on Combustion, 27 (1998) 2283-2291.

[36] M. Hartmann, L. Maier, H.D. Minh, O. Deutschmann, Catalytic partial oxidation of iso-octane over rhodium catalysts: An experimental, modeling, and simulation study, Combustion and Flame, 157 (2010) 1771-1782.

[37] J. Rostrup-Nielsen, I. Dybkjaer, Proceedings of the European Congress on Chemical Engineering, in: European Congress on Chemical Engineering, Firenze, 1997, pp. 3.

[38] J.R. Rostrup-Nielsen, Sulfur-Passivated Nickel-Catalysts for Carbon-Free Steam Reforming of Methane, Journal of Catalysis, 85 (1984) 31-43.

[39] D.L. Trimm, Formation and Removal of Coke from Nickel-Catalyst, Catalysis Reviews-Science and Engineering, 16 (1977) 155-189.

[40] C.H. Bartholomew, Carbon Deposition in Steam Reforming and Methanation, Catal Rev, 24 (1982) 67-112.

[41] E.A. Blekkan, R. Myrstad, O. Olsvik, O.A. Rokstad, Characterization of Tars and Coke Formed during the Pyrolysis of Methane in a Tubular Reactor, Carbon, 30 (1992) 665-673.

[42] L.C.S. Kahle, T. Roussière, L. Maier, K. Herrera Delgado, G. Wasserschaff, S.A. Schunk, O. Deutschmann, Methane Dry Reforming at High Temperature and Elevated Pressure: Impact of Gas-Phase Reactions, Industrial & Engineering Chemistry Research, 52 (2013) 11920-11930.

[43] J.R.H. Ross, A.N.J. vanKeulen, M.E.S. Hegarty, K. Seshan, The catalytic conversion of natural gas to useful products, Catalysis Today, 30 (1996) 193-199.

[44] D. Chen, R. Lodeng, A. Anundskas, O. Olsvik, A. Holmen, Deactivation during carbon dioxide reforming of methane over Ni catalyst: microkinetic analysis, Chemical Engineering Science, 56 (2001) 1371-1379.

[45] J.M. Ginsburg, J. Pina, T. El Solh, H.I. de Lasa, Coke formation over a nickel catalyst under methane dry reforming conditions: Thermodynamic and kinetic models, Industrial & Engineering Chemistry Research, 44 (2005) 4846-4854.

[46] J. Guo, H. Lou, X.M. Zheng, The deposition of coke from methane on a Ni/$MgAl_2O_4$ catalyst, Carbon, 45 (2007) 1314-1321.

[47] D. Chen, R. Lødeng, A. Anundskås, O. Olsvik, A. Holmen, Deactivation during carbon dioxide reforming of methane over Ni catalyst: microkinetic analysis, Chemical Engineering Science, 56 (2001) 1371-1379.

[48] S. Corthals, T. Witvrouwen, P. Jacobs, B. Sels, Development of dry reforming catalysts at elevated pressure: D-optimal vs. full factorial design, Catalysis Today, 159 (2011) 12-24.

[49] K. Tomishige, K. Fujimoto, Ultra-stable Ni catalysts for methane reforming by carbon dioxide, Catalysis Surveys from Asia, 2 (1998) 3-15.

[50] C. Zhou, L. Zhang, A. Swiderski, W. Yang, W. Blasiak, Study and development of a high temperature process of multi-reformation of CH_4 with CO_2 for remediation of greenhouse gas, Energy, 36 (2011) 5450-5459.

[51] J. Xu, G.F. Froment, Methane steam reforming, methanation and water-gas shift: I. Intrinsic kinetics, AIChE Journal, 35 (1989) 88-96.

[52] M.C.J. Bradford, M.A. Vannice, CO_2 reforming of CH_4, Catalysis Reviews, 41 (1999) 1-42.

[53] L.M. Aparicio, Transient Isotopic Studies and Microkinetic Modeling of Methane Reforming over Nickel Catalysts, Journal of Catalysis, 165 (1997) 262-274.

[54] J. Wei, E. Iglesia, Isotopic and kinetic assessment of the mechanism of reactions of CH_4 with CO_2 or H_2O to form synthesis gas and carbon on nickel catalysts, Journal of Catalysis, 224 (2004) 370-383.

[55] D.W. Blaylock, Y.-A. Zhu, W. Green, Computational Investigation of the Thermochemistry and Kinetics of Steam Methane Reforming Over a Multi-Faceted Nickel Catalyst, Top Catal, 54 (2011) 828-844.

[56] J.G. Amar, The Monte Carlo method in science and engineering, Computing in Science & Engineering, 8 (2006) 9-19.

[57] H. Sellers, The generalized UBI-QEP method for modeling the energetics of reactions on transition metal surfaces, Surface Science, 524 (2003) 29-39.

[58] L. Maier, B. Schädel, K. Herrera Delgado, S. Tischer, O. Deutschmann, Steam Reforming of Methane Over Nickel: Development of a Multi-Step Surface Reaction Mechanism, Top Catal, 54 (2011) 845-858.

[59] V.M. Janardhanan, O. Deutschmann, CFD analysis of a solid oxide fuel cell with internal reforming: Coupled interactions of transport, heterogeneous catalysis and electrochemical processes, Journal of Power Sources, 162 (2006) 1192-1202.

[60] O. Deutschmann, in: O. Deutschmann (Ed.) Modeling and Simulation of Heterogeneous Catalytic Reactions, Wiley-VCH Verlag GmbH & Co. KGaA, 2011, pp. 113-143.

[61] F.E. Kühn, Catalysis. From Principles to Applications. By Matthias Beller, Albert Renken and Rutger A. van Santen, Angewandte Chemie International Edition, 52 (2013) 2650-2650.

[62] O. Deutschmann, High temperature catalysis: role of heterogeneous, homogeneous, and radical chemistry, in: R. Beller, van Santen (Eds.) (Ed.) Catalysis, Wiley-VCH Verlag, Weinheim, 2011, pp. 365-385.

[63] R.J. Kee, M.E. Coltrin, P. Glarborg, Chemically Reacting Flow:Theory and Practice, Wiley-Interscience, 2003.

[64] L.C.S. Kahle, Reaktionskinetik der Oxidation und Reformierung von H_2, CO und CH_4 über Platinkatalysatoren, in: Fakultät für Chemie und Biowissenschaften, Karlsruher Institut für Technologie (KIT), Germany
2013.

[65] J. Warnatz, M.D. Allendorf, R.J. Kee, M.E. Coltrin, A model of elementary chemistry and fluid mechanics in the combustion of hydrogen on platinum surfaces, Combustion and Flame, 96 (1994) 393-406.

[66] L. Kunz, L. Maier, S. Tischer, O. Deutschmann, Modeling the Rate of Heterogeneous Reactions, in: Modeling and Simulation of Heterogeneous Catalytic Reactions, Wiley-VCH Verlag GmbH & Co. KGaA, 2011, pp. 113-148.

[67] O. Deutschmann, H. Knözinger, K. Kochloefl, T. Turek, Heterogeneous Catalysis and Solid Catalysts, 1. Fundamentals, in: Ullmann's Encyclopedia of Industrial Chemistry, Wiley-VCH Verlag GmbH & Co. KGaA, 2000.

[68] O. Deutschmann, Computational Fluid Dynamics Simulation of Catalytic Reactors, in: H.K.G. Erlt, F. Schüth, J. Weitkamp (Eds.) Handbook of Heterogeneous Catalysis, Wiley-VCH Verlag GmbH & Co. KGaA, 2008, pp. 1811-1828.

[69] A.P.J. Jansen, J.J. Lukkien, Dynamic Monte-Carlo simulations of reactions in heterogeneous catalysis, Catalysis Today, 53 (1999) 259-271.

[70] A. Chatterjee, D. Vlachos, An overview of spatial microscopic and accelerated kinetic Monte Carlo methods, J Computer-Aided Mater Des, 14 (2007) 253-308.

[71] J.A. Dumesic, D.F. Rudd, L.M. Aparicio, J.E. Rekoske, A.A. Treviño, The microkinetics of heterogeneous catalysis. ACS Professional Reference Book, American Chemical Society, Washington, DC, , 1993.

[72] R.-N. JR, Catalytic steam reforming in catalysis—science and technology, Springer-Verlag, 1984.

[73] D.W. Blaylock, T. Ogura, W.H. Green, G.J.O. Beran, Computational Investigation of Thermochemistry and Kinetics of Steam Methane Reforming on Ni(111) under Realistic Conditions, J Phys Chem C Nanomater Interfaces, 113 (2009) 4898-4908.

[74] E. Shustorovich, H. Sellers, The UBI-QEP method: A practical theoretical approach to understanding chemistry on transition metal surfaces, Surface Science Reports, 31 (1998) 1-119.

[75] E.M. Shustorovich, A.V. Zeigarnik, The UBI-QEP method: Basic formalism and applications to chemisorption phenomena on transition metal surfaces. Chemisorption energetics, Russ. J. Phys. Chem., 80 (2006) 4-30.

[76] E. Schwab, A. Milanov, S.A. Schunk, T. Roussière, G. Wasserschaff, N. Schödel, A. Behrens, O. Deutschmann, L.C.S. Kahle, K. Herrera Delgado, R. Gläser, B. Stoltze, J. Titus, J.A. Lercher, A. Jentys, L. Schulz, Dry Reforming of CH_4 with CO_2 at Elevated Pressures. , in, International Congress on Catalysis, München, Deutschland, 2012.

[77] O. Deutschmann, S. Tischer, S. Kleditzsch, V.M. Janardhanan, C. Correa, D. Chatterjee, N. Mladenov, H.D. Minh, DETCHEM^{TM} Software package, (2013).

[78] L.L. Raja, R.J. Kee, O. Deutschmann, J. Warnatz, L. D. Schmidt, A critical evaluation of Navier–Stokes, boundary-layer, and plug-flow models of the flow and chemistry in a catalytic-combustion monolith, Catalysis Today, 59 (2000) 47-60.

[79] J. Warnatz, M.D. Allendorf, R.J. Kee, M.E. Coltrin, A Model of Elementary Chemistry and Fluid-Mechanics in the Combustion of Hydrogen on Platinum Surfaces, Combustion and Flame, 96 (1994) 393-406.

[80] R.W. Sidwell, H.Y. Zhu, R.J. Kee, D.T. Wickham, C. Schell, G.S. Jackson, Catalytic combustion of premixed methane/air on a palladium-substituted hexaluminate stagnation surface, Proceedings of the Combustion Institute, 29 (2002) 1013-1020.

[81] C. Karakaya, O. Deutschmann, Kinetics of hydrogen oxidation on Rh/Al_2O_3 catalysts studied in a stagnation-flow reactor, Chemical Engineering Science, 89 (2013) 171-184.

[82] H. Karadeniz, C. Karakaya, S. Tischer, O. Deutschmann, Numerical modeling of stagnation-flows on porous catalytic surfaces: CO oxidation on Rh/Al_2O_3, Chemical Engineering Science, 104 (2013) 899-907.

[83] H. Karadeniz, C. Karakaya, S. Tischer, O. Deutschmann, Numerical modeling of stagnation-flows on porous catalytic surfaces: CO oxidation on Rh/Al_2O_3, Chemical Engineering Science.

[84] A.M. De Groote, G.F. Froment, T. Kobylinski, Synthesis gas production from natural gas in a fixed bed reactor with reversed flow, The Canadian Journal of Chemical Engineering, 74 (1996) 735-742.

[85] H. Jakobsen, Packed Bed Reactors, in: Chemical Reactor Modeling, Springer Berlin Heidelberg, 2008, pp. 953-984.

[86] E. Gerhart, Fixed Bed Reactors, in: Ullmann's Encyclopedia of Industnal Chemistry, 1992, pp. 199-238.

[87] T. Kaltschmitt, Catalytic Partial Oxidation of higher Hydrocarbon Fuels for Hydrogen Production: Process Investigation with regard to the Concept of an Auxiliary Power Unit. Dissertation (in: Department of Chemistry and Biosciences, Karlsruhe Institute of Technology (Germany), 2012.

[88] A.S. Pushnov, Calculation of average bed porosity, Chem Petrol Eng, 42 (2006) 14-17.

[89] N.E. McGuire, N.P. Sullivan, O. Deutschmann, H. Zhu, R.J. Kee, Dry reforming of methane in a stagnation-flow reactor using Rh supported on strontium-substituted hexaaluminate, Applied Catalysis A: General, 394 (2011) 257-265.

[90] C. Karakaya, A Novel, Hierarchically Developed Surface Kinetics for Oxidation and Reforming of Methane and Propane over Rh/Al_2O_3, in: Faculty of Chemistry and Bioscience, Karlsruhe Institute of Technology, 2012, pp. 144.

[91] M. Hartmann, L. Maier, O. Deutschmann, Hydrogen production by catalytic partial oxidation of iso-octane at varying flow rate and fuel/oxygen ratio: From detailed kinetics to reactor behavior, Applied Catalysis A: General, 391 (2011) 144-152.

[92] M.B. Lee, Q.Y. Yang, S.L. Tang, S.T. Ceyer, Activated dissociative chemisorption of CH_4 on Ni(111): Observation of a methyl radical and implication for the pressure gap in catalysis, The Journal of Chemical Physics, 85 (1986) 1693-1694.

[93] S.-G. Wang, X.-Y. Liao, J. Hu, D.-B. Cao, Y.-W. Li, J. Wang, H. Jiao, Kinetic aspect of CO_2 reforming of CH_4 on Ni(111): A density functional theory calculation, Surface Science, 601 (2007) 1271-1284.

[94] E. Shustorovich, Reaction Energetics on Transition Metal Surfaces: A Bond-Order Conservation Approach, in: F. Ruette (Ed.) Quantum Chemistry Approaches to Chemisorption and Heterogeneous Catalysis, Springer Netherlands, 1992, pp. 231-252.

[95] T.P. Beebe, D.W. Goodman, B.D. Kay, J.T. Yates, Kinetics of the activated dissociative adsorption of methane on the low index planes of nickel single crystal surfaces, The Journal of Chemical Physics, 87 (1987) 2305-2315.

[96] P. Kratzer, B. Hammer, J.K. No/rskov, A theoretical study of CH_4 dissociation on pure and gold-alloyed Ni(111) surfaces, The Journal of Chemical Physics, 105 (1996) 5595-5604.

[97] R.J. Kee, M.E. Coltrin, P. Glarborg, Chemically Reacting Flow, Theory and Practice
John Wiley & Sons, (2005).

[98] S. Joh, G.H. Evans, Heat transfer and flow stability in a rotating disk/stagnation flow chemical vapor deposition reactor, Numerical Heat Transfer; Part A: Applications, 31 (1997) 867-879.

[99] C. Treviño, Catalytic ignition of very lean mixtures of hydrogen, International Journal of Hydrogen Energy, 36 (2011) 8610-8618.

[100] J.T. Yates Jr, P.A. Thiel, W.H. Weinberg, The catalytic reaction between adsorbed oxygen and hydrogen on Rh(111), Surface Science, 82 (1979) 45-68.

[101] R. Ramachandran, R.K. Menon, An overview of industrial uses of hydrogen, International Journal of Hydrogen Energy, 23 (1998) 593-598.

[102] J.D. Holladay, J. Hu, D.L. King, Y. Wang, An overview of hydrogen production technologies, Catalysis Today, 139 (2009) 244-260.

[103] M. Ó Conaire, H.J. Curran, J.M. Simmie, W.J. Pitz, C.K. Westbrook, A comprehensive modeling study of hydrogen oxidation, International Journal of Chemical Kinetics, 36 (2004) 603-622.

[104] V.P. Zhukov, Verification, Validation, and Testing of Kinetic Mechanisms of Hydrogen Combustion in Fluid-Dynamic Computations, ISRN Mechanical Engineering, 2012 (2012) 11.

[105] M. Rinnemo, O. Deutschmann, F. Behrendt, B. Kasemo, Experimental and numerical investigation of the catalytic ignition of mixtures of hydrogen and oxygen on platinum, Combustion and Flame, 111 (1997) 312-326.

[106] A.T. Larson, F.E. Smith, The synthesis of water over nickel and copper catalyst J. Am. Chem. Soc, 47 (1925) 346.

[107] H. Arif, M. Stoukides, Rate and oxygen activity oscillations during hydrogen oxidation on nickel films in a CSTR, (1986).

[108] A.G. Sault, R.I. Masel, The effect of surface protrusions on self-sustained thermal oscillations during hydrogen oxidation on a nickel foil, Journal of Catalysis, 73 (1982) 294-308.

[109] J.E. Zuniga, D. Luss, Kinetic oscillations during the isothermal oxidation of hydrogen on platinum wires, Journal of Catalysis, 53 (1978) 312-320.

[110] D. Kulginov, V.P. Zhdanov, B. Kasemo, Oscillatory surface reaction kinetics due to coupling of bistability and diffusion limitations, The Journal of Chemical Physics, 106 (1997) 3117-3128.

[111] J.R. Brown, G.A. D'Netto, R.A. Schmitz, Spatial effects and oscillations in heterogeneous catalytic reactions, in: L. Rensing, N. Jaeger (Eds.) Temporal Order, Springer Berlin Heidelberg, 1985, pp. 86-95.

[112] S. Wilke, V. Natoli, M.H. Cohen, Theoretical investigation of water formation on Rh and Pt Surfaces, The Journal of Chemical Physics, 112 (2000) 9986-9995.

[113] C. Saranteas, M. Stoukides, Solid-electrolyte-aided study of hydrogen oxidation on nickel, Journal of Catalysis, 93 (1985) 417-429.

[114] G. Ertl, Kinetics of Chemical Processes on Well-defined Surfaces, in: J. Anderson, M. Boudart (Eds.) Catalysis, Springer Berlin Heidelberg, 1983, pp. 209-282.

[115] P.R. Norton, The Hydrogen-Oxygen Reaction on Metal Surfaces in: The Chemical Physics of Solid Surfaces and Heterogeneous Catalysis, D.A. King and D. P. Woodruff, eds. Elsevier., Amsterdam, 1982, pp. 27.

[116] A.B. Mhadeshwar, D.G. Vlachos, Hierarchical, multiscale surface reaction mechanism development: CO and H2 oxidation, water–gas shift, and preferential oxidation of CO on Rh, Journal of Catalysis, 234 (2005) 48-63.

[117] M. Maestri, A. Beretta, T. Faravelli, G. Groppi, E. Tronconi, D.G. Vlachos, Two-dimensional detailed modeling of fuel-rich combustion over catalyst, Chemical Engineering Science, 63 (2008) 2657-2669.

[118] O. Deutschmann, Modellierung von reaktionen an oberflächen und deren kopplung mit chemish reagierenden strömungen, in: Naturwissenschaftlich-Mathematischen Gesamtfakultät, Ruprecht-Karls-Universität Heidelberg (Germany), 1996.

[119] J. Rostrup-Nielsen, Catalytic Steam Reforming, in: J. Anderson, M. Boudart (Eds.) Catalysis, Springer Berlin Heidelberg, 1984, pp. 1-117.

[120] H.S. Bengaard, J.K. Nørskov, J. Sehested, B.S. Clausen, L.P. Nielsen, A.M. Molenbroek, J.R. Rostrup-Nielsen, Steam reforming and graphite formation on Ni catalysts, Journal of Catalysis, 209 (2002) 365-384.

[121] R.V. Kasza, K. Griffiths, J.G. Shapter, P.R. Norton, D.A. Harrington, Interaction of water with stepped Ni(760): associative versus dissociative adsorption and autocatalytic decomposition, Surface Science, 356 (1996) 195-208.

[122] C. Mundt, C. Benndorf, Influence of steps on the H_2O adsorption on Ni(111), Surface Science, 287–288, Part 1 (1993) 119-124.

[123] A. Winkler, K.D. Rendulic, Adsorption kinetics for hydrogen adsorption on nickel and coadsorption of hydrogen and oxygen, Surface Science, 118 (1982) 19-31.

[124] K.D. Rendulic, A. Winkler, H.P. Steinrück, The role of surface defects in the adsorption and sesorption of hydrogen on Ni(111), Surface Science, 185 (1987) 469-478.

[125] K.D. Rendulic, A. Winkler, H. Karner, Adsorption kinetics of H2/Ni and its dependence on surface structure, surface impurities, gas temperature, and angle of incidence, Journal of Vacuum Science & Technology A, 5 (1987) 488-491.

[126] K.D. Rendulic, G. Anger, A. Winkler, Wide range nozzle beam adsorption data for the systems H2/nickel and H2/Pd(100), Surface Science, 208 (1989) 404-424.

[127] J.T. Stuckless, C.E. Wartnaby, N. Al-Sarraf, S.J.B. Dixon-Warren, M. Kovar, D.A. King, Oxygen chemisorption and oxide film growth on Ni{100}, {110}, and {111}: Sticking probabilities and microcalorimetric adsorption heats, The Journal of Chemical Physics, 106 (1997) 2012-2030.

[128] A. Winkler, K.D. Rendulic, K. Wendl, Quantitative measurement of the sticking coefficient for oxygen on nickel, Applications of Surface Science, 14 (1983) 209-220.

[129] K. Christmann, Introduction to Surface Physical Chemistry, Steinkopf Verlag, Darmstadt, New York, 1991.

[130] H.P. Steinrück, K.D. Rendulic, A. Winkler, The sticking coefficient of H_2 on Ni(111) as a function of particle energy and angle of incidence: A test of detailed balancing, Surface Science, 154 (1985) 99-108.

[131] H. Pölzl, G. Strohmeier, A. Winkler, Adsorption and abstraction of H(D) on clean and modified Al(111) and Ni(111) surfaces, The Journal of Chemical Physics, 110 (1999) 1154-1162.

[132] C. Bartholomew, Hydrogen adsorption on supported cobalt, iron, and nickel, Catalysis Letters, 7 (1990) 27-51.

[133] G.D. Weatherbee, C.H. Bartholomew, Effects of support on hydrogen adsorption/desorption kinetics of nickel, Journal of Catalysis, 87 (1984) 55-65.

[134] P. Kratzer, B. Hammer, J.K. Norskov, A theoretical study of CH_4 dissociation on pure and gold-alloyed Ni(111) surfaces, The Journal of Chemical Physics, 105 (1996) 5595-5604.

[135] X.Y. Zhu, J.M. White, Hydrogen interaction with nickel(100): a static secondary ion mass spectroscopy study, The Journal of Physical Chemistry, 92 (1988) 3970-3974.

[136] P.E.M. Siegbahn, U. Wahlgren, A theoretical study of atomic oxygen chemisorption on the Ni(100) and Ni(111) surfaces, International Journal of Quantum Chemistry, 42 (1992) 1149-1169.

[137] R.H. Stulen, P.A. Thiel, Electron-stimulated desorption and thermal desorption spectrometry of H_2O on nickel (111), Surf Sci 157 (1985) 99-118.

[138] T. Pache, H.P. Steinrück, W. Huber, D. Menzel, The adsorption of H_2O on clean and oxygen precovered Ni(111) studied by ARUPS and TPD, Surface Science, 224 (1989) 195-214.

[139] I.I. Zakharov, V.I. Avdeev, G.M. Zhidomirov, Non-empirical cluster model calculations of the adsorption of H_2O on Ni(111), Surface Science, 277 (1992) 407-413.

[140] A.K. Santra, D.W. Goodman, Catalytic oxidation of CO by platinum group metals: from ultrahigh vacuum to elevated pressures, Electrochimica Acta, 47 (2002) 3595-3609.

[141] J. Szanyi, D.W. Goodman, Surface science and kinetic studies on model Cu/Rh(100) catalysts, in: F.S. L. Guczi, T. P (Eds.) Studies in Surface Science and Catalysis, Elsevier, 1993, pp. 1599-1602.

[142] G.-C. Wang, Jiao, X.-H. Bu, Detailed mechanism for CO oxidation on $AuNi_3$(111) extended surface: A density functional theory study, The Journal of Physical Chemistry C, 111 (2007) 12335-12339.

[143] J.H.B.J. Hoebink, A.J.L. Nievergeld, G.B. Marin, CO oxidation in a fixed bed reactor with high frequency cycling of the feed, Chemical Engineering Science, 54 (1999) 4459-4468.

[144] J. Szanyi, W.K. Kuhn, D.W. Goodman, CO oxidation on palladium. 2. A combined kinetic-infrared reflection absorption spectroscopic study of Pd(111), The Journal of Physical Chemistry, 98 (1994) 2978-2981.

[145] J. Anderson, CO oxidation over alumina supported platinum catalyst, Catalysis Letters, 13 (1992) 363-369.

[146] B. L'vov, A. Galwey, Catalytic oxidation of CO on platinum, J Therm Anal Calorim, 111 (2013) 145-154.

[147] K. Sakuma, K. Miyajima, F. Mafuné, Oxidation of CO by nickel oxide clusters revealed by post heating, The Journal of Physical Chemistry A, 117 (2013) 3260-3265.

[148] J.T. Kummer, Use of noble metals in automobile exhaust catalysts, The Journal of Physical Chemistry, 90 (1986) 4747-4752.

[149] W. Boll, S. Tischer, O. Deutschmann, Loading and aging effects in exhaust gas after-treatment catalysts with Pt as active component, Industrial & Engineering Chemistry Research, 49 (2010) 10303-10310.

[150] D. Chatterjee, O. Deutschmann, J. Warnatz, Detailed surface reaction mechanism in a three-way catalyst, Faraday Discussions, 119 (2002) 371-384.

[151] E. Perry Murray, T. Tsai, S.A. Barnett, A direct-methane fuel cell with a ceria-based anode, Nature, 400 (1999) 649-651.

[152] J. Knudsen, L.R. Merte, G. Peng, R.T. Vang, A. Resta, E. Lægsgaard, J.N. Andersen, M. Mavrikakis, F. Besenbacher, Low-temperature CO oxidation on Ni(111) and on a Au/Ni(111) surface alloy, ACS Nano, 4 (2010) 4380-4387.

[153] C. Laberty, C. Marquez-Alvarez, C. Drouet, P. Alphonse, C. Mirodatos, CO oxidation over nonstoichiometric nickel manganite spinels, Journal of Catalysis, 198 (2001) 266-276.

[154] G. Parravano, The catalytic oxidation of carbon monoxide on nickel oxide. I. Pure nickel oxide, Journal of the American Chemical Society, 75 (1953) 1448-1451.

[155] L. Mond, C. Langer, F. Quincke, L.-Action of carbon monoxide on nickel, Journal of the Chemical Society, Transactions, 57 (1890) 749-753.

[156] B. Christian Enger, R. Lødeng, A. Holmen, A review of catalytic partial oxidation of methane to synthesis gas with emphasis on reaction mechanisms over transition metal catalysts, Applied Catalysis A: General, 346 (2008) 1-27.

[157] M.P. D'Evelyn, R.J. Madix, Reactive scattering from solid surfaces, Surface Science Reports, 3 (1983) 413-495.

[158] A. Boisen, T.V.W. Janssens, N. Schumacher, I. Chorkendorff, S. Dahl, Support effects and catalytic trends for water gas shift activity of transition metals, Journal of Molecular Catalysis A: Chemical, 315 (2010) 163-170.

[159] E. Bjorgum, D. Chen, M.G. Bakken, K.O. Christensen, A. Holmen, O. Lytken, I. Chorkendorff, Energetic mapping of Ni catalysts by detailed kinetic modeling, The journal of physical chemistry. B, 109 (2005) 2360-2370.

[160] N. Al-Sarraf, J.T. Stuckless, C.E. Wartnaby, D.A. King, Adsorption microcalorimetry and sticking probabilities on metal single crystal surfaces, Surface Science, 283 (1993) 427-437.

[161] J.B. Benziger, R.J. Madix, The decomposition of formic acid on Ni(100), Surface Science, 79 (1979) 394-412.

[162] B.Z. Nikolic, H. Huang, D. Gervasio, A. Lin, C. Fierro, R.R. Adzic, E.B. Yeager, Electroreduction of carbon-dioxide on platinum single-crystal electrodes - electrochemical and insitu FTIR studies, Journal of Electroanalytical Chemistry, 295 (1990) 415-423.

[163] A. Rodes, E. Pastor, T. Iwasita, Carbon-dioxide reduction on platinum single-crystal surfaces - voltammetric and ftirs results, Anales De Quimica, 89 (1993) 458-464.

[164] F. Solymosi, The bonding, structure and reactions of CO_2 adsorbed on clean and promoted metal-surfaces, Journal of Molecular Catalysis, 65 (1991) 337-358.

[165] S.-G. Wang, D.-B. Cao, Y.-W. Li, J. Wang, H. Jiao, Chemisorption of CO_2 on Nickel Surfaces, The Journal of Physical Chemistry B, 109 (2005) 18956-18963.

[166] M.V. Twigg, Catalyst handbook/ edited by Martyn V in: M.V. Twigg (Ed.), Manson Pub, London, 1996.

[167] L. Bollmann, J.L. Ratts, A.M. Joshi, W.D. Williams, J. Pazmino, Y.V. Joshi, J.T. Miller, A.J. Kropf, W.N. Delgass, F.H. Ribeiro, Effect of Zn addition on the water–gas shift reaction over supported palladium catalysts, Journal of Catalysis, 257 (2008) 43-54.

[168] J.R. Rostrup-Nielsen, J. Sehested, J.K. Nørskov, Hydrogen and synthesis gas by steam- and C02 reforming, in: Advances in Catalysis, Academic Press, 2002, pp. 65-139.

[169] C.H. Bartholomew, J.F. Farrauto, Fundamentals of Industrial Catalytic Processes, Wiley Interscience, New York, 2006.

[170] T. Bunluesin, R.J. Gorte, G.W. Graham, Studies of the water-gas-shift reaction on ceria-supported Pt, Pd, and Rh: Implications for oxygen-storage properties, Applied Catalysis B: Environmental, 15 (1998) 107-114.

[171] S. Hilaire, X. Wang, T. Luo, R.J. Gorte, J. Wagner, A comparative study of water-gas-shift reaction over ceria supported metallic catalysts, Applied Catalysis A: General, 215 (2001) 271-278.

[172] G. Jacobs, P.M. Patterson, L. Williams, E. Chenu, D. Sparks, G. Thomas, B.H. Davis, Water-gas shift: in situ spectroscopic studies of noble metal promoted ceria catalysts for CO removal in fuel cell reformers and mechanistic implications, Applied Catalysis A: General, 262 (2004) 177-187.

[173] J. Sun, J. DesJardins, J. Buglass, K. Liu, Noble metal water gas shift catalysis: Kinetics study and reactor design, International Journal of Hydrogen Energy, 30 (2005) 1259-1264.

[174] S.H. Kim, S.-W. Nam, T.-H. Lim, H.-I. Lee, Effect of pretreatment on the activity of Ni catalyst for CO removal reaction by water–gas shift and methanation, Applied Catalysis B: Environmental, 81 (2008) 97-104.

[175] Y. Li, Q. Fu, M. Flytzani-Stephanopoulos, Low-temperature water-gas shift reaction over Cu- and Ni-loaded cerium oxide catalysts, Applied Catalysis B: Environmental, 27 (2000) 179-191.

[176] P. Mierczynski, W. Maniukiewicz, T. Maniecki, Comparative studies of Pd, Ru, Ni, Cu/$ZnAl_2O_4$ catalysts for the water gas shift reaction, cent.eur.j.chem., 11 (2013) 912-919.

[177] D.C. Grenoble, M.M. Estadt, D.F. Ollis, The chemistry and catalysis of the water gas shift reaction: 1. The kinetics over supported metal catalysts, Journal of Catalysis, 67 (1981) 90-102.

[178] T. Salmi, R. Hakkarainen, Kinetic study of the low-temperature water-gas shift reaction over a Cu—ZnO catalyst, Applied Catalysis, 49 (1989) 285-306.

[179] M.J.L. Ginés, A.J. Marchi, C.R. Apesteguía, Kinetic study of the reverse water-gas shift reaction over $CuO/ZnO/Al_2O_3$ catalysts, Applied Catalysis A: General, 154 (1997) 155-171.

[180] D. Andreeva, I. Ivanov, L. Ilieva, J. Sobczak, G. Avdeev, K. Petrov, Gold based catalysts on ceria and ceria-alumina for WGS reaction (WGS Gold catalysts), Top Catal, 44 (2007) 173-182.

[181] G. Jacobs, U.M. Graham, E. Chenu, P.M. Patterson, A. Dozier, B.H. Davis, Low-temperature water–gas shift: impact of Pt promoter loading on the partial reduction of ceria and consequences for catalyst design, Journal of Catalysis, 229 (2005) 499-512.

[182] A. Goguet, S.O. Shekhtman, R. Burch, C. Hardacre, F.C. Meunier, G.S. Yablonsky, Pulse-response TAP studies of the reverse water–gas shift reaction over a Pt/CeO_2 catalyst, Journal of Catalysis, 237 (2006) 102-110.

[183] A. Andreev, V. Idakiev, K. Kostov, M. Gabrovska, Water-gas shift reaction over nickel hydroxides, Catalysis Letters, 31 (1995) 245-252.

[184] G. Jacobs, P.M. Patterson, U.M. Graham, A.C. Crawford, B.H. Davis, Low temperature water gas shift: the link between the catalysis of WGS and formic acid decomposition over Pt/ceria, International Journal of Hydrogen Energy, 30 (2005) 1265-1276.

[185] G. Jacobs, L. Williams, U. Graham, D. Sparks, B.H. Davis, Low-temperature Water-Gas Shift: In-Situ DRIFTS−Reaction study of a Pt/CeO_2 catalyst for fuel cell reformer applications, The Journal of Physical Chemistry B, 107 (2003) 10398-10404.

[186] C.M. Kalamaras, G.G. Olympiou, A.M. Efstathiou, The water-gas shift reaction on $Pt/\gamma\text{-}Al_2O_3$ catalyst: Operando SSITKA-DRIFTS-mass spectroscopy studies, Catalysis Today, 138 (2008) 228-234.

[187] G. Jacobs, P.M. Patterson, U.M. Graham, D.E. Sparks, B.H. Davis, Low temperature water-gas shift: kinetic isotope effect observed for decomposition of surface formates for Pt/ceria catalysts, Applied Catalysis A: General, 269 (2004) 63-73.

[188] D. Tibiletti, A. Goguet, D. Reid, F.C. Meunier, R. Burch, On the need to use steady-state or operando techniques to investigate reaction mechanisms: An in situ DRIFTS and SSITKA-based study example, Catalysis Today, 113 (2006) 94-101.

[189] T. Shido, Y. Iwasawa, Reactant-promoted reaction mechanism for Water-Gas Shift reaction on Rh-Doped CeO_2, Journal of Catalysis, 141 (1993) 71-81.

[190] T.S. Jones, M.R. Ashton, N.V. Richardson, An electron energy loss study of the surface formate species chemisorbed on Ni(110): Dipole, impact, and resonance scattering for adsorbate covered surfaces, The Journal of Chemical Physics, 90 (1989) 7564-7576.

[191] C.V. Ovesen, P. Stoltze, J.K. Nørskov, C.T. Campbell, A kinetic model of the water gas shift reaction, Journal of Catalysis, 134 (1992) 445-468.

[192] I. Fishtik, R. Datta, A UBI–QEP microkinetic model for the water–gas shift reaction on Cu(111), Surface Science, 512 (2002) 229-254.

[193] A.A. Gokhale, J.A. Dumesic, M. Mavrikakis, On the mechanism of low-temperature Water Gas Shift reaction on copper, Journal of the American Chemical Society, 130 (2008) 1402-1414.

[194] Y. Chen, H. Wang, R. Burch, C. Hardacre, P. Hu, New insight into mechanisms in water-gas-shift reaction on $Au/CeO_2(111)$: A density functional theory and kinetic study, Faraday Discussions, 152 (2011) 121-133.

[195] R. Burch, A. Goguet, F.C. Meunier, A critical analysis of the experimental evidence for and against a formate mechanism for high activity water-gas shift catalysts, Applied Catalysis A: General, 409–410 (2011) 3-12.

[196] L.C. Grabow, A.A. Gokhale, S.T. Evans, J.A. Dumesic, M. Mavrikakis, Mechanism of the Water Gas Shift Reaction on Pt: First Principles, Experiments, and Microkinetic Modeling, The Journal of Physical Chemistry C, 112 (2008) 4608-4617.

[197] C. Karakaya, R. Otterstätter, L. Maier, O. Deutschmann, Kinetics of the water-gas shift reaction over Rh/Al_2O_3 catalysts, Applied Catalysis A: General, 470 (2014) 31-44.

[198] O.R. Inderwildi, S.J. Jenkins, D.A. King, An Unexpected Pathway for the Catalytic Oxidation of Methylidyne on Rh(111) as a Route to Syngas, Journal of the American Chemical Society, 129 (2007) 1751-1759.

[199] O.R. Inderwildi, S.J. Jenkins, D.A. King, Mechanistic Studies of Hydrocarbon Combustion and Synthesis on Noble Metals, Angewandte Chemie International Edition, 47 (2008) 5253-5255.

[200] W.Z. Weng, M.S. Chen, Q.G. Yan, T.H. Wu, Z.S. Chao, Y.Y. Liao, H.L. Wan, Mechanistic study of partial oxidation of methane to synthesis gas over supported rhodium and ruthenium catalysts using in situ time-resolved FTIR spectroscopy, Catalysis Today, 63 (2000) 317-326.

[201] E. Shustorovich, The Bond-Order Conservation Approach to Chemisorption and Heterogeneous Catalysis: Applications and Implications, in: H.P. D.D. Eley, B.W. Paul (Eds.) Advances in Catalysis, Academic Press, 1990, pp. 101-163.

[202] M.J. Hei, H.B. Chen, J. Yi, Y.J. Lin, Y.Z. Lin, G. Wei, D.W. Liao, CO_2-reforming of methane on transition metal surfaces, Surface Science, 417 (1998) 82-96.

[203] D. Chan, S. Tischer, J. Heck, C. Diehm, O. Deutschmann, Correlation between catalytic activity and catalytic surface area of a Pt/Al_2O_3 DOC: An experimental and microkinetic modeling study, Applied Catalysis B: Environmental, 156-157 (2014) 153-165.

[204] A. Szabó, M.A. Henderson, J.T. Yates, Oxidation of CO by oxygen on a stepped platinum surface: Identification of the reaction site, The Journal of Chemical Physics, 96 (1992) 6191-6202.

[205] G.S. Zafiris, R.J. Gorte, CO Oxidation on $Pt/\alpha\text{-}Al_2O_3(0001)$: Evidence for Structure Sensitivity, Journal of Catalysis, 140 (1993) 418–423.

[206] J. Segner, C.T. Campbell, G. Doyen, G. Ertl, Catalytic-oxidation of CO on Pt(111) - the influence of surface-defects and composition on the reaction dynamics, Surface Science, 138 (1984) 505-523.

[207] C. Wheeler, A. Jhalani, E.J. Klein, S. Tummala, L.D. Schmidt, The water–gas-shift reaction at short contact times, Journal of Catalysis, 223 (2004) 191-199.

[208] K.C. Waugh, Methanol synthesis, Catalysis Letters, 142 (2012) 1153-1166.

[209] S. Wang, G.Q.M. Lu, CO_2 reforming of methane on Ni catalysts: Effects of the support phase and preparation technique, Applied Catalysis B: Environmental, 16 (1998) 269-277.

[210] M.B. Lee, Q.Y. Yang, S.L. Tang, S.T. Ceyer, Activated dissociative chemisorption of CH4 on Ni(111): Observation of a methyl radical and implication for the pressure gap in catalysis, Journal of Chemical Physics, 85 (1986) 1693.

[211] J.T.P. Beebe, D.W. Goodman, B.D. Kay, J.J.T. Yates, Kinetics of the activated dissociative adsorption of methane on the low index planes of nickel single crystal surfaces, Journal of Chemical Physics, 87 (1987) 2305-2315.

[212] I. Chorkendorff, I. Alstrup, S. Ullmann, Xps study of chemisorption of CH_4 on Ni(100), Surface Science, 227 (1990) 291-296.

[213] H. Yang, J.L. Whitten, Dissociative chemisorption of CH_4 on Ni(111), The Journal of Chemical Physics, 96 (1992) 5529-5537.

[214] J. H. Larsen, I. Chorkendorff, From fundamental studies of reactivity on single crystals to the design of catalysts, Surface Science Reports, 35 (1999) 163-222.

[215] G. Henkelman, A. Arnaldsson, H. Jonsson, Theoretical calculations of CH_4 and H_2 associative desorption from Ni(111): Could subsurface hydrogen play an important role?, The Journal of Chemical Physics, 124 (2006) 044706.

[216] R.M. Watwe, H.S. Bengaard, J.R. Rostrup-Nielsen, J.A. Dumesic, J.K. Nørskov, Theoretical studies of stability and reactivity of CHx species on Ni(111), Journal of Catalysis, 189 (2000) 16-30.

[217] A. Michaelides, P. Hu, A first principles study of CH_3 dehydrogenation on Ni(111), The Journal of Chemical Physics, 112 (2000) 8120-8125.

[218] C. Pistonesi, A. Juan, B. Irigoyen, N. Amadeo, Theoretical and experimental study of methane steam reforming reactions over nickel catalyst, Applied Surface Science, 253 (2007) 4427-4437.

[219] R. Jin, Y. Chen, W. Li, W. Cui, Y. Ji, C. Yu, Y. Jiang, Mechanism for catalytic partial oxidation of methane to syngas over a Ni/Al2O3 catalyst, Applied Catalysis A: General, 201 (2000) 71-80.

[220] S. Shen, C. Li, C. Yu, Mechanistic study of partial oxidation of methane to syngas over a Ni/Al2O3 catalyst, in: D.S.F.F.A.V. A. Parmaliana, A. F (Eds.) Studies in Surface Science and Catalysis, Elsevier, 1998, pp. 765-770.

[221] J.-H. Ryu, K.-Y. Lee, H. La, H.-J. Kim, J.-I. Yang, H. Jung, Ni catalyst wash-coated on metal monolith with enhanced heat-transfer capability for steam reforming, Journal of Power Sources, 171 (2007) 499-505.

[222] H. Jung, W.L. Yoon, H. Lee, J.S. Park, J.S. Shin, H. La, J.D. Lee, Fast start-up reactor for partial oxidation of methane with electrically-heated metallic monolith catalyst, Journal of Power Sources, 124 (2003) 76-80.

[223] Z.-F. Yan, R.-G. Ding, L.-H. Song, L. Qian, Mechanistic Study of Carbon Dioxide Reforming with Methane over Supported Nickel Catalysts, Energy & Fuels, 12 (1998) 1114-1120.

[224] X. Chen, K. Honda, Z.-G. Zhang, A comprehensive comparison of CH_4-CO_2 reforming activities of NiO/Al_2O_3 catalysts under fixed- and fluidized-bed operations, Applied Catalysis A: General, 288 (2005) 86-97.

[225] M.C.J. Bradford, M.A. Vannice, CO2 reforming of CH4, Catal Rev, 41 (1999) 1-42.

[226] F.T.V.I. Golovitchev, L. Chomial, SAE paper 1999-01-3552, in: http://www.tfd.chalmers.se/~valerie/MECH.html 1999.

[227] J. Warnatz, R.W. Dibble, U. Maas, Combustion, Physical and Chemical Fundamentals, Modeling and Simulation, Experiments, Pollutant Formation,, Springer Verlag, New York, 1996.

[228] M. Dente, E. Ranzi, A.G. Goossens, Detailed Prediction of Olefin Yields from Hydrocarbon Pyrolysis through a Fundamental Simulation-Model (Spyro), Comput Chem Eng, 3 (1979) 61-75.

[229] A.M. Dean, Detailed Kinetic Modeling of Autocatalysis in Methane Pyrolysis, J Phys Chem-Us, 94 (1990) 1432-1439.

[230] W. Tsang, R.F. Hampson, Chemical Kinetic Database for Combustion Chemistry .1. Methane and Related-Compounds, J Phys Chem Ref Data, 15 (1986) 1087-1279.

[231] H. Wang, M. Frenklach, A detailed kinetic modeling study of aromatics formation in laminar premixed acetylene and ethylene flames, Combustion and Flame, 110 (1997) 173-221.

[232] F. Solymosi, G. Kutsan, A. Erdohelyi, Catalytic reaction of CH_4 with CO_2 over alumina-supported Pt metals, Catalysis Letters, 11 (1991) 149-156.

[233] T. Kaltschmitt, L. Maier, M. Hartmann, C. Hauck, O. Deutschmann, Influence of gas-phase reactions on catalytic reforming of isooctane, Proceedings of the Combustion Institute, 33 (2011) 3177-3183.

[234] A. Holmen, O. Olsvik, O.A. Rokstad, Pyrolysis of Natural-Gas - Chemistry and Process Concepts, Fuel Process Technol, 42 (1995) 249-267.

[235] I.I. Bobrova, N.N. Bobrov, V.V. Chesnokov, V.N. Parmon, Catalytic steam reforming of methane: New data on the contribution of homogeneous radical reactions in the gas phase: II. A ruthenium catalyst, Kinet Catal+, 42 (2001) 805-812.

[236] R.A. Migone, S.K. Agarwal, G. Marcelin, Differences in Catalytic and Gas-Phase Reactions in Methane Coupling, J Chem Soc Chem Comm, 3 (1990) 223-225.

[237] K. Norinaga, O. Deutschmann, Detailed kinetic modeling of gas-phase reactions in the chemical vapor deposition of carbon from light hydrocarbons, Industrial & Engineering Chemistry Research, 46 (2007) 3547-3557.

[238] B.T. Schädel, O. Deutschmann, Steam reforming of natural gas on noble-metal based catalysts: Predictive modeling, Natural Gas Conversion VIII, 167 (2007) 207-212.

[239] A. Becker, K.J. Huttinger, Chemistry and kinetics of chemical vapor deposition of pyrocarbon - IV - Pyrocarbon deposition from methane in the low temperature regime, Carbon, 36 (1998) 213-224.

[240] A.J. Li, O. Deutschmann, Transient modeling of chemical vapor infiltration of methane using multi-step reaction and deposition models, Chemical Engineering Science, 62 (2007) 4976-4982.

[241] A.L. Cava, D.L. Trimm, Growth of Carbon Particles during Pyrolysis, Carbon, 16 (1978) 505-506.

[242] K. Norinaga, V.M. Janardhanan, O. Deutschmann, Detailed chemical kinetic modeling of pyrolysis of ethylene, acetylene, and propylene at 1073-1373 K with a plug-flow reactor model, International Journal of Chemical Kinetics, 40 (2008) 199-208.

[243] J. Sehested, S. Dahl, J. Jacobsen, J.R. Rostrup-Nielsen, Methanation of CO over Nickel: Mechanism and Kinetics at High H_2/CO Ratios, The Journal of Physical Chemistry B, 109 (2004) 2432-2438.

[244] J.R. Rostrup-Nielsen, K. Pedersen, J. Sehested, High temperature methanation: Sintering and structure sensitivity, Applied Catalysis A: General, 330 (2007) 134-138.

[245] J.C. Tracy, Structural Influences on Adsorption Energy. II. CO on Ni(100), The Journal of Chemical Physics, 56 (1972) 2736-2747.

[246] P. Sabatier, J.B.C.R. Senerens, Acad. Sci., Paris, 134 (1902) 514.

[247] J.W.E. Coenen, P.F.M.T. van Nisselrooy, M.H.J.M. de Croon, P.F.H.A. van Dooren, R.Z.C. van Meerten, The dynamics of methanation of carbon monoxide on nickel catalysts, Applied Catalysis, 25 (1986) 1-8.

[248] I. Alstrup, On the Kinetics of Co Methanation on Nickel Surfaces, Journal of Catalysis, 151 (1995) 216-225.

[249] G.A. Mills, F.W. Steffgen, Catalytic Methanation, Catalysis Reviews, 8 (1974) 159-210.

[250] R. Yadav, R.G. Rinker, Steady-state methanation kinetics over a Ni/Al_2O_3 catalyst, The Canadian Journal of Chemical Engineering, 71 (1993) 202-208.

[251] S.V. Ho, P. Harriott, The kinetics of methanation on nickel catalysts, Journal of Catalysis, 64 (1980) 272-283.

[252] J.A. Dalmon, G.A. Martin, The kinetics and mechanism of carbon monoxide methanation over silica-supported nickel catalysts, Journal of Catalysis, 84 (1983) 45-54.

[253] J.R. Rostrup-Nielsen, K. Pedersen, Sulfur poisoning of Boudouard and methanation reactions on nickel catalysts, Journal of Catalysis, 59 (1979) 395-404.

[254] D. Wayne Goodman, J.T. Yates Jr, T.E. Madey, Interaction of hydrogen, carbon monoxide, and methanol with Ni(100), Surface Science, 93 (1980) L135-L142.

[255] R.D. Kelly, D.W. Goodman, In The Chemical Physics of Solid Surfaces and Heterogeneous Catalysis, Elsevier: Amsterdam, 1982.

[256] A. Berkó, H.P. Bonzel, Modification of the methanation activity on a Ni(111) surface by Ar ion bombardment, Surface Science, 251–252 (1991) 1112-1116.

[257] A.P. Grosvenor, M.C. Biesinger, R.S.C. Smart, N.S. McIntyre, New interpretations of XPS spectra of nickel metal and oxides, Surface Science, 600 (2006) 1771-1779.

[258] M.W. Roberts, R.S.C. Smart, The defect structure of nickel oxide surfaces as revealed by photoelectron spectroscopy, Journal of the Chemical Society, Faraday Transactions 1: Physical Chemistry in Condensed Phases, 80 (1984) 2957-2968.

[259] H. Guo, F. Zaera, The reactivity of hydroxyl groups toward ammonia on Ni(110) surfaces, Surface Science, 524 (2003) 1-14.

[260] R.E. Hayes, W.J. Thomas, K.E. Hayes, A study of the nickel-catalyzed methanation reaction, Journal of Catalysis, 92 (1985) 312-326.

[261] A. Berkó, F.P. Coenen, H.P. Bonzel, Structure sensitivity of methanation on nickel, Vacuum, 41 (1990) 147-149.

[262] R.D. Kelley, S. Semancik, On the mechanism of fischer-tropsch synthesis on a single crystal nickel catalyst, Journal of Catalysis, 84 (1983) 248-251.

[263] P. Biloen, J.N. Helle, F.G.A. van den Berg, W.M.H. Sachtler, On the activity of Fischer-Tropsch and methanation catalysts: A study utilizing isotopic transients, Journal of Catalysis, 81 (1983) 450-463.

[264] R.S. Polizzotti, J.A. Schwarz, Hydrogenation of CO to methane: Kinetic studies on polycrystalline nickel foils, Journal of Catalysis, 77 (1982) 1-15.

[265] S. Fujita, H. Terunuma, M. Nakamura, N. Takezawa, Mechanisms of methanation of carbon monoxide and carbon dioxide over nickel, Industrial & Engineering Chemistry Research, 30 (1991) 1146-1151.

[266] R.P. Underwood, C.O. Bennett, The COH_2 reaction over nickel-alumina studied by the transient method, Journal of Catalysis, 86 (1984) 245-253.

[267] R.Z.C. van Meerten, J.G. Vollenbroek, M.H.J.M. de Croon, P.F.M.T. van Nisselrooy, J.W.E. Coenen, The kinetics and mechanism of the methanation of carbon monoxide on a nickel-silica catalyst, Applied Catalysis, 3 (1982) 29-56.

[268] G. Mills, Catalytic Methanation, Catalysis reviews-science and engineering, 8(2) (1973) 159-210.

[269] M.P. Andersson, F. Abild-Pedersen, I.N. Remediakis, T. Bligaard, G. Jones, J. Engbæk, O. Lytken, S. Horch, J.H. Nielsen, J. Sehested, J.R. Rostrup-Nielsen, J.K. Nørskov, I. Chorkendorff, Structure sensitivity of the methanation reaction: H2-induced CO dissociation on nickel surfaces, Journal of Catalysis, 255 (2008) 6-19.

[270] H. Nakano, K. Okazaki, Y. Ajiro, T. Suzuki, K. Oba, Clinical usefulness of the common carotid artery blood flow velocity ratio as measured by an ultrasonic quantitative flow measurement system:

evaluation with respect to prevalence of ischemic heart disease, Journal of Nippon Medical School = Nihon Ika Daigaku zasshi, 68 (2001) 482-489.

[271] K. Pedersen, A. Skov, J.R. Rostrupnielsen, Catalytic aspects of high-temperature methanation, Abstracts of Papers of the American Chemical Society, 179 (1980) 60.

[272] W.M. Shen, J.A. Dumesic, C.G. Hill Jr, Criteria for stable Ni particle size under methanation reaction conditions: Nickel transport and particle size growth via nickel carbonyl, Journal of Catalysis, 68 (1981) 152-165.

[273] J. Engbæk, O. Lytken, J.H. Nielsen, I. Chorkendorff, CO dissociation on Ni: The effect of steps and of nickel carbonyl, Surface Science, 602 (2008) 733-743.

[274] D.W. Goodman, R.D. Kelley, T.E. Madey, J.T. Yates Jr, Kinetics of the hydrogenation of CO over a single crystal nickel catalyst, Journal of Catalysis, 63 (1980) 226-234.

[275] R.D. Kelley, D.W. Goodman, Catalytic methanation over single crystal nickel and ruthenium: Reaction kinetics on different crystal planes and the correlation of surface carbide concentration with reaction rate, Surface Science, 123 (1982) L743-L749.

[276] C.H. Bartholomew, Mechanisms of catalyst deactivation, Applied Catalysis A: General, 212 (2001) 17-60.

[277] C.H. Bartholomew, Carbon deposition in steam reforming and methanation, Catalysis reviews, 24 (1982) 67-112.

[278] M. Agnelli, M. Kolb, C. Mirodatos, CO hydrogenation on a nickel catalyst . 1. Kinetics and modeling of a low-temperature sintering process, Journal of Catalysis, 148 (1994) 9-21.

[279] H. Godoy Guerrero, Study of the methanation reaction with a non-perfectly purified synthesis gas, in: Chemical Fuels, Engler- Bunte Institut, Karlsruhe Institute of Technology, Karlsruhe, 2012, pp. 62.

Acknowledgements

I would like to express my gratitude to all of those who have provided me with opportune advice and constant motivation, for your support was of great importance in the successful completion of my dissertation.

For his valuable and constructive suggestions during the planning and development of this research work, as well as for his willingness to give me the opportunity to grow as a scientist within his research group, I wish to extend my very great appreciation to Prof. Dr. Olaf Deutschmann.

I would also like to thank Dr. Stephan Schunk, Thomas Roussière and Guido Wasserschaft from the AG, as well as E. Schwab and A. Milanov from BASF for facilitating the experimental data as well as the catalysts.

For the contribution granted through a valuable teamwork along with opportune discussions, I would like to thank the participants of the BMWi-project DRYREF: E. Schwab (BASF), A. Milanov (BASF), S. Schunk (hte AG), T. Roussière (hte AG), G. Wasserschaft (hte AG), J. Klein (hte AG), T. Mäurer (hte AG), A. Behrens (Linde AG), N. Schödel (Linde AG), R. Gläser (Uni Leipzig), J. Titus (Uni Leipzig), B. Stolze (Uni Leipzig), A. Jentys (TU München), J. Lercher (TU München), L. Schulz (TU München), as well as M. Gahr.

I would like to thank Prof. Dr. Jan-Dierk Grunwaldt for agreeing to be my co-supervisor.

Special gratitude should be expressed towards Dr. Lubow Maier, for her guidance and disposition to constantly sharing her valuable knowledge, thus becoming a mentor for me. I would like to thank Dr. Steffen Tischer for his opportune advice and priceless contributions to this work. I am particularly grateful to Dr. Maier, Dr. Tischer, and Dr. Diehm for proof-reading this dissertation.

Assistance provided Alex Zellner and Azize Ünal during the experimental work is deeply appreciated, as well the technical support provided by Leonahard Rutz.

I would like to acknowledge the collaboration, through a valuable scientific exchange, of Dominik Schollenberger in the CO methanation, as well as the inestimable contribution made by Canan Karakaya in performing the stagnation flow experiments.

Within my research group, I wish to express my gratitude towards my colleagues in the AKD group, especially Vikram Menon and Sivaram Kannepalli for proof-reading this thesis and for their much appreciated friendship.

Advice and support given by Dr. Matthias Hettel and Ursula Schwald during the development of this project is deeply appreciated. I would like to express my profound gratitude to my dear friend Yvonne Dedecek, for her affection and friendship, and for always making my days more enjoyable.

Finally, I wish to thank my family, particularly my mother, for her infinite support and encouragement throughout my study. I cannot find the words to express my gratitude towards Pablo Granados, for his inexhaustible support in every possible way, for being a source of motivation, and for playing a fundamental role in my life.

Publications

[1] L. Maier,B. Schödel, K. Herrera Delgado, S.Tischer, O. Deutschmann. Steam Reforming of Methane Over Nickel: Development of a Multi-Step Surface Reaction Mechanism, Topics in Catalysis. 2011, 54, 845-858.

[2] L.C.S. Kahle, T. Roussière, L. Maier, K. Herrera Delgado, G. Wasserschaff, S.A. Schunk, O. Deutschmann. Methane Dry Reforming at High Temperature and Elevated Pressure: Impact of Gas-Phase Reactions, Industrial & Engineering Chemistry Research. 2013, 52 (34),11920-11930.

[3] K. Herrera Delgado, L. Maier, A. Zellner, O. Deutschmann. Development of a unified surface reaction mechanism for oxidation and reforming of CH_4 over nickel based catalyst, in preparation.

[4] K. Herrera Delgado, L. Maier, O. Deutschmann. Kinetics of hydrogen, CO oxidation, water-gas shift and its reverse reaction over nickel catalyst, in preparation.

Conferences Participation

Conference presentations

[1] E. Schwab, A. Milanov, T. Roussière, S. Schunk, G. Wasserschaff, A. Behrens, N. Schödel, L.Burger, O. Deutschmann, K. Herrera Delgado, R. Gläser, J. Titus, B. Stolze, A. Jentys, J. Lercher, L. Schulz. Dry Reforming of CH_4 with CO_2 at Elevated Pressures.15th International Congress on Catalysis 2012. München, Germany.

[2] K. Herrera Delgado, L. Kahle, L. Maier, S. Tischer, O. Deutschmann, G. Wasserschaff, T. Roussière, S. Schunk. Surface Reaction Kinetics of Steam- and CO_2-reforming as well as Oxidation of Methane over Ni. 46. Jahrestreffen Deutscher Katalytiker, 13. - 15. March 2013, Weimar, Germany.

[3] K. Herrera Delgado, L. Maier, O. Deutschmann. Surface Reaction Kinetics of Steam- and CO_2-reforming as well as Oxidation of Methane over Ni. 23rd North American Catalysis Society Meeting- NAM, 2. - 7. June 2013, Louisville, Kentucky, USA.

Poster presentations

[1] K. Herrera Delgado, L. Maier, O. Deutschmann. Development of a Combined Surface Reaction Mechanism for Steam- and Dry Reforming of Methane over Nickel. 44. Jahrestreffen Deutscher Katalytiker, 2011, Weimar, Deutschland.

[2] K. Herrera Delgado, L. Maier, O. Deutschmann. Modeling the Steam and Dry Reforming of Methane over Nickel. European Congress on Catalysis – EuropaCat X, 2011, Glasgow, Scotland.

[3] K. Herrera Delgado, L. Maier, O. Deutschmann Modeling Oxidation and Reforming of Hydrogen, Carbon Monoxide, and Methane over Nickel Catalysts. 45. Jahrestreffen Deutscher Katalytiker, 2012, Weimar, Germany.

[4] T. Roussiére, S. Schunk, G. Wasserschaff, A. Milanov, E. Schwab, A. Behrens, N. Schödel, L. Burger, O. Deutschmann, K. Herrera Delgado,R. Gläser, J. Peters, B. Stolze, A. Jentys, J. Lercher, L. Schulz DRYREF: Dry Reforming of CO_2 at Elevated Pressures. 45. Jahrestre_en Deutscher Katalytiker 2012, Weimar, Germany.

[5] K. Herrera Delgado, L. Maier, O. Deutschmann. Modeling Oxidation and Reforming of Hydrogen, Carbon Monoxide, and Methane over Nickel Catalysts. 15th International Congress on Catalysis 2012. München, Germany.

[6] K. Herrera Delgado, L. Maier, O. Deutschmann. Surface Reaction Kinetics for Oxidation and Reforming of Methane over Ni/Al2O3. European Congress on Catalysis- EuropaCat XI, 2013, Lyon; France.

Eidesstattliche Erklärung

Hiermit versichere ich, die vorliegende Doktorarbeit selbstständig angefertigt und keine anderen als die von mir angegebenen Quellen und Hilfsmittel verwendet, sowie wörtliche und sinngemäße Zitate als solche gekennzeichnet zu haben. Die Arbeit wurde in gleicher oder ähnlicher Form keiner anderen Prüfungsbehörde zur Erlangung eines akademischen Grades vorgelegt.

Karlsruhe, den

18 Juli, 2014 

Datum und Unterschrift